Interner Bericht

DLR-IB-SL-HF-2026-30

Development and Evaluation of Advanced Air Mobility Supported Logistics for Offshore Wind Energy with Agent-Based Simulation

Masterarbeit

Nils Raaf

Deutsches Zentrum für Luft- und Raumfahrt

Institut für Systemarchitekturen in der Luftfahrt
Hamburg

Deutsches Zentrum
für Luft- und Raumfahrt

Dokumenteigenschaften

Titel	Development and Evaluation of Advanced Air Mobility Supported Logistics for Offshore Wind Energy with Agent-Based Simulation
Betreff	Masterarbeit
Institut	Institut für Systemarchitekturen in der Luftfahrt
Erstellt von	Nils Raaf
Beteiligte	Patrick Ratei (DLR, Betreuer)
Geprüft von	Martin Wagner (HAW Hamburg, Erstprüfer) & Prajwal Shiva Prakasha (DLR, Zweitprüfer)
Freigabe von	-
Zugänglichkeit	Stufe 1: Allgemein zugänglich (in elib ohne Zugangsbeschränkung)
Datum	März 2026
Version	1.0
Datei Info	-

HAW
HAMBURG

Master Thesis

Nils Raaf

Development and Evaluation of Advanced Air Mobility supported Logistics for Offshore Wind Energy with Agent-Based Simulation

Fakultät Luftfahrt- und Fahrzeugsysteme

Faculty of Aviation and Automotive Systems

Nils Raaf

Development and Evaluation of Advanced Air Mobility supported Logistics for Offshore Wind Energy with Agent-Based Simulation

Master thesis submitted as part of the Master examination

in the degree course Aeronautical Engineering
at the Faculty of Aviation and Automotive Systems
of the Hamburg University of Applied Sciences

In Cooperation with:
German Aerospace Center (DLR)
Institute of System Architectures in Aeronautics
Department of Aviation System Concepts and Assessment
Hein-Saß-Weg 22
21129 Hamburg

First Examiner: Prof. Dr.-Ing. Martin Wagner
Second Examiner: Prajwal Shiva Prakasha, M.Sc.

Submission date: 03.03.2026

Advanced Air Mobility for Maritime Logistics

Development and Evaluation of Advanced Air Mobility supported Logistics for Offshore Wind Energy with Agent-Based Simulation

Task for a Master Thesis

German Aerospace Center (DLR)
Institute of System Architectures in Aeronautics
Aviation System Concepts and Assessment
Hein-Saß-Weg 22, 21129 Hamburg

Student: Nils Raaf

1st Examiner: Prof. Dr.-Ing. Martin Wagner (HAW Hamburg)
2nd Examiner: Prajwal Shiva Prakasha, M.Sc. (DLR)
Supervisor: Patrick Ratei, M.Sc. (DLR)

Background

Offshore wind energy is rapidly expanding, particularly in the North Sea, driven by national and European renewable energy strategies. As installed capacities and the age of existing wind farms increase, innovative logistic solutions are intensively researched and trialed, one of which is the use of unmanned cargo drones.

Task

The task of this thesis is situated in the field of logistics for offshore wind energy, with a specific focus on the use of Advanced Air Mobility (AAM) aircraft for maintenance and repair operations. The main objective is the integration and evaluation of AAM based logistics concepts within the DLR System of Systems Inverse Design (SoSID) Toolkit. For this purpose, the offshore environment shall be represented in the simulation framework, and different aircraft concepts must be embedded into realistic operational scenarios. By varying parameters from both the aircraft design level and the fleet configuration level, the performance of the overall System of Systems (SoS) can be systematically assessed and compared.
In summary, the task can be divided into the following subtasks:

- Conducting a literature study on existing logistics operations and AAM applications in offshore wind energy
- Implementing the offshore environment and operational scenarios in the SoSID Toolkit
- Developing suitable AAM aircraft agents
- Performing parametric variations of aircraft design parameters (e.g. payload capacity, range) and fleet-level parameters (e.g. fleet size)
- Evaluating the impact of these variations on the efficiency and robustness of the SoS
- Identifying potentials and limitations of AAM based logistics concepts for offshore wind applications

Abstract

Nils Raaf

Title of the Thesis: Development and Evaluation of Advanced Air Mobility supported Logistics for Offshore Wind Energy with Agent-Based Simulation

Keywords: AAM, Agent-based Simulation, Offshore Logistics, Maritime Aviation, Offshore Wind Farms, UAV, VTOL

Abstract: Offshore wind farm operations and maintenance depend on reliable logistics for personnel transfer and time-critical equipment deliveries under environmental and operational constraints. Integrating uncrewed aerial vehicles (UAVs) adds flexibility, but interactions between vehicles, dispatching, and mission timing introduce effects that are difficult to assess analytically. This thesis develops and applies an agent-based System of Systems simulation framework to evaluate offshore logistics concepts combining crew transfer vessels, helicopters, and VTOL-capable UAVs. A design of experiments varies wind farm distance, fleet sizes, maintenance durations, and stochastic spontaneous material demands. Performance is evaluated using fleet energy consumption, enabled maintenance hours. The results show that UAV-supported strategies can reduce fleet energy consumption and improve turbine availability. UAV-based spontaneous delivery of spare parts and tools is identified as a effective near-term concept, while full UAV equipment transport can increase enabled maintenance activity but may increase energy demand depending on UAV sizing and mission structure.

Kurzzusammenfassung: Der Offshore-Betrieb und die Instandhaltung von Windparks sind auf zuverlässige Logistik für Wartungsteams und zeitkritische Materiallieferungen angewiesen, eingeschränkt durch Umwelt- und Betriebsvorgaben. Die Integration unbemannter Luftfahrzeuge (UAVs) erhöht die Flexibilität, Wechselwirkungen zwischen Fahrzeugen, Dispatching und Missionsablauf führen aber zu Effekten, die analytisch nur schwer zu bewerten sind. Diese Arbeit entwickelt und nutzt ein agentenbasiertes System-of-Systems-Simulationsframework zur Bewertung von Offshore-Logistikkonzepten, die Schiffe, Hubschrauber und VTOL-fähige UAVs kombinieren. Ein Design of Experiments variiert Windparkentfernung, Flottengrößen, Wartungsdauern und stochastische spontane Materialbedarfe. Bewertet wird anhand von Gesamtflottenenergieverbrauch, ermöglichten Wartungsstunden und der Verfügbarkeit der Anlagen. Die Ergebnisse zeigen, dass UAV-gestützte Strategien den Energieverbrauch senken und die Anlagenverfügbarkeit erhöhen können. Effektiv und kurzfristig umsetzbar ist die UAV-gestützte Nachlieferung von kleinen Ersatzteilen und Werkzeugen, während Equipmenttransporte per UAV zwar die möglichen Wartungsstunden erhöhen können, aber je nach UAV-Auslegung und Missionsstruktur auch den Energieverbrauch der Gesamtflotte steigern.

“[T]ruth […] is much too complicated to allow anything but approximations.”

John von Neumann[1]

Contents

List of Figures

List of Tables

List of Abbreviations

AAM	Advanced Air Mobility
ABM	Agent-Based Modeling
AWZ	Ausschließliche Wirtschaftszone (Exclusive Economic Zone)
BDLI	Bundesverband der Deutschen Luft- und Raumfahrtindustrie (German Aerospace Industries Association)
BE	Batteryelectric
BMDV	Federal Ministry for Digital and Transport (Germany)
BVLOS	Beyond Visual Line of Sight
BWO	Bundesverband Windenergie Offshore (German Offshore Wind Farm Operators Association)
CE	Combustion Engine
CFD	Computational Fluid Dynamics
ConOps	Concept of Operations
CTV	Crew Transfer Vessel
DLR	Deutsches Zentrum für Luft- und Raumfahrt (German Aerospace Center)
ECMWF	European Centre for Medium-Range Weather Forecasts
EHF	Equipment Health Factor
ERA5	ECMWF reanalysis dataset (ERA5)
eVTOL	Electric Vertical Take-Off and Landing
FAA	Federal Aviation Administration
FoM	Figure of Merit
HEMS	Helicopter Emergency Medical Services
ICE	Internal Combustion Engine
INOP	Inoperable State
ISA	International Standard Atmosphere
JSON	JavaScript Object Notation
L+C	Lift + Cruise Configuration
MET	Norwegian Meteorological Institute
MTOM	Maximum Take-Off Mass
NOAA	National Oceanic and Atmospheric Administration
NORA3	High-resolution weather hindcast/reanalysis for Northern Europe
OpEx	Operational Expenditures
OSV	Offshore Support Vessel
OWF	Offshore Wind Farm
PCHIP	Piecewise Cubic Hermite Interpolating Polynomial
SAR	Search and Rescue
SFC	Specific Fuel Consumption
SoS	System of Systems

SoSID	System of Systems Inverse Design
SOV	Service Operation Vessel
SSV	Service Support Vessel
SWATH	Small Waterplane Area Twin Hull
TAS	True Airspeed
TLARs	Top Level Aircraft Requirements
TR	Tiltrotor
TW	Tiltwing
UAM	Urban Air Mobility
UAV	Uncrewed Aerial Vehicle
UTC	Coordinated Universal Time
VTOL	Vertical Take-Off and Landing

List of Symbols

A	Rotor Disk Area
a	Year
AR	Wing Aspect Ratio
$c_{1\ldots4}$	Deaves-Harris Fit Coefficient
C_D	Total Drag Coefficient
$C_{D,0}$	Zero-Lift Drag Coefficient
$C_{D,f}$	Fuselage Drag Coefficient (Reference Area)
$C_{D,i}$	Induced Drag Coefficient
$C_{f,eq}$	Equivalent Skin-Friction Coefficient
C_P	Power Coefficient
C_Q	Torque Coefficient
C_T	Thrust Coefficient
$decl$	Solar Declination
$eqtime$	Equation of Time
f_{UAV}	Equivalent Flat-Plate Area (UAV Method)
f_{VTOL}	Equivalent Flat-Plate Area (VTOL Method)
FM	Figure of Merit
g	Gravitational Acceleration
g_0	Standard Gravity
h_{utc}	UTC Hour
ha	Solar Hour Angle
lat	Latitude
lon	Longitude
M	Mach Number
m_{eng}	Engine Mass
m_{lg}	Landing-Gear Mass
m_{wing}	Wing Mass
N_d	Day Number in Year
N_Z	Ultimate Load Factor
n_{CTVs}	Number of available CTVs
n_{Helis}	Number of available Helicopters
n_{Teams}	Number of Technician Teams on Turbines
n_{wheels}	Number of Landing-Gear Wheels
p	Pressure
P	Power
P_{AW}	Wave-Induced Power Share
P_{CW}	Calm-Water Power Share
P_{CW,v_D}	Calm-Water Power at Design Speed v_D
P_{tot}	Total Power

Q	Rotor Torque
R	Rotor Radius
R^2	Coefficient of Determination
S	Area
S_{ref}	Reference Area
S_{wet}	Wetted Area
S_{wing}	Wing Area
$t_{\text{forced,CTV}}$	Conservative Time until last Pickup by CTV
$t_{\text{forced,Heli}}$	Conservative Time until last Pickup by Helicopter
t_{hoist}	Time for one Hoisting Transfer
t_{init}	CTV Time from Loiter Point to first Turbine
t_{inter}	CTV Travel Time Between Turbines
t_{leg}	Flight Duration of one Leg
t_{SunEvent}	UTC Time of Sunrise or Sunset Event
t_{transfer}	Time required for one CTV Transfer at a Turbine
T	Thrust
$U(z)$	Wind Speed at Height z
U_{ref}	Reference Wind Speed at z_{ref}
u_*	Friction Velocity
v	Induced Velocity
v_c	Vertical Climb/Descent Speed
v_D	Design Vessel Speed
v_S	Sailing Speed
V_{GS}	Ground Speed
V_{hw}	Headwind Component
V_{TAS}	True Airspeed
V_∞	Free-Stream Flight Speed
V_{tip}	Rotor Blade Tip Speed
V_w	Wind Speed
W	Weight
z	Height Above Sea Surface
z_0	Aerodynamic Surface Roughness Length
z_{ref}	Reference Height
z_{sea}	Ocean Surface Roughness Length
$(t/c)_{\text{root}}$	Relative Airfoil Thickness at Wing Root
$\Delta\gamma$	Bearing-Wind Direction Difference
Δm_{fuel}	Fuel Mass Consumed per Time Step
Δt	Simulation Time Step
Δt_{UTC}	UTC Time Correction
α	Charnock Constant
γ	Fractional Year Length
γ_w	Wind Direction
κ	Von Kármán Constant
λ	Wing Taper Ratio
ψ_f	Flight Bearing
ζ	Significant Wave Height
ζ_{max}	Maximum Significant Wave Height

Chapter 1

Introduction

Climate change and the continued dependence on fossil resources are not only major societal challenges but also pose significant challenges for aviation and aviation research. In addition to measures applied to existing aircraft, efforts include the development of entirely new aircraft concepts and the adaptation of operational procedures to reduce fossil fuel consumption and associated emissions. At the same time, concepts and technologies originating from aviation are directly applied in the low-emission generation of renewable energy, which can in turn supply novel aircraft concepts, for example hydrogen-powered aircraft.

Wind turbines, operating according to the principles of aerodynamics and employing structural components made from fibre-reinforced composites, have for several years contributed a substantial share to global renewable energy production. Both onshore and offshore installations show a clear growth trend, reflected in increasing turbine numbers, rated power and physical size. However, to meet climate targets set by countries and alliances such as the European Union, a considerable further expansion of renewable energy capacity remains necessary.

Offshore wind farms (OWFs), such as Baltic 1 shown in Figure 1.1, are particularly relevant. Due to more favourable wind conditions compared to onshore locations and additional environmental factors, they allow the installation of particularly high-performance turbines that can be operated more effectively than their onshore counterparts [2]. Although OWFs are generally spreading globally, the coastal waters of Europe along the North Sea and the Baltic Sea stand out, as do the Chinese, Taiwanese, and Korean waters in the East China and Yellow Seas, with Chinese expansion far surpassing that of all other Asian and European countries [3]. Within Europe, the United Kingdom and Germany can be regarded as leading regions [3]. In addition, there remains significant potential in scarcely developed or yet undeveloped offshore regions worldwide, where improved or new technologies such as floating turbines may enable OWFs in previously unsuitable locations [4]. Nevertheless, the current expansion targets are ambitious. In Germany alone, installed capacity is due to increase from approximately 10 GW in 2025 to 70 GW by 2045 [5]. The European Union has likewise adopted targets that require high growth rates. From the 37 GW installed by the end of 2024 [6], 60 GW are to be reached by 2030 and 300 GW by 2050 [7].

The intention to continue pursuing these goals and, in particular, to establish the North Sea as a central pillar of European energy generation was reaffirmed again at the beginning of 2026 at the North Sea Summit by nine coastal states. By 2050, according to German Minister for Economic Affairs Katharina Reiche, 100 GW of wind power capacity is to be installed in the North Sea. The expansion and operation of the installed assets are intended to create jobs, increase security of supply, and reduce electricity prices [8].

Figure 1.1: Offshore Wind Farm EnBW Baltic 1, Source: EnBW / Matthias Ibeler [9]

With the increasing number of turbines, the rising complexity of modern systems, and the heterogeneous fleets of turbines installed over the past two decades, a range of challenges, questions, and tasks arises. While the rated power of turbines in the first commercial OWF in German waters Baltic 1 was still 2.3 MW [10], current projects deploy turbines with a capacity of 15 MW [11]. This trend is globally observable [12]. This development necessitates significant changes in operational processes and decision-making, which is evident for example in the selection of larger helicopter models for installation and maintenance logistics [13]. The increasing distance of new wind farms from the coast also leads to challenges for emergency response chains, since the helicopter models currently used can no longer reach the sites within the required response times [14]. Logistics for OWFs are inherently complex, which has led to numerous studies on the use of different vessel or helicopter fleets and their operational strategies [15, 16, 17].

A promising approach to meet the existing and future demand for logistics in installation and maintenance operations, while using cost-efficient and lower-emission vehicles, lies in the use of Uncrewed Aerial Vehicles (UAVs), particularly those with vertical take-off and landing (VTOL) capabilities. Multicopter UAVs are already widely used for inspection tasks, and recent years have seen numerous projects, studies, and trials exploring UAVs for cargo applications in OWFs [18]. However, the environmental conditions and other operational requirements of this use case present considerable challenges for commercial implementation, although initial steps toward commercialisation have already been taken [19]. Successful deliveries of parts required for maintenance, as shown in Figure 1.2, have been made in recent months.

UAVs for cargo logistics have been an active field of research for many years, with particular focus on use cases in an Advanced Air Mobility (AAM) context [21, 22, 23]. These concepts typically aim to transport small cargo items below 10 kg, such as retail prod-

Figure 1.2: VTOL Cargo Drone approaching an Offshore Wind Farm, Source: RWE [20]

ucts or medical supplies, over short distances directly to end users. Several of these ideas have already been realised in practice. In the United States, for example, goods can be delivered directly from central warehouses to customers' backyards in certain regions [24], and the use of drones for rapid delivery of blood products and vaccines in Africa has demonstrated positive effects on emergency medical care [25]. Larger UAVs designed for longer-range logistics applications, for example for time-critical spare parts transport or poorly connected regions, have also been investigated [26]. A maritime use case closely related to OWF logistics has already been demonstrated: in 2020, spare parts were transported over a distance of 80 km to a Norwegian gas production platform using a helicopter drone [27]. This trend toward greater range and payload capacity is reinforced by military applications, particularly in maritime contexts [28].

Although several UAV models have been tested in maritime environments and in OWFs, they have not yet reached regular operational use. A detailed, specific assessment of the benefits and feasibility of drone-supported logistics processes remains difficult for this use case because it constitutes a system of systems composed of different constituent systems, each with its own requirements and constraints. No comprehensive assessment of drone-supported logistics for OWFs that considers different UAV models, wind farms, and operational strategies has yet been published. Such an analysis would enable the evaluation and optimisation of existing UAV models or the derivation of Top Level Aircraft Requirements (TLARs) for adapted UAVs. Therefore, the aim of this work is to develop a simulation framework that enables such investigations and to evaluate initial concepts of operations and aircraft models.

Specifically, the following research question will be answered:

> *How do UAVs and UAV-enabled logistics strategies influence offshore wind energy generation at the System-of-Systems level?*

Chapter 2

Background

2.1 VTOL Cargo Drones

2.1.1 Categorization within AAM

Advanced Air Mobility (AAM) is a comparatively loosely defined term. However, despite differing definitions, the underlying meaning is largely consistent across sources. The Federal Aviation Administration (FAA) of the United States defines AAM as “a rapidly-emerging, new sector of the aerospace industry which aims to safely and efficiently integrate highly automated aircraft” into the existing airspace system. It further describes AAM as “a collection of new and emerging technologies being applied to the aviation transportation system, particularly in new aircraft types” [29]. In addition to passenger transport, particularly in urban and regional contexts, “large cargo delivery” is explicitly named as an AAM use case. The German Aerospace Industries Association (BDLI) similarly refers to the integration of new and innovative aircraft into existing airspace operations and likewise includes not only passenger but also cargo transport [30]. Civil drones are mentioned explicitly, and emphasis is placed on efficiency, sustainability, safety, and cost-effective aircraft. The company BAE Systems defines AAM in a very similar manner as “an air transport system concept that integrates new, transformational aircraft designs and flight technologies into existing and modified airspace operations” [31]. As an objective of AAM, the transport of people and cargo is described as being carried out more effectively than within existing transport systems. With regard to vehicles, it is stated that “innovative, yet cost-effective aircraft with a low carbon footprint” will emerge from the AAM concept. It is also highlighted that “virtually all of the developed AAM vehicles have all-electric or hybrid-electric power systems”, and UAVs are explicitly mentioned as well. The global consulting company PwC characterizes AAM as the deployment of “particularly electric vertical / conventional takeoff and landing (eVTOL/eCTOL) air taxis and heavy-lift cargo drones”. As a vision, “fast, flexible, cost-effective, and sustainable air transportation” is described as a complement to existing aviation infrastructure, enabling new use cases [32].

For Germany, an AAM Strategy was published in 2025 by the Federal Ministry for Digital and Transport (BMDV). Here, AAM is also described as the integration of new aviation technologies into the existing airspace structure: “Safe, orderly, seamless, sustainable and highly automated aviation and relevant systems protected against intentional harm, primarily taking place in the lowest airspace and between urban and rural areas and used to transport goods and passengers and for other aviation purposes, such as inspection and rescue operations. The technologies used in AAM are new aircraft, automated air traffic management systems, digital ecosystems and communication systems, which permit the integration of the new transport technologies into the multimodal transport system" [33].

Based on these definitions and characterizations, cargo transport by VTOL drones within the established offshore airspace, using new or recent vehicle concepts and particularly (hybrid) electric propulsion systems, can be classified as an AAM use case, with the objective of a more cost-efficient and more sustainable logistics system. The integration into the existing offshore infrastructure, which has already been investigated with regard to operational procedures and communication by Donkels et al. [34], and into an airspace environment used by general aviation, helicopters supporting offshore installations, and military aviation, constitutes a task that is fully consistent with the AAM concept.

The economic relevance of Advanced Air Mobility is supported by several studies. The BMDV AAM Strategy reports the global AAM economy in billion US dollars and projects, for 2030, a cargo market volume of approximately $15 billion, followed by significant growth to approximately 64 billion US $ by 2040 [33]. The PwC AAM report states that, between 2019 and 2023, cargo drone companies secured more than $2.8 billion in funding. For heavy-lift cargo drones, a market valuation of $1.2 billion is reported for 2024, with a forecast of $6.3 billion for 2034 [32]. This indicates a financially strong development landscape that can advance AAM use cases beyond the concept phase and into practical testing.

2.1.2 VTOL UAV Configurations and Powertrains

VTOL drones can generally be categorized by their configuration and the powertrain employed, where the choice of configuration and powertrain are closely linked. Configurations that are typically associated with the passenger-carrying eVTOL category are also common in this context, but configurations from traditional manned aviation can be found as well, such as the conventional helicopter. A coarse classification of configurations commonly used for VTOL UAVs is shown in Figure 2.1, based on the aircraft surveyed and summarised in Appendix A and on established eVTOL classification schemes [35, 36, 37].

Helicopter UAVs use one or more main rotors to generate lift and control forces in hover and in forward flight additionally the horizontal propulsion. Thrust, lift, and control authority are coupled through rotor speed, collective pitch, and cyclic pitch. A representative example is the Schiebel Camcopter S-100 with one main two-bladed rotor and a tail rotor to control the yaw moment [38].

Multicopters generate lift through multiple vertically oriented rotors, typically driven by battery-electric motors. Control is usually achieved by differential thrust across the rotor set consisting of fixed pitch propellers, which results in a mechanically simple airframe and few moving parts. An example is the DJI FlyCart 30, which targets cargo transport tasks at limited range [39]. Mechanically more complex solutions are possible as well, but significantly less common.

Lift + Cruise aircraft separate vertical lift and forward propulsion into dedicated propulsors, for example lift rotors for takeoff and landing and one or multiple separate cruise propeller for forward flight and a conventional fixed wing for lift in cruise. This decoupling allows the cruise propulsion system to be optimized for efficient forward flight while the lift system is optimized for hover. The transition from hover to forward flight is comparatively simple, while the cruise propulsor spools up, the wing produces increasing lift and the vertical lift system power can be reduced, until the aircraft is fast enough to fly only with the aerodynamic lift of the wing. A relevant example is the Skyways V2, which represents a fixed-wing VTOL with an electric lift propulsion system and an internal combustion engine directly driving a propeller for cruise propulsion [40].

Tilt wing aircraft vector thrust by tilting the entire wing together with the mounted propulsors, from a vertical orientation in hover to a horizontal orientation in cruise. In hover, the propulsors act as lift rotors, while in cruise the wing provides lift aerodynamically and the propulsors provide forward thrust. Transitioning is therefore more complex. An example for a tilt wing cargo UAV is the Dufour Aerospace Aero-200 with four wing mounted electrically driven propellers and a hybrid drivetrain [41].

Tiltrotor aircraft achieve VTOL capability by rotating the rotors, while the wing itself remains fixed. In hover and low-speed flight, the rotors generate the required vertical lift. During transition, the rotors are progressively tilted forward until they primarily provide thrust, while the wing delivers lift in cruise. This arrangement requires mechanically robust tilt mechanisms and flight control laws that can manage the strongly changing rotor inflow conditions and aerodynamic interactions during transition. The Bell Eagle Eye UAV is such an aircraft, the two three bladed propellers and nacelles are mounted on the wingtips with the combustion engine located in the fuselage [42].

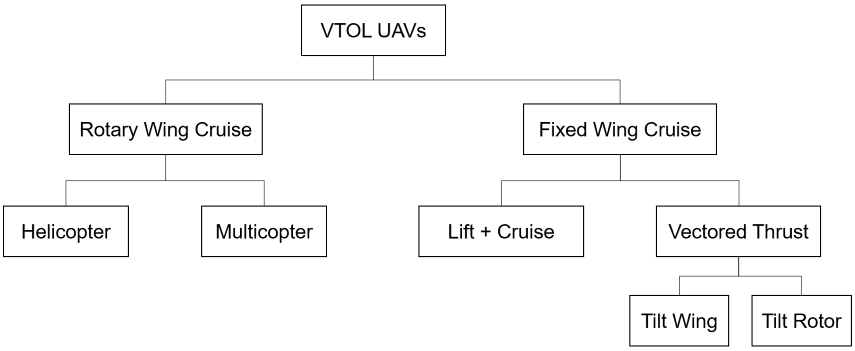

Figure 2.1: Classification of VTOL UAV Configurations

Numerous variations exist within the individual configurations. For helicopters, for example, tandem or coaxial rotor arrangements and compound helicopter concepts are possible. Multicopters can employ fixed-pitch or variable-pitch rotors, and for tiltrotor aircraft either all propulsion units can be tiltable or only a subset More exotic configurations are also possible, but they are not considered further here due to their limited number and low market penetration.

With regard to powertrains, battery-electric systems are widely used, particularly when a larger number of rotors is to be driven. For increased range, hybrid-electric systems are suitable, and several architectures are possible. These can be represented clearly as topologies. The legend for the following topologies is provided in Figure 2.2. Within the scope of this thesis, the topologies are simplified, and additional components such as rectifiers, inverters, or gearboxes are not shown.

Several implementation options exist for hybrid powertrains. The two versions shown in

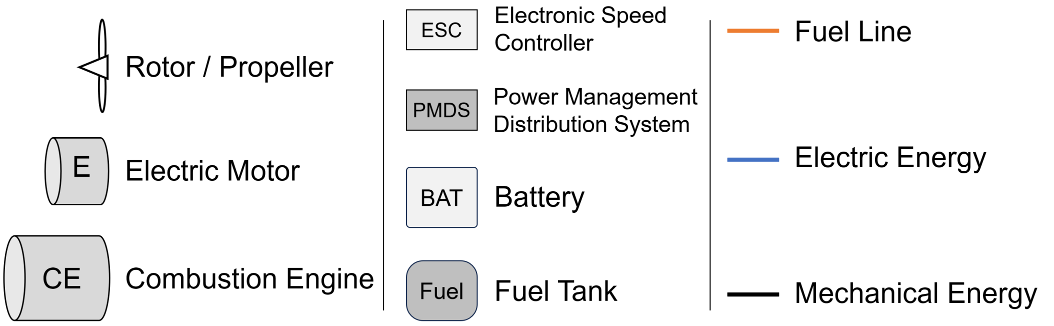

Figure 2.2: Powertrain Topology Legend

Figure 2.3 are particularly suitable for VTOL aircraft with electric vertical lift propulsion. To achieve increased range, either a combustion engine coupled to a generator is used to provide electrical energy only, or the combustion engine is additionally mechanically connected to a propeller. If the combustion engine, which may be installed as a piston engine or a turboshaft engine, drives only a generator and all propellers are driven directly by electric motors, the topology can be referred to as a serial hybrid-electric architecture according to Hammer and Graaf [43].

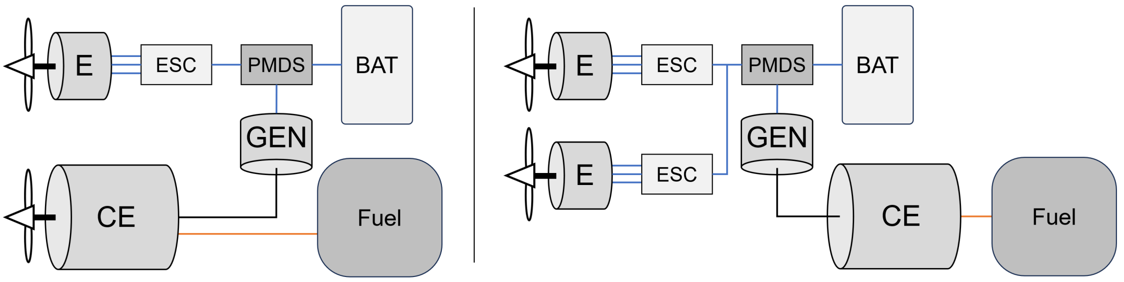

Figure 2.3: Battery-electric (left) and Combustion Engine (right) Propulsion Topology, adapted from Hammer and Graaf [43]

Without a direct connection between the electric propulsion system and the combustion engine, the architecture is referred to as a parallel hybrid-electric topology. For VTOL UAVs in a Lift + Cruise configuration, this concept is comparatively well suited. The vertical lift propulsors can be designed as purely battery-electric, while the cruise propulsion system can be designed to be driven directly by the combustion engine.

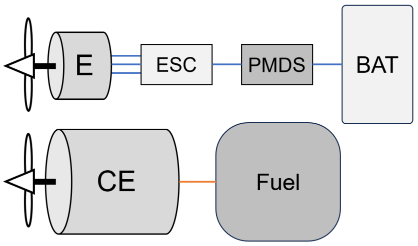

Figure 2.4: Parallel Hybrid Propulsion Topology, adapted from Hammer and Graaf [43]

Conventional combustion-based propulsion systems are widely used for helicopter UAVs, and both piston engines and turboshaft engines can be employed.

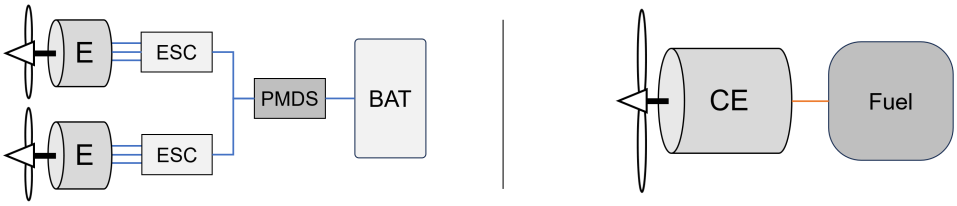

Figure 2.5: Battery-electric (left) and Combustion Engine (right) Propulsion Topology

2.1.3 Development Timeline

Unmanned VTOL aircraft and use cases within the AAM spectrum are relatively new in comparison to other aviation concepts. Predominantly electric or hybrid-electric VTOL UAVs only emerged in the early 2010s. In 2013, Amazon presented an early concept for last-mile logistics using UAVs [32]. In 2014, the German logistics company DHL conducted a pilot project in which the island of Juist in the German North Sea was supplied with medical products from the mainland using UAVs [44]. However, this marks neither the beginning of uncrewed aviation nor the start of employing uncrewed systems in a maritime context.

The first aircraft that were remotely controlled for simple missions were already developed and tested during World War I [45]. At that time, internal combustion engines were the only propulsion source, and the aircraft were not VTOL-capable. With the emergence of the helicopter, VTOL concepts also became feasible. In the 1960s, the QH-50C became the first VTOL drone to be placed into operational service with the U.S. Navy and deployed from ships [46]. During its operational phase, the technologically highly advanced program suffered from issues, particularly in the area of flight control. As a result, the UAVs were removed from active service by 1970 and reassigned to other roles, for example as target drones. In parallel, military use of fixed-wing drones, especially for reconnaissance purposes, became more widespread [45]. Another notable project first flew in 1998 in the form of the Bell Eagle Eye. This tiltrotor UAV was specifically intended for ship-based operations and was designed to support not only reconnaissance and surveillance tasks but also the transport of critical supplies [42]. However, it never reached operational deployment.

While these comparatively large drones were developed for highly specific professional applications, advances in computer and sensor technology, particularly miniaturization, as well as the widespread availability of modern batteries and small brushless AC motors, created the conditions that made smaller electrically powered VTOL UAVs feasible in the first place. In addition to applications in the hobby segment and in professional and military contexts as camera platforms, concepts for using drones for logistics emerged in the 2010s, as mentioned above, and gained traction as one of the main use cases of UAVs in the AAM sector [47]. Due to the range limitations caused by the low energy density of the batteries used, last-mile delivery was especially prominent.

This use case refers to the transport of typically small and lightweight goods, usually well below 10 kg, from a warehouse or a logistics vehicle to the end customer [48, 49]. Amazon has been working on this use case for several years under the name Amazon Prime Air. After presenting the concept in 2013, the first delivery by UAV was carried out in Cambridge in 2016, although commercial rollout has not yet been achieved [50]. While drone delivery was expanded to additional locations, primarily in the United States, operational issues also became apparent and led to interruptions in service [51, 52]. In the United States, other retailers are also deploying drones in increasing numbers, including Walmart, which reported more than 6000 successful deliveries in 2022 [52].

In Germany, last-mile deliveries by UAV were also tested in flight trials and pilot projects, as already mentioned for the island of Juist and in the Alps. In both cases, limited accessibility by conventional delivery vehicles and consequently longer and more expensive delivery processes were key drivers. It must be mentioned that these projects were discontinued by 2021 [53]. In 2023, within a publicly funded project, groceries and other consumer goods were delivered directly to end customers in two selected towns in the German state of Hesse [54]. The first commercial initiative in Germany started in 2024 in North Rhine-Westphalia. In this case, the primary target group is not end customers, but businesses that are intended to receive parcels weighing up to 6.5 kg [55].

Beyond deliveries of products to end customers, another use case has become particularly prominent, namely the supply of medical goods. While trials and projects in this area have also been conducted in Germany, such as the previously mentioned flights to the island of Juist, the Medifly research project investigating the transport of samples and medication between hospitals and laboratories, or the most recent flights between two Asklepios clinics in Schleswig-Holstein located approximately 60 km apart, regions in the global South are relevant in this context as well [56, 57, 32, 48, 22]. The company Zipline as a very prominent example operates drones in Rwanda, Ghana, Nigera, Kenya and the Cote d'Ivoire to transport medical items, especially those which cannot endure long transport periods without ensured cooling like vaccines and blood [25].

2.1.4 Recent Developments

Technological developments and advances in recent years have resulted in significantly more capable VTOL aircraft. In particular, the transport of heavier payloads over longer distances has become feasible, and further performance increases can be expected. This applies in particular to operations in maritime environments, as well as to military use cases.

The projects mentioned earlier in the introduction, involving flights to offshore wind farms and oil and gas platforms, were conducted using aircraft that are based on military considerations and procurement programs. The Skyways V2 VTOL UAV shown in Figure 1.2 successfully participated in the U.S. Navy's Blue Water Logistics UAS program, the Pterodynamics P4 Transwing drone was also tested by the U.S. Navy, and the Schiebel Camcopter S-100 used for flights to Norwegian offshore platforms was developed, among other purposes, for military and governmental operations over water and from ships [20, 38]. Kaman, a helicopter manufacturer, is developing the Kargo UAV in cooperation with the U.S. military. This platform was also designed specifically for maritime scenarios and is intended to be applicable to logistics operations for offshore oil and gas installations [58].

While the aircraft mentioned above were developed from the ground up as uncrewed systems, another trend is emerging that enables comparatively high payloads and ranges. Originally crewed systems can be equipped with adapted flight control systems and thereby become drones as well. This has already been demonstrated for conventionally taking off and landing fixed-wing aircraft used for cargo transport over longer distances, and also for helicopters [59]. Specifically for logistics purposes, prototypes of two such helicopters were presented in 2025. A modified Airbus Helicopters H145 under the name MQ-72C

Lakota Connector, and the S-70UAS U-Hawk from Sikorsky based on a UH-60L helicopter [60, 61]. The Airbus VSR700 helicopter, intended for maritime military missions, is also based on an ultralight model that originally provides seating for a pilot and one passenger [62].

A similar development can be observed for eVTOL designs, where automated flight control systems are already integrated into the aircraft. Both the eVTOL developer Beta and Joby have presented uncrewed versions of their aircraft featuring hybrid powertrains that are intended to support military missions such as logistics [63, 64].

Appendix A summarizes selected data for aircraft that are relevant in the context of this thesis. For clarity, the powertrain and configuration classifications are provided in abbreviated form. Battery-electric powertrains are abbreviated as BE, powertrains based exclusively on combustion engines as CE, and hybrid powertrains as H. Multicopter configurations are denoted as MC, tiltrotors as TR, tiltwings as TW, Lift + Cruise configurations as L+C, and helicopters as H. By plotting the gathered values from Appendix A, several aspects become apparent regarding the general capabilities of different aircraft configurations and the relationships between range, payload and the maximum take-off mass.

To gather an overall overview of the relevant aircraft, the data regarding the $MTOM$ and range is shown in Figure 2.6. It must be noted that if multiple data entries with different payload and range combinations are available for a given aircraft, multiple data points are plotted.

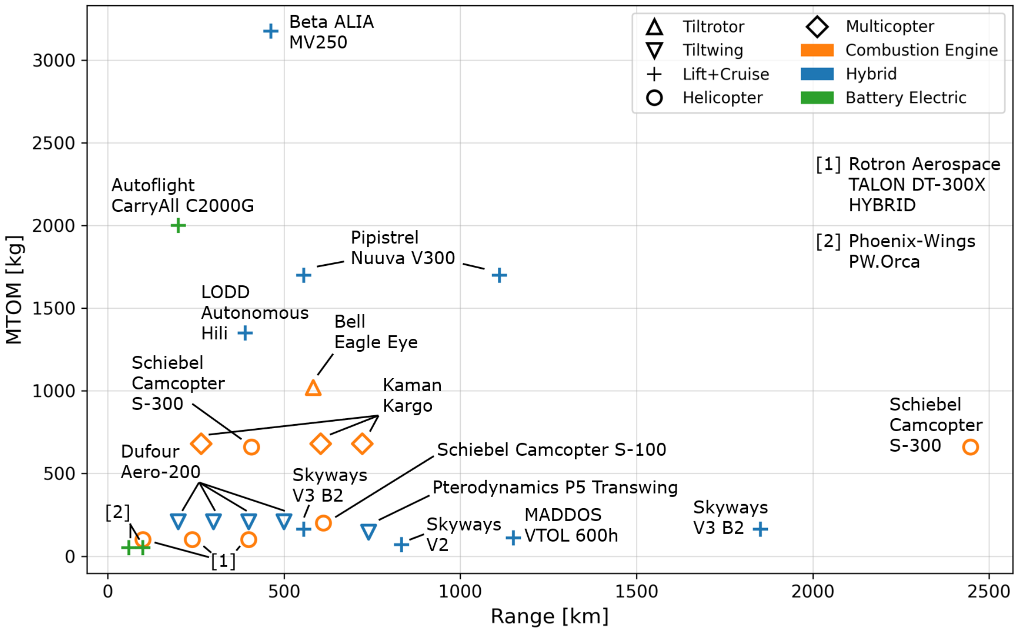

Figure 2.6: MTOM over Range Plot of commercial VTOL UAVs

It can be observed that most designs fall below a range of 1500 km and an $MTOM$ of 2000 kg. Only a few configurations extend beyond this region.

One example is the Beta ALIA MV250, which stands out from the remaining designs due to its significantly higher payload. Only a single data point could be collected for this aircraft, and its hybrid propulsion architecture suggests that substantially greater ranges can be expected at reduced freight mass. For the ferry range, the manufacturer specifies a range of more than 2400 km [63].

The Skyways V3 B2 combines comparatively low weight and a rather small payload capacity with a very large range, which is exceeded only by the Schiebel Camcopter S-300. According to the available data, this helicopter is designed to fly for up to 24 h with a payload of 50 kg; together with the specified cruise speed of 28.3 m/s, this implies a comparatively very large range [65]. It must be noted, however, that it is not explicitly stated whether this endurance figure is valid at that cruise speed. The range values for this aircraft should therefore be regarded as optimistic estimates.

Plotting the payload over the $MTOM$ results in a visible proportional trend between both variables in Figure 2.7. A dense cluster below 250 kg of $MTOM$ and 60 kg of payload is visible and shown in Figure 2.8. Above 1000 kg of $MTOM$, soley Lift+Cruise configurations are present. In the area between these two sections, rotorcraft configurations with combustion engine powertrains form a second cluster.

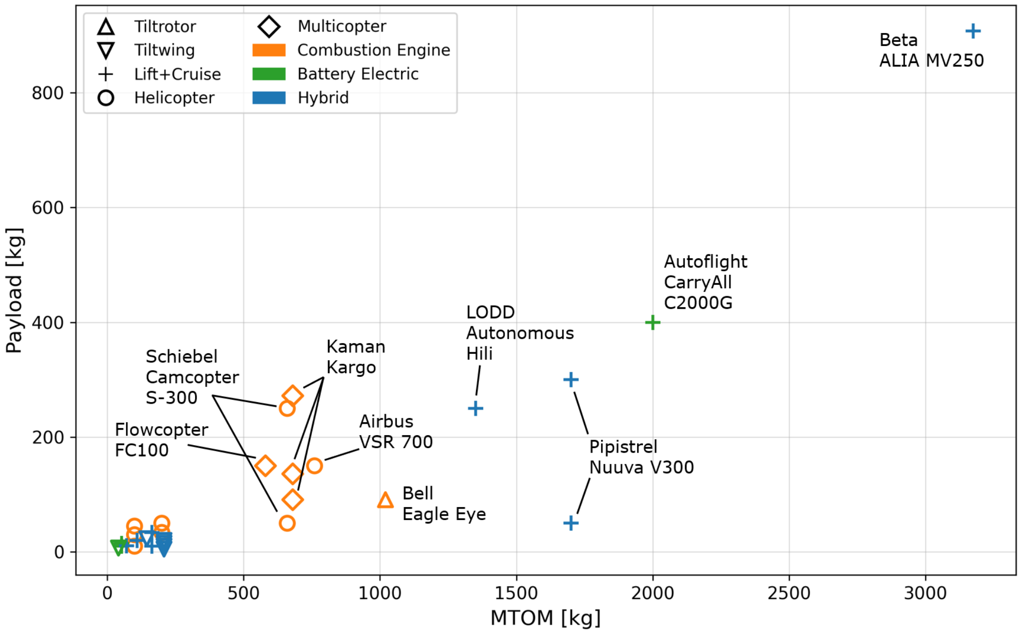

Figure 2.7: Payload over MTOM Plot of commercial VTOL UAVs

Looking more closely at the cluster below 250 kg of MTOM, a relatively large variety of configurations can be observed, while no clear trends within the cluster can be identified.

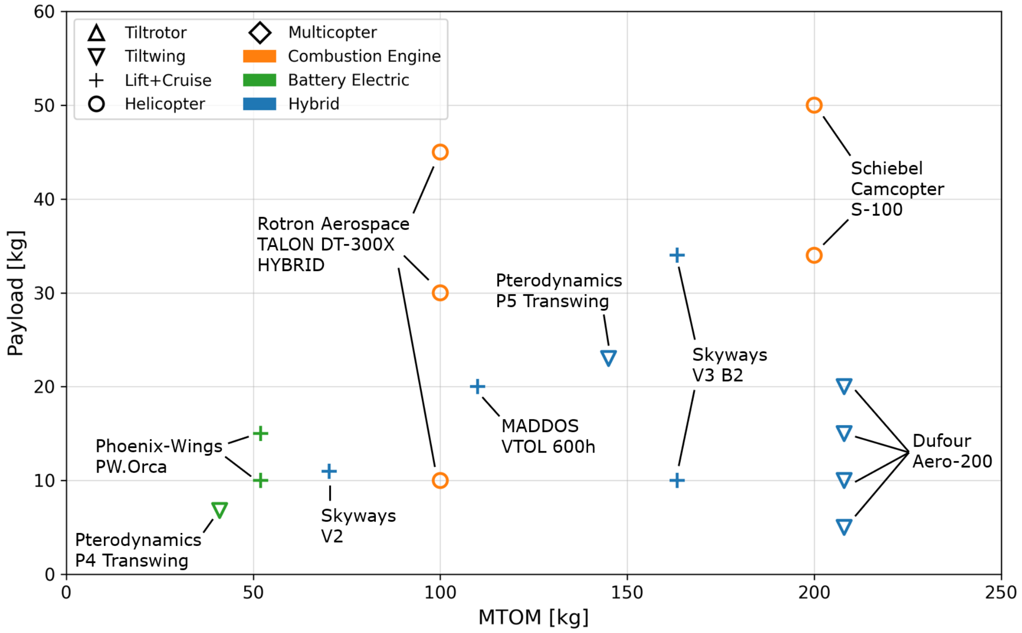

Figure 2.8: Payload over MTOM Plot of commercial VTOL UAVs below 250 kg MTOM

2.2 Offshore Wind Energy Use Case

2.2.1 Offshore Wind Farm Operation and Maintenance

The operation of offshore wind energy installations, commonly referred to as Operating and Maintenance (O&M), is significantly more complex and cost-intensive than that of onshore wind farms due to environmental conditions, the distance to service hubs, and the considerably larger size of the installations [66]. The operational expenditures (OpEx) incurred after the installation of a wind farm increase the cost of the energy generated in comparison to other forms of energy production, particularly when compared to onshore wind energy. Larger and more efficient wind turbines represent a trend aimed at counterbalancing these effects. However, higher failure rates can lead to increased repair and maintenance costs [66]. As a result, O&M costs account for a substantial proportion of the total energy cost for this type of energy production. They may represent up to 30% of the total investment costs, while in onshore projects they typically account for only around 5% [67, 66]. Within the O&M costs, maintenance-related expenses are of particular importance. Consequently, maintenance is considered one of the most critical tasks for offshore wind farms and constitutes a significant lever for reducing energy costs [66].

According to Wiggert et al. [17], maintenance serves the following purposes based on DIN 31051:

- Ensuring operational functionality, for example by refilling consumables such as lubricants
- Assessing and evaluating the condition of the wind turbine, for example through inspections or sensors
- Repairing detected faults and damages, for example by replacing a defective electronic component

- Implementing improvements to the installation that enhance performance, safety or reliability, for example by installing new warning lights for aircraft

According to Ren et al. [66], maintenance measures for wind turbines can generally be classified into the following three categories:

- Corrective Maintenance
- Proactive Maintenance
- Opportunistic Maintenance

The most common form of maintenance is corrective maintenance, which is carried out once a fault has occurred and been identified. Damage detection can take place during inspections or via sensors or turbine performance. Due to the limited accessibility of the asset resulting from maritime environmental conditions and the distance from the mainland, significant downtimes may occur.

Proactive maintenance aims to prevent major failures by conducting planned inspections and early maintenance activities. The goal is to identify and address issues at an early stage in order to avoid extremely costly major component replacements.

Opportunistic maintenance can be broadly described as a combination of the two aforementioned strategies. For example, if a turbine is already undergoing maintenance due to a failure in a subcomponent, other components can also be serviced at the same time. This eliminates the need for a separate transfer to the turbine and avoids additional downtime.

Inspections also play a significant role. They are in part required to ensure safety and environmental protection [68], while regular inspections also enable the early detection of damage, allowing maintenance to be scheduled and conducted at lower cost [66].

This thesis focuses on the maintenance of conventional horizontal-axis turbines with three rotor blades, which, with few exceptions, represent almost all offshore wind turbines installed globally. An overview of the main components of such an offshore wind turbine is shown in Figure 2.9.

Different components have distinct failure probabilities and inspection requirements. In particular, the rotor blades made of fibre-reinforced composites are among the most maintenance-intensive components. Dynamic loads over the turbine's lifetime, as well as environmental influences such as rain, ice, gusts, and lightning strikes, cause damage to both the outer and inner surfaces of the rotor blades. These blades can only be accessed from the nacelle using rope-based access techniques [66]. In the case of major damage that cannot be repaired this way, the rotor blade must be replaced using a floating crane, which is a complex and costly procedure.

Rotating components within the nacelle also show elevated failure rates. Most notably, the gearbox which increases the rotational speed of the rotor blades to drive the generator is prone to faults [66]. For this reason, gearless wind turbines have been developed in recent years, promising lower maintenance costs [69]. However, the nacelle also houses the shaft, the generator itself, bearings, and numerous electrical and hydraulic systems [17, 66].

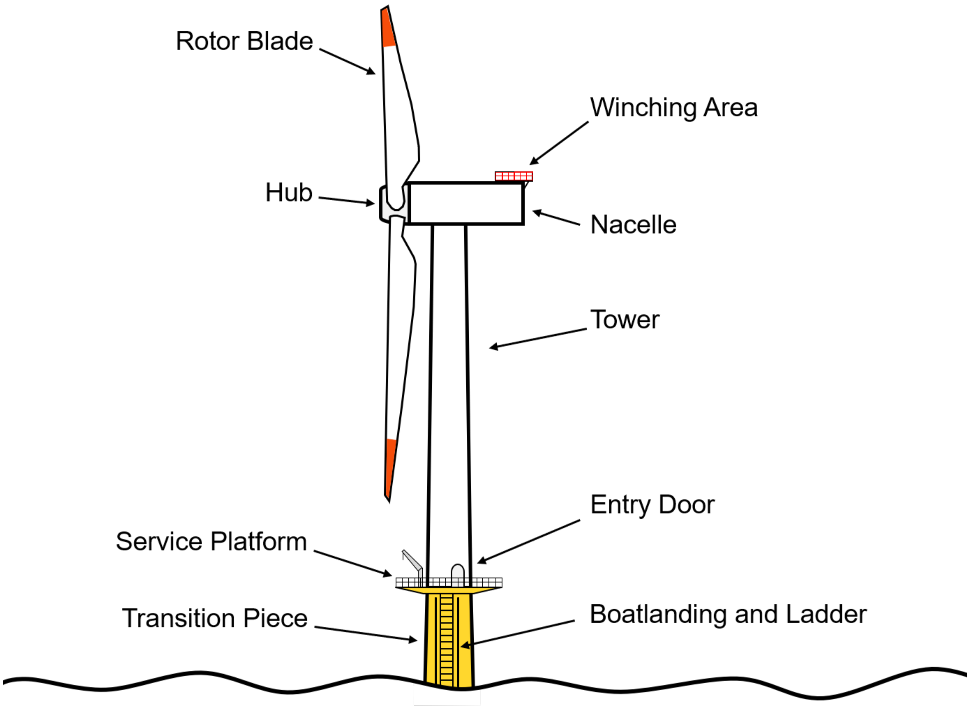

Figure 2.9: Overview and Components of an Offshore Wind Turbine

Nevertheless, the tower structure itself, the electrical systems and connectors at the tower base and the transition piece and foundation are also subject to maintenance, although their failure rates are significantly lower. Overall, this results in the majority of maintenance operations requiring access to the nacelle.

2.2.2 Maritime Aviation for Wind Farms

2.2.2.1 Crewed Flights

2.2.2.1.1 Maintenance Operations

Helicopters are used as a means of transport for offshore wind farms, flying personnel and equipment directly to wind turbines or to offshore substations or larger vessels, from which transport to the individual turbines is carried out [17]. Landings on the wind turbines are not possible. Instead, technicians are lowered onto or retrieved from the winching area by hoist. Due to the limited flight time and high cost per flight minute, the helicopter does not remain in the wind farm but usually returns to the mainland after a successful transfer [70].

A clear advantage compared to vessels is the relative independence from wave conditions. However, the emergency equipment, in the form of an emergency flotation system in case of a forced water landing, still imposes limits on the maximum wave height to allow safe evacuation of the occupants [71]. There is also an advantage over vessels in marine regions heavily affected by tides. Since hoisting occurs directly to the nacelle, the actual maintenance activities can begin more quickly. The time-consuming process of personnel transfer, material transfer, and internal ascent within the turbine is eliminated, as explained in more detail in Section 2.2.3.

Such a hoisting manoeuvre is shown in Figure 2.10. The helicopter is positioned parallel to the rotor plane of the wind turbine, with its nose pointed into the wind. This positioning minimises the impact of the turbine's wake flow on the helicopter. The turbine blades are not rotating during the manoeuvre [18].

Figure 2.10: Hoisting Maneuver [72]

According to Donkels et al. [18], the following boundary conditions apply for the execution of offshore helicopter flights:

- Minimum altitude: 150 m above the highest obstacle at a distance of 150 m on all sides, 300 m at night
- Transits through OWFs may only be performed with sufficient distance to wind turbines, the minimum distance is 900 m
- Main cloud base: min. 200 m during the day and min. 400 m at night

- Flight visibility: 1.5 km during the day and 5 km at night, during the day the flight visibility may drop to 800 m for a short time if land visibility is available
- Wind: max. wind speed (mean or gust) generally up to 100 km/h, wind operation areas in OWFs have their own wind limitations up to which an approach is possible
- Weather: no flights during thunderstorm or icing conditions
- Waves: max. sea state according to certification of emergency floatation system

A network of waypoints and predefined routes, as illustrated in Figure 2.11, is available for helicopter operations in the German Bight and published online [73]. This network enables the coordination of flight trajectories between different stakeholders in the offshore industry and governmental acteurs by declaring planned flight paths and times over this platform.

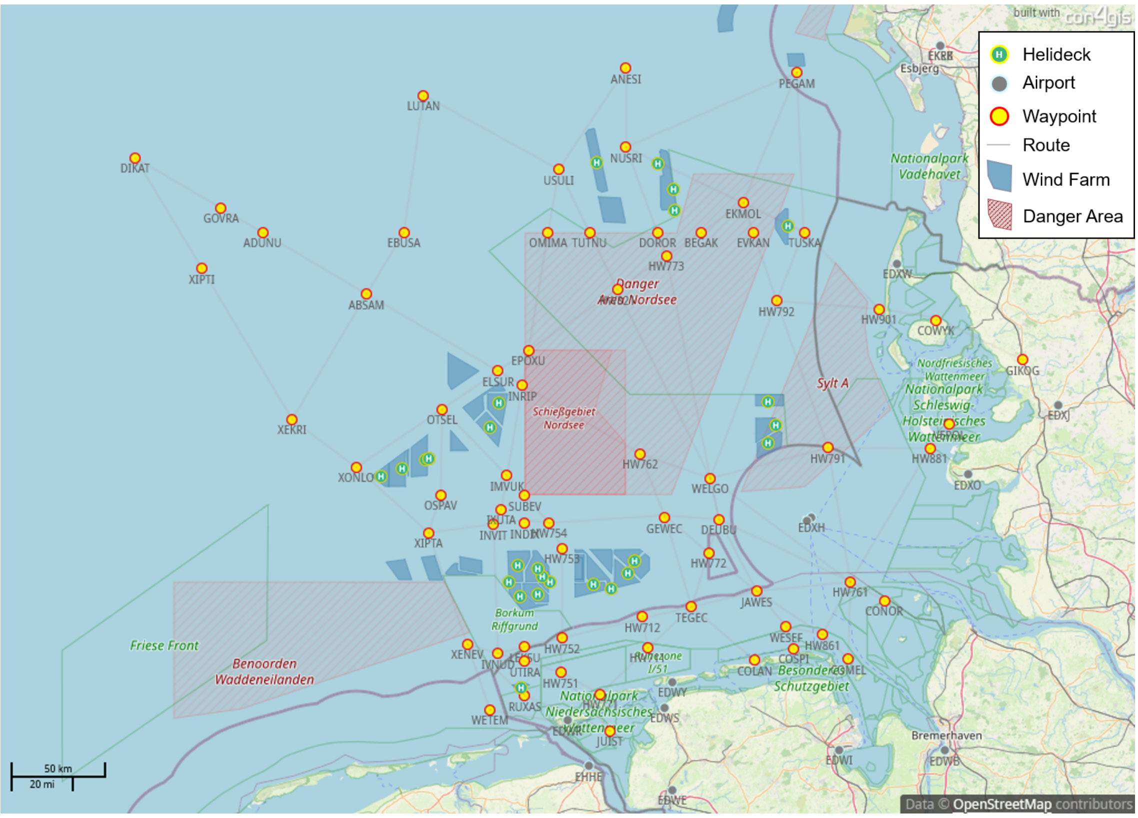

Figure 2.11: Waypoint and Route Network for Offshore Helicopter Operations in the German Bight [73]

In the German Bight, offshore operations are commonly performed using relatively small twin-engine helicopters like the H135, H145 or AW169. Per sortie, these aircraft typically transport a maximum of two to three teams and can then return to the mainland while work on the wind turbine proceeds. More recently, larger helicopter types such as the H175 are already being contracted for new wind farms with larger turbines [13].

With suitable equipment and training, nighttime operations may be possible within the limits of local regulations, but they require careful assessment because of the high accident risk [74]. In German wind farms, hoist operations on wind turbines at night are strictly prohibited [75].

An overview of the basic technical and performance data of helicopters used in the offshore wind context in the German Bight is given in Table 2.2.2.1.1.

	H135 [76]	H145 [76]	AW169 [77]	AW139 [78]	H175 [76]
MTOM [kg]	2,980	3,800	4,800	7,000	7,800
Useful Load [kg]	1,417	1,905	1,973	2,275	3,083
Range [km]	633	650	785	1,187	1,160
Fast Cruise Speed [km/h]	252	240	267	306	267
Seats (incl. Pilots)	7	10	12	17	20

Table 2.1: Comparison of Technical Data for selected Helicopters

2.2.2.1.2 HEMS

Helicopters also play a critical role in offshore wind operations in the context of Helicopter Emergency Medical Services (HEMS). In contrast to the mostly planned maintenance flights, HEMS constitutes a fully independent rescue capability that offshore wind farm operators are legally required to provide. These services are fulfilled by specialised contractors who supply dedicated rescue helicopters and crews, entirely separate from the logistics and maintenance fleet. As a consequence, HEMS operations must not be conflated with regular offshore maintenance activities, since they follow different regulatory, operational and organisational frameworks [79, 75].

Figure 2.12: HEMS Operation in an Offshore Wind Farm[80]

Offshore HEMS missions place significantly different demands on the aircraft and crew than comparable land-based emergency operations. The helicopters must be equipped and certified for winch operations, overwater missions and night operations, and missions typically involve a larger and more specialised crew configuration [75]. In practice, HEMS flights can be conducted even under heavily challenging weather conditions, since timely medical evacuation is essential for the safety of offshore personnel.

A central constraint for the future expansion of offshore wind energy in the German Bight arises from the limited reach of current rescue helicopter concepts. Reliable medical evacuation is presently considered feasible only up to a distance of approximately 180 km from the coast [14]. A substantial share of planned wind farm areas lies beyond this radius, which creates a critical bottleneck for further offshore development. Although ships may also be employed for medical emergency response, their applicability is constrained by the demanding transfer of injured personnel to the vessel and significantly higher transit durations. As a result, helicopters remain essential to the offshore rescue chain, which in turn motivates ongoing explorations into new concepts for forward-stationed helicopters [79, 14].

Although HEMS is not treated further in the present work, its relevance for the offshore system-of-systems is evident. The need to guarantee rescue capability influences spatial planning, permissible operating areas, and the overall feasibility of offshore wind projects. Future extensions of the SoSID-Toolkit could therefore incorporate HEMS-related constraints or evaluate alternative concepts for offshore medical evacuation, providing an additional dimension for scenario analysis.

2.2.2.2 Uncrewed Flights

2.2.2.2.1 Inspections

The use of UAVs in connection with wind turbines, both onshore and offshore, is not fundamentally new and has been practised in Germany since at least 2019 [81]. Multicopter platforms are already employed in regular commercial operation for inspection flights, performed by specialised service providers [82, 83, 84]. Equipped with various sensors, they survey the turbines and can complement or partially replace conventional rope-access inspections [85, 86]. At present, visual rotor blade inspections are the most common drone-based inspection type, enabling the detection of damage in fibre-reinforced structures. This is especially relevant since the rotor blades are most maintenance intensive components of wind turbines, leading to possible reductions in annual operations and maintenance costs according to Schläger, Lorenz, and Baumgärtner [87]. Besides the UAV hardware and sensing payloads themselves, advances in image processing, including reinforcement learning methods for data evaluation, act as important enablers [86].

Figure 2.13: Inspection Drone surveying an Onshore Wind Turbine [88]

In most cases, the multicopters are sub-20 kg systems launched in the immediate vicinity of the turbines, from where they autonomously traverse the relevant components as can be seen in Figure 2.13. This substantially reduces the time required per inspection, which translates directly into lower maintenance costs and reduced turbine downtime, and can also marginally decrease the levelised cost of wind energy [89]. The optimised use of inspection drones for offshore wind farms, accounting for fleet sizing and environmental influences, has already been studied and indicates further potential to shorten inspection durations [90, 91]. In this case, the multicopters are launched from vessels near the turbine.

Beyond optical cameras, thermal imaging as well as LiDAR and ultrasonic systems can be employed [86, 89]. In addition, lightning protection systems can be assessed using drones [92].

The use of fixed-wing aircraft for collecting environmental data is also possible, but comparatively new and less integrated into O&M measures [93].

2.2.2.2.2 Cargo Delivery - Ship to Turbine

As described in Section 2.2.1, most maintenance and inspection tasks are carried out in the area of the nacelle. When transferring personnel and equipment from a vessel, technicians must first ascend inside the turbine with the equipment. Unmanned aerial vehicles (UAVs) can be used to transport equipment from the vessel to the nacelle while the technicians climb the tower. Due to the short flight distance, battery-electric multicopters can be used for this task. Various commercially available multicopter systems are suitable for this application, which can be used in a relatively straightforward manner as a kind of airborne crane.

This approach has already been tested in initial trials and campaigns. The offshore wind farm operator Vattenfall, in collaboration with offshore service provider Ampelmann, has tested this concept in the DanTysk and Sandbank wind farms, both located in the German North Sea [94]. Ørsted has also explored this use case extensively in wind farms off the east coast of England and in the Irish Sea. In collaboration with drone service provider Skylift UAV and drone manufacturer FlyingBasket, more than 600 flights were conducted, transporting a total of 38.1 tonnes of cargo. An approach of an UAV from this campaign to a wind turbine's nacelle is shown in Figure 2.14.

Figure 2.14: FlyingBasket FB3 UAV approaching an Offshore Wind Turbine with Equipment [95]

Significant advantages in terms of time, cost, and safety were reported by the involved partners during these operations [96]. This type of drone application has also been investigated and successfully demonstrated in research projects such as FOD4Wind [97].

2.2.2.2.3 Cargo Delivery - Shore to Turbine

With the increased range and payload capacity of drones equipped with VTOL capabilities, an additional use case emerges. The transport of equipment from the onshore service base to the turbines has already been investigated and tested in recent years by several offshore wind farm operators, although commercialization and integration into routine operations beyond test campaigns has not yet taken place. The most recent campaign was conducted in 2025 by RWE in cooperation with the drone service provider Skyports at the wind farms “Nordsee Ost” in the German Bight and “Arkona” in the Baltic Sea, during which more than 80 flights were carried out to supply spare parts, equipment and consumables [98]. Figure 1.2 originates from this campaign. In 2024, 40 flights were conducted by the drone service provider Holo to the “Anholt” OWF operated by Ørsted, during which payloads were successfully dropped onto the turbines [99, 100]. In the same year, the “Offshore Drones Challenge” was held by the operator EnBW in collaboration with DLR. As part of the research project “Upcoming Drone Windfarm” (UDW), this challenge evaluated the use of several different UAVs [101]. The research project itself delivered results concerning route planning, flight behavior within the wind farm, integration into offshore wind farm systems and economic perspectives [102, 18, 103].

Closely related to this use case are the cargo drone flights to oil and gas platforms operated by Equinor off the Norwegian coast in 2020 and 2024 [104, 27]. In 2024, operational integration was demonstrated in collaboration with the drone service provider Skyports, with flights of up to 125 km conducted to eight offshore installations. A key difference is that the drones on oil and gas platforms are able to land and be recharged or refueled. This is not possible on the winching platforms of offshore wind turbines. Instead, the drones must be capable of either dropping equipment precisely above the turbine’s winching area or using a winch system to lower and, if needed, retrieve the cargo.

All campaigns share the characteristic that the flights were conducted beyond visual line of sight (BVLOS), meaning that control of the drones was executed remotely without the presence of a pilot or operator within the wind farm. Positioning above the wind turbine or offshore oil platform was achieved using visual markers, as shown in Figure 2.15, which are detected by sensors on board the drone and used to calculate its relative position to the structure.

An advantage of drone usage in offshore wind logistics is the increased flexibility compared to ships and helicopters. The case of spontaneously required items, which are typically small and comparatively lightweight, often arises during inspections and maintenance activities and is particularly well suited for drone deployment. The transport costs and emissions for a single item are very high when using helicopters or ships. In addition, there is a significant delay until the item is retrieved from the spare parts storage, transferred to the transport vehicle, and finally delivered into the hands of the technicians.

Due to these high costs, the availability of suitable vehicles must be taken into consideration. As a result, drone deployment in such cases is highly attractive, both due to the reduced transport costs and the shortened delivery time, which in turn enables earlier completion of maintenance activities and thereby leads to increased energy production. In this scenario, no payload has to be picked up from the turbine, which further simplifies drone operation. As demonstrated by the conducted campaigns, such use cases are already feasible with the current state of the art.

By combining the described advantages for spontaneous use cases with higher UAV pay-

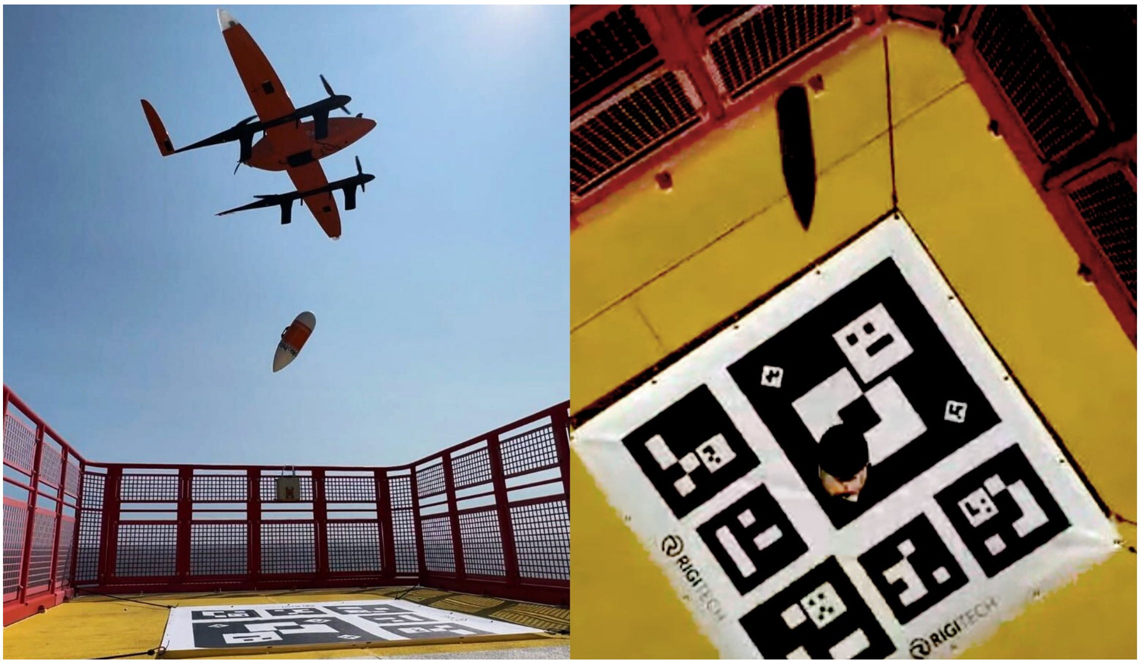

Figure 2.15: UAV dropping a Payload Container on the Winching Area of an Offshore Wind Turbine [100]

load capacities and direct delivery to the nacelle, a further advanced application can be envisioned. The transport of personnel and material can be decoupled, with only the equipment being transported via UAVs, while technicians are brought to the turbines using the existing means of transport. In the case of helicopters, this would reduce fuel consumption due to the lowered payload, or alternatively allow more maintenance personnel to be transported. In the case of ships, this approach could lead to faster transfers to the turbines and earlier starts of maintenance tasks.

When operating drones in this environment, it must be ensured that good visibility conditions prevail, especially for the optical sensors required during the final approach to the turbine. Additional restrictions are imposed by icing conditions, wind, rain, or thunderstorms, where the specific technical capabilities of each UAV are critical. As the airspace is shared with helicopters still in operation, civil aviation, as well as governmental and military aircraft, and since seabirds may also occupy similar altitudes, appropriate systems and operational procedures must be implemented. Furthermore, vessels with tall superstructures must also be considered. Within the UDW project, a flight altitude of 120 m was therefore proposed [18].

Most of the UAVs used in this context are lift+cruise aircraft with battery-electric or hybrid propulsion using a piston engine. Additionally, the use of uncrewed helicopters in this operational environment has also been investigated [27].

2.2.3 Ship Based Logistics

Offshore wind farms can not only be accessed by helicopter. Ships are also among the commonly used means of transport. In general, two types of vessels can be distinguished that are primarily used in this context:

- Crew Transfer Vessel (CTV)
- Service Operation Vessel (SOV)

Additional vessels such as Offshore Support Vessels (OSVs) and floating cranes are also used to support both maintenance and installation activities. However, they are less commonly deployed during regular operation [17, 66].

Crew Transfer Vessels (CTVs) are relatively small vessels that transport personnel and equipment from a service port to the wind farm on a daily basis. They are typically equipped with a larger, seated passenger area for technicians during transit and a deck for equipment and spare parts. The size and weight of these parts are limited by the vessel's specifications and the constraints of the transfer process to the wind turbine. Various types and sizes exist, with vessels using a Small Waterplane Area Twin Hull (SWATH) design, such as those shown in Figure 2.16, offering higher operational limits with regard to sea state conditions [17].

Figure 2.16: Three CTVs in the 27 m Class: Ares 27 CTV, StratCat 27 Hybrid, Damen FCS 2710 [105, 106, 107]

The transfer of personnel and equipment from a CTV to a wind turbine involves several steps. First, the vessel approaches the boat landing and presses its specially shaped bow against the transition piece of the wind turbine, while waves continue to cause significant vertical motion. Personnel then disembark and climb onto the service platform. From there, equipment can be lifted onto the wind turbine using a crane, as shown in Figure 2.17. Particularly the transfer of personnel involves a higher safety risk and can only be carried out under suitable conditions [17, 66].

Daylight conditions can also be included in these constraints. Transfers as well as work on or inside the wind turbine at night may offer economic advantages but also lead to increased risks, which can be mitigated, for example, by the use of spotlights mounted on the CTV [17, 108].

Figure 2.17: Transfer of Equipment from CTV to a Turbine's Transition Piece [109]

After the teams on board have transferred onto the turbines, the CTV remains in the wind farm. Once the maintenance tasks of the current work shift have been completed, the personnel are picked up and brought back to the service port. The relatively long transit times, which are additionally influenced by sea conditions such as wave height and wind speed, represent a disadvantage of CTVs [17].

For wind farms located far offshore, SOVs are therefore used, which remain in the wind farm for extended periods. They are significantly larger than CTVs and feature accommodations for the teams, spare parts storage, daughter vessels, helicopter decks, cranes, and other facilities. Teams can be transported from the mainland to the SOVs by CTV or helicopter, and from the SOV to the wind turbines by daughter vessel, helicopter, or motion compensated gangway, as shown in Figure 2.18 [66].

The selection of optimal vehicles depending on wind farm parameters has already been extensively investigated in scientific research, while new technologies related to wind turbines, vessels, maintenance procedures, and other influencing factors continue to raise further research questions and new trade-offs [17, 66, 87, 111, 15].

Figure 2.18: SOV Bibby WaveMaster 1 during a Transfer to an Offshore Wind Turbine [110]

2.3 System of Systems

2.3.1 Definition and Characteristics

The concept and terminology of Systems of Systems (SoS) represent a relatively recent approach in engineering, first emerging in the 1970s in the context of the operational behaviour and interaction of systems [112]. According to ISO 21839:2019, a SoS is defined as a collection of independent systems that interact with each other and, through cooperation, achieve capabilities that cannot be accomplished by the individual constituent systems [113]. A broader definition states: ”SoS are large scale concurrent and distributed systems that are comprised of complex systems” [114]. The IPEK Institute of Product Engineering at KIT defines Systems of Systems as follows [115]:

”A System of Systems (SoS) is a system consisting of a set of interacting systems, each of which can be considered a system in itself. The main characteristics of SoS are:

- each system can interact independently and has its own purpose
- the individual systems of the quantity are independently organised to fulfil their purposes
- the combination of systems delivers results that cannot be achieved by individual systems

The characteristics can be pronounced to varying degrees.”

A widely accepted approach for characterising Systems of Systems is the ”OMGEE” framework as defined by Maier [116], which states that a SoS should exhibit the following characteristics:

- **O**perational and **M**anagerial Independence,

- **G**eographic Distribution,
- **E**mergence, and
- **E**volutionary Behavior

The SoS approach is particularly suitable for analysing complex system structures and is therefore applied, for example, to the study of renewable energy systems, infrastructure questions, transportation systems, and issues of safety and defence [117]. A specific example is the civil air transport system of a given region [118].

As various definitions and characterisations indicate, collaboration and interaction between the constituent systems are of particular importance. This also includes the fact that constituent systems are not necessarily part of the SoS at all times. They may become unavailable due to autonomous decisions or other constraints [118]. Consequently, the behaviour of the systems within the SoS must be managed in a way that allows the system objectives to be achieved, while keeping the SoS robust and flexible enough to adapt to changes through internal adjustments.

The way in which this management or controlling instance is implemented also allows for a classification of Systems of Systems [118]:

- **Directed SoS:** The System of Systems exists for a specific purpose and has been assembled and is managed during operation by a central authority. The constituent systems act autonomously within a defined framework but follow the objectives set by this authority.
- **Acknowledged SoS:** The systems are guided by overarching goals and a central authority, but can determine their own operations and objectives independently.
- **Collaborative SoS:** The cooperation of constituent systems is voluntary and based on shared or common interests, resulting in a high degree of autonomy. Rules are primarily defined through standards rather than authority.
- **Virtual SoS:** The constituent systems are loosely connected, and no centrally agreed-upon purpose for the association exists. Each system pursues its own goals, while the overall behaviour emerges as a System of Systems.

2.3.2 Offshore Wind Farm Logistics as Systems of Systems

Within the scope of this work, the logistics for the operation and maintenance of offshore wind farms is examined as a System of Systems (SoS). The goal of this SoS is the safe, compliant, and economically efficient continuation of energy production. The constituent systems, namely the energy production units, transport vehicles, and the organisations and operators of the various vehicles and infrastructures, can only fulfil this objective through cooperation.

Using the OMGEE characteristics, this SoS can be described as follows:

- **Operational and Managerial Independence:** Ships, helicopters, and UAVs are independent systems that can be operated outside the context of the wind farm. They are managed independently by their respective operators. Wind turbines themselves are also autonomous technical systems. The different operators aim to optimise their own system’s performance, primarily in terms of cost-efficiency. Final decisions regarding operations lie with the respective system operators.

- **Geographic Distribution:** The wind turbines, service hubs, and vehicles are spatially distributed. Coupling occurs through both information exchange (e.g. work orders, dispatching procedures, weather data) and through the exchange of mass and energy.
- **Emergence:** At the SoS level, performance indicators and behavioural patterns emerge that cannot be attributed to any single constituent system. Due to the interplay of maintenance schedules, weather conditions, and vehicle capabilities, system behaviour is not entirely predictable.
- **Evolutionary Behavior:** The performance and characteristics of turbines and vehicles change over time. New systems, such as UAVs, are introduced, and the expansion of wind energy alters the surrounding parameters. Constituent systems can exit the SoS, for instance if a vehicle type becomes obsolete or economically unviable.

Applying the classification by DeLaurentis, Moolchandani, and Guariniello [118], offshore wind farm logistics can be characterised as an Acknowledged SoS. The offshore wind farm operator acts as a higher-level instance with defined goals for the overall SoS and coordinates it through control centres and dedicated operations and management strategies. The goals primarily consist of maximising economic energy production with high availability while ensuring compliance with relevant regulations, standards, and safety requirements. The constituent systems, such as operators of transport vehicles or inspection and maintenance services, retain operational and managerial independence, including individual objectives and independent funding. Standards and regulations are not solely set by the controlling instance, but also apply to the subsystems via existing aviation or maritime regulations, legal safety requirements, and system-specific certification data.

In individual cases, aspects of a Directed SoS may apply, for example when the operator of a wind farm owns and operates its own transport vehicles, as in the case of the ”Impulse” CTV operated by EnBW for its OWFs in the Baltic Sea [119].

2.4 Agent-based Modelling

2.4.1 Introduction to Agent-based Modelling

A suitable approach to simulate Systems of Systems can be found in agent-based modelling (ABM), particularly when these SoS are complex and adaptive and their properties emerge from the interaction of individual components, as is the case with transport systems. According to DeLaurentis, Moolchandani, and Guariniello [118], ABM is a ”computational method that enables a researcher to create, analyze, and experiment with models composed of agents that interact within an environment”. The constituent systems and, if necessary, their system components are modelled individually and implemented within the environment. The overall system behaviour is then derived from the interactions between the actors. This eliminates the need to directly implement the highly complex and difficult-to-describe behaviour of an SoS as a whole. Instead, the participating systems and stakeholders can be modelled individually using appropriate methods, and their interactions can be implemented. This can be referred to as a bottom-up approach. The individual stakeholders, constituent systems, and actors that are modelled in the simulation are referred to as agents.

The components of an agent-based simulation can be characterised according to DeLaurentis, Moolchandani, and Guariniello [118]:

- **Agents** represent the active entities within the simulation that make decisions
- **Objects** are passive components without decision-making capabilities, but can interact with agents.
- The **environment** is the context in which agents and objects exist and where the resources required by the agents are located
- **Communication** refers to all interactions between the system components, including not only information exchange but also material and energy flows

The modelling process is divided into the phases of composition, configuration, and control, each of which includes definition, abstraction, and implementation steps. The composition phase describes the development of the agent models. It defines which agents are to be modelled and in what form. In the configuration phase, the interactions and interfaces between agents, objects, and the environment are examined and implemented. The control phase involves specifying agent behaviour based on the concepts of operations that have been observed in the real-world SoS or are to be investigated, as well as the actual execution of the simulation.

Agent behaviour can also be used to classify agents, as shown in Table 2.2.

Agent-based modelling (ABM) has a experimental character, especially when stochastic influences are involved [118]. A single simulation run is therefore not sufficient to obtain reliable results. Instead, investigations with varied parameters are required to identify and analyse behavioural patterns.

In the present use case, ABM was considered suitable from the outset because offshore wind farm logistics combine multiple heterogeneous and partially autonomous actors, that interact under strongly time-dependent operational constraints. Mission execution de-

Agent type	Description
Autonomous	Runs without continuous user input
Interface	Requires assistant user
Info-gathering	Collects, filters, and classifies information
Goal-based	Does not have a set solution path, and does not care about a utility value
Utility	Does not have a set solution path but cares about a utility value
Reactive	Has a set solution path but cannot change its behavior based on past experiences
Adaptive	Can change its behavior based on past experiences
Mobile	Can move

Table 2.2: Classification of Agent types

pends not only on vehicle performance, but also on the sequencing of transport tasks, environmental restrictions, stochastic spontaneous material demands, and the current state of maintenance activities. As a result, relevant system-level outcomes cannot be derived sufficiently from isolated vehicle analyses or static process descriptions alone. Instead, they arise from the dynamic interaction of many local decisions and constraints. Accordingly, the expected emergence in this work was not limited to abstract system complexity, but specifically concerned emergent logistics patterns and SoS-level performance effects, such as non-linear changes in fleet utilisation, mission timing, enabled maintenance hours, and wind farm energy production when fleet composition, transport concepts, or interruption mechanisms are varied.

2.4.2 Agent-based Modelling for Maritime Scenarios

Agent-based modelling has already been applied in the context of maritime scenarios in order to represent the complex systems found there, which are characterised by numerous heterogeneous, spatially distributed actors, environmental conditions and interactions. Typical fields of application include maritime security situations, search and rescue operations, as well as transport and logistics systems. Several studies also show that ABM can be used for questions in the context of offshore wind energy, particularly for the investigation of operation and maintenance strategies, resource allocation and weather windows.

A tool for agent-based modelling of modern piracy and corresponding countermeasures was developed by Vaněk et al. [120], in which merchant vessels, pirate boats and naval units act as agents in an environment geographically defined by polygons with ports, anchor points and navigation obstacles. The model is used to evaluate anti-piracy measures such as transit corridors or patrols. Environmental variables such as wind, current and significant wave height are considered as influencing factors on behaviour and manoeuvrability, especially for smaller units, while merchant shipping traffic is represented through fleet and route statistics. Ships were modelled as agents, and the environment through wind speeds, wave heights and sea currents. For the behaviour of pirate units, merchant vessels and naval units, process flows derived from real strategies as well as risk calculation models for piracy incidents were used. To appropriately account for stochastic influences, 50 simulation runs per experiment with identical input parameters were conducted, and mean values and confidence intervals were determined for evaluation.

Several studies use ABM in the context of maritime search and rescue (SAR) operations, where the agent-based representation enables coupling of search resources, the search object and a dynamic environment. An ABM simulation was developed by Xiong et al. [121] using SAR helicopters and survivors drifting in the sea as agents, with the drift of survivors determined by environmental conditions. The helicopter agent includes properties such as fuel consumption, cruise speed and tank capacity, as well as the detection range in which survivors can be located during a flyover. The focus is on the implemented search strategies with drift predictions, confined search zones and flight grids, allowing the results to provide the probability of successful rescue depending on the search strategy and delay before mission start.

Ashrafi et al. [122] investigated the evacuation of passengers and crew from a distressed ship in the Barents Sea using ABM, with the NORA10 hindcast used for weather influences. In addition to wind speed, significant wave height and air temperature, the wind chill index was calculated, affecting the performance of passengers and rescue crew. The investigations included, among other things, the influence of the season, which particularly impacts rescue via weather conditions, the number of deployed rescue resources and the type of rescue equipment. Ships and helicopters with corresponding performance parameters were simulated as agents, as well as the persons to be evacuated. Simple process flows and phases within a rescue operation were derived from reality and implemented for agent behaviour.

An ABM simulation for maritime SAR missions was developed by Schön [123], providing metrics such as time-to-detection and mission success. The implementation uses a probabilistic search map environment, with search assets in the form of various crewed and uncrewed aerial vehicles, as well as the search object (life raft), modelled as agents with performance and movement parameters. The study investigated in particular how the model fidelity of individual subsystems, especially the sensor, influences the results.

The suitability of ABM for offshore petroleum platform logistics was conceptually examined by Engelseth and Pettersen [124], showing good applicability. Due to the similar stakeholders, vehicles and environmental conditions, the approach can also be transferred to offshore wind logistics.

ABM was used by Mast, Kuik, and Bussel [125] to develop scenarios for the expansion of offshore wind energy in the Netherlands, focusing on sector and supply chain development. Stakeholders are modelled as agents who communicate with each other and pursue their strategies, which may be risk-averse or risk-tolerant, in interaction with limited resources. Resources themselves are represented as non-acting objects with variable states. Limiting resources include installation vessels, port and grid capacities, as well as human resources, including the timeframe in which these resources can be built up. An example is the multi-year development and construction time of a vessel. The environment model includes factors such as public acceptance and market conditions. Scenarios are created through variation of environmental assumptions and agent strategies. Evaluation is carried out using indicators such as required investment efforts or impacts on the North Sea.

Niemi et al. [126] investigated the maintenance and restoration of operational capability of offshore wind farms under disruption scenarios, by coupling a failure model with an explicit O&M process model. A central boundary condition is the restricted access to turbines, which is represented in the simulation via operational limits and weather windows. Specifically, wind speed, significant wave height and daylight are used as conditions for safe interventions. The weather data is not based on a hindcast model but is synthetically generated. Operationally, resource pools for personnel and vessels are modelled, including different vessel types and process phases of a service mission, consisting of transit, service and manoeuvring within the park, as well as return. The methodology is applied, among other things, to normal operation without external disruptions, a cyberattack scenario with increased failure rates, and a ship collision scenario, in order to assess resilience under simultaneous failures and long restoration times.

A multi-agent model for representing operation and maintenance strategies for offshore wind farms was presented by Sahnoun et al. [127], explicitly modelling the dynamic interactions between technical assets, maintenance organisations and the environment. Turbines, maintenance, resources, monitoring and weather were implemented as agent types, with each turbine tracking state variables such as the equipment health factor (EHF) and generated energy, influenced by both maintenance and weather conditions. A cost model for maintenance measures, energy losses and installed monitoring systems was also implemented. As environmental parameters, wind speed, wave height, temperature and lightning events were considered. Maintenance resources were parameterised as engineers, technicians, boats and cranes. Several maintenance strategies were compared to make effects on energy production and costs visible, including seasonal weather fluctuations.

2.4.3 SoSID-Toolkit

To enable the implementation of ABM in aviation related SoS contexts, the System of Systems Inverse Design (SoSID) Toolkit was developed within the DLR, a Python-based framework that supports the definition of environments, agents and their interactions, including graphical visualisation and modular extensibility for application-specific models. A key characteristic of the toolkit is its focus on linking realistic operational scenarios to aircraft design decisions, such that vehicle-level parameters and assumptions propagate into system-level performance metrics like vehicle utilisation, energy consumption or mission success.

In the SoSID-Toolkit, vehicles are defined through aircraft-specific JSON input files that provide aircraft characteristics like the $MTOM$, maximum fuel mass or maximal electrical energy as well as mission-profile parameters such as cruise speed and energy consumption across aircraft masses. Performance and energy consumption behaviour is computed with a dedicated propulsion model. With regard to maritime scenarios, a helicopter performance model was already implemented in the SoSID-Toolkit, which adds rotorcraft to the already existing models for conventional fixed wing and VTOL aircraft with combustion and battery-electric drivetrains [128].

In the past, SoSID has been used to model Urban Air Mobility (UAM) scenarios, where eVTOL aircraft agents operate within a network of nodes representing infrastructure elements like vertiports [129, 130, 131]. The eVTOL aircraft were designed with the VTOL-AD tool and inserted into the Toolkit with standardised input files. In addition to vehicle agents, organisational agents such as dispatchers and vertiport managers were implemented to represent assignment and capacity-management logic, which strongly affects waiting times, passenger throughput and fleet requirements. Supplementary demand models were developed to generate passenger requests and to enable realistic on-demand operations under varying demand levels and uncertainty. This enabled comprehensive analysis on how both design parameters and decisions and operational factors jointly shape UAM system performance.

SoSID has been used for multimodal simulations as well, integrating additional transport modes such as cars and rail to evaluate door-to-door performance rather than aircraft operations in isolation [132]. In these studies, traveller demand and mode choice interact with network connectivity, transfer processes and infrastructure constraints, making it possible to quantify the system benefit of advanced air mobility concepts in the context of complete travel chains. The multimodal integration leads to shifting evaluation from isolated mission metrics to end-to-end service measures such as total travel time, accessibility and network-wide passenger flow.

Beyond UAM, the toolkit has been used to investigate aerial wildfire suppression, in which the operational environment includes a model of fire behaviour and spread that is influenced by weather conditions [133]. Aircraft agents represent firefighting assets executing tactical suppression strategies, and their effectiveness emerges from the interaction of vehicle capabilities, tactical behaviour and the evolving fire dynamics. The studies highlight that tactical choices, such as suppression patterns and resource allocation policies, can materially change mission outcomes, and therefore need to be considered alongside vehicle-level performance assumptions in design assessments.

SoSID has also been adapted for strategic cargo airlift in humanitarian and disaster-relief contexts, using agent-based modelling to link aircraft capabilities and Concepts of Operations (CONOPS) [134]. In this application, aircraft, cargo and airbase entities interact through dispatching and assignment logic, while the operational environment is represented by a network of airbases with capacity and process constraints and by stochastic disruptions such as changing accessibility or unplanned demand. Aircraft design parameters are introduced into the simulation as performance and capacity characteristics and scenario outcomes are evaluated across repeated runs to quantify how design choices and operational strategies jointly affect fleet-level performance.

Chapter 3

Conceptualization of Scenarios

3.1 Methodology

In order to investigate the present system of systems and the related research questions, the real-world system of systems must be conceptualized. According to DeLaurentis, Moolchandani, and Guariniello [118], the following aspects must be identified and taken into account when modelling a system of systems (SoS):

- System capabilities
- Interactions
- Interfaces
- Policies
- Boundaries
- Layers

A robust simulation model, according to DeLaurentis, Moolchandani, and Guariniello [118], should fulfill the following qualities:

- Systems must be modeled with the components, interactions, and policies or rules that are essential to explain the system behavior
- The model must apply the correct level of abstraction and should focus on the aspects relevant to the research question
- The model must offer an appropriate resolution, such that it remains manageable and usable, while still being sufficiently detailed to draw meaningful conclusions
- The model should be flexible and extensible

The fundamental analysis of offshore wind farm logistics as a system of systems has been carried out in Section 2.3.2. Its results must be systematically transferred into the agent-based modelling approach of the DLR SoSID-Toolkit framework, building on the implementations, workflows, and lessons learned from previously examined SoS such as

Advanced Air Mobility.

The modelling of vehicles, as in prior studies, is implemented in the form of individual agents with variable positions. Their energy consumption is calculated during the simulation using the energy module.

The airport agents continue to exist, now serving as service hubs, which also handle vessel operations.

Newly introduced are the energy generation agents. They represent the core of this work and are spatially fixed. The energy production of these agents is modeled using the specifically developed energy generation model.

The dispatching logic differs significantly from previously implemented scenarios, which necessitates the development of a dedicated dispatching model that accurately reflects the foundations, rules, and constraints of the offshore environment.

Weather and general environmental conditions have previously been adapted to the context of wildfire response and considered in the model [133]. However, this model is not suited for the offshore environment, which requires a new approach.

As in the previous studies conducted with the toolkit, scenarios must be provided along with aircraft models, which are generated using a dedicated design tool. The results of simulations run with these input parameters can then be evaluated. In addition to the metrics commonly used so far, such as fleet utilization and energy consumption, new metrics specific to the maritime context are introduced, including generated energy, wind turbine downtime, and enabled maintenance time.

A graphical representation of this simulation framework is shown in Figure 3.1.

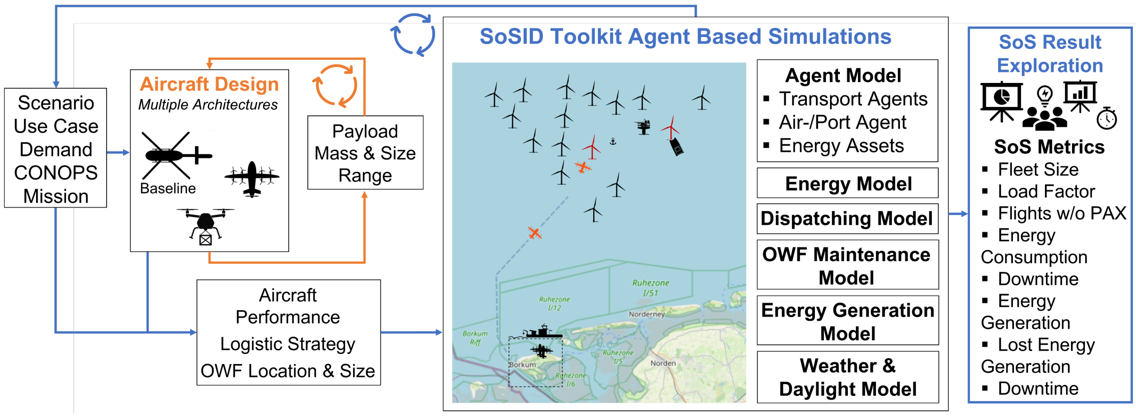

Figure 3.1: SoSID Toolkit Simulation Framework for OWF Logistics and Aircraft Design

3.2 Goal and Scope Definition

The overall objective of the simulations in agreement with the task for this thesis is to evaluate the impact of varied UAV parameters as well as the general use of UAVs for logistics purposes on the SoS, and to identify both the potential and limitations of drones in offshore wind farm logistics. While the integration of aircraft follows the established approach of previous studies using the SoSID toolkit via standardised JSON input files, equivalent mechanisms must be defined to parameterise and vary the offshore environment as well. The simulation is intended to allow the evaluation of the energy production of the offshore wind farm, the analysis of the vehicles used, and the assessment of the maintenance hours performed on the wind turbines. Based on this data, initial evaluations can be performed directly and economic assessment models can be connected.

To capture developments and trends on both the aircraft side and the wind farm side, the location of the simulated wind farms should be variable, and the installed wind turbines should differ in size and rated power. In order to analyse how robust the SoS is with respect to the duration of maintenance activities, the number of turbines requiring maintenance, or the probability of failure of a wind turbine, these parameters must also be definable and variable within the simulation. The same applies to the size or mass of the equipment to be transported, which may vary depending on the maintenance type or the size of the turbine. The simulation should also allow the consideration of real weather conditions, using either historical weather data or synthetic values.

Accordingly, the following input parameters are to be considered in the simulation:

- Simulation day
- Logistics strategy
- Vehicle parameters
- Number of vehicles
- OWF location
- Service hub location
- Number of wind turbines
- Turbine size
- Maintenance parameters

The following output parameters are to be evaluated as particularly relevant:

- Energy consumption of the overall transport system
- Energy production during the simulation period
- Performed maintenance hours
- Total travel and flight time of all transport vehicles
- Fleet utilisation

3.3 Scenarios

For the operation of offshore wind farms, different optimal logistics strategies exist depending on the distance between the wind farm and the coast [17]. In addition to the use of helicopters, as described in Section 2.2.2.1.1, vessels can also be employed, either crew transfer vessels (CTVs) or service support vessels (SSVs) that remain within the wind farm for extended periods, as discussed in Section 2.2.3. Larger offshore platforms may also serve as permanent or semi-permanent service hubs [17].

All of these options can be combined as needed, and all could potentially be complemented by the use of logistics drones. In this work, the focus is placed on the use of CTVs and helicopters, and only these types of vehicles are implemented within the simulation model.

Helicopters and CTVs are particularly suitable for offshore wind farms located up to approximately 130 km from the coastal service base [17]. Numerous existing and planned wind farms in the German Bight fall within this range, allowing the simulation results to be representative for real-world OWF operations despite this restriction.

For the scope of this work, three distances between OWFs and the chosen service hub on the island of Borkum were determined, with 80 km as the lowest distance, 120 km as an intermediate distance and 160 km as the largest. By choosing multiple distances, emerging trends with larger distances from shore were expected to be observable. With the two lower distance steps, all currently operational OWFs in the German Bight can be reached from service hubs along the coast or on the island of Heligoland, as can be seen in Figure 3.2. The largest distance is oriented at the planned farms further away from the coast and servicehubs.

With the described focus on helicopters and CTVs as logistics vehicles, two baseline strategies are defined, in which all operations are carried out either exclusively with CTVs or exclusively with helicopters. Accordingly, all processes are completed either by one or more CTVs via the sea route or by one or more helicopters via the air. In the agent-based modelling approach of the SoSID toolkit, a more flexible procedure would be possible, in which the optimal vehicle is selected through an auction-based mechanism [132]. However, due to the long-term contracts and the high costs associated with short-notice vehicle bookings that are common in the offshore industry, the vehicle selection implemented in this simulation is fixed and determined by the chosen strategy.

For the CTV strategy, the daily schedule or Concept of Operations (ConOps) illustrated on the left in Figure 3.3 was developed based on the analysed maintenance procedures in the form of a process diagram. In addition to the vehicle remaining in the wind farm during maintenance activities, it is important to note that if equipment is needed spontaneously during a maintenance operation, it is not delivered, as this would require a time- and cost-intensive round trip to the service hub. Instead, the team is picked up immediately, and the maintenance task can be resumed the next day with all necessary equipment. In the case of the helicopter strategy, small spontaneous equipment deliveries can be carried out in contrast to the CTV only strategy, as shown in the right process chart in Figure 3.3.

In the following, these strategies are referred to as ”CTV only” and ”Helicopter only”. In all strategies, adherence to daylight and working time restrictions is of great importance and determines the start and end of activities in the wind farm.

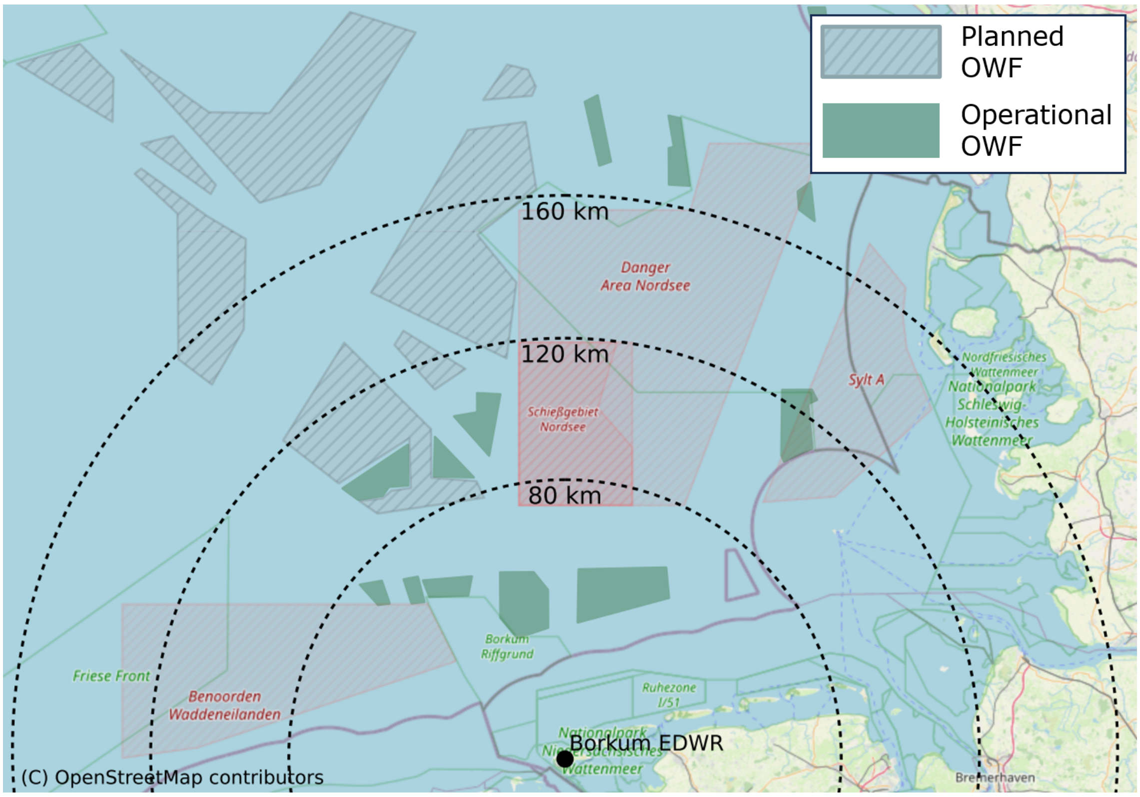

Figure 3.2: Map of the German Bight with planned and installed OWPs and selected Distances to the Service Hub

Based on these baseline scenarios, logistics strategies involving the use of drones have been developed and corresponding concepts of operation (ConOps) have been derived. As a currently technically feasible strategy, the transport of spontaneously required, relatively small equipment parts and spare components from the service hub to the turbine is considered, as already demonstrated in the campaigns described in Section 2.2.2.2.3. The drones are only required to transport one item and either drop it above the winching area or lower it via winch. Automated pick-up of items or the return of components to the service hub is explicitly not intended.

Both baseline vehicles can serve as the basis for the logistics strategies that include this type of drone support. When combined with CTVs, a maintenance task that is temporarily interrupted can be continued immediately after a drone delivery. In combination with helicopters, this strategy avoids a costly return flight from the coast to the turbine by a helicopter with a multi-person crew to deliver a lightweight item.

These strategies are referred to as the respective baseline vehicle “and UAV for spontaneous deliveries”. The ConOps for the strategy with CTVs as the baseline are shown in Figure 3.4. The ConOps for the drone or drones does not change when helicopters are used as the baseline vehicle. Therefore, a separate representation of the ConOps for the ”Helicopter and UAV for spontaneous deliveries” strategy is not provided.

With larger uncrewed aerial vehicles capable of not only delivering but also picking up cargo autonomously, an additional scenario becomes feasible that offers potential benefits for the operation of an offshore wind farm [103]. In this case, personnel continue to be transported by CTV, while the equipment is delivered by drone directly from the service

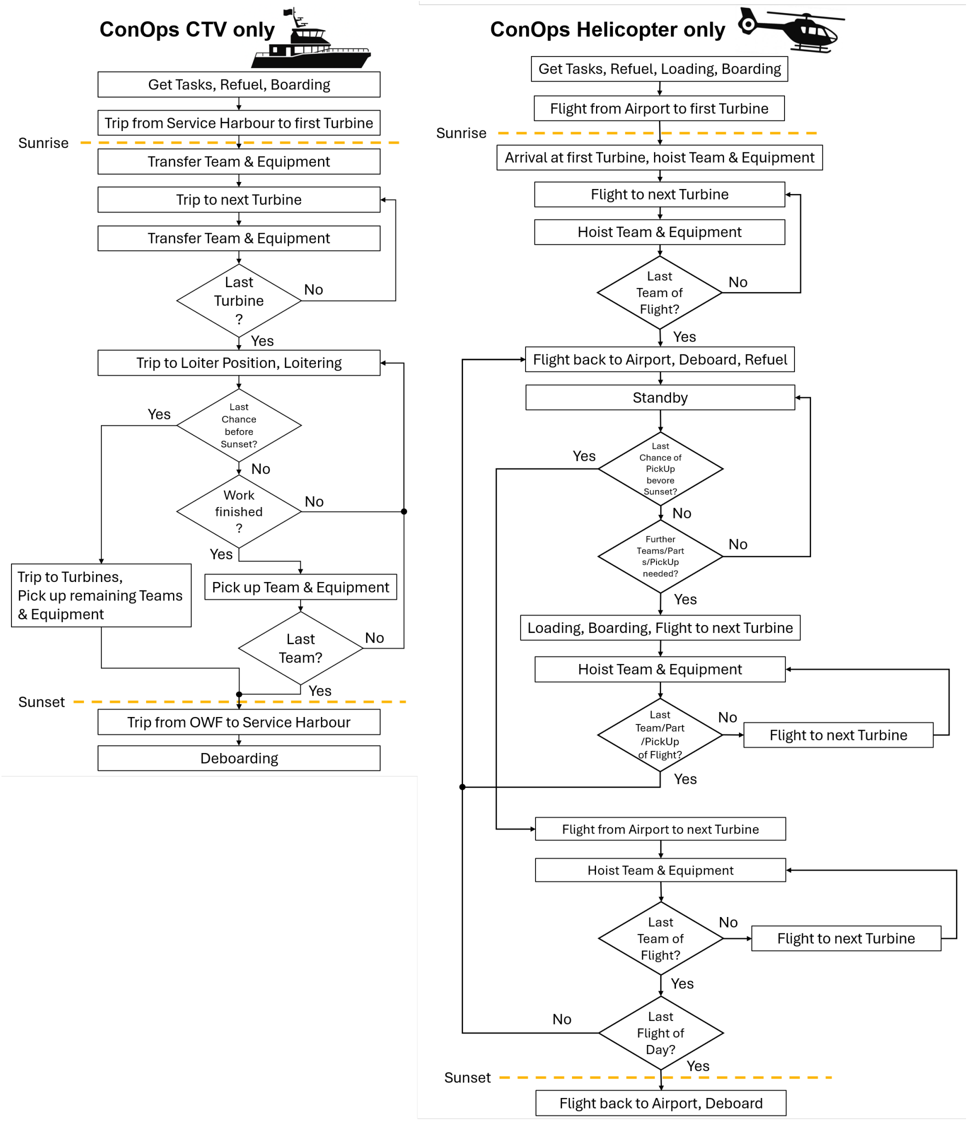

Figure 3.3: Process Chart of the CTV Only (left) and Helicopter Only (right) Strategy ConOps

hub to the winching area of the turbine. This reduces the transfer time from the CTV to the wind turbine and enables maintenance activities to start sooner, as the equipment is already positioned near the nacelle. This strategy combines the lower operating costs of a CTV with the faster maintenance execution enabled by air transport. Spontaneous demands are also fulfilled using the same drones.

As long as the environmental conditions, in this case mainly daylight, are still suitable, the equipment is collected from the wind turbine by drone. As part of this work, it was decided not to force any work to be completed early in order to have all the equipment collected by drone before sunset. This would have to take place the next day, but it would allow the technicians' working time to be used optimally. The representation of the ConOps in a process chart as in Figure 3.5 shows, in contrast to Figure 3.4, the significantly higher effort required for dispatching.

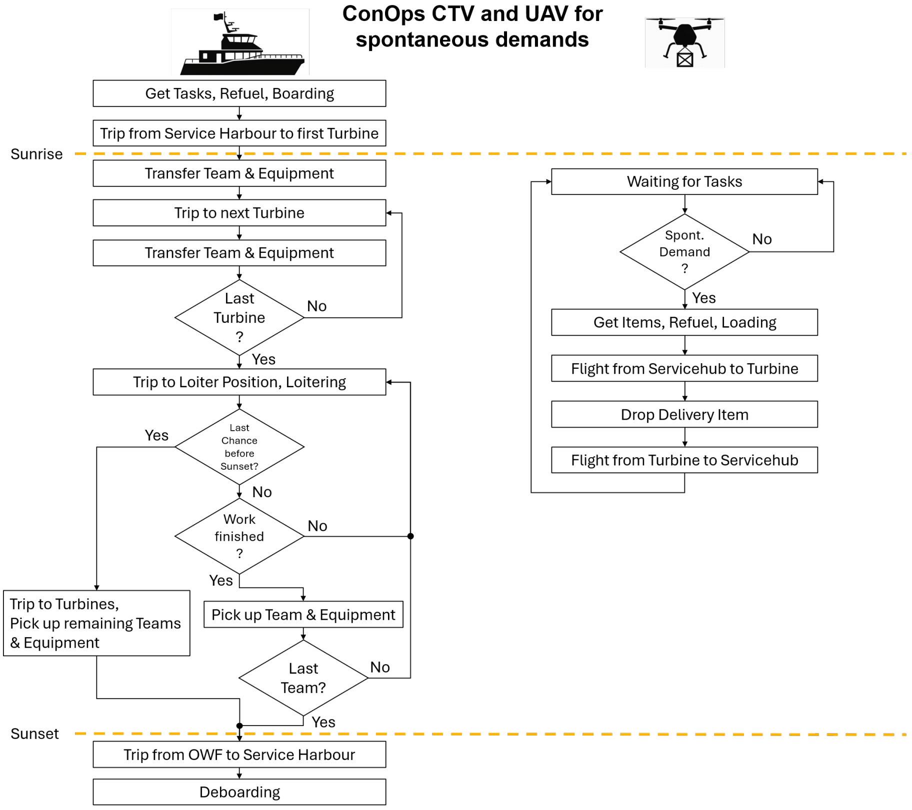

Figure 3.4: Process Chart of the CTV and UAV for spontaneous Deliveries Strategy ConOps

Figure 3.6 provides an overview of the five strategies implemented.

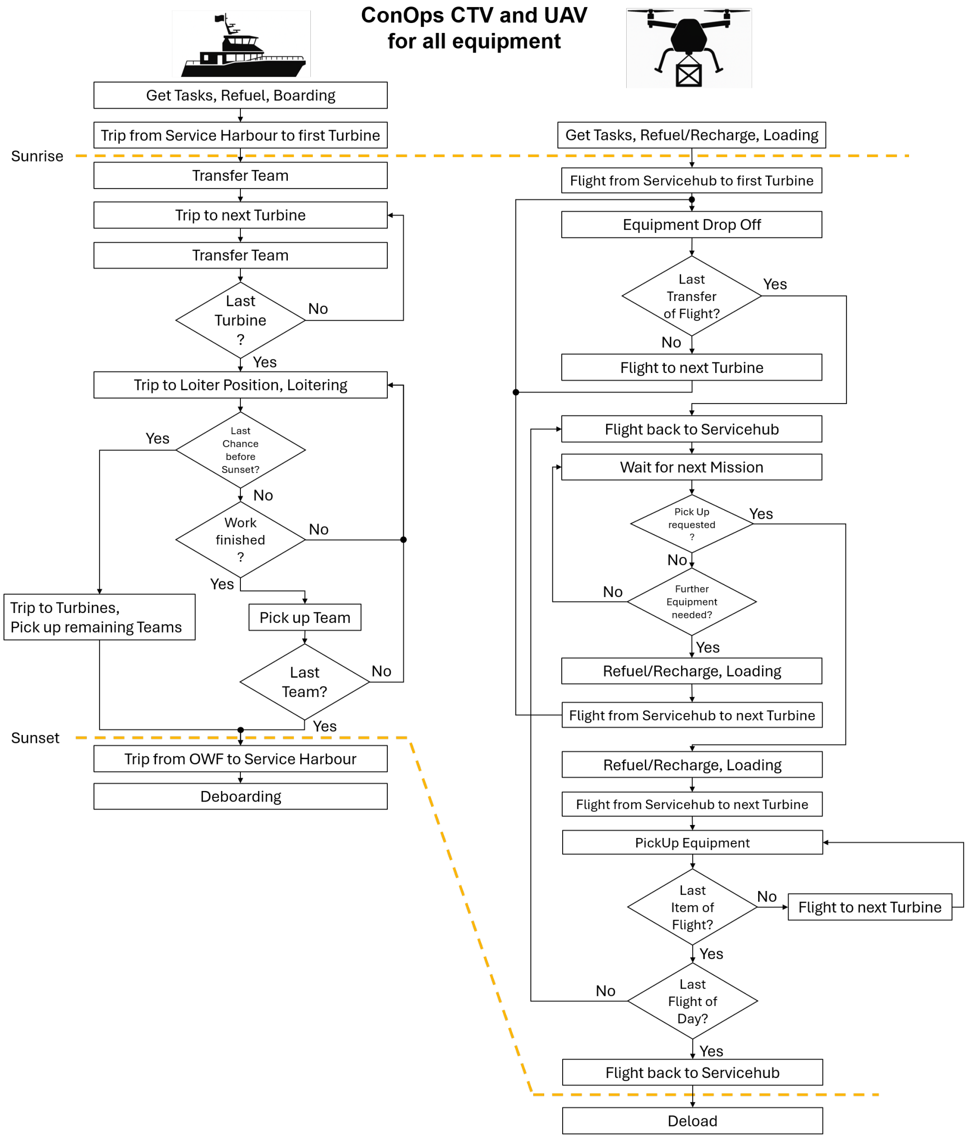

Figure 3.5: Process Chart of the CTV and UAV for all Equipment Strategy ConOps

3.4 Limitations

Even when considering the described input parameters and strategies, the result is a complex system of systems that is still not identical to reality. Several limitations were accepted during implementation or introduced deliberately in order to avoid unnecessary complexity that would not add value for the objectives of this study, or whose inclusion would in itself raise additional questions and require further investigations. These aspects can be integrated after the basic implementation and analyses and are therefore outside the scope of what can and should be implemented in this thesis.

With respect to the scenarios, the restrictions to a single offshore wind farm and a single service hub must be mentioned. For investigating the influence of drones on a logistics concept, this is assessed as fully sufficient. However, multiple wind farms located in proximity can, independent of the selected strategy, lead to synergy effects, which can naturally differ in magnitude depending on the strategy. Based on the analyses for a sin-

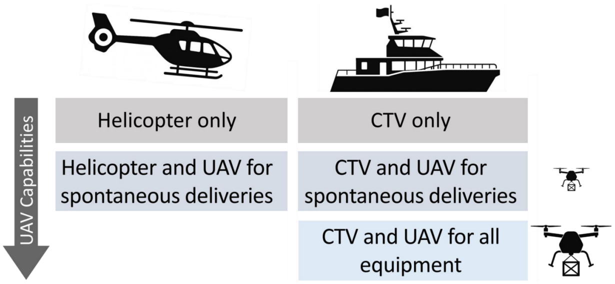

Figure 3.6: Visual Representation of the identified and implemented Logistics Strategies

gle OWF, this can be investigated in a targeted manner in future works. The same applies to the use of multiple service hubs.

In addition, vehicle fleets within a vehicle category (helicopter, CTV, UAV) are defined as homogeneous. On the one hand, this provides fleet advantages with respect to personnel training, maintenance, and acquisition cost, so this restriction does not prevent plausible results. This assumption is also common in other studies on this topic [17, 135]. A mixed fleet can indeed offer advantages as well, but it requires a dispatching algorithm adapted to such a fleet, which would need to be developed and investigated separately.

Regarding dispatching, there is a significant limitation that can lead to less efficient operations compared to reality. Once an aircraft or vessel has departed, mission planning is fully completed and is not modified any further, even if another physically feasible mission becomes available during travel or flight time. In reality, mission changes can also be made on short notice through coordination between the dispatching unit and pilots or ship captains. In the simulation, either the active vehicle must complete its current mission and return to the service hub, or another vehicle must be available to take over the mission. Furthermore, missions are planned as one-way transports only. Within one flight, teams or equipment are either delivered and the return leg is flown empty, or the vehicle flies empty to the wind farm and returns with one or more teams or items. This restriction is less relevant for CTVs because they have very short distances within a wind farm, but for helicopters and large drones used for equipment delivery and pick up, it also results in less efficient operations within the simulation.

Chapter 4

Implementation of the Offshore Environment in the SoSID-Toolkit

4.1 Weather Model

Fundamentally needed for the representation of the offshore environment is a weather model. Without wind speeds, no wind energy generation can take place, and both wind speed and significant wave height represent relevant operational constraints for the vehicles, in particular for the feasibility of a safe transfer from the vehicle to the wind turbine. Given the geographical dimensions of the offshore environment, where distances between offshore wind farms and onshore service bases can exceed one hundred kilometres, an approach assuming a spatially uniform wind speed across the simulation domain, as applied by Kalliatakis et al. [133] for wildfire scenarios in the SoSID-Toolkit, was not considered sufficiently accurate for this application.

For offshore wind farm planning, a variety of weather models is available, covering different regions, datasets, and spatial or temporal resolutions [136]. Some of these models are openly accessible, while others are commercially distributed. Based on the available data, the high resolution, and the coverage of the German Bight and other European coastal and offshore regions, this work selects the NORA3 weather model provided by the Norwegian Meteorological Institute (MET). NORA3 is based on the ERA5 reanalysis of the European Centre for Medium-Range Weather Forecasts (ECMWF), which provides global atmospheric data, and it covers the North Sea, Baltic Sea, Norwegian Sea, and Barents Sea [136]. With a spatial resolution of 3 km, the NORA3 hindcast provides hourly data at the altitude levels 10 m, 20 m, 50 m, 100 m, 250 m, 500 m and 750 m, thereby covering both typical hub heights of offshore wind turbines and typical helicopter operating altitudes in offshore environments [137]. Using weather stations on oil and gas platforms as well as measurement masts in the Norwegian Sea and North Sea, the model has been successfully validated [138]. For OWF planning and analysis in particular, the specialised NORA3-WP dataset is available, which directly supports assessments based on geographic positioning and turbine specifications [139]. Due to its comparatively high spatial and temporal resolution and its demonstrated suitability for offshore wind applications, the required simulation inputs were retrieved from the NORA3 model using the Metocean API.

The Metocean API is an open-source Python library designed for the automated extraction of metocean time series from various hindcast and reanalysis datasets, most notably the NORA3 hindcast dataset provided by MET Norway and the global ERA5 reanalysis from ECMWF [140]. It provides a programmatic interface through which temporally and spatially resolved data such as wind speed, wave height, temperature and other oceanographic variables can be queried and retrieved. The result of such a query for the wind speed at the lowest available altitude is displayed in Figure 4.1, displaying the spatial distribution of wind speeds in the German Bight during the storm Aina.

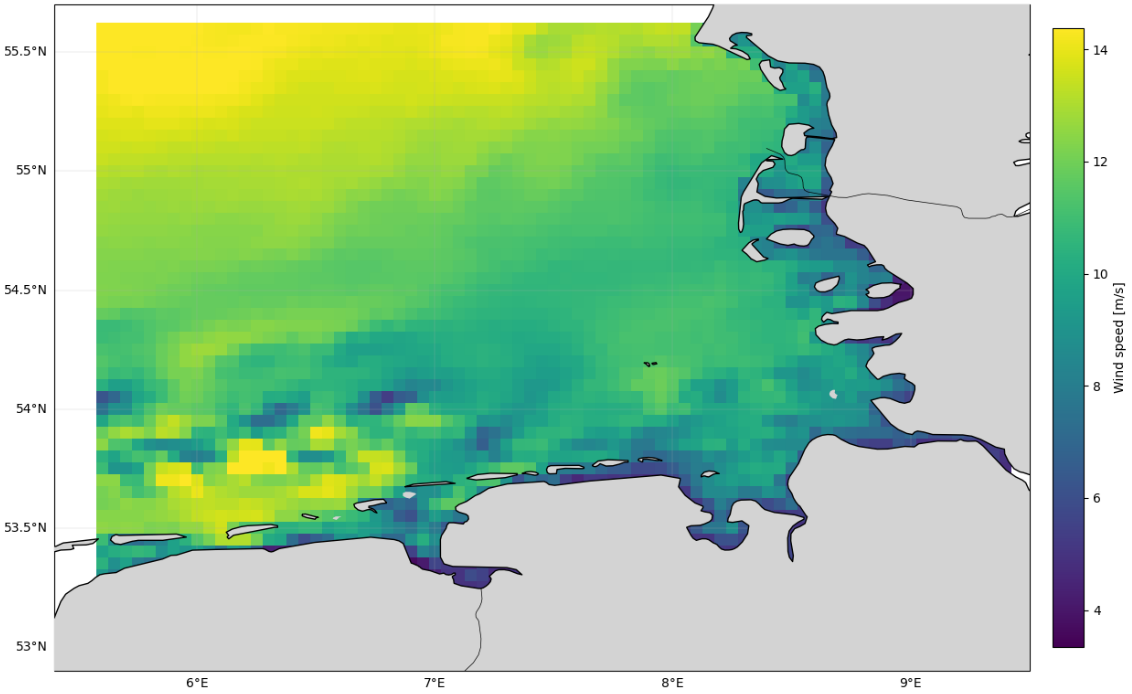

Figure 4.1: Wind Speed in the German Bight taken from the NORA3_wind_sub Dataset (8th December 2017, 4 AM)

To keep the simulation framework extensible for future integration of alternative weather models, for example forecasts, the weather data is not to be downloaded directly from the NORA3 datasets during runtime. Instead, they must be provided prior to simulation in a JSON file, which is then evaluated by the weather module developed within this work. This approach also improves robustness, as the simulation does not depend on a successful data download during execution, and it becomes less sensitive to network issues and download speeds.

The following parameters have been identified as relevant for the simulation and are retrieved from the weather model once per hour and for the specified coordinates: It must be noted, that the directions are defined in this work as the direction in which the vector of the wind or the waves points.

- Significant wave height [m]
- Wave direction [°]
- Wind speed (per altitude step) [m/s]
- Wind direction (per altitude step) [°]

- Air temperature (per altitude step) [°C]

The simulation is provided with these parameters in the form of a JSON file, structured as shown in Listing 4.1.

Listing 4.1: JSON Input File for the Weather Model

```
{
  "date": "2024-08-21",
  "heights": [10, 100, 150, 500],
  "points": {
    "53.00_5.50": [
      {
        "hour": 0,
        "significant wave height": 0.69,
        "wave direction": 150.4,
        "wind profile": [
          {
            "height": 10.0,
            "wind speed": 4.55,
            "wind direction": 147.8,
            "temperature": 14.75
          },
          {
            "height": 100.0,
            ...
          },
          ...
        ]
      },
      {
        "hour": 1,
        ...
      },
      ...
    ],
    "53.00_5.50": [
      ...
    ],
    ...
  }
}
```

4.1.1 Wind

As can be seen from the specified altitude, it is not necessary to define heights that exactly match the vertical levels available in the NORA3 dataset. When generating the JSON input file, the desired values are already interpolated from the available data points of the NORA3_wind_sub dataset, with the aim of shifting as much computational effort as possible to this preprocessing step. To achieve this, a vertical wind profile is constructed for a given location and time, from which the desired values at arbitrary heights can be derived.

In parallel to the airflow inside the boundary layer of an airfoil, the wind speed near the Earth's surface can be described with a logarithmic profile [141]. To represent wind speeds at higher altitudes above sea level, the Deaves-Harris formulation is applied to fit the wind-speed profile [142, 143]. The required input parameters for this method are the surface roughness length over the ocean z_{sea} and the friction velocity u^*. Based on the wind speed at the lowest available vertical level of the NORA3 dataset, the Charnock equation can be solved to obtain z_{sea} [143].

To compute the surface roughness length z_0 over the ocean, the Charnock relation as shown in Equation 3.1.1.1 is used [143]. This equation connects the wind speed U_{ref} at a reference height z_{ref}, which is obtained by using the lowest altitude step the NORA3 dataset offers, to the aerodynamic surface roughness. The gravitational acceleration g and the von Kármán number κ must be known as well as the Charnock constant α. Higher wind speeds result in higher waves and rougher water surfaces, which in turn affect the wind profile and thus the wind speed near the water surface. The relation is implicitly nonlinear and needs to be solved iteratively.

$$z_0 \cdot \frac{g}{\alpha} \cdot \left[\ln \left(\frac{z_{ref}}{z_0} \right) \right]^2 = (\kappa \cdot U_{ref})^2 \tag{3.1.1.1}$$

While generating the weather data input file for the simulations discussed in this work, the von Kármán number was set to $\kappa = 0.41$ [144] and the Charnock constant to $\alpha = 0.011$, which has proven to be a good approximation for open seas [145]. The Charnock constant does influence the quality of the results especially in certain weather situations like storms and cyclones and methods with adjusted values are better in this regard, but as a simplified approach for comparatively calm weather scenarios, a constant value in the typical range vor this constant was seen as sufficient [146, 143, 145].

The friction velocity u^* is calculated assuming a logarithmic wind speed profile again based on the lowest available datapoint of the NORA3 dataset while using the calculated surface roughness length z_0.

$$u^* = \frac{\kappa \cdot U_{ref}}{\ln(z_{ref}/z_0)} \tag{3.1.1.2}$$

To model the vertical distribution of wind speed $U(z)$ in variable altitudes z within the atmospheric boundary layer over the sea, the simulation employs the Deaves-Harris profile formulation. This profile extends the classic logarithmic wind law by incorporating additional polynomial terms, thereby allowing a more accurate representation of the wind speed at higher altitudes. To achieve this, the parameters c_1, c_2, c_3 and c_4 are needed. The formulation reads:

$$U(z) = \frac{u_*}{\kappa} \cdot \ln\left(\frac{z}{z_0}\right) + c_1(z - z_0) + c_2(z - z_0)^2 - c_3(z - z_0)^3 - c_4(z - z_0)^4 \qquad (3.1.1.3)$$

To adapt the generic form in Equation (3.1.1.3) to the actual atmospheric state at each time step and grid location, the wind speed values from the NORA3 dataset at the available native heights are used as fitting targets. With the previously determined values for u^* and z_0, the remaining parameters c_1 to c_4 are identified via nonlinear least-squares fitting.

This yields a locally and temporally adapted continuous profile $U(z)$, which can then be evaluated at arbitrary target heights depending on the simulation requirements. The continuous Deaves-Harris profile as well as the native NORA3 datapoints are displayed in Figure 4.2 for the storm Aina at a location near the Norwegian city of Bergen as an example.

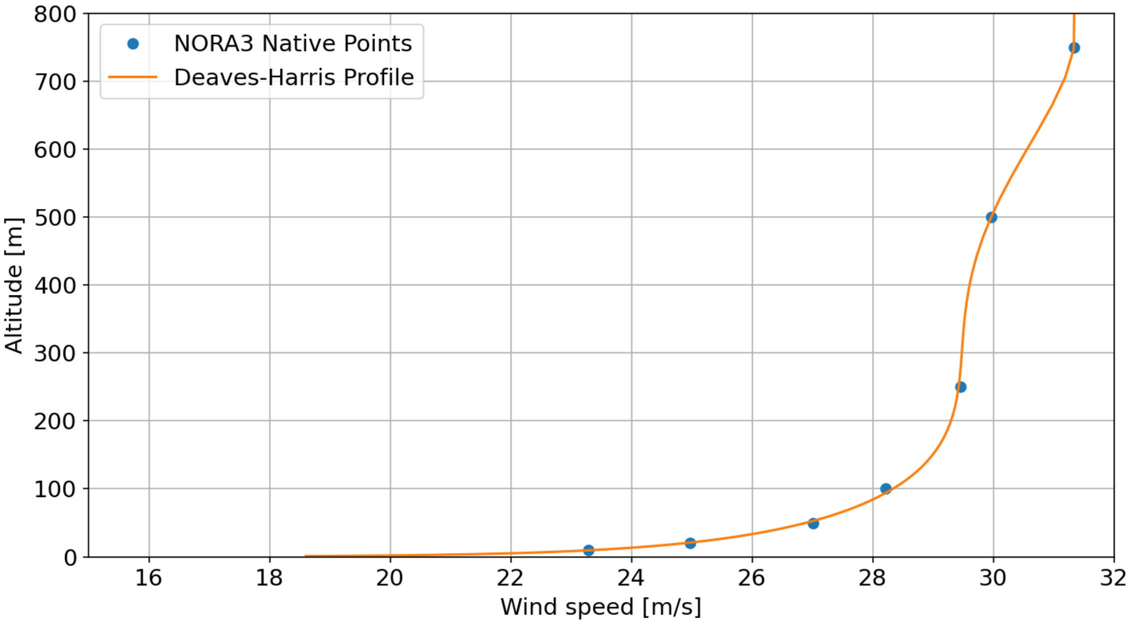

Figure 4.2: Wind Speed Profile resulting from the Deaves-Harris Fit and the NORA3 Datapoints (8th December 2017, 4 AM, 60° N, 5° O)

The values gained with this method are then stored in the JSON file for each hour and location. For the air temperature, the values are simply interpolated in a linear manner from the native NORA3 datapoints. Once the hourly wind profiles for each grid cell have been calculated and saved in the JSON input file, they can be efficiently retrieved at any point in time, position and altitude during the simulation. This is done using a three-step interpolation process, in which temporal, spatial and vertical interpolations are performed sequentially to obtain continuous wind and temperature values from the discrete NORA3 data.

If the location falls exactly on a coordinate contained in the JSON input file, the first step is to perform a temporal interpolation of the wind speed for each stored height z_j, based on the two neighbouring full hours t_i and t_{i+1} between which the current simulation time t lies. This interpolation is performed separately for each grid cell according to equation (3.1.1.4).

$$U_j^{(k)}(t) = (1-\alpha) \cdot U_j^{(k)}(t_i) + \alpha \cdot U_j^{(k)}(t_{i+1}) \quad \text{mit} \quad \alpha = \frac{t - t_i}{t_{i+1} - t_i} \tag{3.1.1.4}$$

Whereas $U_j^k(t)$ denotes the wind speed at height z_j, time t and grid point k. For any simulation point (x, y) that does not lie exactly on a coordinate point location included in the JSON input file, the four nearest points are identified. At each of these four grid points, temporal interpolation is first performed independently according to equation (3.1.1.4). This is followed by bilinear interpolation in space, for each height z_j individually:

$$U_j(x, y, t) = \sum_{k=1}^{4} w_k(x, y) \cdot U_j^{(k)}(t) \tag{3.1.1.5}$$

Here, $wk(x, y)$ are the interpolation weights for the four surrounding grid points $k = 1...4$, which result from the relative position of the target coordinate (x, y) within the grid area. The result of this step is a fully temporally and spatially interpolated profile $U_j(x, y, t)$ in the elevation steps specified in the JSON input file.

In the final step, the wind speed at the target height z is determined from the previously interpolated profile in terms of time and space. For this purpose, piecewise linear interpolation is performed between the neighbouring height values, assuming that the wind speed does not change significantly between two height levels defined in the JSON file and therefore no major errors occur. This eliminates the need for iterative solution of the Charnock equation and fitting of the Deaves-Harris parameters, which has a positive effect on the simulation runtime. However, the heights specified in the JSON file should correspond as closely as possible to the heights at which, for example, the rotor hubs of the wind turbines are located or at which the aircraft are flying. The general interpolation formula is used for the height-dependent wind speed calculation as specified in equation (3.1.1.6).

$$U(z) = U_j + \frac{U_{j+1} - U_j}{z_{j+1} - z_j} \cdot (z - z_j) \quad \text{für} \quad z_j \leq z \leq z_{j+1} \tag{3.1.1.6}$$

Here, z_j denotes the next lower known altitude level below the target altitude z, z_{j+1} denotes the next higher level, and U_j, U_{j+1} denote the corresponding wind speeds at the respective time and location.

The same procedure is applied similarly to other meteorological variables such as wind direction, which must first be converted into Cartesian components, and air temperature.

4.1.2 Waves

The intensity and severity of waves are naturally particularly relevant for seagoing vessels and have a direct influence on energy consumption and the general feasibility of a trip, with significant wave height typically being used as a criterion [147, 111, 15]. However, this restricts air transport as well.

It is not the actual flight that is affected by the waves, but the scenario of an emergency landing. Helicopters and their emergency equipment can be operated safely up to certain limits, which are usually specified in the form of a maximum safe Sea State [71]. Sea States combine several wave parameters such as height, wavelength, period and directional wave energy flux [148]. Since this work considers normal maintenance and repair operations that should not be carried out under particularly critical circumstances or high risks, these limits are strictly taken into account. However, the corresponding Sea States for modern helicopters are relatively high with at least Sea State 4, compared to the restrictions that apply to travel by ship and, in particular, to boarding, which is why no major restrictions are expected in the simulations [71].

To model the influence of waves in the simulation, the significant wave height is used, which is obtained directly from the NORA3_wave_sub dataset with the Metocean API. Figure 4.3 displayes the result for a chosen resolution of 0.05° for the storm Aina in the German Bight.

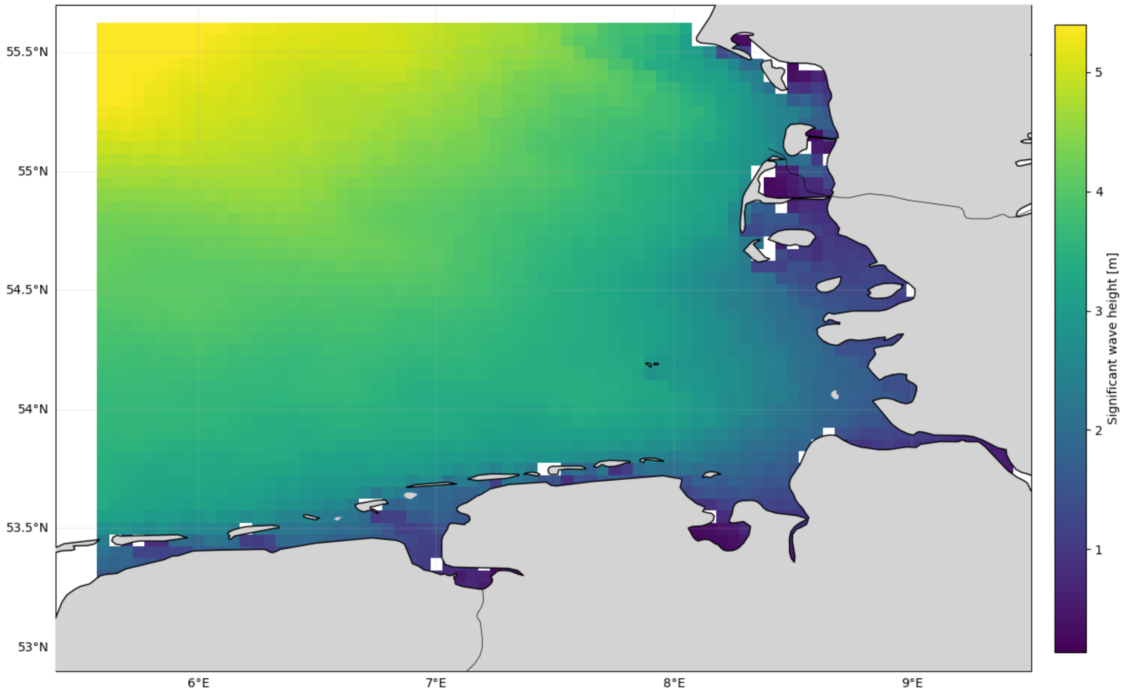

Figure 4.3: Significant Wave Height in the German Bight taken from the NORA3_wave_sub Dataset (8th December 2017, 4 AM)

In principle, there are more parameters that characterise waves more accurately, but in line with other simulations in the offshore logistics environment, only this value is used for the sake of simplicity [111, 15, 122]. The significant wave height reflects the average wave height of the top third of all waves occurring in a specific sea area during a specific period of time, whereby individual significantly higher waves may also occur due to the averaging [149]. The Sea State data can also be converted into significant wave height in a simplified manner, the equivalent data are listed in Table 4.1 [150].

Sea state	**Mean significant wave height [m]**	**Description**
0	0	Smooth sea surface
1	0.05	Ripples
2	0.3	Wavelets
3	0.875	Small waves
4	1.875	Moderate waves
5	3.25	Large waves
6	5.0	Moderatly high waves
7	7.5	Very high waves
8	11.5	Exceptionally high waves
9	$>$14.0	

Table 4.1: Sea States and corresponding Mean Significant Wave Height [150]

4.2 Energy Production Model

4.2.1 Wind Turbine Implementation

The wind turbines form the cornerstone of the energy-generation modelling in this work and are modelled as individual agents. As for the aircraft, the input parameters of the turbine models are defined in a JSON file, which allows different wind turbine types to be integrated into the simulation. The number and positions of turbines as well as maintenance campaigns are not part of the wind turbine inputs and defined separatly. The input parameters of the turbine models only represent the power generation properties.

For this purpose, the turbine's power curve is used and evaluated with the wind speed at hub height. This approach is widely used and enables realistic energy-generation data, even though local effects such as wake shading by neighbouring turbines or the non-uniform wind-speed profile over the full rotor diameter are not taken into account [151, 152, 153, 154].

For this work, the Siemens SWT-6.0-154 wind turbine was selected. These turbines, with a rated power of 6 kW and a rotor diameter of 154 m, are designed for offshore operation and were first installed in 2012 [155]. Since then, this model has been deployed in several OWFs in the German North Sea and Baltic Sea as well as off Taiwan and the United Kingdom [156]. In German waters alone, 224 turbines of this type are currently in operation, out of 1639 installed offshore wind turbines [157, 158, 159]. The average turbine in German waters has a rated power of 5.6 kW, rising with the current trend of larger turbines. Due to its established presence in the German market and its rated power, which is close to the mean value, this turbine is considered a good starting point for studies within the scope of this thesis.

The SWT-6.0-154 power curve is adopted from Lanzilao and Meyers [154] and is shown in Figure 4.4.

The turbine power curves can be divided into three segments. In the low wind-speed range, the generated power increases. From a certain wind speed onward, the rated region begins in which the rated power is reached. This region is limited by the maximum operating wind speed, above which the turbine shuts down as a protective measure.

The representation of this curve in the input JSON file follows this common form. The range below rated power is specified by a variable number of data points. The rated region is set to a constant value equal to the rated power, and once the maximum operating wind speed is reached, the power output drops to $0\ MW$. For a real wind turbine, this condition would not allow an immediate return to rated power once the wind speed falls back into the permissible range. Instead, the turbine would first have to ramp its power output back up. Such hysteresis behaviour is not implemented in the present work, since the focus lies primarily on operating scenarios in which maintenance campaigns can in principle be carried out and particularly extreme weather conditions are therefore not examined in detail at this stage.

In addition to the power curve specifications, the turbine name and icon for graphical representation as well as the hub height are defined in the JSON. The hub height is relevant not only for obtaining the wind speed from the weather model described in Section 4.1.1, but also for the altitude at which the aircraft are required to hover in order to transfer personnel or equipment to the turbine.

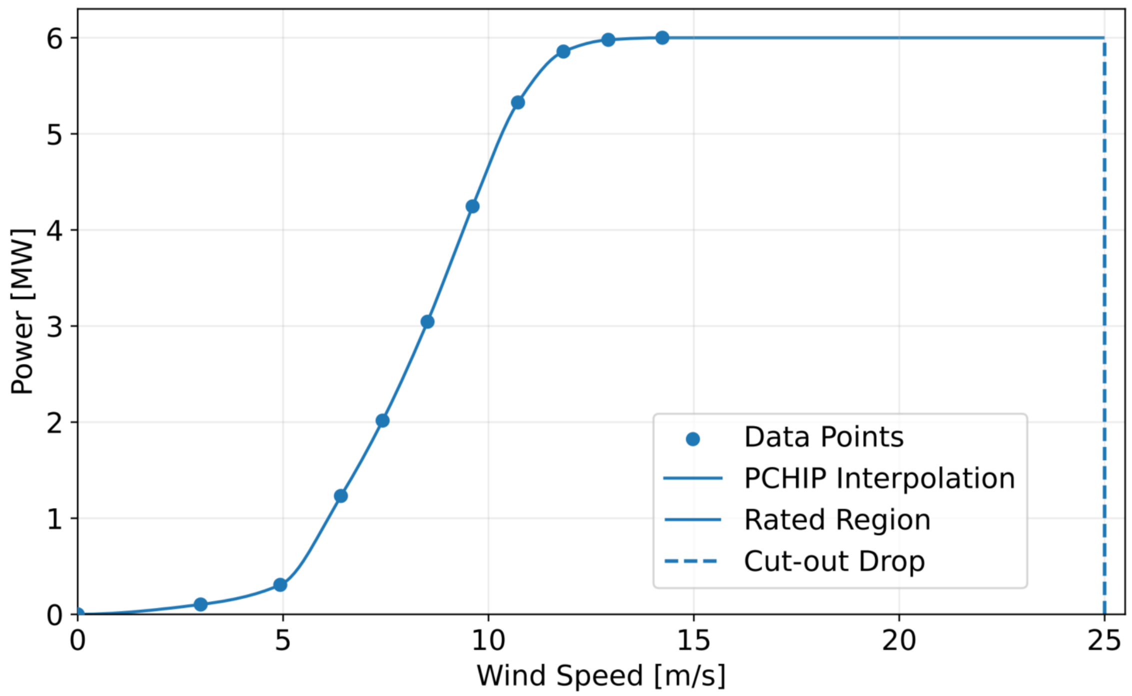

Figure 4.4: Power Curve of a Siemens SWT-6.0-154 Wind Turbine [154]

Listing 4.2: JSON Input File for a Siemens SWT-6.0-154

```
{
  "turbine_name": "SWT-6.0-154",
  "turbine_icon": "WindTurbine_Icon.svg",
  "hub_height": 105,
  "units": { "wind_speed": "m/s", "power": "MW" },
  "curve_points": [
    [0.0, 0.0],
    [2.9941, 0.1024],
    [4.931, 0.3067],
    [6.4075, 1.2318],
    [7.4228, 2.016],
    [8.5168, 3.0447],
    [9.6139, 4.2452],
    [10.7195, 5.3265],
    [11.8256, 5.8563],
    [12.9182, 5.9785],
    [14.234, 6.0]
  ],
  "rated_region": {
    "start_wind": 14.234,
    "end_wind": 25.0,
    "rated_power": 6.0
  }
}
```

To evaluate this information, the data points in the variable part of the curve must be converted into a continuous form. Classical polynomial fits are not ideal here, since the shape of the curve can lead to oscillations and overshoots, in particular in the transition region towards the rated power section. Instead, the piecewise cubic hermite interpolating polynomial (PCHIP) method was chosen, which, as shown in Figure 4.4, results in a smooth continuous curve.

4.2.2 Wind Farm Implementation

A wind farm consists, both in reality and in the present implementation, of a large number of wind turbines. In addition, there are offshore substations (OSS), which usually act as transformer platforms and collect the electrical power generated within the farm. They can also serve as bases for maintenance activities, and some of these stations offer overnight accommodation for personnel, although this is not the case for all OSS. Pure accommodation platforms exist as well; however, in the context of this work only OSS-type stations without overnight facilities are considered [17]. They are defined, like the wind turbines, as individual agents with fixed coordinates and sum up the energy production of the individual turbines.

To implement an OWF in the DLR SoSID-Toolkit, the individual wind turbines and the OSS must therefore be combined into a coherent layout. For this purpose, two approaches were realised. To represent already existing or planned wind farms with given positions of the individual turbines and the OSS, a JSON input format was created into which any wind farms can be specified.

Listing 4.3: JSON Input File for a Siemens SWT-6.0-154

```
"owp_name": "Albatros",
"number_of_turbines": 16,
"location_oss":
  [54.4870,
  6.2705],
"icon_oss": "OSS.svg",
"type_oss": "Hoist Deck",
"height_oss": 35,
"refueling_possible": "No",
"ground_power_available": "Yes",
"turbine_data": {
  "WT1": {
    "wt_type": "SWT-154-6",
    "location":
      [54.486811,
      6.283428]
  },
  "WT2": {
  "wt_type": "SWT-154-6",
  "location":
    [54.489848,
    6.210405]
  },
  ...
  "WT16": {
    "wt_type": "SWT-154-6",
    "location":
      [54.495327,
      6.202054]
  }
}
```

For the Albatros OWF in the German Bight, this results in the graphical representation in the SoSID-Toolkit shown in Figure 4.5.

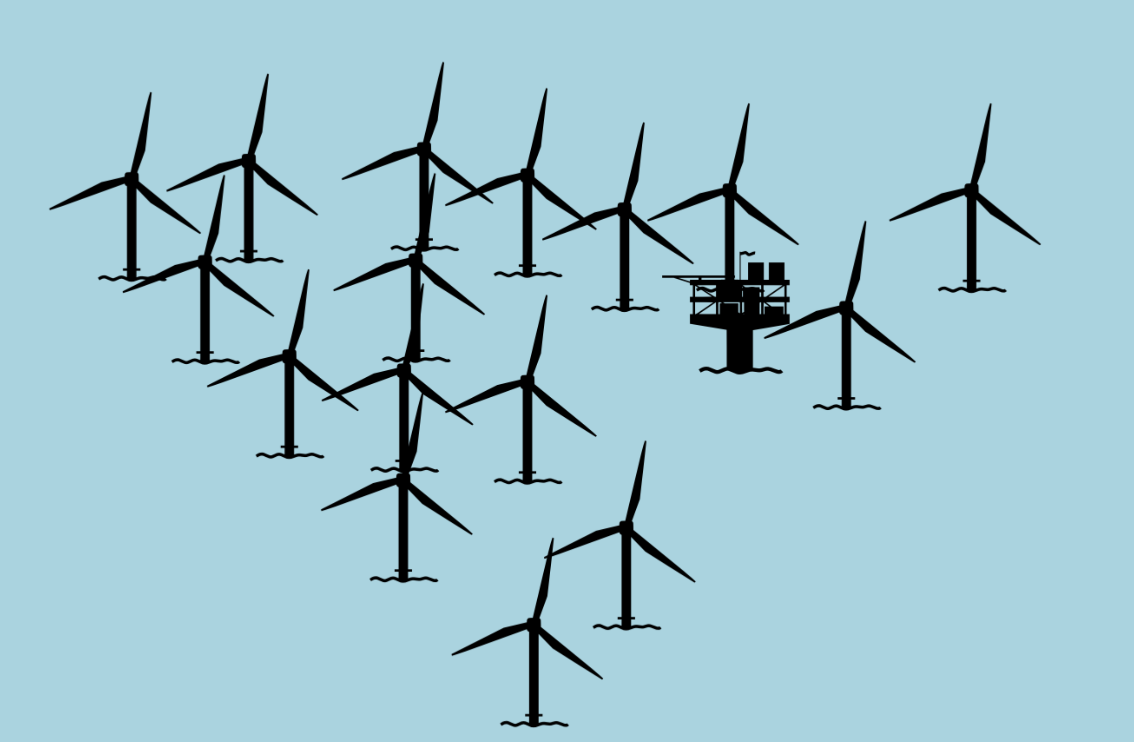

Figure 4.5: Graphical Representation of the Albatros OWF in the DLR SoSID-Toolkit

For simulations that must handle variable parameters and multiple scenarios, a large number of fictional wind farms would first have to be written into this file format, which is comparatively labour-intensive due to the required coordinates for each turbine. Therefore, a wind farm can alternatively be specified in the general scenario input file by the distance and bearing from the chosen service base together with the number of turbines of a given type to be created, and the positions of the wind turbines around the OSS are then determined automatically.

Listing 4.4: JSON Input File for a Siemens SWT-6.0-154

```
"owf_generator": {
  "service_base_name": "BORKUM",
  "service_base_gps": [53.598135, 6.703398],
  "wt_type": "SWT-154-6",
  "n_turbines": 8,
  "owp_name": "Demo OWF from BORKUM",
  "distance_km": 80,
  "bearing_deg": 329,
  "type_oss": "Hoist Deck",
  "oss_height_m": 35.0,
  "refueling_possible": "No",
  "ground_power_available": "Yes"
}
```

The wind turbines are arranged in a grid around the OSS, with the spacing between turbines set to five times the rotor diameter and the minimum distance to the OSS set to seven times the rotor diameter [160]. The resulting layouts are shown in Figure 4.6 for the example cases of 8 and 18 turbines. The anchor symbol next to the OSS indicates the point at which the CTV waits within the OWF while the teams are working on the turbines.

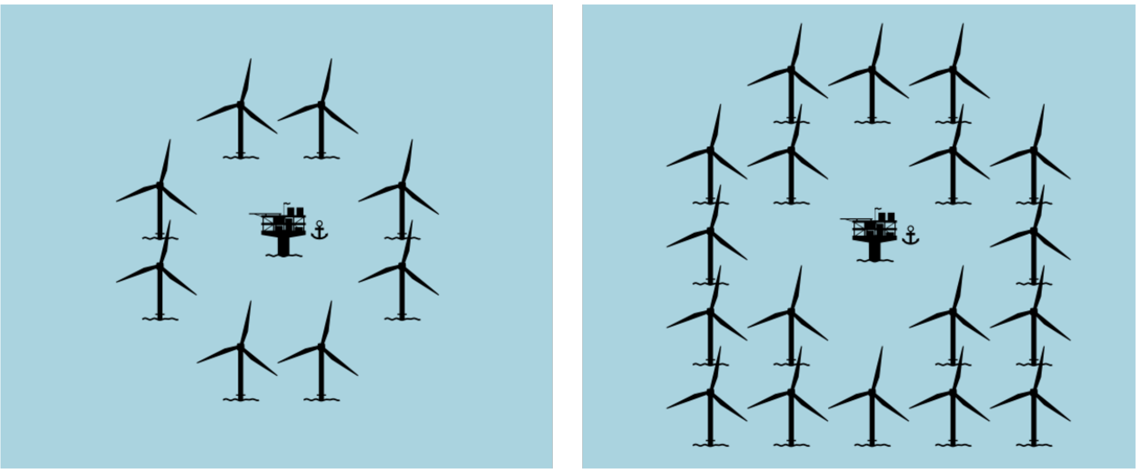

Figure 4.6: Graphical Representation of an automatically generated OWF with 8 and 18 Turbines in the DLR SoSID-Toolkit

4.3 Maintenance Model

4.3.1 Discretisation of Failures and Maintenance

To trigger a demand for material and personnel at a specific turbine, a maintenance model must be defined within the simulation environment. Various modelling approaches can be applied in this context. For example, based on historical failure data, assumptions regarding damage probabilities over the operational life of a turbine, typically represented by a so called bathtub curve, as well as standard inspection intervals for different components, a dedicated model can be developed for each turbine. Such a model could generate maintenance and inspection demands as a function of operational time and environmental conditions [17]. This approach is particularly well-suited for long term simulations spanning multiple years or the entire design lifetime of an offshore wind farm and was implemented, for instance, in the Offshore TIMES research project for operational planning of OWFs [17].

Although failure datasets from various OWFs are available, significant discrepancies between them exist due to differences in turbine models and site-specific boundary conditions. Given that the focus of this work is limited to the simulation of a single operational day, the advantages of a detailed lifetime-based modelling approach, accurate results across the full life cycle, cannot be meaningfully transferred to this scenario. Accordingly, a simplified alternative was implemented.

For the selected simulation day, all planned and potentially spontaneous maintenance, inspection, and repair operations are to be provided by the user in a standardised input format. This enables the incorporation of more detailed maintenance models in future extensions, where these models would then supply the relevant data for each simulation day. For now, however, the simulation focuses exclusively on a single, representative day in the operational life of an offshore wind farm.

The previously introduced bathtub curve is shown in Figure 4.7 and can be divided into three distinct phases [161]. Immediately following the installation of the OWF, a period of elevated but decreasing failure probability is observed, commonly referred to as infant mortality. After a certain operational period and accumulation of experience, these early failures are typically resolved, and the turbine enters the useful life phase, characterised by a constant failure probability. The current implementation is primarily focused on representing this phase, although an extension of the simulation to incorporate time-dependent failure rates remains technically feasible in later steps. Towards the end of the operational life, the failure probability increases again as the effects of aging and component wear become significant.

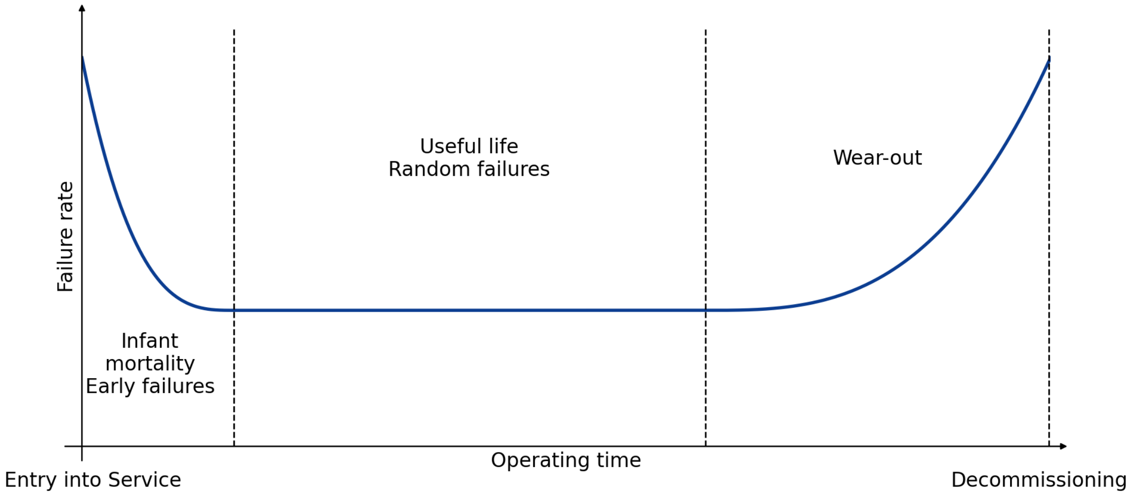

Figure 4.7: Quantitative Bathtub Curve of a Wind Turbines Failure Rate over its Lifetime

Based on the generic maintenance and repair tasks for offshore turbines proposed by Dinwoodie et al. [162], which were already used in other investigations concerning optimal transport vehicle selection for OWFs, four maintenance task types are predefined, as shown in Table 4.2 [15]. Additional maintenance operations can be freely defined in the same format, allowing the simulation to incorporate updated procedures and generally modified maintenance requirements for newer and larger turbine models.

Maintenance Task	**Manual Reset**	**Minor Repair**	**Medium Repair**	**Annual Service**
Maintenance time [h]	3	7.5	22	60
Required technicians	2	2	3	3
Failure rate [1/turbine/a]	7.5	3.0	0.275	1

Table 4.2: Maintenance Tasks based on Dinwoodie et al. [162]

Using the specified failure rates, the probability of a maintenance event occurring within a single simulation step is computed. For each individual asset, a uniformly distributed random number between 0 and 1 is drawn in every simulation step to determine whether the maintenance event is triggered at that point in time.

However, this information alone is not sufficient for a complete representation of maintenance activities as envisioned for this work since especially the transport of items and personnel is to be researched. The simulation also requires data on the amount of equipment that must be transported by personnel for each maintenance task. Various factors can influence the maintenance process in both real-world and simulated environments, many of which occur randomly. The duration of maintenance operations can vary depending on the location of the issue inside or outside the turbine, the accessibility of the affected components, the skill level of the assigned team and the nature of the failure itself. As these durations cannot be predicted with absolute precision, the user must define an additional parameter for each task, the maximum allowable deviation from the standard maintenance time. In the simulation, a uniformly distributed random number between -1 and 1 is drawn for each maintenance event. This value is multiplied by the specified maximum deviation and added to the nominal duration, resulting in a final, randomised task duration. During the simulation, a team with the required size and equipment must be present at a turbine for this amount of time, until the task is resolved and the turbine back in operation.

Another relevant aspect concerns spontaneous demands that arise during the execution of a maintenance or inspection task. This term refers to any equipment or material not initially transported to the turbine but subsequently required to proceed with the task. Typical examples include inspection devices, maintenance tools, spare parts, or other repair materials. For each maintenance task type, the weight of a single spontaneous item must be defined. In addition, the probability that such a demand will occur during a given maintenance or inspection activity must be specified. The evaluation of spontaneous demands is carried out analogously to the determination of maintenance task initiation. It is performed in each simulation step but only for turbines that are currently undergoing a maintenance procedure.

In the absence of standardised values for these parameters, assumptions must be made for the simulations. These assumptions should be compared against empirical data and operational experience from the offshore wind energy sector or examined as part of a sensitivity analysis.

4.3.2 Definition and Format

A dedicated JSON format has also been defined for this input, which can either be stored as a separate file and referenced within the general scenario input JSON, or directly embedded into that file. Following the structure shown in Listing 4.5, additional maintenance tasks can be defined using the same scheme.

Listing 4.5: JSON Input File for Maintenance Operations with Exemplary Data

```
"campaign_name": "Campaign_1",
"campaign_days": 1,
"manual_resets": {
  "hours": 3.0,
  "persons": 2,
  "trigger": "STOCHASTIC",
  "failure_rate_per_year": 7.5,
  "max_duration_deviation_h": 0.5,
  "number_of_items": 1,
  "item_weight_kg": 50.0,
  "spontaneous_probability": 0.33,
  "spontaneous_item_weight_kg": 10.0,
  "affected": "All"
},
"minor_repairs": {
  "hours": 5,
  "persons": 2,
  "trigger": "FORCED",
```

```
  "failure_rate_per_year": 3.0,
  "max_duration_deviation_h": 1.0,
  "number_of_items": 2,
  "item_weight_kg": 50.0,
  "spontaneous_probability": 0.5,
  "spontaneous_item_weight_kg": 50.0,
  "affected": ["WT1", "WT2", "WT3"]
},
"medium_repairs": {
  ...
},
"annual_services": {
...
}
```

Two options have been implemented for triggering a maintenance task. With the setting ”STOCHASTIC”, the previously described probability-based check is performed in each simulation step for all assets listed under ”affected”, leading to the dispatching of a corrective maintenance action. This list can include either specific turbine identifiers or the keyword ”All”. Additionally, the Offshore Sub Station can also be included, either bei adding ”OSS” to the list of affected assets for the existing maintenance operations or by creating an entry especially for the OSS. For actions that have been scheduled in advance as part of an organised campaign, the trigger can be set to ”FORCED”. Organised campaigns are usual in the offshore energy sector, since they allow specialised teams to perform tasks efficiently. Examples are proactive maintenance activities, inspections or upgrades to turbines which affect typically the entire fleet or at least multiple turbines [84]. These tasks are therefore known at the start of an simulation and to be handled over the course of the day until there are no more available teams, the worktime limit is reached or the sun sets. The equipment required for each task is specified by indicating the number of equipment units to be carried and the weight, which is characterised by the heaviest non-divisible item.

4.3.3 Maintenance Demand Queue

Based on the inputs and the implementation for triggering maintenance needs, a complete task description can now be generated, which includes how many personnel are to work with which equipment, for how long and on which asset. This requires an interface to the dispatching logic and by that finally to the vehicle agents so that these tasks and needs result in helicopter flights, drone flights or CTV trips. For this purpose, a demand queue was implemented. This lists all individual demands per turbine that have occurred since the start of the simulation and have not been resolved, so that dispatching can use this information to assign a mission to an available vehicle. Two different entries are shown as examples in Listing 4.6.

Listing 4.6: Exemplary Maintenance Demand Queue with 2 Entries

```
{
  "asset": "WT2",
  "spec_key": "manual_resets",
  "base_duration_h": 3.0,
  "wea_index": 2,
  "created_step": 1,
  "persons": 2,
```

```
  "number_of_items": 2,
  "item_weight_kg": 50.0,
  "item_bundles": [],
  "is_spontaneous": false,
  "is_pickup": false
},
{
  "asset": "WT5",
  "spec_key": "pickup_after_finish",
  "base_duration_h": 0.0,
  "wea_index": 5,
  "created_step": 1301,
  "persons": 2,
  "number_of_items": null,
  "item_weight_kg": null,
  "item_bundles": [
    {"count": 2, "weight_kg": 50.0},
    {"count": 1, "weight_kg": 20.0}
  ],
  "is_spontaneous": false,
  "is_pickup": true
}
```

Applied to the real world, this queue is managed by the operator of the offshore wind farm. Usually, the vehicles used to handle the requests are provided by contractors and do not prioritize the requests themselves. This is done by the operator's control room. [17]. Therefore, this queue must be sorted or prioritised so that further dispatching only has to take the first entry and process it. There are numerous methods for prioritisation, which vary greatly in terms of optimisation and computational effort. Wiggert et al. [17] compiled the sorting methods listed in Table 4.3 for maintenance measures in offshore wind farms.

Prioritisation	**Concept**	**Computational Effort**
First-In-First-Out	Strict ordering by time of occurrence	Lowest
Most Tickets	Maximise number of tickets completed per shift	Medium
Most Turbines Repaired	Maximise number of turbines restored per shift	Higher
Economic benefit	Maximise financial benefit over a longer period	Highest

Table 4.3: Comparison of Prioritisation Strategies for Maintenance Dispatch

Since there are several demands at the same time in the case of planned campaigns, the pure FiFo strategy does not work in the context of this work. However, the other methods require more effort and increasingly more data from the energy generation and weather models. In the event that there are several demands in the queue at the same time, all of which represent transport requests to a plant, these deliveries are sorted according to the nominal maintenance period. The underlying principle here is the same as for the Most Tickets or Most Turbines Repaired method. Deliveries for maintenance tasks with a longer duration are completed first, so that more time is available for repairs within that working day. Since there are several turbines with the same maintenance duration within a campaign, a tiebreaker must be introduced. The number of the wind turbine concerned is used here. If spontaneous maintenance tasks are added while earlier demands from a planned campaign are still in the queue, the spontaneous tasks are given higher priority. It is assumed that a planned campaign is not as time-critical as a spontaneously occurring failure. Furthermore, this ensures that equipment is sent as quickly as possible to a team currently waiting for a missing item so that they can complete the maintenance work. Within the spontaneous deliveries, priority is given according to the FiFo principle. With that, all types of deliveries are covered.

When picking up personnel and equipment, a rapid response is required in order to comply with the time constraints. Therefore, all pickup demands are generally prioritised above deliveries in the queue.

A special case is formed by demands related to the offshore substation (OSS). These are always prioritised above all other demands as failures at the OSS cause the greatest economic damage.

4.3.4 Maintenance Process

The wind turbines must track the progress of maintenance and switch from energy generating operation to maintenance mode without energy generation and back again, so an interface between the maintenance progression and the energy generation is required. In order to handle the ”FORCED” maintenance tasks of the planned campaigns, all these tasks are evaluated once at the beginning of the simulation. As the simulation progresses, this only happens when a maintenance task or a spontaneously required equipment delivery occurs stochastically. To resolve the maintenance progress and potential interruptions and to enable a clear visual representation of asset status in graphical outputs and a link to the energy generation model, several distinct states have been defined for both turbines and the OSS. These states are listed in Table 4.4.

State	Description	Colour
RUNNING	Asset produces energy, stochastic failures can occur	Black
INOP	Maintenance demand was triggered, no energy production	Yellow
MAINTENANCE	Asset under maintenance, maintenance time progresses, spontaneous equipment demands can occur	Red
MAINTENANCE_INTERRUPTED	Maintenance was interrupted due to incomplete equipment or personnel, no maintenance progress	Orange
MAINTENANCE_FINISHED	Maintenance was finished, personnel and equipment must be picked up, no energy production	Green

Table 4.4: Energy Asset States

A complete maintetance process is displayed in Figure 4.8 as are the corresponding icons and colours for each state.

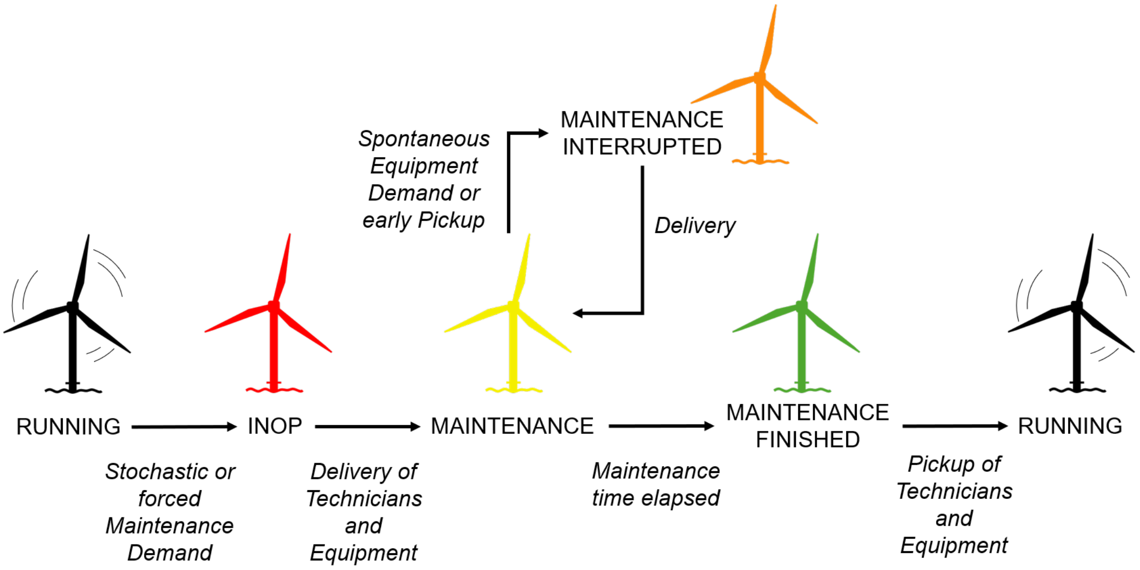

Figure 4.8: Implemented Maintenance Process

The transition from the RUNNING state to the INOP state occurs, as described in Section 4.3, through the triggering of a maintenance demand. In the case of planned maintenance campaigns, this transition takes place at the start of the simulation, meaning that the turbines affected by such campaigns begin in the INOP state.

The transition from the INOP state to the MAINTENANCE state occurs once sufficient resources for the respective maintenance task are available at the asset and the required preparation time has elapsed. This time represents the duration needed by the team from the completed transfer onto the asset until the actual start of the maintenance activities. For vessel based transfers, this duration is longer, since most subcomponents of a wind turbine are located in the nacelle area and therefore require an ascent from the transition piece to the nacelle. In the case of helicopter transfers, the technicians land directly on the nacelle and can therefore begin work more quickly. For transfers from a CTV where no equipment needs to be transported, the required preparation time is reduced. The preparation time parameters constitute an essential part of the scenario description and are defined in the scenario input file, as shown in Listing 4.7, in units of seconds.

Listing 4.7: Preparation Time Definition

```
[
"preparation_time_sea_transfer": 1800,
"preparation_time_sea_transfer_crew_only": 900,
"preparation_time_air_transfer": 300,
]
```

If a spontaneous demand is triggered during ongoing maintenance activities, the required amount of material to complete the maintenance task changes. This can happen multiple times for the same turbine during a maintenance process. By evaluating the available maintenance resources at each simulation step for each asset currently under maintenance, the simulation identifies whether the maintenance must be interrupted. In such cases, the state changes from MAINTENANCE to MAINTENANCE_INTERRUPTED. This check also applies when the maintenance team must be retrieved before task completion due to either the approaching sunset or the expiration of the allowed work duration. The same verification mechanism ensures that, once sufficient material and personnel are again available, maintenance work can resume and the asset state returns from MAINTENANCE_INTERRUPTED to MAINTENANCE.

Once maintenance is completed and the remaining maintenance time has reached zero, the asset state changes to MAINTENANCE_FINISHED. At this point, a corresponding pickup demand is generated and inserted into the demand queue. Although in real-world operations it is possible to estimate the approximate time of maintenance completion based on the experience of the maintenance team and to request a vehicle accordingly in advance, this behavior is difficult to implement in a simulation context and was therefore not considered.

From this state, the asset transitions back to the RUNNING state once both personnel and equipment have been fully picked up. This condition is checked after each pickup operation at a turbine. The respective preparation times must also be taken into account in this context.

For helicopter-based logistics strategies, the preparation time is typically shorter than the flight time from the service base to the turbine. As a result, the required waiting period is considered automatically fulfilled.

In contrast, CTVs remain within the wind farm throughout the day and are able to reach turbines relatively quickly. However, the time required to descend from the nacelle to the transition piece with all equipment is comparatively longer. To account for this, a waiting function is implemented for CTV-based transfers, ensuring that the actual pickup only takes place once the full preparation time has elapsed since maintenance completion.

4.4 Baseline Logistic Vehicles

4.4.1 Helicopter

4.4.1.1 Rotorcraft Modelling

The use of helicopters for maintenance activities, as outlined in 2.2.2.1.1, is integrated into the SoSID-Toolkit based on the existing helicopter performance model presented in the project thesis [128]. For this work, the Airbus Helicopters H135, pictured in Figure 4.9, was chosen as well, based on the aircraft parameters derived and validated in Raaf [128]. The selection was justified by the suitability and operational use of this aircraft for these purposes in the German Bight, as well as by the availability of a validated parameter file [128, 72, 163].

Figure 4.9: Airbus Helicopters H135 flying over an Offshore Wind Farm [163]

Two aspects regarding the helicopter implementation had to be implemented for the maritime simulations:

- In the AAM-focussed mission logic, flights are executed point-to-point only. Dedicated hover segments required for hoisting at wind turbines are not yet represented.
- Wind effects on the aircraft are presently not accounted for and must be incorporated to obtain realistic mission energy estimates.

4.4.1.2 Hoisting Task

In the AAM implementation, missions are executed point to point between an origin and a destination. The trajectory consists of typed segments such as climb, cruise, and descent, and a so called follower traverses these segments until the destination node. The typical task sequence at the destination is a vertiport landing with turnaround procedures, not in-air work over an asset.

A *segment* is a static piece of the trajectory, a path portion with start and end point, phase label (such as climb, cruise, descent, hover) and target altitude and speed values. It contains no behavior. In contrast, a *task* is a behavioral or mission state of the agent that, at each simulation step, evaluates conditions, triggers events, and decides which segments are flown when and what additional actions are executed.

Based on this framework, the hoisting process was implemented. The trajectory object already categorizes segments and waypoints, which allows the addition of hovering as a new segment type. The mission logger and its callbacks were retained to record offshore events such as approach, hover start, dwell completion, and pickup or delivery, and to inform the dispatcher through a callback. The offshore extension introduces both a new trajectory segment type "hover" and a dedicated hoisting task. The segment ensures the aircraft physically reaches and holds the hover fix over the asset, the task governs dwell timing, the single mass-exchange event, logging, and the transition to the next leg.

During multi-stop planning the offshore dispatcher inserts a hover segment at the correct position for every turbine. These hover points are part of the flown trajectory.

At the asset, the new hoisting task takes control as displayed by the process chart in Figure 4.10.

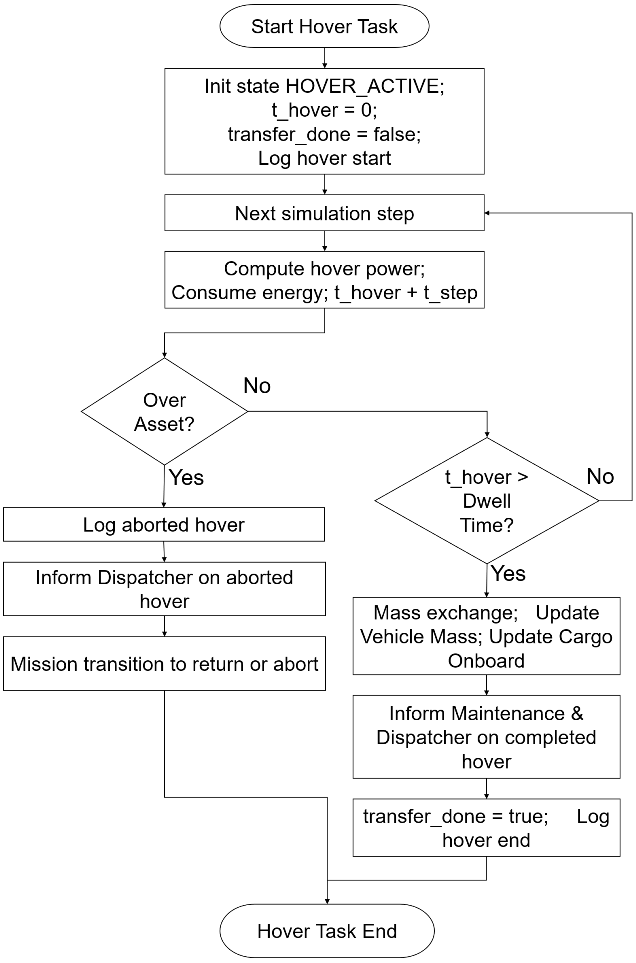

Figure 4.10: Process Chart of Hover Task

The aircraft transitions to hovering over the turbine, holds position, accumulates the dwell time or time needed for the hoisting process, executes the hoist operation, and triggers one mass exchange for delivery or pickup. When the dwell time is met, the task marks the stop as complete and hands back to either the return leg or the onward leg of the mission.

Payload changes during hover are reflected in the vehicle mass, which feeds into the energy need as does the fuel consumption. Coupling with the dispatcher is achieved through mission annotations that capture the offshore context, including the list of stops, dwell times, expected payload and a callback reference. Once a stop completes, the task fires the callback so that maintenance progress is booked, the demand queue is updated, payload states are synchronised, and the next leg is released.

This implementation only uses the power required for an otherwise undisturbed hover to compute the hover energy consumption, as described above. Accordingly, additional power contributions are neglected, for instance those caused by operating the hoist. This also applies to the influence of the wind turbine on the local flow conditions. Following the common hoisting manoeuvre as shown in Figure 2.10, the nacelle of the wind turbine is rotated so that the plane of the rotor blades is aligned parallel to the wind direction and the turbine is stopped. The helicopter approaches the hoist area on the aft of the nacelle against the wind direction, so that the effects of the rotor and nacelle wake on the helicopter can be reduced to a minimum. For this reason, the modelling of these effects is not part of this work. The orientation of the turbine's rotor plane and the exact approach of the helicopter is not modelled as well. For all possible vehicles, transfer and hoisting maneuvers are possible from all directions and the approach is idealised as a straight line from the last waypoint to the turbine. This may be an optimistic assumption and shortens the overall distance of a mission, but since it is constant for all scenarios and vehicles, no significant error is expected for the comparison of the results.

Entering the wake of operating turbines does have an effect on a helicopter and can increase the required power [164]. Such situations can happen during flights within a wind farm, but are not further considered in this work. It is assumed that an OWF has no influence on aircraft performance.

The developed task is not only used for the helicopter aircraft, but for the UAVs as well. In the real world, the approach of a drone to a turbine and the behavior during the material transfer might not be identical to the behavior of helicopters as implemented in the Toolkit. Donkels et al. [18] developed procedures especially for the delivery of goods with UAVs to OWFs that include communication and decision-making between the uncrewed aircraft, the operator of the wind farm and the drone operator. Such procceses are not implemented at the current stage of the simulation, since their impact on the Systems-of-Systems level is regarded as low. For an operational implementation of logistic drones in a rea OWF however, they would be necessary nonetheless.

4.4.1.3 Wind Influence

The wind influence is computed based on the environmental data model introduced in Section 4.1.1. For the current position of the aircraft, both the wind speed and the wind direction are obtained. A fully comprehensive treatment would require additional aircraft parameters that are not available within the existing vehicle implementation. Therefore, a simplified approach is adopted in which only the headwind component is considered, while the ground speed is kept constant. This results in a true airspeed (TAS) that depends on the current local wind magnitude and its orientation relative to the direction of flight.

In order to determine the wind influence on the power consumption, both the flight direction of the aircraft and the wind vector at the corresponding location and altitude must be evaluated. The flight direction ψ_f in degrees, relative to the global north, is obtained from the agent's heading parameter. The meteorological inputs are provided by the weather module, which returns the local wind speed V_w in metres per second and the wind direction γ_w in degrees. The wind direction is herefore defined as the direction towards which the wind is blowing. To compute the wind effect relative to the aircraft's motion, the angular difference between the wind direction and the flight bearing is required. The angular difference $\Delta\gamma$ is given by

$$\Delta\gamma = \text{rad}\big((\gamma_\text{w} - \psi_\text{f}) \bmod 360\big) \tag{3.4.1.1}$$

where $\Delta\gamma$ is expressed in radians. The operator mod ensures that the angular difference is cyclically mapped to the range 0° to 360°, which is required for the subsequent trigonometric evaluation of the headwind component. With this angular difference, the headwind component acting on the aircraft can be determined. The headwind velocity V_hw follows directly from a projection of the wind vector onto the aircraft's flight vector:

$$V_\text{hw} = V_\text{w} \cdot \cos(\Delta\gamma) \tag{3.4.1.2}$$

A positive value of V_hw indicates a headwind condition that increases the required propulsive power or energy consumption. Negative values represent a tailwind, which reduces the aerodynamic resistance in the direction of flight. This formulation allows a physically consistent estimation of wind effects for each trajectory segment without introducing additional computational cost within the simulation loop. The TAS then follows as:

$$V_{TAS} = V_{GS} + V_\text{hw} \tag{3.4.1.3}$$

Using the TAS, the power curves are evaluated to determine the required propulsion power. Although this approach is the most straightforward to integrate into the existing toolkit, it must be ensured that the maximum speed of the helicopter is not exceeded. For highly demanding weather conditions, for example during storm events, this method is therefore not suitable. However, since maintenance operations under such circumstances are associated with considerable risks, this limitation is regarded as acceptable for the purposes of this work. To make sure no unplausible speeds can be reached and influence the simulation results, a warning function was implemented.

4.4.2 Crew Transfer Vessel

The vessels used for transporting personnel and equipment, which were introduced in section 2.2.3, must be discretised appropriately for their application in the Toolkit simulation environment. Until now, the DLR SoSID Toolkit did not include a suitable propulsion model for Crew Transfer Vessels (CTVs). Furthermore, the influence of relevant environmental parameters, in particular wave height, must be incorporated in order to represent both vessel performance and operational limits adequately.

To derive a representative generic CTV model, several commercially operated CTVs as well as CTV data from publications in which maintenance concepts and fleet configurations were analysed were evaluated. An overview of these models and their main parameters is provided in Table 4.4.2.

OEM	Model	Length [m]	Installed Power [kW]	Fuel Mass [t]	Cruise Speed [kts]	Max. Speed [kts]	PAX	Wave Limit [m]	Wind Speed Limit [m/s]	Fuel Consumption [kg/kWh]
Damen	FCS 2710 [165]	26.8	2162	25.6	–	25	24	–	–	–
Ares	27 CTV [166]	27.5	2386	29.4	26	28	24	–	–	–
Strategic Marine Group	StratCat 27 Hybrid CTV [167]	27	2162	29.4	24	26	24	1.75	–	0.23
Research CTV [168]	–	–	–	–	15	–	12	1	20	–
Research CTV [111]	–	18	1118	–	24	–	12	1.5	20	–
Research CTV [169]	–	30	2386	7.0	15	22.7	24	2	–	0.22

Table 4.5: Comparison of technical data for selected CTV models

Among commercially available CTVs, the 27 m SWATH class is especially noteworthy due to its comparatively high passenger capacity and overall size. Since this thesis investigates offshore wind farms located at greater distances from shore, and since this vessel class provides a consistent and sufficiently detailed data basis across the considered models, a generic model was developed from this dataset. This model, denoted in the following as *CTV_27m/24pax*, is used throughout all simulations conducted in this work. Its specific parameters are listed in Table 4.6.

Model	Length [m]	Installed Power [kW]	Fuel Mass [t]	Cruise Speed [kts]	Max. Speed [kts]	PAX	Wave Limit [m]	Wind Speed Limit [m/s]	Fuel Consumption [kg/kWh]
CTV_27m/24pax	27	2162	29.4	24	26	24	1.5	25	0.23

Table 4.6: Main Characteristics of the generic CTV_27m/24pax Model

To model the influence of waves and wind on vessel propulsion, several approaches exist that range from simplified semi-empirical formulations to more sophisticated simulation methods. Depending on the chosen approach, numerous input parameters are required, many of which cannot be provided with the currently available data in the maritime SoSID Toolkit environment. Additional information regarding vessel-specific design characteristics is also necessary [147]. More advanced models such as the meta-model presented by Kim, Esmailian, and Steen [170] or the Townsin-Kwon model [171] could in principle be applied, and their required parameters could be supplied as additional environmental or vehicle inputs. However, for the purposes of this work, a simplified semi-empirical method describing the effect of significant wave height on required propulsion power was selected. The significant wave height can be directly obtained from the implemented weather module describes in Section 4.1.2. This simplified approach limits the number of approximated parameters, which increases robustness given the available data, while still providing results of sufficient fidelity and computational efficiency.

Following the formulations presented by Lampe et al. [147], the total propulsion power P_{tot} is decomposed into a calm-sea power component P_{CW} and an additional wave-induced power component P_{AW}. The relation is

$$P_{\text{tot}} = P_{\text{CW}} + P_{\text{AW}} \tag{3.4.2.1}$$

The calm-sea power component depends on the vessel's design or maximum speed v_D, the actual sailing speed v_S, and the power required at design speed, denoted as $P_{\text{CW,v}_\text{D}}$.

$$P_{\text{CW}} = \left(\frac{P_{\text{CW,v}_\text{D}}}{v_D^3}\right) \cdot v_S^3 \tag{3.4.2.2}$$

This formulation permits variable transit speeds in the simulation. For example, wind-induced reductions in attainable vessel speed could be incorporated into a more detailed future model. The dependence of P_{CW} on vessel speed is illustrated in Figure 4.11.

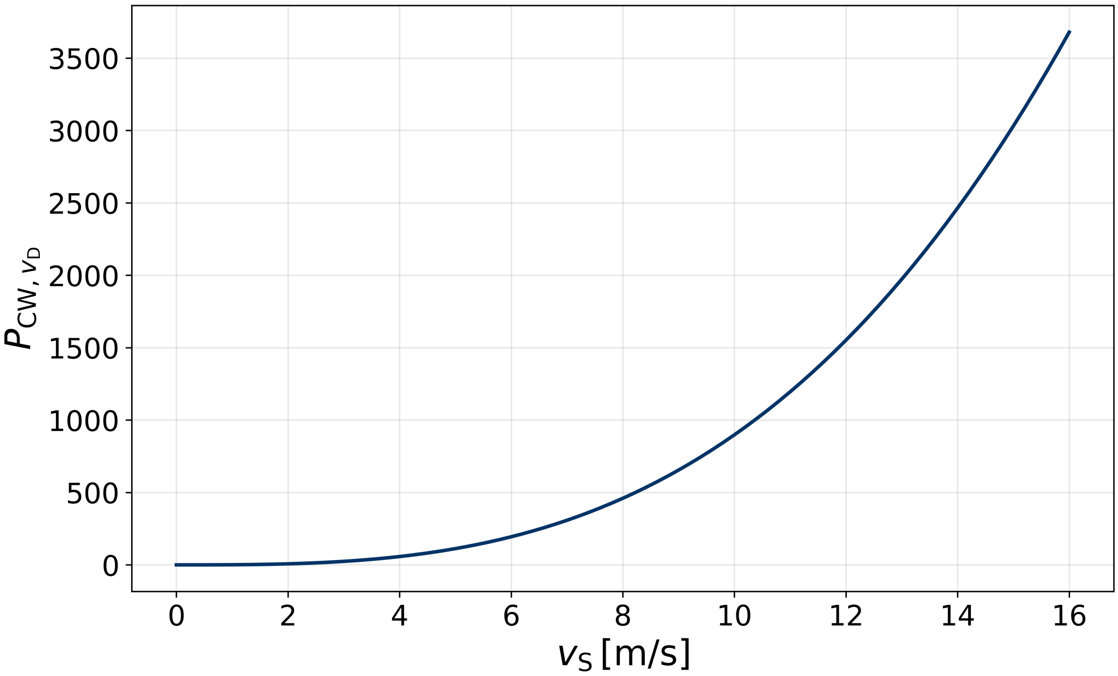

Figure 4.11: Power Share for Calm Waters as a Function of Cruise Speed

The additional power required due to waves is expressed as a function of $P_{\text{CW,v}_\text{D}}$, the maximum significant wave height for which the vessel is designed ζ_{max}, and the current significant wave height ζ. The semi-empirical formulation from Lampe et al. [147] yields

$$P_{\text{AW}} = \frac{0.15 \cdot P_{\text{CW},\text{v}_\text{D}}}{\zeta_{\text{max}}^2} \cdot \zeta^2 \tag{3.4.2.3}$$

Following Lampe et al. [147], a value of $\zeta_{\text{max}} = 3.0\ m$ is used. This assumption originates from significantly larger transport vessels, which operate at comparable speeds but differ in other design parameters. For SWATH CTVs values of over 2.5 m are typical, making this assumption optimistic, but not unrealistic.

As illustrated in Figure 4.12, ζ_{max} can noticeably influence the total required propulsion power.

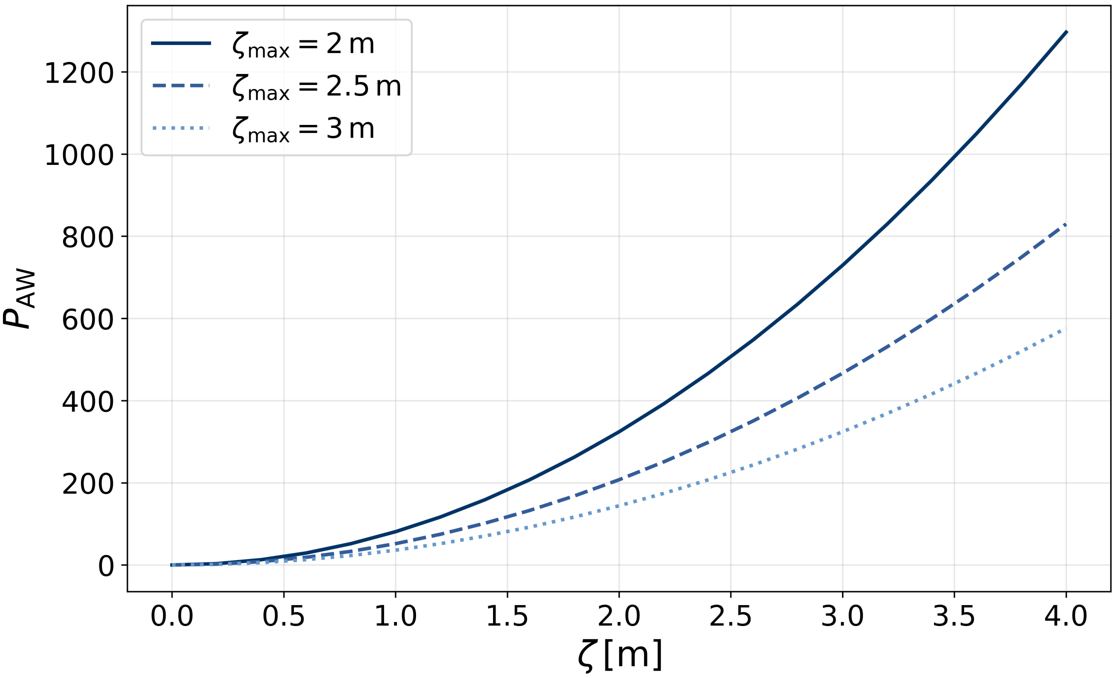

Figure 4.12: Power Share under wave conditions for as a Function of Wave Height with varying Design Wave Heights

For the *CTV_27m/24pax*, a sea state with $\zeta = 1.5\ m$ during cruise results in an underestimation of the required propulsion power by up to 101.3 kW, depending on the assumed value of ζ_{max}. This corresponds to approximately 5.46 % of the total required power. Considering the overall simplifications inherent in this model, this deviation is deemed acceptable.

Fuel consumption in the simulation follows the same formulation used for the aircraft already implemented in the Toolkit. It is computed from the total power P_{tot}, the specific fuel consumption SFC, and the simulation time step Δt as

$$\Delta m_{\text{fuel}} = P_{\text{tot}} \cdot \text{SFC} \cdot \Delta t \tag{3.4.2.4}$$

The specific fuel consumption was derived from the values listed in Table 4.4.2. Using a diesel fuel density of 0.84 kg/l, this resulted in a value of 0.23 kg/kWh.

4.5 Behaviour and Agent Strategies

4.5.1 Dispatching

The dispatching process plays a particularly important role in the context of this work. As outlined in Section 4.3.3, vehicle mission requests are generated based on the maintenance model and entered into the demand queue, such that the dispatcher would, in principle, only need to assign the first entry in the queue to a vehicle. However, this approach is insufficient in the offshore environment due to environmental constraints and operational boundary conditions.

All offshore maintenance activities are subject to two major constraints. The first is the local time of sunrise and sunset, the second is the maximum daily working time of the maintenance personnel.

The maximum daily working time for offshore activities in Germany is regulated by the Offshore-ArbZV, §3(1), and limited to 12 h, with additional restrictions applying to subsequent days once 10 h have been exceeded. In the present implementation, it is assumed that the working time starts at the beginning of the simulation. Maintenance activities are interrupted and the return to the service base is initiated once the legal limits would otherwise be exceeded.

In the simulation, personnel transfers, and thus maintenance activities in the OWF as well, are intended to take place only during daylight. This applies both to hoisting operations with helicopters and to personnel transfer from the CTV. In principle, such operations are not completely ruled out in practice, but they are associated with increased risk both during transfer and during the work itself [108, 74]. Other works have identified considerable potential for improvement compared with strict daylight-only operation, even if no full night shifts are introduced and maintenance activities are merely allowed to continue beyond sunset until they can be completed but the increased accident risk and the generally negative effects on personnel were highlighted [108]. Some exclude transfers and work at night [111, 126], whereas others allow CTV transfers after sunset because the work area can be illuminated by the vessel [17]. Adjustments along these lines are also possible within the SoSID-Toolkit implementation developed here. In the present work, however, transfers and maintenance activities at night are excluded.

These constraints also imply that CTVs and helicopters may depart from the harbour or take off before sunrise. This does not apply to UAVs. Given the demanding environment, where civil and military aviation, maritime traffic, and static obstacles such as wind turbines of neighbouring OWFs coincide, night flights are entirely excluded for UAVs in the present work. To simulate this behavior, a guard function for the dispatch process was implemented.

An approximation from the National Oceanic and Atmospheric Administration (NOAA) is used to calculate the times of sunrise and sunset in the simulation [172]. The calculation is based on the calendar day, the geographical latitude lat and longitude lon, and a fixed time zone offset Δt_{UTC}, which in summertime is 2 h for the German Bight.

First, the fractional year γ is determined in radians according to Formula 3.5.1. The calendar day N_d is specified as the number of the day in the year, i.e. from 1, the first of January, to 365, the 31st of December. In addition, the time of day in hours in Coordinated Universal Time (UTC) h_{utc} is required. This is set to $h_{utc} = 12h$ as a simplification.

$$\gamma = \frac{2\pi}{365} \cdot \left(N_d - 1 + \frac{h_{utc} - 12}{24} \right) \tag{3.5.1}$$

Based on the fractional year length γ , the auxiliary time variable $eqtime$ in minutes and the solar declination $decl$ in radians are then determined. $eqtime$ describes the deviation of true solar time from an idealised mean solar time, while $decl$ indicates the angle between the sun's rays and the equatorial plane.

$$\begin{aligned} eqtime = 229.18 \cdot \big(&0.000075 + 0.001868 \cdot \cos(\gamma) - 0.032077 \cdot \sin(\gamma) \\ &- 0.014615 \cdot \cos(2\gamma) - 0.040849 \cdot \sin(2\gamma)\big) \end{aligned} \tag{3.5.2}$$

$$\begin{aligned} decl = &\, 0.006918 - 0.399912 \cdot \cos(\gamma) + 0.070257 \cdot \sin(\gamma) \\ &- 0.006758 \cdot \cos(2\gamma) + 0.000907 \cdot \sin(2\gamma) \\ &- 0.002697 \cdot \cos(3\gamma) + 0.00148 \cdot \sin(3\gamma) \end{aligned} \tag{3.5.3}$$

For the sunrise and sunset periods, the zenith angle is set to $90.833°$. The formula 3.5.4 yields the time of sunrise when calculated with a positive sign and the time of sunset when calculated with a negative sign.

$$ha = \pm \arccos \left\{ \frac{\cos(90.833)}{\cos(lat)\, \cos(decl)} - \tan(lat)\, \tan(decl) \right\} \tag{3.5.4}$$

The UTC time in minutes of the corresponding $Sun\ Event$ is then calculated using formula 3.5.5.

$$Sun\ Event = 720 - 4 \cdot \{lon + ha\} - eqtime \tag{3.5.5}$$

The result must be added by the local Δt_{UTC} in minutes and then converted into the usual time format hh:mm:ss.

With the known timeframe, every dispatch can be evaluated. The corresponding guard function is visualised as a process chart in Figure 4.13. For deliveries, a buffer was added to ensure that no missions are performed close to the working peroid end.

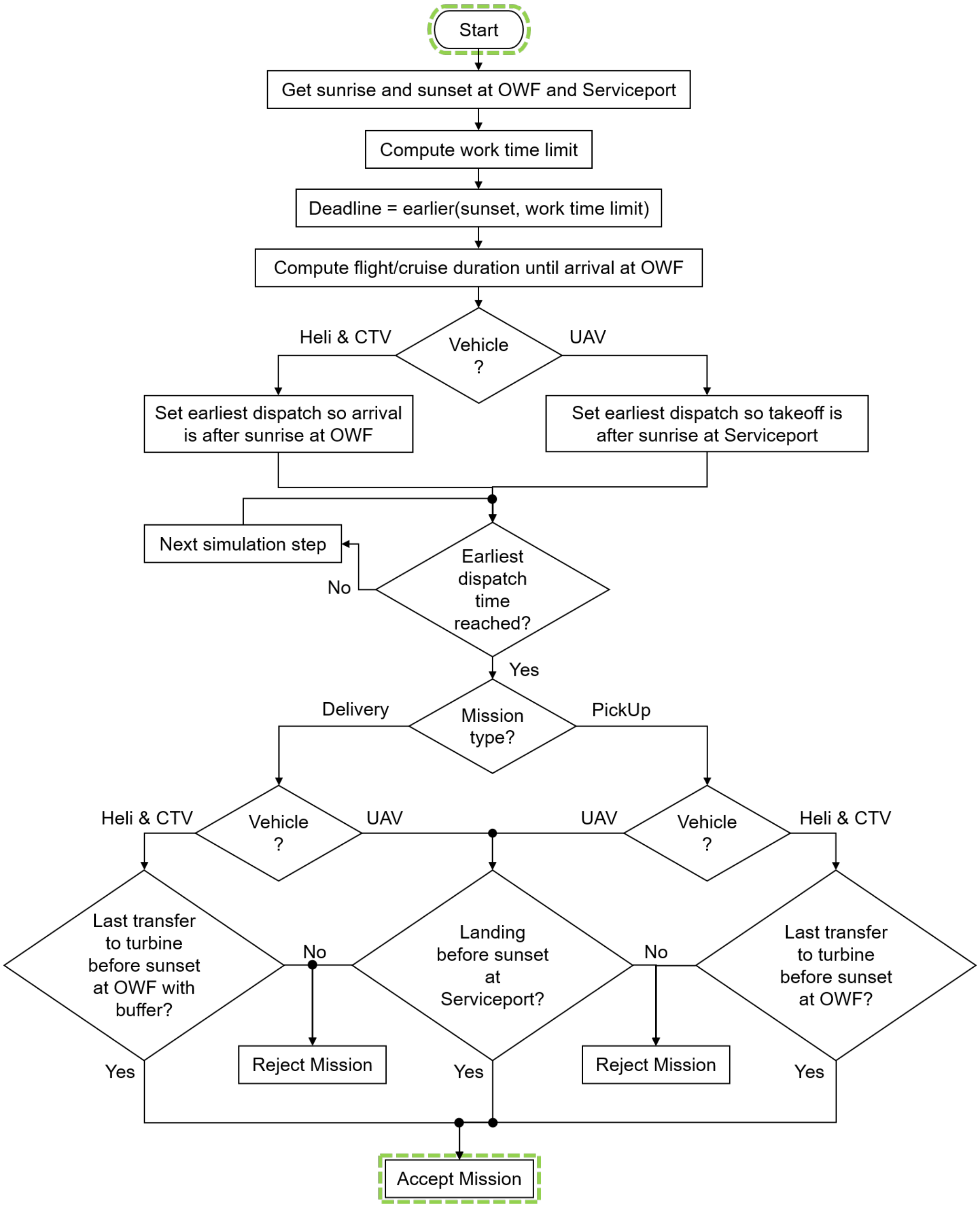

Figure 4.13: Process Chart of the Daylight and Worktime Guard

To ensure that all required maintenance actions are only beeing done within the acceptable timeframe, a forced dispatch mechanism was implememted. This mechanism dispatches the available vehicles to pick up the workers in the OWF before their maximum work time is reached or the sun sets by entering pick up demands with the highest possible priority in the demand queue as mentioned in Section 4.3.3. Together with the sunset and worktime guard this leads to a situation in which all vecihles work to gather the technicians from the OWF while no new demands, which would include the transport of items or personnel to the OWF, are beeing fulfilled. Naturally, still ongoing maintenance operations are paused after the personnel is transferred off the turbine and would have to be revisited on the next day.

While the time of the sunset and the maximum worktime is known, this mechanism needs an approach to calculate, how long the transport of all workers back to the service point would take, so that the maintenance operations do not have to be paused unnecessarily early. For this problem of visiting a known number of spatially distributed points with a given number of vehicles, several methods are possible, however, most do require comparatively large computational effort. This calculation however must be performed every single step during the simulation, which is why the most simple approach was chosen. For the two implemented methods of personnel transport, CTV and helicopter, two different formulas were derived based on their different operational behavior.

For logistic strategies with helicopters, it is assumed in the scope of this thesis that only one team can be flown at a time, since the helicopter model chosen in Section 4.4.1 could reach is performance limits with more teams and the aircrew. Therefore, the time until the last transfer from a turbine to a helicopter can be conservatively approximated by Equation (3.5.6) with the number of available aircraft n_{Helis}, the number of technician teams still on turbines n_{Teams}, the flight duriation of one leg (from the servicepoint to the OWF) t_{leg} and the time needed for a hoisting transfer t_{hoist}. Instead of the exact flight time to the individual turbines, only the flight time to the OSS is computed once and then used.

$$t_{forced,Heli} = (2 \cdot \left\lceil \frac{n_{Teams}}{\text{max}(1, n_{Helis})} \right\rceil - 1) \cdot (t_{leg} + t_{hoist}) \tag{3.5.6}$$

If the strategy is based on the use of a CTV, the time until the last transfer is approximated with Equiation (3.5.6). t_{init} denotes the time the CTV needs from its loiter position in the OWF near the OSS to the first turbine, t_{inter} the time it needs between the turbines while hopping from one to the next and $t_{transfer}$ the time needed for each transfer.

$$t_{forced,CTV} = t_{init} + \text{max}(0, \left\lceil \frac{n_{Teams}}{\text{max}(1, n_{CTVs})} \right\rceil) \cdot t_{inter} + \left\lceil \frac{n_{Teams}}{\text{max}(1, n_{CTVs})} \right\rceil \cdot t_{transfer} \tag{3.5.6}$$

For the duration of the first initial trip, the first asset by turbine agent number is condsidered, as for the entire forced pickup mechanism. No optimised order was implemented for simplicity and runtime reasons. In order to calculate the following segments between the remaining turbines, the distances between each turbine in the chain sequence structured by the tubine agents number are computed. The mean distance is then taken and used together with the CTVs speed as specified in the vehicles JSON input file to compute the time per segment.

The demands generated in this manner are transferred to the dispatcher via the demand queue in the same way as all other missions.

In addition to the previously described guards, the dispatching process applies an additional filtering step to the currently available vehicles. This ensures at an early stage that the selected vehicle complies with the chosen strategy and that, in general, no personnel are transported using UAVs. The filtering logic for the vehicles is illustrated in Figure 4.14.

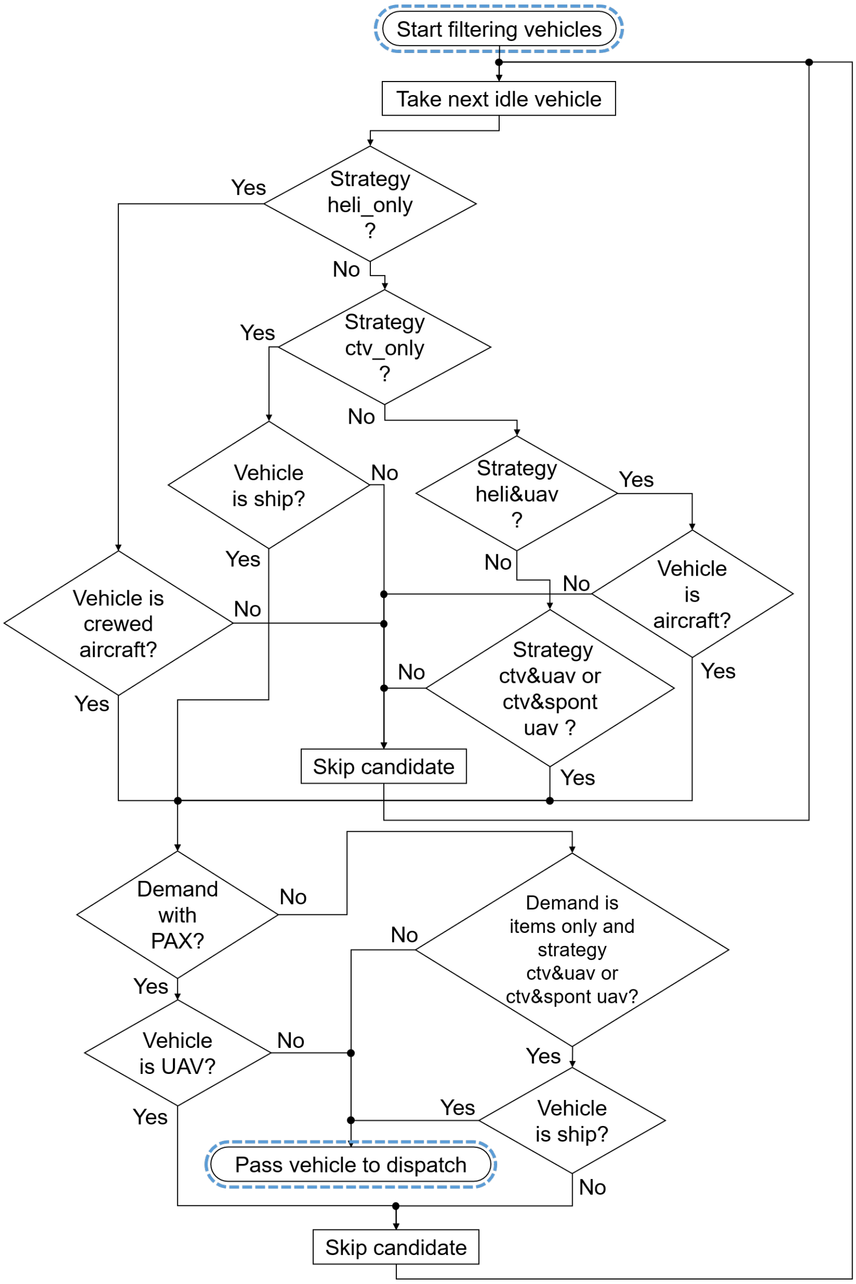

Figure 4.14: Process Chart of the Vehicle Filter Process

The first vehicle in the resulting list is then used to plan the first mission, as illustrated in Figure 4.15. It is necessary to verify whether the mission can be executed by the selected vehicle. This concerns both the vehicle's maximum payload capacity and its effective range under the specific payload and planned flight path. For this purpose, the energy requirement is calculated for each segment of the flight path, taking into account the prevailing weather conditions. This improves the accuracy of the energy estimation and prevents situations such as a vehicle running out of fuel due to headwinds and crashing or drifting without power. In addition, vehicle-specific limits are validated with this check.

In the case of pure cargo missions, which mainly occur in combination with transport drones, the simulation also checks whether the individual items of a demand can be transported by the selected vehicle. For example, if a mission consists of several items that can only be carried individually by a UAV, the mission can be split across multiple UAVs. Any remaining items that cannot be transported within the current mission are inserted into the demand queue as a new, separate demand.

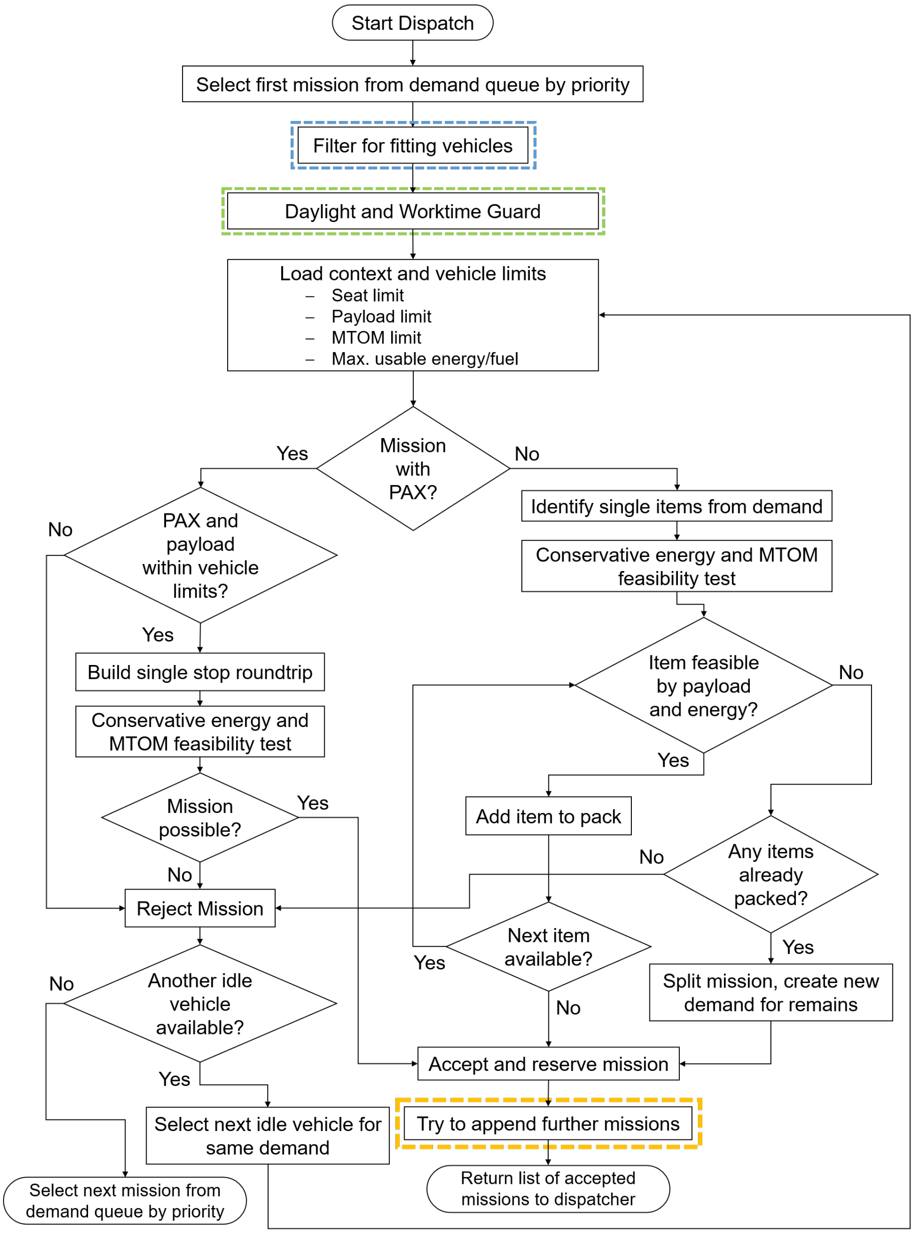

Figure 4.15: Process Chart of the Vehicle Dispatching Routine

If all items of a mission can be transported and also in the case of personnel transport all required checks are successfully passed, an additional process is performed to determine whether further entries in the demand queue can be realised within the same mission. This enables the vehicle to carry out multiple transfers or hoisting operations at the wind farm as long as the vehicle is capable of it. The corresponding routine is illustrated as a process chart in Figure 4.16. It must be noted that only demands of the same kind can be attached, meaning that only deliveries can be added to a delivery mission and only pickups can be added to a pickup mission.

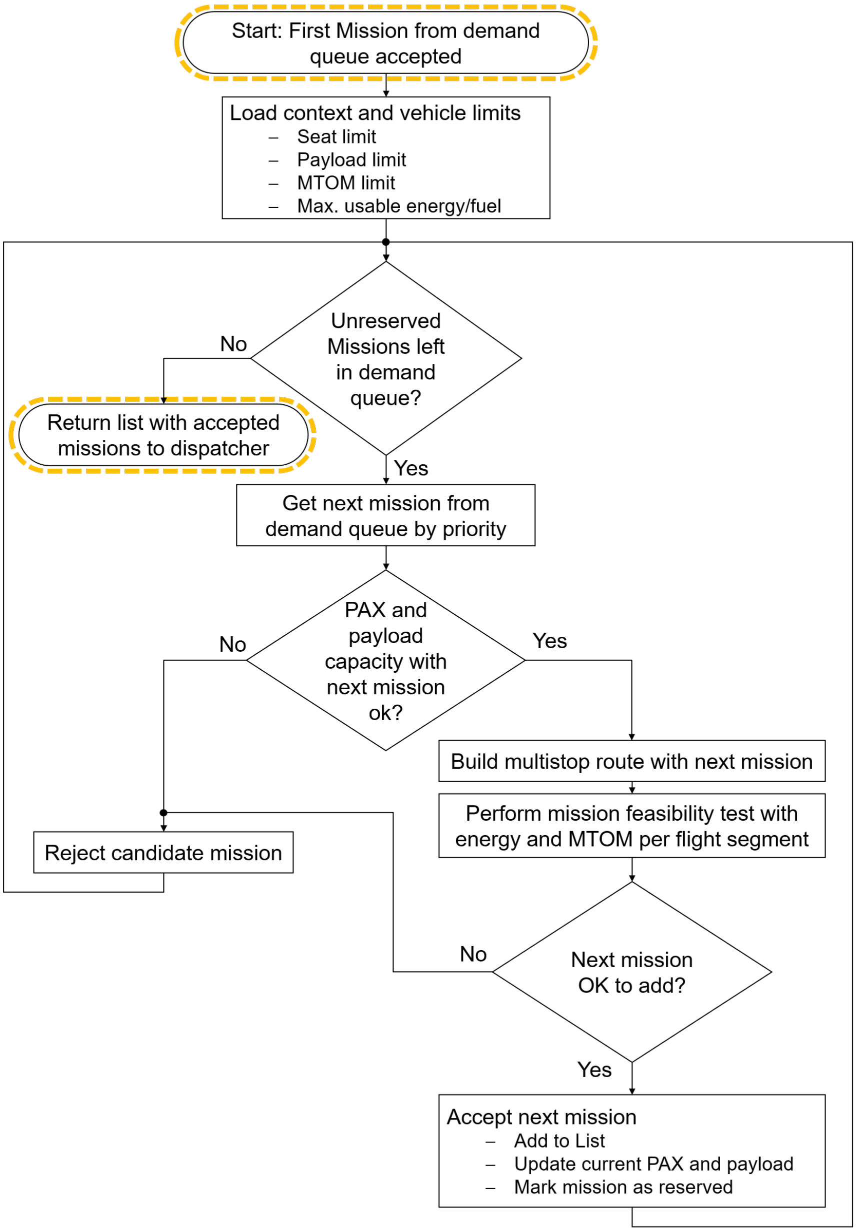

Figure 4.16: Process Chart of the Routine for appending further Missions

With this step, the dispatching for a vehicle is completed. The resulting mission includes the coordinates of all target assets and the respective personnel or equipment to be transported. As a result, the vehicle departs with the appropriate load, follows the intended flight path, and performs the transfer over or at the designated assets.

Once a mission planning is finalised, the corresponding demand is reserved in the demand queue. This prevents duplicate dispatching and enables clear tracking of both pending and ongoing demands, which is particularly valuable for debugging purposes.

From this point onwards, the mission cannot be modified and will be executed as planned. In real-world operations, it would be possible for a vehicle to carry out additional tasks spontaneously, provided sufficient fuel reserves and operational margins remain. However, within the scope of this work, this limitation has been deemed acceptable. Given that this constraint applies uniformly across all strategies and vehicle types, the simulation results remain comparable without introducing significant bias.

4.5.2 Helicopter Operations

In this work, the waypoint network described in Section 2.2.2.1 and illustrated in Figure 2.10 is used for helicopter operations and UAV operations, following the approach proposed by Donkels et al. [18]. Based on these waypoints and the corresponding wind data, it is possible to compute optimised routes that reduce flight time or fuel consumption, as demonstrated for rotorcraft UAVs by Heinze, Schopferer, and Uijt de Haag [173]. The necessary optimisation processes require additional computational effort. With the hardware used by Heinze, Schopferer, and Uijt de Haag [173], the computation of one optimised trajectory needed a median time of 9.82 seconds. While this constitutes no issue for real mission planning, it is not ideal for an agent-based simulation environment in which each simulation step needs to remain computationally efficient if longer time periods are to be examined. For this reason, flight corridors are defined as fixed sequences of waypoints entered in an input file before the simulation runs. Following the waypoint paths results in longer flight distances compared with direct great-circle connections from the service hub to an OWF. For three representative offshore wind farms located 80 km, 120 km, and 160 km from the airport of the island of Borkum, the resulting corridor trajectories are shown in Figure 4.17.

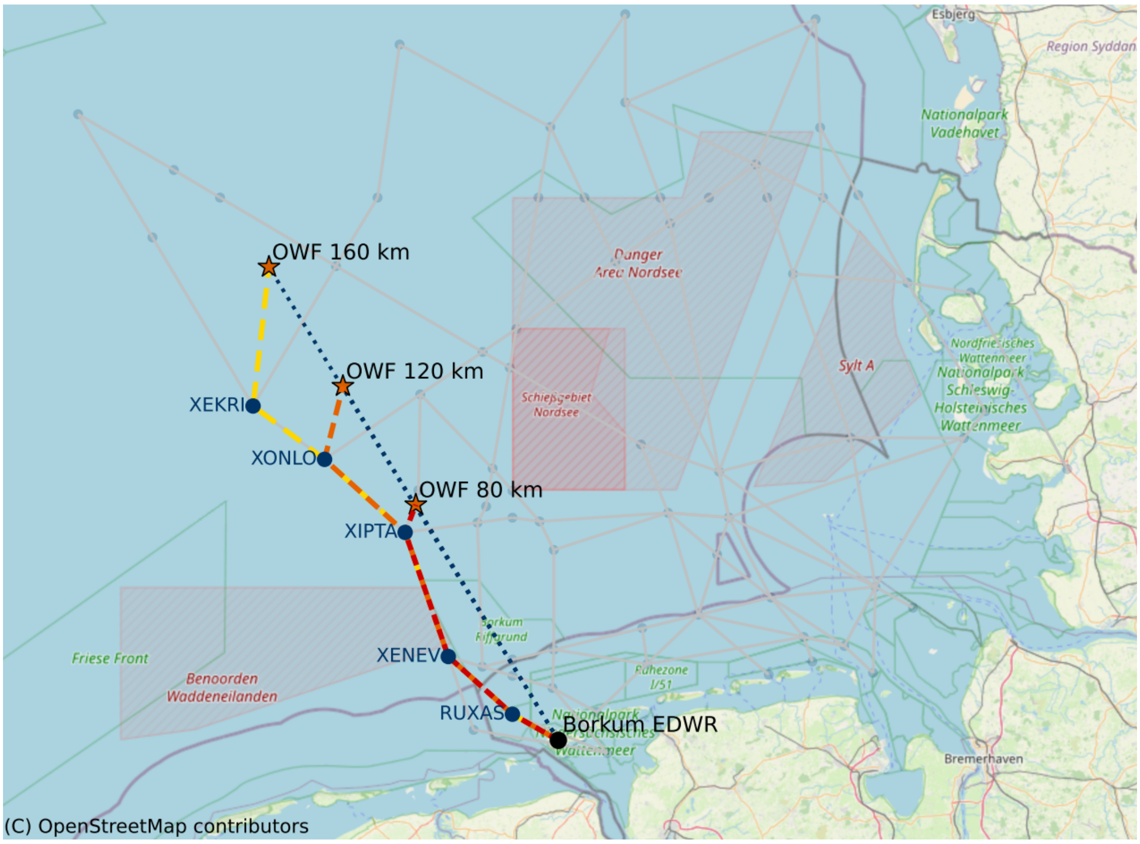

Figure 4.17: Comparison between direct Flight Paths and predefined Waypoint-based Corridors for three Offshore Wind Farms at different Distances from Borkum EDWR

The resulting route lengths and the deviation from the direct distance are summarised in Table 4.7.

	OWF 1	OWF 2	OWF 3
Direct distance [km]	80	120	160
Waypoint route length [km]	87.3	131.8	175.7
Deviation [%]	9.1	9.8	9.8

Table 4.7: Comparison of waypoint-based routes and direct great-circle distances for three offshore wind farms.

4.5.3 Crew Transfer Vessel Operations

Defined routes also exist for vessels operating in the North Sea [174], along with restrictions imposed by environmental protection zones, islands and shallow waters. For this reason, a waypoint-based implementation is also applied to CTV operations. Within the scope of this work, the waypoints are only defined for the coastal section and the inbound and outbound passages from the service base port to ensure that the vessel's path does not cross over islands or other unrealistic areas. From the last defined waypoint, the CTV proceeds directly into the offshore wind farm. Potential evasive manoeuvres due to civil, governmental or military maritime traffic, as well as the influence of tides, are not part of the simulation.

The defined vessel route for the port on Borkum is shown as an example in Figure 4.18.

After the last waypoint leading out of the harbour, the displayed three dashed lines represent the routes to the same exemplary OWFs as in Figure 4.17.

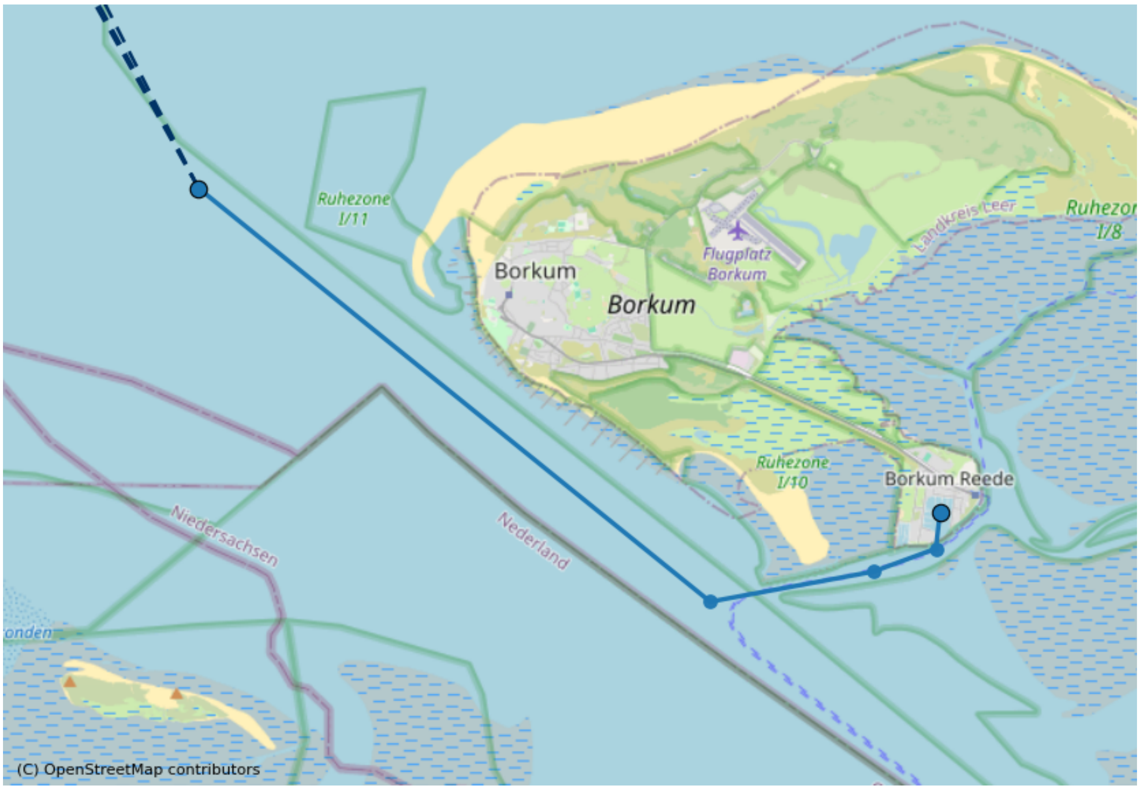

Figure 4.18: Waypoint Corridor for CTVs based at Borkum Harbour

A clear distinction compared to operations involving aerial vehicles, whether crewed or uncrewed, is the vessel's stay within the offshore wind farm during maintenance operations [17]. Instead of returning after each mission, the vessel remains in the wind farm, which is modelled in the simulation through a defined loiter point. During dispatching, a decision is made whether the vessel returns to the service base or proceeds to the loiter point after completing a mission. This routine is represented as a process chart in Figure 4.19. The outcome of this check is then used to construct the vessel's route.

The personnel transfer and equipment handover to the wind turbine is also performed from the CTV using the task described in Section 4.4.1.2, along with the preparation times defined in Section 4.3.4. Apart from the differing durations, the procedure follows the same logic.

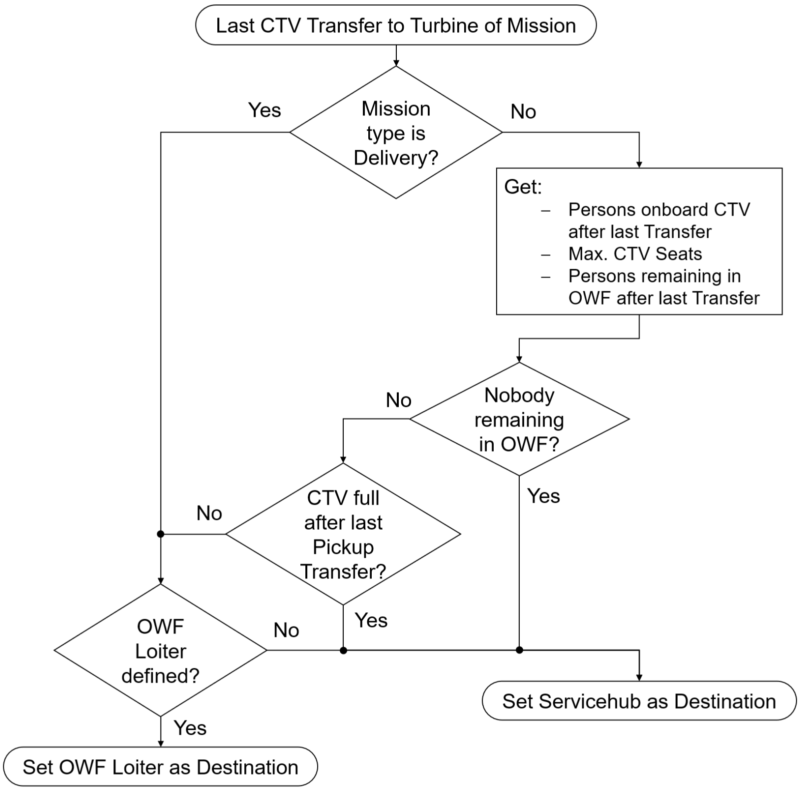

Figure 4.19: Process Chart of the Loiter after Mission or Return to Service Hub Routine

4.6 Baseline Studies

4.6.1 Timestep Size

All simulations performed with the SoSID-Toolkit, independent of the implemented SoS scenarios, share a fundamental setting that significantly affects both the computational time per simulation run and the resulting outputs. This setting is the simulation time step size in seconds. At this interval, the state of all agents and other implemented models is updated. To obtain results that are as accurate as possible, and to minimize errors caused for example by “overshooting” a waypoint position when time intervals are too large, the time step size should be chosen as small as possible. However, this directly increases simulation runtime, which becomes particularly relevant for DOEs with numerous parameter variations and repeated runs under stochastic influences. Therefore, before executing the DOEs, a study with varied step sizes was conducted. The simulation settings are listed in Table 4.8. The absolute numerical results and the exact simulation settings are less relevant than the effects of varying the time step size. Due to the pronounced operational differences, the study was conducted for both the helicopter-only strategy and the CTV-only strategy.

Parameter	Value	Unit
Day	21.08.2024	[DD.MM.YYYY]
Time Frame	0700 - 2400	[HHMM]
Deployment Time	30	[s]
De-/Boarding Time	90	[s]
Preparation Time Sea Transfer	1800	[s]
Preparation Time Air Transfer	300	[s]
Dwell Time Sea	900	[s]
Dwell Time Air	180	[s]
Service Hub	Borkum	[-]
OWF Distance	80	[km]
Number of Turbines	8	[-]
Turbine Model	SWT-154-6	[-]
Maintenance Mode	Planned Campaign on all Turbines	[-]
Maintenance Hours per Turbine	3	[-]
Technicians	2	[-]
Equipment	100	[kg]
Spontaneous Demands	Not Active	[-]
Strategies	CTV Only, Helicopter Only	[-]
CTV Fleetsize	1	[-]
Helicopter Fleetsize	3	[-]
Time Steps	2, 3, 4, 6, 8, 10, 12, 14, 16, 18, 20	[s]

Table 4.8: Simulation Parameters for Time Step Size Study

For each parameter variation, 10 simulation runs were performed, resulting in a total of 220 individual simulation runs, and the results were averaged. The results for simulation runtime are shown in Figure 4.20 as a percentage deviation from the result obtained with the smallest simulated step size. The trend is typical for simulation approaches and shows a very pronounced reduction in runtime for the first increases in step size, after which the effect on runtime becomes noticeably smaller. Increasing the step size from 2 s to 4 s already reduces simulation runtime by approximately 50% while no clear difference regarding the chosen strategy is visible.

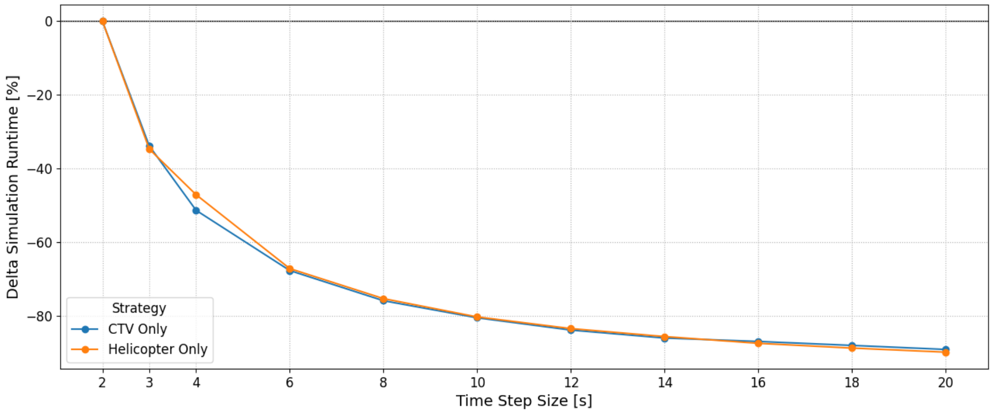

Figure 4.20: Plot of the Simulation Runtime Delta as a Function of the Time Step Size

The effects described above, such as overshooting waypoints, can introduce deviations in the total distances accumulated over the full simulation. These deviations can also propagate into further metrics such as total energy consumption or flight time. However, as shown in Figure 4.21, these effects remain negligible, with deviations below one percent up to a step size of 16 s.

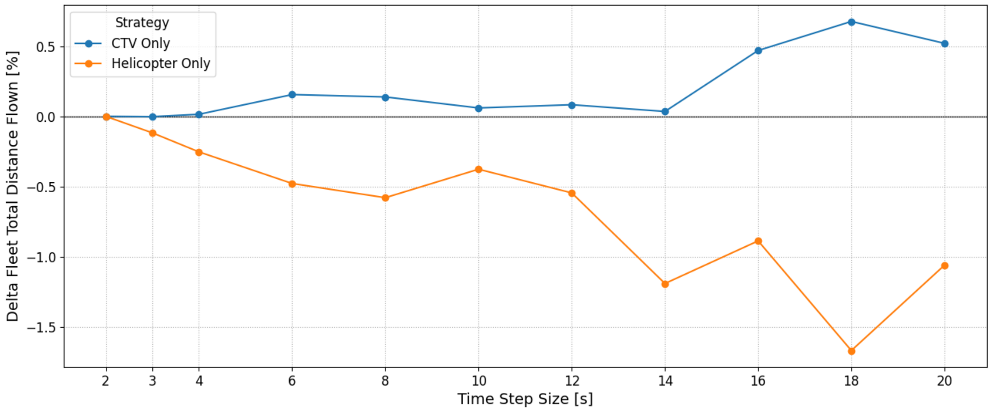

Figure 4.21: Plot of the total Distance Delta Flown or Driven by the entire Fleet as a Function of the Time Step Size

The deviations are more pronounced for the accumulated flight time. Figure 4.22 indicates an approximately linear trend. As expected, this trend is quantitatively more pronounced for the helicopter-only strategy. This can be explained, among other factors, by the simultaneous use of multiple helicopters and the resulting accumulation of errors, as well as by the higher travel speeds involved.

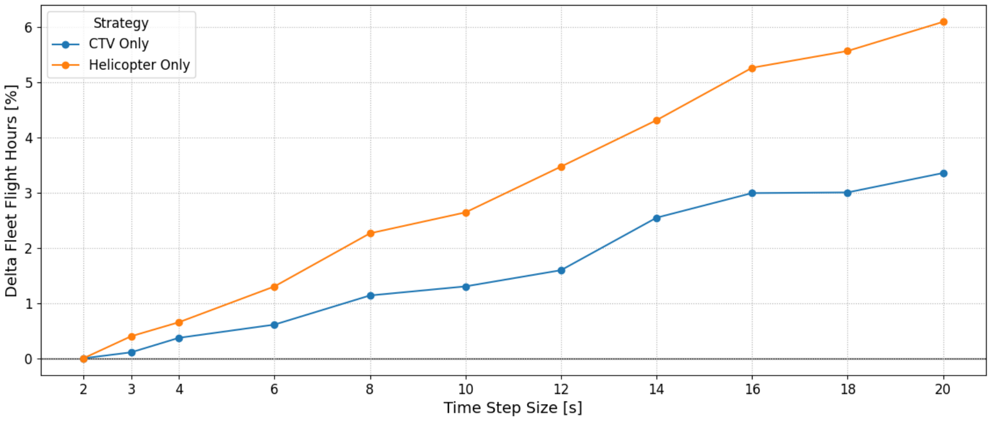

Figure 4.22: Plot of the total Flight or Trip Time Delta by the entire Fleet as a Function of the Time Step Size

The plots shown in Figure 4.23 for the total energy consumed by the fleets exhibit a quantitatively very similar trend, although the difference between the CTV and helicopter cases is slightly larger. As in the preceding evaluations, the results remain below a 1% deviation up to a step size of 4 s.

For the deviations in energy generation of the simulated wind turbines shown in Figure 4.24, a quantitatively very small decreasing trend can be observed as the step size increases. This trend can be explained by the fact that, with larger step sizes, the end of maintenance activities is artificially delayed by several seconds, until the turbine is returned to its operational state in the next time step after the maintenance duration has elapsed. This delay accumulates across the individual time phases within an overall maintenance operation, from the transfer at the turbine to the completed pickup.

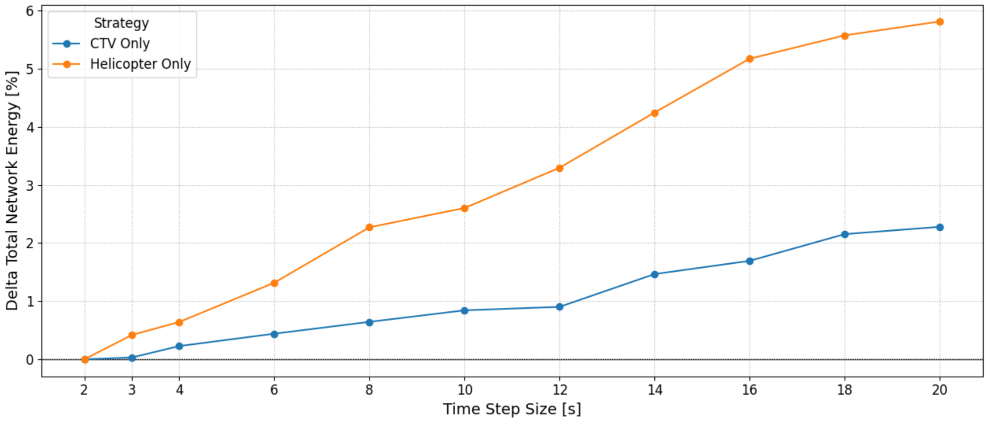

Figure 4.23: Plot of the total Consumed Energy Delta by the entire Fleet as a Function of the Time Step Size

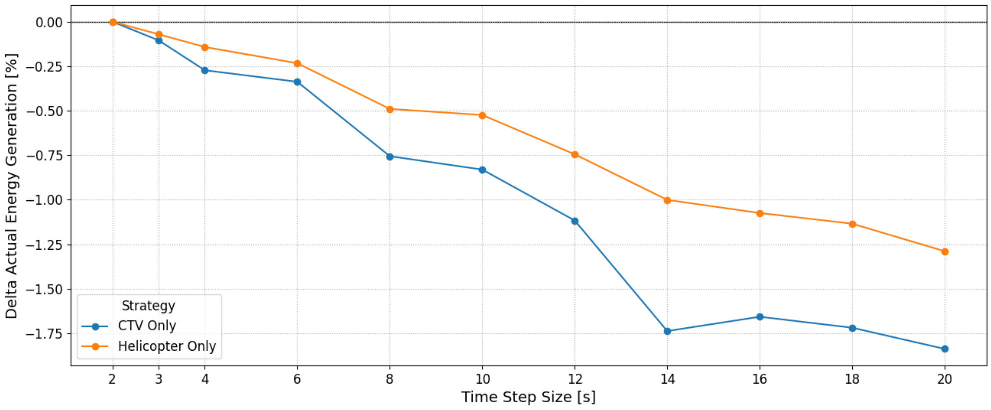

Figure 4.24: Plot of the Generated Energy Delta as a Function of the Time Step Size

The same effect leads to a very small but highly linear increase in the maintenance time at the turbines, as shown in Figure 4.25, where the values are accumulated across all maintenance processes. Since this metric includes only the maintenance process itself, and does not include dwell, transfer, or preparation times, the deviations are significantly smaller.

Based on these results, a time step size of 4 s was selected as the optimal setting for the subsequent simulations. With this choice, simulation runtimes can be reduced by approximately 50%, while deviations across the evaluated simulation outputs remain below one percent compared to the solutions obtained with the smallest time step size.

4.6.2 Design of Experiments

Building on the stepsize studies, the baseline simulations can be conducted. These simulations provide the results for the traditional logistics vehicles, which serve as the reference for later comparisons with UAV-supported strategies.

As already applied for the time step size simulations and for all further simulation runs in this thesis, 21 August 2024 was selected as the simulation day. This date represents an exemplary late-summer day within a period in which maintenance activities are typi-

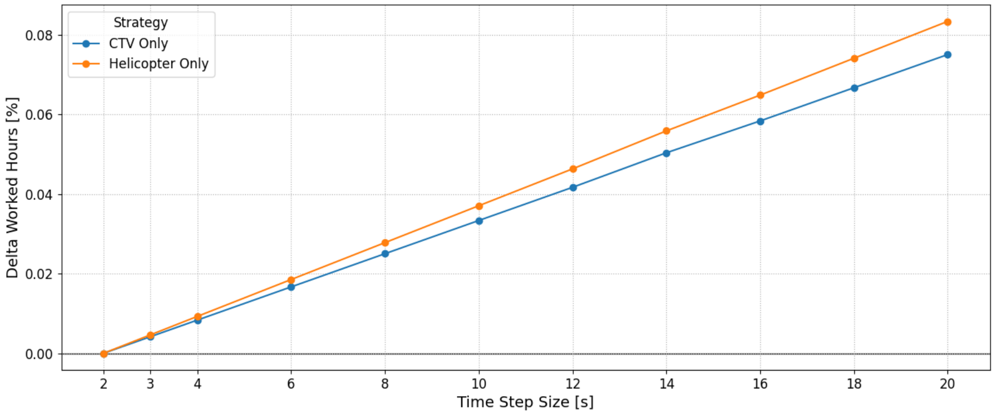

Figure 4.25: Plot of the Worked Hours Delta as a Function of the Time Step Size

cally conducted, since weather conditions are comparatively favorable and maintenance operations are therefore less frequently disrupted. At the same time, the most productive period in autumn and winter still lies ahead, during which more potentially generated energy would be lost during maintenance processes. The selected day does not exhibit extreme wind or wave conditions, so the evaluation of the strategies is not dominated by additional influences. Weather-related disturbances are not less relevant, but they are not part of the investigations performed here and can be addressed later based on the implemented models.

A simulation start time of 7:00 AM local time was chosen, with the simulation ending at 12:00 PM. The defined end time is important for two reasons. First, it ensures that potentially very long transfer times, particularly for CTV operations and larger distances, are fully represented. Second, these transfer times are relevant for assessing energy production, especially in cases where maintenance processes are started but may be terminated before completion. If, for example, a turbine requires 6 h of maintenance but is serviced for only 5.5 h before the team is picked up, the evaluation of completed maintenance hours would appear comparatively favorable. Nevertheless, the turbine cannot be returned to operation until another team is transported to the turbine on the following day. By limiting the simulation time to 12:00 PM, this effect is captured in the energy production assessment, enabling an evaluation that is better aligned with the needs and constraints of the use case. When interpreting absolute values, this must be taken into account, since it primarily enables meaningful comparisons within the simulations performed under this setting.

Further assumptions were derived from the evaluation of videos and experiences of the offshore wind industry regarding the time required for vehicles and teams to conduct the transfer onto the turbine and to begin maintenance work. These parameters can also be varied in more detailed sensitivity studies. For the establishment of a baseline and the fundamental comparison of logistics strategies, this was assessed as unnecessary.

The distances of the wind farms from the service hub were varied as discussed in Section 3.3. The bearing was adjusted such that the wind farms are located at generally plausible positions in the German Bight within the existing helicopter route network, as shown in Figure 4.17.

For the wind farm, eight wind turbines of the type SWT-154-6 were selected, all of which

Parameter	Value	Unit
Day	21.08.2024	[DD.MM.YYYY]
Time Frame	0700 - 2400	[HHMM]
Deployment Time	30	[s]
De-/Boarding Time	90	[s]
Preparation Time Sea Transfer	1800	[s]
Preparation Time Air Transfer	300	[s]
Dwell Time Sea	900	[s]
Dwell Time Air	180	[s]
Service Hub	Borkum	[-]
OWF Distance	80, 120, 160	[km]
OWF Bearing from Service Hub	329	[°]
Number of Turbines	8	[-]
Turbine Model	SWT-154-6	[-]
Maintenance Mode	Planned Campaign	[-]
Affected Turbines	All	[-]
Maintenance Hours per Turbine	3, 6	[-]
Technicians	2	[-]
Equipment	2 x 50	[kg]
Spontaneous Demand Probability	0.3, 0.6	[-]
Spontaneous Equipment	1 x 20	[kg]
Strategies	CTV Only, Helicopter Only	[-]
CTV Fleetsize	1	[-]
Helicopter Fleetsize	1, 2, 3	[-]
Time Steps	4	[s]

Table 4.9: Simulation Parameters for Baseline Logistic Strategy Study

are to be serviced during the campaign. To investigate the influence of maintenance duration at the SoS level, three and six hours of maintenance time were chosen as variation. For the same reason, the probability of spontaneous material or equipment demand during a maintenance task was simulated with values of 0.3 and 0.6, where the higher probability leads to an increased number of flights and interruptions of the maintenance processes.

For the CTV Only strategy, fleet size was not varied, and one CTV was defined as the baseline. For the Helicopter Only strategy, up to three H135 were simulated. A higher number was considered unrealistic and was therefore not included in the simulation.

Regarding equipment, it was assumed that each technician requires 50 kg of material packed in individual work bags. While the specific division of this equipment is not relevant for the pure helicopter and CTV strategies, it is already considered here in the same way as for the drone-supported strategies later on.

The spontaneously required equipment was assumed to weigh 20 kg for the baseline studies.

The selected simulation parameters are listed in Table 4.9.

4.6.3 Simulation Results

The simulation execution was monitored at selected points within the DOE using the Toolkit GUI. In Figure 4.26, with the distance between the OWF and the service hub reduced for improved graphical readability, the service hub is shown in the lower right corner of the left image. The helicopter shown there is not used in the running simulation, since the CTV-only strategy was selected. The CTV can be seen en route to the OWF, which consists of eight wind turbines automatically arranged around the OSS. At the start of the simulation, all turbines are out of operation, as indicated by the red coloring of the turbine icons. The right side shows a detailed view of the wind farm after several teams have already transferred from the CTV onto the turbines. This is indicated by the yellow coloring, which shows that maintenance activities are actively being performed.

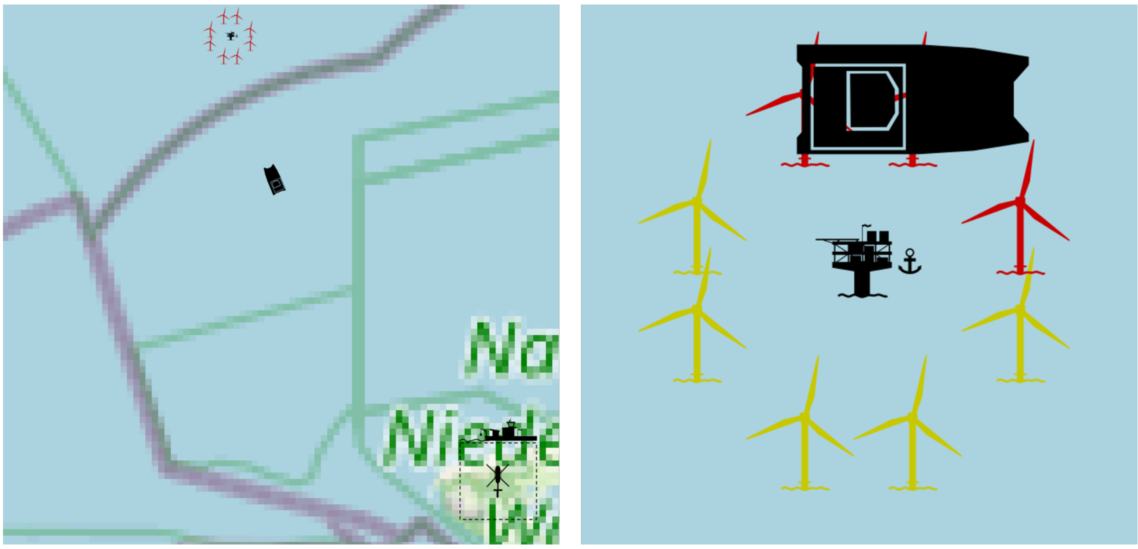

Figure 4.26: Initial CTV Trip to the OWF (left) and OWF Close Up after multiple successful Transfers (right)

If, as shown in the left GUI view in Figure 4.27, a spontaneous equipment demand occurs during maintenance activities, which is indicated by the orange coloring of the wind turbine, the team is picked up immediately in accordance with the strategy ConOps. In the right view, the state of the OWF near the end of a working day is shown. On the turbines highlighted in green, maintenance work has been completed and the teams are waiting for pickup by the CTV. The turbine marked in black has already returned to energy-producing operation, since the team was picked up after completion of maintenance. One turbine is still shown in yellow, indicating that maintenance work is still ongoing. The red coloring of the CTV indicates that the vessel is still executing its current pickup assignment, which is also reflected by the fact that the wind turbine still visible beneath the CTV icon is shown in green.

Figure 4.28 shows, in the left view, the initial transport of teams to the turbines using two helicopters under the helicopter-only strategy. Based on the two turbines that have already been supplied, it can be seen that this corresponds to the second delivery wave. The black helicopter icons indicate that a maintenance team is on board. During the return flight without a team on board, the icon changes to red. In the right GUI view, all maintenance activities in the OWF are in progress. However, a spontaneous demand occurred at the turbine shown in orange, and a helicopter is therefore en route to deliver additional material. This flight without a maintenance team but with cargo on board is indicated by an orange helicopter icon.

Once maintenance work is completed, a helicopter flies to the respective turbine and picks

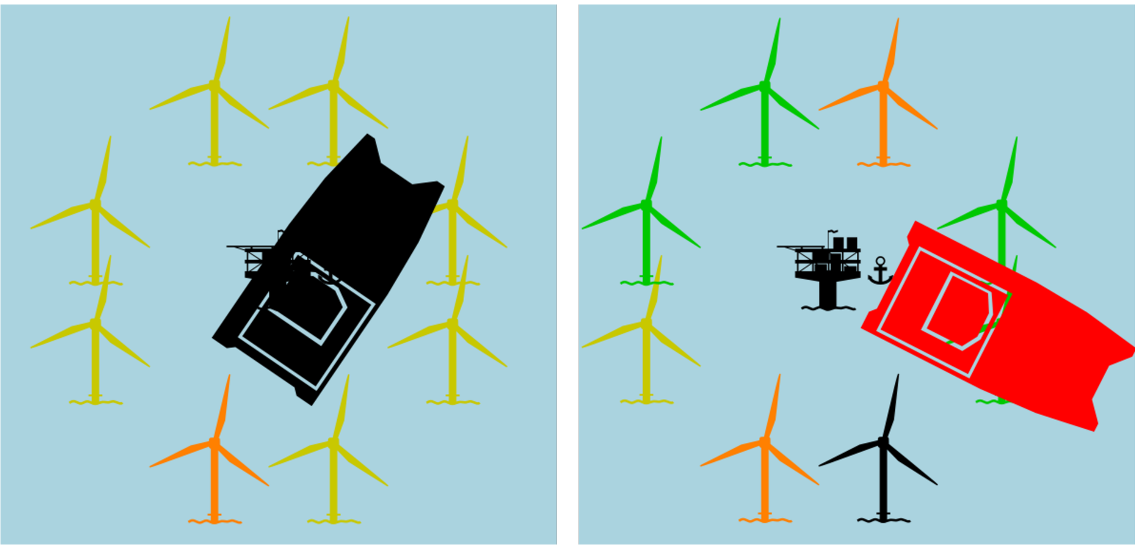

Figure 4.27: Pick up of a Team after an spontaneous Equipment Demand (left) and Pick ups after finished Maintenance Works (right)

up the team. During this outbound leg it is shown in red. In the left plot of Figure 4.29, two turbines are shown in green, meaning that the teams are waiting there for pickup. One helicopter is close to reaching the OWF, while the second helicopter has already accepted the pickup mission for the second team, as indicated by its red coloring, but has not yet taken off from the airfield. The right plot shows the state after both teams have been picked up successfully. The helicopter shown in black is still transporting the second team back to the service hub. Since two additional teams have become ready for pickup in the meantime, the helicopter that performed the first pickup mission is already flying back to the wind farm.

Accordingly, the baseline scenarios were simulated using 10 runs per parameter set with different random seeds for the stochastic effects. The results were averaged arithmetically across the runs and the 95% confidence interval was determined. To gather a first basic understanding of the results, threedimensional bar charts were derived. Several trends and patterns are evident here, these are explained in detail using two-dimensional plots in the following.

The threesimensional plot for the consumed energy by the entire fleet in Figure 4.30 shows clearly the influence of the distance of an OWF to its servicehub. For more than one helicopter, the energy consumption is comparatively similar to the consumption of a CTV. A single helicopter leads to the lowest resulting fleet energy, independed of the distance.

The visualisation of the produced energy in Figure 4.31 demonstrates the impact of the distance for the helicopter fleets similar to the results of the fleet energy consumption, however, the results for the CTV are not significantly influenced by this.

Comparing the energy production results to the hours worked on all turbines in Figure 4.32, similar trends can be observed. As a contrast, with more helicopters in use, the influence of the distance on the time the technicians get on the assets decreases.

Figure 4.33 shows the energy consumed by the entire vehicle fleet across the different strategies and fleet sizes for the three investigated distances between the OWF and the

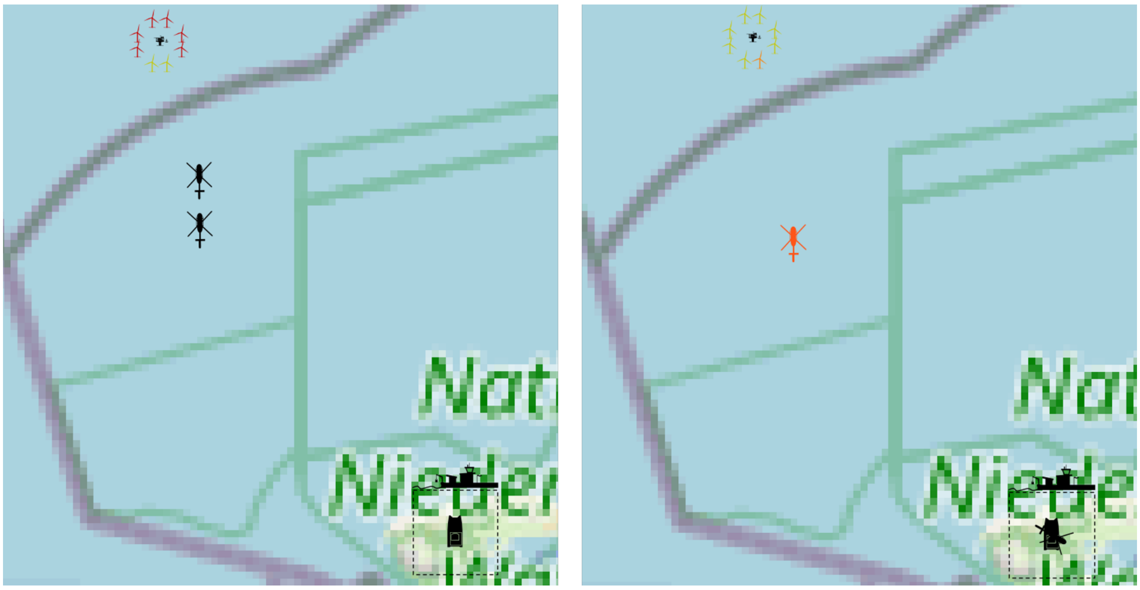

Figure 4.28: Initial Helicopter Flights to the OWF (left) and Delivery of a spontaneously needed Item (right)

service hub. For the simulation with one CTV and for the cases with two and three helicopters, the expected trend of higher energy consumption for longer distances is observed. Within a given strategy and fleet size, the relationship between distance and energy consumption is approximately proportional. For the case in which only one helicopter is used, a significantly lower energy consumption is observed compared to larger fleets, and this value remains nearly constant across the OWF distances. This is attributed to the fact that a single helicopter cannot satisfy the high demand by a wide margin and therefore remains airborne throughout the operationally available time in order to serve demands. As a result, the single helicopter cannot consume more energy within the predefined time window. Since cruise flight requires less energy than more frequent hover phases, this also explains the slightly reduced energy consumption at the largest distance compared to the shorter distances.

Figure 4.34 shows the energy production over the simulation period. The results indicate that using a single CTV leads to higher wind farm energy production than using a single helicopter, and this difference becomes more pronounced as the distance between the wind farm and the service hub increases. A clear advantage of operating multiple helicopters is also evident. However, the additional benefit of a third helicopter compared to a fleet of two aircraft is smaller at the shortest distance than at the larger distances.

The coupling between completed maintenance work and the return of the wind turbines to energy-producing operation becomes clear when comparing Figure 4.34 and Figure 4.35, where the latter reports the maintenance hours actually performed in the OWF. The advantage of a CTV over a single helicopter, as well as the advantage of operating two or three helicopters compared to one helicopter and compared to the CTV strategy, is preserved. However, the nearly identical maintenance hours for a fleet of three helicopters across all distances indicate that, with this fleet size, all maintenance tasks can be completed and that increasing the number of helicopters no longer affects this metric. For the 80 km distance, a similarly high value is already achieved with only two helicopters.

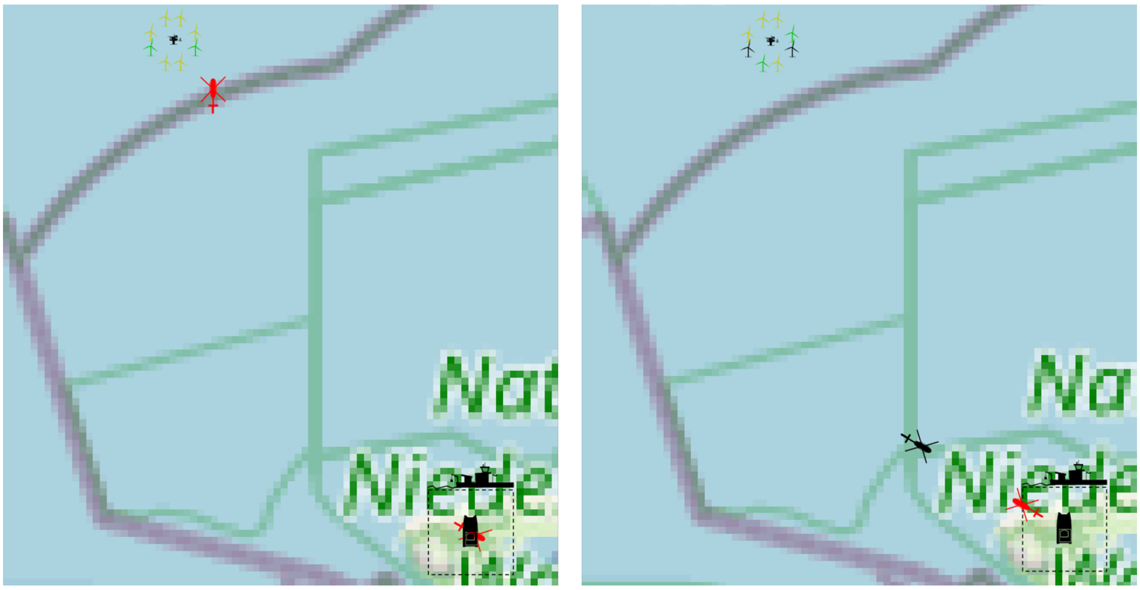

Figure 4.29: Flight to OWF after finished Maintenance Tasks (left) and Flight Operations after two successful Pick ups (right)

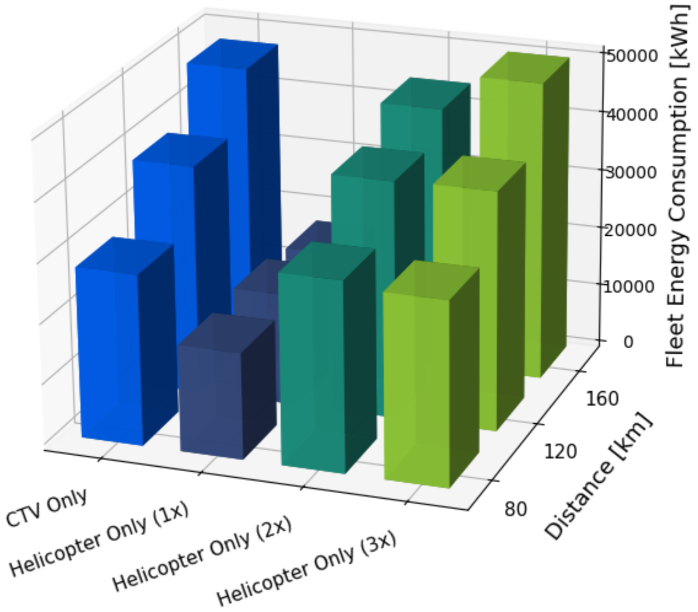

Figure 4.30: 3D Visualisation of Fleet Energy Consumption Results for the simulated Strategies and Fleet Sizes at 3h of Maintenance Time per Turbine and a 0.3 Possibility of Spontaneous Demands

The remaining differences in wind farm energy production can be explained by the fact that larger fleets enable teams to start work earlier and, correspondingly, to complete their tasks sooner, which increases the time during which the turbines are in operation. Due to the comparatively short maintenance duration of 3 h, evening pickup and interrupted work phases do not have a major impact on the simulation results.

To investigate the influence of a longer maintenance duration, a maintenance time of 7 h

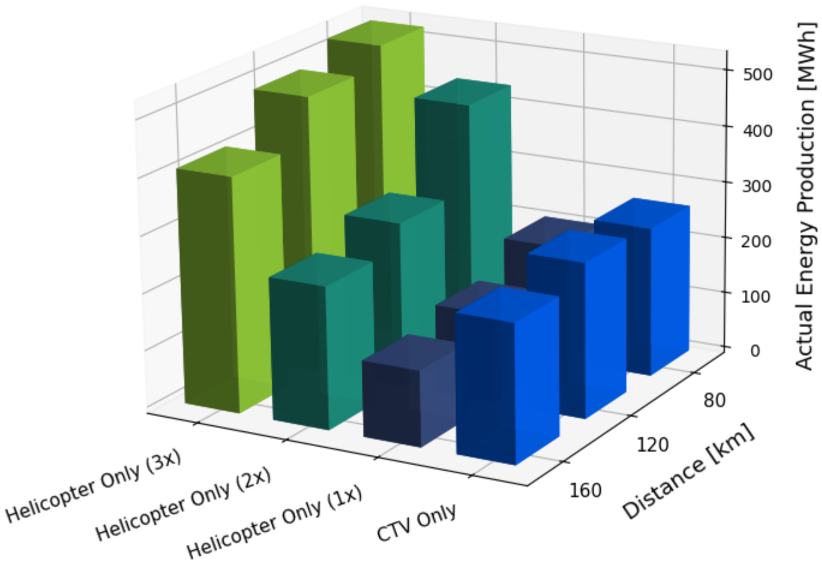

Figure 4.31: 3D Visualisation of Energy Production Results for the simulated Strategies and Fleet Sizes at 3h of Maintenance Time per Turbine and a 0.3 Possibility of Spontaneous Demands

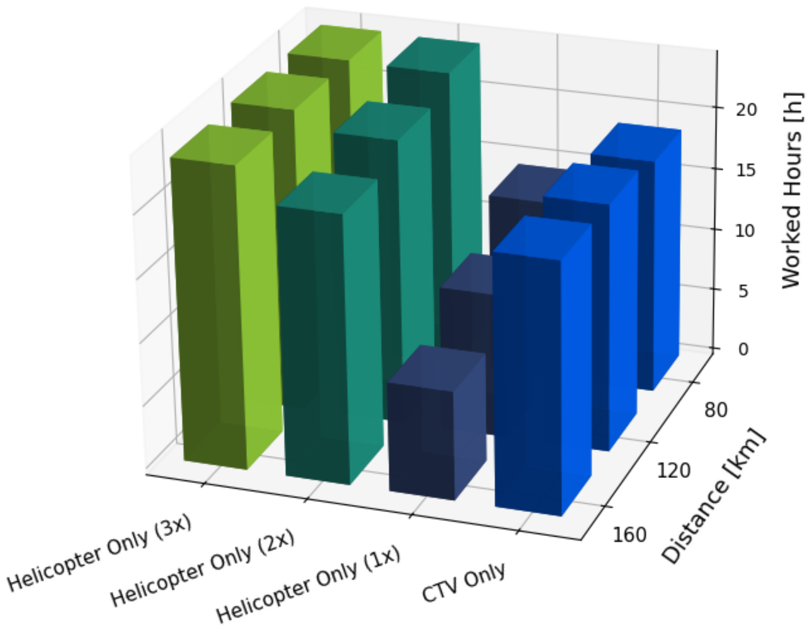

Figure 4.32: 3D Visualisation of Work Hours Results for the simulated Strategies and Fleet Sizes at 3h of Maintenance Time per Turbine and a 0.3 Possibility of Spontaneous Demands

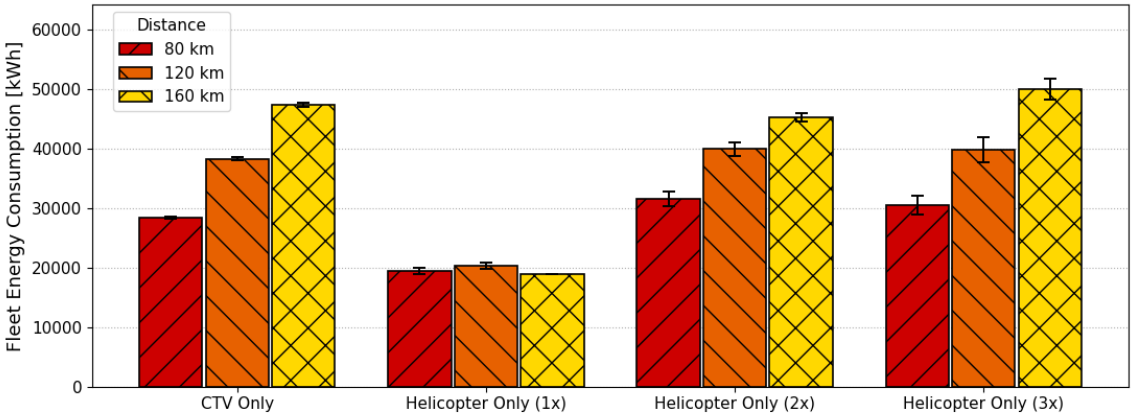

Figure 4.33: Fleet Energy Consumption for the simulated Strategies and Fleet Sizes at 3h of Maintenance Time per Turbine and a 0.3 Possibility of Spontaneous Demands

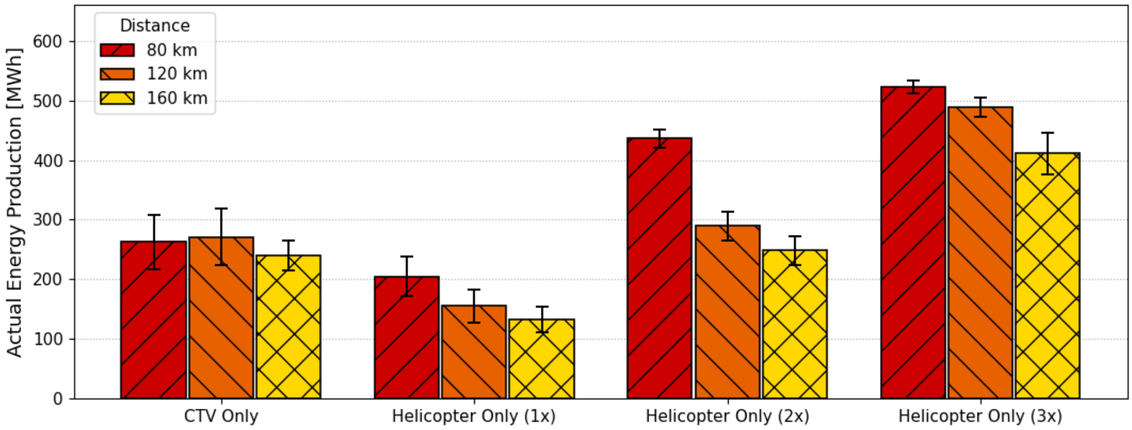

Figure 4.34: Generated Energy during the Simulation for the simulated Strategies and Fleet Sizes at 3h of Maintenance Time per Turbine and a 0.3 Possibility of Spontaneous Demands

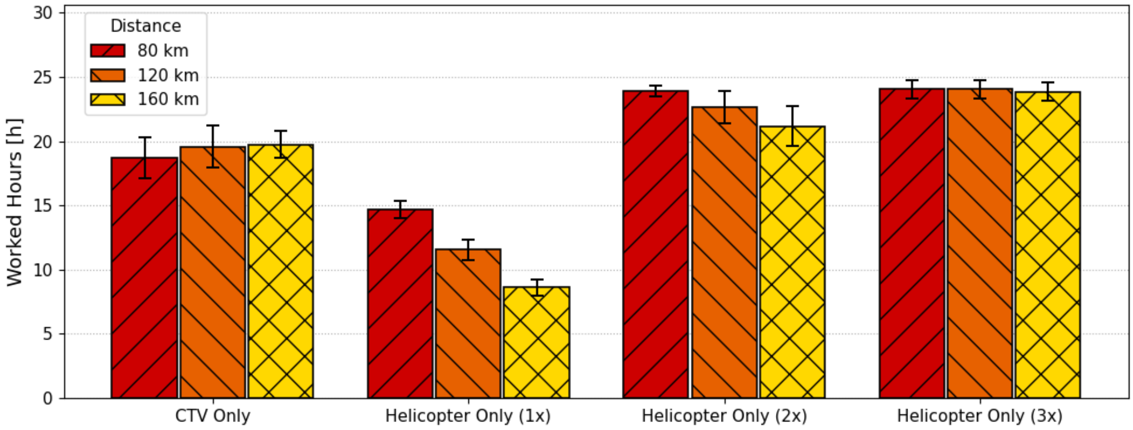

Figure 4.35: Enabled Maintenance Time for the simulated Strategies and Fleet Sizes at 3h of Maintenance Time per Turbine and a 0.3 Possibility of Spontaneous Demands

was simulated using the same probability for spontaneous material demands. Figure 4.36 extends the results shown in Figure 4.33 by adding these cases. No significant changes due to the increased maintenance duration are visible with respect to total fleet energy consumption, since the same number of teams still needs to be transported to the turbines and picked up again.

As indicated by the additional evaluations, for the longer maintenance cases, especially at larger distances and with smaller fleets, maintenance end times are often not reached. Due to daylight and shift constraints, teams are picked up before completing the work. Since the probability of a spontaneous demand is normalized by the maintenance duration, the number of triggered spontaneous demands therefore decreases. This can explain the slightly reduced fleet energy, for example for the CTV simulation and the two-helicopter case at 80 km and 120 km distance. Apart from this effect, the same trends as for the shorter maintenance duration can be observed.

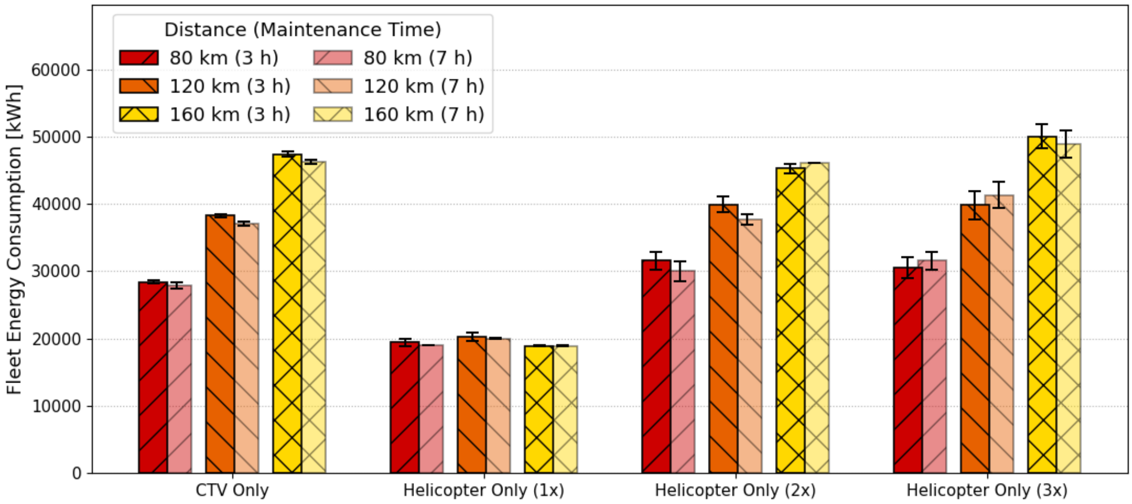

Figure 4.36: Fleet Energy Consumption for the simulated Strategies and Fleet Sizes at 3h and 7h of Maintenance Time per Turbine and a 0.3 Possibility of Spontaneous Demands

In contrast, the energy production shown in Figure 4.37 exhibits pronounced differences. While the qualitative trends remain unchanged, no meaningful energy production is observed for simulations with small fleets at larger distances. Accordingly, maintenance could not be completed for any of the eight wind turbines. The helicopter-only strategy with a single helicopter yields the same result for all distances, including the shortest distance of 80 km. In comparison, the CTV strategy leads to a relevant wind farm energy output at least for the 80 km distance between the OWF and the service hub.

The comparison of the cumulative maintenance hours performed within the wind farm is also of interest. Increasing the required maintenance duration leads to a clear step change in this metric, while the use of only a single helicopter results in a comparatively small increase. The longer maintenance duration introduces several effects that can lead to non-linear and non-proportional differences in the results, since the interruption of maintenance activities forces pickup operations. That this mechanism introduces larger deviations for several simulation points is indicated by the wider error bars.

The influence of the probability of a spontaneous demand was also investigated by simulating a higher value, here 0.6 instead of 0.3. As expected, this does not lead to a significant

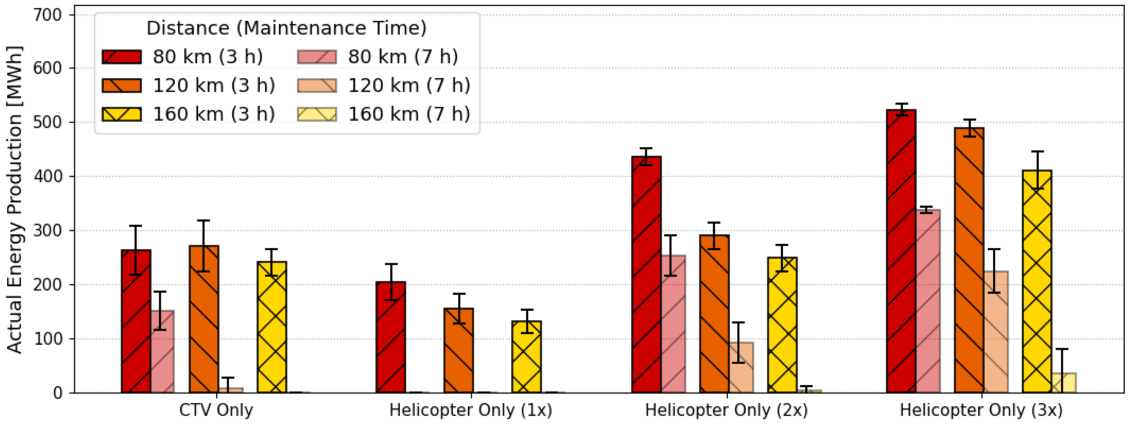

Figure 4.37: Generated Energy during the Simulation for the simulated Strategies and Fleet Sizes at 3h and 7h of Maintenance Time per Turbine and a 0.3 Possibility of Spontaneous Demands

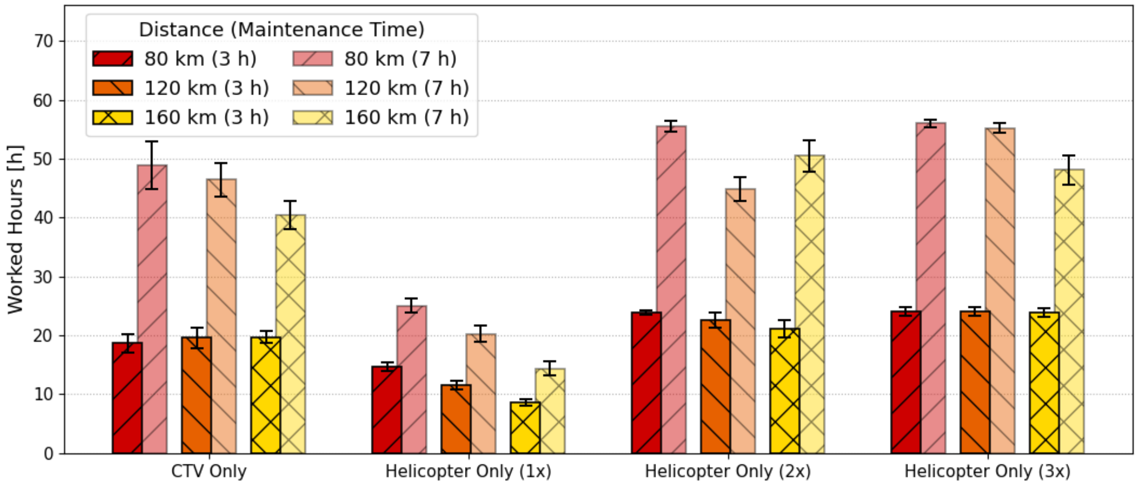

Figure 4.38: Enabled Maintenance Time for the simulated Strategies and Fleet Sizes at 3h and 7h of Maintenance Time per Turbine and a 0.3 Possibility of Spontaneous Demands

change in the fleet energy consumption of the CTV shown in Figure 4.39. While a triggered spontaneous demand causes the team to be picked up earlier from the respective turbine, the total travel distance remains unchanged. The results for a single helicopter also show no major variation. As discussed previously, the single helicopter is already heavily utilized by the maintenance operations, such that spontaneous demands do not result in additional trips. In contrast, for larger helicopter fleets, significant increases in fleet energy consumption can be observed, since the additional flight missions can be executed in these cases.

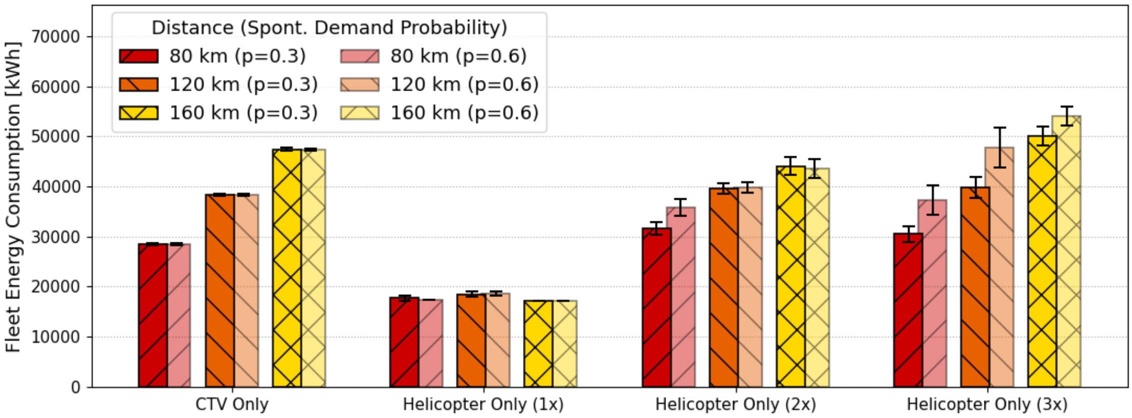

Figure 4.39: Fleet Energy Consumption for the simulated Strategies and Fleet Sizes at 3h of Maintenance Time per Turbine and 0.3 and 0.6 Possibility of Spontaneous Demands

For the generated energy shown in Figure 4.40, the effect of the higher probability of equipment resupply is clearly visible across all strategies and fleet sizes. For the CTV simulations, the reduction in generated energy is more pronounced than for the helicopter cases, since there is no option to complete maintenance after a spontaneous demand has occurred. For the helicopter fleets in particular, it is also notable that the confidence intervals are wider. This can be explained by the increased influence of the stochastic seeds on the simulation progression and on how the spontaneous demands are handled.

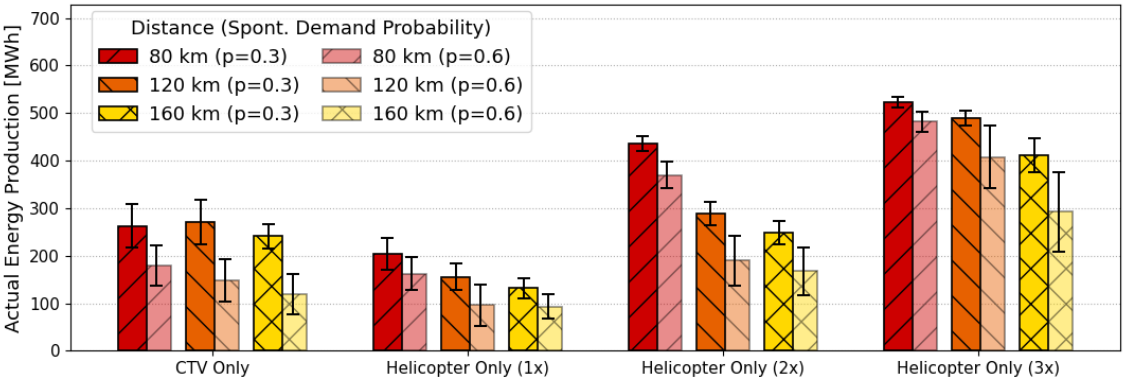

Figure 4.40: Generated Energy during the Simulation for the simulated Strategies and Fleet Sizes at 3h of Maintenance Time per Turbine and 0.3 and 0.6 Possibility of Spontaneous Demands

The evaluation of maintenance hours in Figure 4.41 also provides useful insights. Overall, a reduction in completed work hours can be observed. This results either from the interrupted maintenance activities in the CTV-only strategy, or from the additional waiting time required for the helicopter to deliver replacement parts. With two helicopters at an 80 km distance, or with three helicopters up to 120 km, the total required maintenance hours can still be achieved, but at a later point in time than in the case with a lower probability of spontaneous demands. This also explains the lower energy production despite comparable maintenance hours.

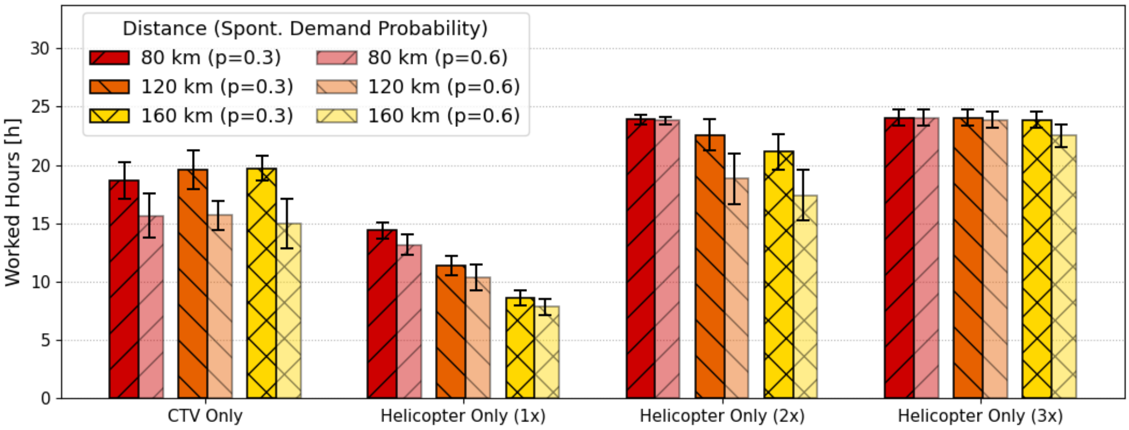

Figure 4.41: Enabled Maintenance Time for the simulated Strategies and Fleet Sizes at 3h of Maintenance Time per Turbine and 0.3 and 0.6 Possibility of Spontaneous Demands

Based on the collected data for the currently used common logistics vehicles, cost models can be developed in further steps or the data can be integrated into such models to also assess the economic dimension. However, a preliminary evaluation can already be made based on the examined results. The CTV strategy leads to more desirable outcomes than a helicopter-based strategy relying on only one aircraft. For the investigated distances and scenarios, two and three helicopters proved to be the most flexible solution overall, enabling the most working hours and the highest energy production of the OWF. At shorter distances between the wind farm and the service hub and lower probabilities for spontaneous demands, two helicopters can already lead to favorable outcomes that are not significantly improved by adding a third helicopter. On this basis, strategies involving drones can be evaluated in the next steps.

Chapter 5

UAV Conceptual Design and Operational Assessment

5.1 VTOL Aircraft Design Tool

5.1.1 VTOL-AD

VTOL-AD is a conceptual aircraft design tool that was developed in the context of Urban Air Mobility and focuses on battery-electric and hybrid VTOL aircraft that operate in this environment [130]. The tool is designed for typical UAM concepts such as multicopter or tiltrotor configurations, that carry a small number of passengers and which could be flown without a pilot on board. Within this scope, VTOL-AD is intended for early design-space exploration by providing a consistent sizing and performance framework that links mission requirements, propulsion architecture, and mass estimation. This conceptual approach leads to fast results and the possibility of a larger amount of designs with different parameters or constraints, which can then be evaluated in the DLR SoSID-Toolkit framework for agent-based simulations.

The design process in VTOL-AD starts from top-level requirements such as mission profile, payload, range and cruise speed. Based on these inputs, the tool performs a conceptual sizing loop in which the aircraft mass, wing and rotor geometry and propulsion system are iteratively adjusted until the mission can be flown with sufficient performance margins and energy reserves according to the input data. This process is illustrated by Figure 5.1. Aerodynamic properties of fixed lifting surfaces are represented by simplified lift and drag models. Hover and low-speed performance are evaluated from prescribed propeller disk loading, figure of merit, and tip-speed limits, so that power requirements in the vertical phases remain within realistic bounds.

The mass breakdown is obtained from semi-empirical relations for UAM-VTOLs, which are mostly based on traditional conceptual sizing approaches for helicopters or general aviation aircraft. The propulsion system is adaptable to different powertrains and can represent conventional, hybrid-electric, and all-electric architectures. In particular, VTOL-AD includes a serial hybrid-electric powertrain model in which a gas turbine, generator, power management, electric motors, and battery are treated as separate components with assigned power densities and efficiencies. For a given mission, VTOL-AD integrates the power and energy demand over all segments, including hover, climb, cruise, descent,

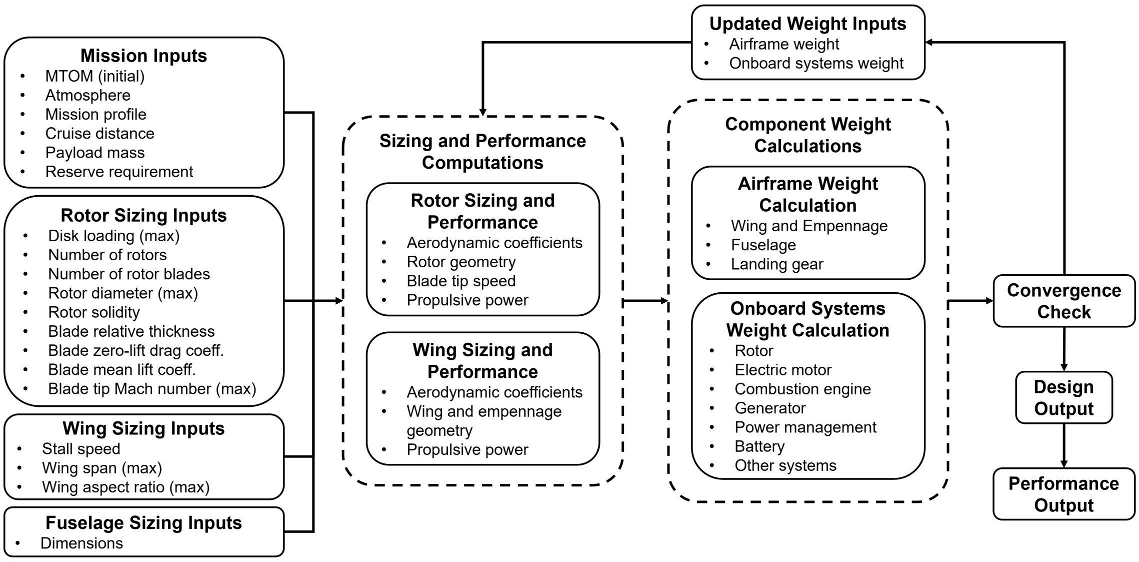

Figure 5.1: VTOL-AD Sizing Loop, adapted from Ratei [130]

and reserves, and checks consistency with the installed power and stored energy.

Due to VTOL-AD's originally intended focus on UAM applications, a design process for uncrewed aircraft cannot be initiated directly.

The implemented methods for mass estimation and performance calculation were examined with regard to their suitability for VTOL-UAVs in the MTOM range between 100 kg and 1500 kg. For such aircraft, comparatively few published data are available, and many publications on this topic focus either on smaller VTOL vehicles or on conventionally launched fixed-wing reconnaissance UAVs [175, 176, 177]. This results in a wide variety of approaches that, depending on their underlying assumptions, may be more or less appropriate for different UAV configurations [178, 179]. An improvement over the results obtained with the previously implemented methods in VTOL-AD for passenger carrying VTOLs is therefore not guaranteed.

For this reason, the existing approaches for crewed VTOL aircraft were first reviewed with respect to their boundary conditions and data basis. Where discrepancies were identified, the existing methods were replaced by methods that are considered more suitable for the present problem. Modifications were introduced for the following design aspects, which are discussed in more detail in the subsequent sections:

- Parasite Drag,
- Wing Mass,
- Landing Gear Mass,
- Powertrain Energy Density,
- Powertrain Efficiency.

5.1.2 Parasite Drag

Up to now, the parasitic drag coefficient $C_{D,0}$ has been computed by VTOL-AD using the method preseted by Kadhiresan and Duffy [180] [130]. The coefficient results from the ratio of the reference area S_{ref}, which represents the wing area, and the equivalent flat-plate area f_{VTOL}:

$$C_{D,0} = \frac{f_{VTOL}}{S_{ref}} \tag{4.1.2.1}$$

For crewed VTOL and eVTOL aircraft, the following approximation for the equivalent flat-plate area was developed, drawing on data from conventional crewed helicopters as well as tiltrotor and tiltwing aircraft:

$$f_{VTOL} = 1.6\left(\frac{m_{mto}}{1000}\right)^{\frac{2}{3}} \tag{4.1.2.2}$$

The available dataset does not extend below take-off masses of 1000 kg. While this constitutes a sufficient lower bound for crewed vertical-flight aircraft, it represents the upper end of the vehicle classes examined in this work.

Consequently, a method for computing parasitic drag was implemented that is better suited to smaller weight ranges and aircraft configurations. In Götten et al. [176], UAVs with take-off masses from 25 kg to 630 kg were investigated by modelling them, including landing gear and sensor pods, using CFD methods. Although these UAVs are conventional fixed-wing configurations without VTOL capability, this approach is nevertheless considered substantially more representative of the VTOL-UAVs of interest here, especially during cruise. While VTOL cargo UAVs may require smaller sensor pods and lack conventional wheel-type landing gear compared to the surveillance drones studied by Götten et al. [176], additional drag contributions are added by the vertical propulsion units and their supporting structures. For the parasitic (zero-lift) drag coefficient $C_{D,0}$, using the wetted area S_{wet} and the equivalent skin-friction coefficient C_{feq}, it follows that:

$$C_{D,0} = C_{feq} \cdot \frac{S_{wet}}{S_{ref}} = \frac{f_{UAV}}{S_{ref}} \tag{4.1.2.3}$$

The wetted area S_{wet} is determined as a function of the maximum take-off mass (MTOM) based on a UAV database [176].

$$S_{wet} = 0.26241 \cdot MTOM^{0.744625} \tag{4.1.2.4}$$

Based on CFD simulations and design studies, Götten et al. [176] proposed using an equivalent skin-friction coefficient of $C_{feq} = 0.01105$, which is adopted in this work. Compared to the drag estimates commonly used for light aircraft in conceptual design, significant differences were found in the energy consumption of a fixed-wing drone during flight, which has a direct impact on the overall aircraft sizing [176]. The consequently higher energy consumption values calculated for uncrewed aircraft lead to an increase in total aircraft mass of more than 20% for the researched surveillance UAV configuration.

When comparing the equivalent flat-plate area functions obtained from the method previously applied to crewed VTOLs by Kadhiresan and Duffy [180] with the newly introduced UAV method by Götten et al. [176], the resulting difference between the two approaches already becomes apparent, as shown in Figure 5.2.

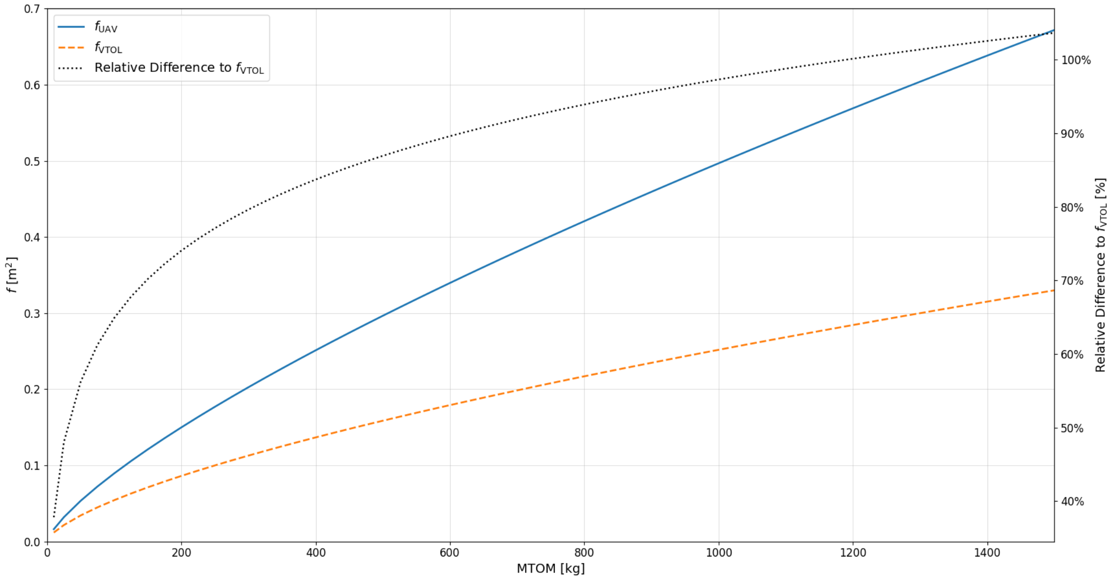

Figure 5.2: Equivalent flat-plate Areas with VTOL- and UAV-Methods

With a complete design process carried out in VTOL-AD for both methods under identical TLARs, the impact on the overall aircraft design was confirmed. The results for the tiltrotor configuration AT M 100P/500R, which is described in detail in Section 5.1.9, are summarised in Table 5.1. A substantially higher cruise energy consumption and an increased take-off mass are observed, comparable to the findings reported by Götten et al. [176].

Method	**Wing Area** $[m^2]$	**Wing Span** $[m]$	**Flat-plate Area** $[m^2]$	**MTOM** $[kg]$	**Cruise Power** $[kW]$
VTOL [180]	3.5	8.57	0.15	476.24	14.91
UAV [176]	4.05	9.23	0.32	551.33	25.95
Difference (rel. to UAV)	13.58%	7.15%	53.13%	13.62%	42.54%

Table 5.1: Comparison of Design Results for the AT M 100P/500R Configuration with different Parasite Drag Methods

5.1.3 Wing Mass

Another aspect based on assumptions outside of the typical design space of UAVs was identified in the wing-mass estimation. Up to now, this mass fraction in VTOL-AD has been determined according to the method by Roskam [181] as proposed by [180], which is based on data for crewed, powered fixed-wing aircraft. The Equation 4.1.3.1 gives the wing mass in lbs and therefore needs the $MTOM$ in lbs and the wing area S_{wing} in ft^2. Additionaly, the ultimate load factor N_Z and the aspect ratio AR are required for this approach.

$$m_{wing}[lbs] = 0.04674 \cdot (MTOM[lbs])^{0.347} \cdot (S_{wing}[ft^2])^{0.25} \cdot N_Z^{0.397} \cdot AR^{1.712} \quad (4.1.3.1)$$

An approach for the wing mass of uncrewed aircraft based on sailplane wing masses was proposed by Gundlach [175]. This formulation is given in Equation 4.1.3.2 following Gerard [182]. The wing mass m_{wing} is depended of the ultimate load factor N_Z, the $MTOM$, the aspect ratio AR, the wing area S_{wing}, the taper ratio λ and the relative profile thickness at the wing root $(t/c)_{root}$.

$$m_{wing} = 0.0038 \cdot (N_Z \cdot MTOM)^{1.06} \cdot AR^{0.38} \cdot S_{wing}^{0.25} \cdot (1 + \lambda)^{0.21} \cdot (t/c)_{root}^{-0.14} \quad (4.1.3.2)$$

With respect to MTOM, aspect ratio, materials, and construction methods, there is a strong similarity to UAV wings, although VTOL-UAV wings typically exhibit a lower aspect ratio. A stated limitation is that no wing sweep should be present, which is unproblematic for the UAVs investigated here that operate well below the transonic speed regime. Furthermore, this approach already includes control surfaces [175].

The relevance of this modification can be clearly seen in Table 5.2. All other methods and boundary conditions, such as the maximum aspect ratio, were kept constant for both calculations. Using the method proposed by Roskam [181], the wing mass increases to disproportionately high values. Although the UAV-based approach neglects the mass of the propulsion mounting structures, the resulting values are much more consistent with existing designs [175, 178].

Method	**Wing Area** $[m^2]$	**Wing Span** $[m]$	**Aspect Ratio** $[-]$	**MTOM** $[kg]$	**Wing Mass** $[kg]$
eVTOL [181]	14.21	17.28	21.0	1933.64	863.14
UAV [175]	4.05	9.23	21.0	551.33	128.88
Difference rel. to UAV	250.86%	87.22%	-	250.72%	569.72%

Table 5.2: Comparison of Design Results for the AT M 100P/500R Configuration with different Wing Mass Methods

5.1.4 Landing Gear Mass

The calculation of the landing-gear mass in VTOL-AD is based on the approach by Kadhiresan and Duffy [180], which applies the classical aircraft-design method by Roskam [181] and evaluates it for the number of wheels $n_{wheels} = 2$ [130]. The mass m_{lg} follows from Equation 4.1.4.1 as a function of the $MTOM$ and the number of wheels.

$$m_{lg}[lbs] = 40 \cdot (\frac{MTOM[lbs]}{1000})^{0.67} \cdot N_{wheels}^{0.54} \quad (4.1.4.1)$$

Since VTOL UAVs do not necessarily feature wheels, are subject to different landing-gear load cases, and no uniform landing-gear type could be identified among the current aircraft in Section 2.1.4, this mass fraction is not modelled explicitly for UAVs. Instead, it is assumed as an approximation that the landing gear is part of the fuselage mass and covered by the existing fuselage-mass estimation.

5.1.5 Powertrain Energy Density

Since the analysis of performance data from existing uncrewed aircraft in Section 2.1.4 indicates that a hybrid architecture with fossil fuel as the primary energy source is the most suitable option for offshore use cases, the drone concepts in this work are likewise equipped with a hybrid drivetrain and the corresponding mass fraction is estimated accordingly at the conceptual level. The existing VTOL-AD implementation already provides a basic method to model hybrid propulsion architectures. Following Bertram et al. [183], a serial hybrid-electric architecture was adopted in which all propellers are driven by electric motors and the gas-turbine shaft powers a generator only, with no mechanical connection to the propellers. The assumed power density refers specifically to a gas turbine, and the referenced passenger-carrying VTOL aircraft fall in the mass range of 880 kg to 1730 kg. As shown in Section 2.1.4, alternative engine types can be viable for UAVs and the overall weight, size and with that also the power demand can differ fastly.

To comply with this, a relationship was sought that is not dependent on the drive type and can be applied to the entire relevant power range. For this purpose, literature values for power densities of combustion engines and manufacturer data for engines in the relevant power range were compared. In the process, several engine classes were identified [175, 184]:

- Two-stroke engines (uncrewed aircraft),
- Four-stroke engines (uncrewed aircraft),
- Rotary/Wankel engines,
- Turboshaft engines,
- Ultralight aircraft engines,
- General-aviation aircraft engines.

Two- and four-stroke engines originate largely from model-aviation applications and are primarily suited to the lower power range [175]. For larger uncrewed aircraft with higher power demand, Wankel engines and engines from the crewed ultralight domain become attractive, as do turboshafts. This diversity is reflected in the corresponding specific-power trends. In Finger [184], the following relationships for engine masses m_{eng} as a function of shaft power P are provided:

Two-stroke engine ($2\,kW < P < 75\,kW$):

$$m_{\text{eng}} = 8.804 \cdot 10^{-7}\,P^4 - 1.577 \cdot 10^{-4}\,P^3 + 8.233 \cdot 10^{-3}\,P^2 + 0.504\,P \tag{4.1.5.1}$$

Four-stroke engine ($2\,kW < P < 118\,kW$):

$$m_{\text{eng}} = 8.733 \cdot 10^{-7}\,P^4 - 2.858 \cdot 10^{-4}\,P^3 + 2.363 \cdot 10^{-2}\,P^2 + 0.46\,P \tag{4.1.5.2}$$

Rotary engine ($23\ kW < P < 88\ kW$):

$$m_{\text{eng}} = 9.331 \cdot 10^{-4}\, P^2 + 0.625\, P \tag{4.1.5.3}$$

It must be noted that each curve is only valid within a specific power range and reflects the state of technology as of 2016. Since this work explicitly examines the intermediate regime between existing smaller UAVs and larger, crewed VTOL aircraft, simple extrapolation beyond the published validity ranges yields unrealistic values. Moreover, technological progress can reasonably be assumed in the meantime. For these reasons, the cited relationships cannot be applied here in a direct manner.

Further power-density figures and ranges were compiled from literature for UAVs and hybrid-electric powertrains and are summarised in Table 5.3.

Reference	**Power Density** $[kW/kg]$	**Scope**
Gas Turbine (Bertram et al. [183])	8.2	
Turboshaft (Gundlach [175])	min: 4.26 max: 9.0	
Ultralight Aircraft Engine (Gundlach [175])	min: 0.90 max: 3.44	$15\ kW/kg \leq P \leq 90\ kW/kg$
General Aviation Engine (Gundlach [175])	min: 0.79 max: 0.84	$67\ kW/kg \leq P \leq 224\ kW/kg$
Internal Combustion Engine (Cakin et al. [185])	min: 0.25 max: 3.0	

Table 5.3: Power-density Figures and Ranges for UAV and hybrid-electric Powertrains

Plotting the literature values, relations, and manufacturer data listed in Appendix B does not reveal a clear overarching trend, as illustrated in Figure 5.3. In the figure, the various reciprocating combustion engines are grouped under Internal Combustion Engines (ICE). In addition, several data points represent propulsion units that include an integrated generator, although this generator mass is not yet accounted for in the engine mass m_{eng}. The pronounced heterogeneity across engines becomes evident, which reflects not only different operating principles but also inconsistencies such as dry-mass specifications and the inclusion or omission of starters and accessories.

Given this variability, a simplified conceptual approach is adopted for the present work. The combustion engine power density is fixed to 2 kW/kg over the entire range of output power and engine types. Between 50 and 150 kW this assumption tends to underestimate engine mass, above that range, which represents turbojet engines, it tends to overestimate it. The approach is nevertheless considered a suitable starting point for initial investigations. For concrete aircraft designs, specific candidate engines should be preselected, which is feasible within the formulation used here. A more detailed assessment based on a larger dataset, especially for medium to higher power ranges, would be beneficial nonetheless.

For the generator, following Bertram et al. [183], a power density of 4 kW/kg is assumed to determine the generator mass m_{gen} as a function of power. The same applies to the power-management mass m_{pm}, where the proposed value of 5 kW/kg is used. The mass of the

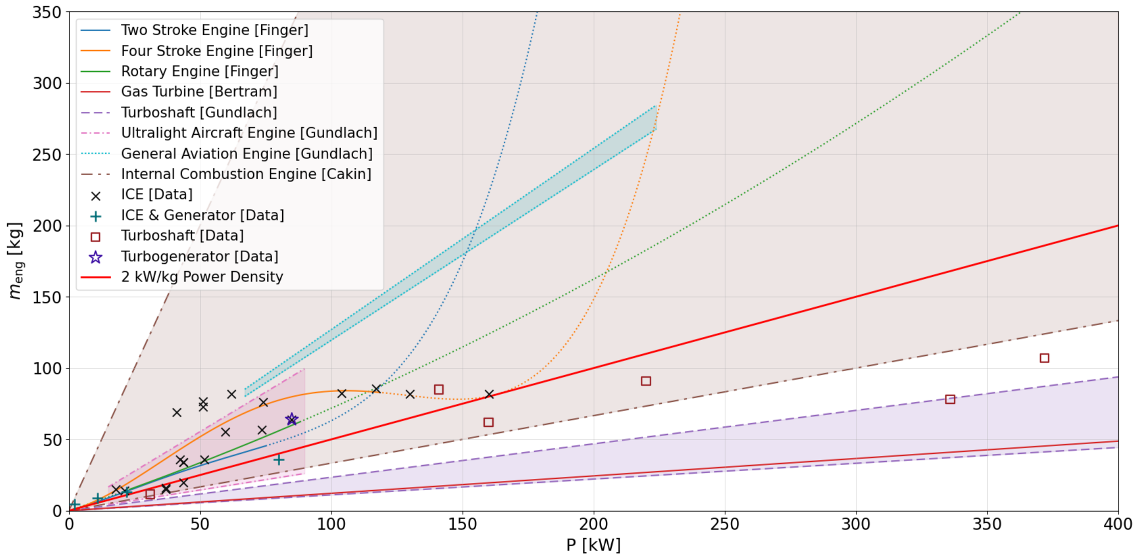

Figure 5.3: Engine Weight and Power Data according to Literature and Manufacturer Specifications

electric motors is likewise computed with a power density of 4 kW/kg as suggested. For UAVs, gearboxes between the combustion engines and generatores are not necessarily needed and therefore not included in the current conceptual design process [177].

A different approach was chosen to estimate the battery mass. As a first approximation, the battery is assumed to act only as a buffer to accommodate power fluctuations, since the combustion engine and the generator are sized for the maximum power. With a specific energy of 250 Wh/kg, its mass is set to 10% of the fossil-fuel mass and limited to a maximum of 10 kg.

5.1.6 Powertrain Efficiency

Since a new approach was taken for the powertrain design, the assumptions regarding propulsion efficiency must also be re-evaluated for the different size and power ranges relevant to UAVs. According to Bertram et al. [183], it consists of the components and component efficiencies listed in Table 5.4, which are already implemented in VTOL-AD.

Component	**Efficiency** $[-]$
Gas Turbine	0.50
Gear Box	0.98
Generator	0.95
Power Management	0.98
Electric Motor	0.95
Powertrain	0.43

Table 5.4: Component and Overall Powertrain Efficiencies according to Bertram et al. [183]

As discussed in Section 5.1.5, the gearbox can be omitted in this context, and the gas turbine data from Bertram et al. [183] is not applicable across the entire UAV design range. The combustion-engine data points in the relevant power range listed in Appendix B were therefore evaluated with respect to efficiency, the result is shown in Figure 5.4. Using the given specific fuel consumptions or fuel flow rates together with the fuel properties, they were converted such that the resulting Figure of Merit (FoM) indicates how much mechanical energy can be generated from the fuel energy. However, the data must be interpreted with care, since the underlying sources are not ideally comparable and rarely provide values that are valid across the full operating range of the engine. Especially for turbines, the specific fuel consumption typically increases at partial load [128]. The compiled data should therefore be regarded as an optimistic approximation.

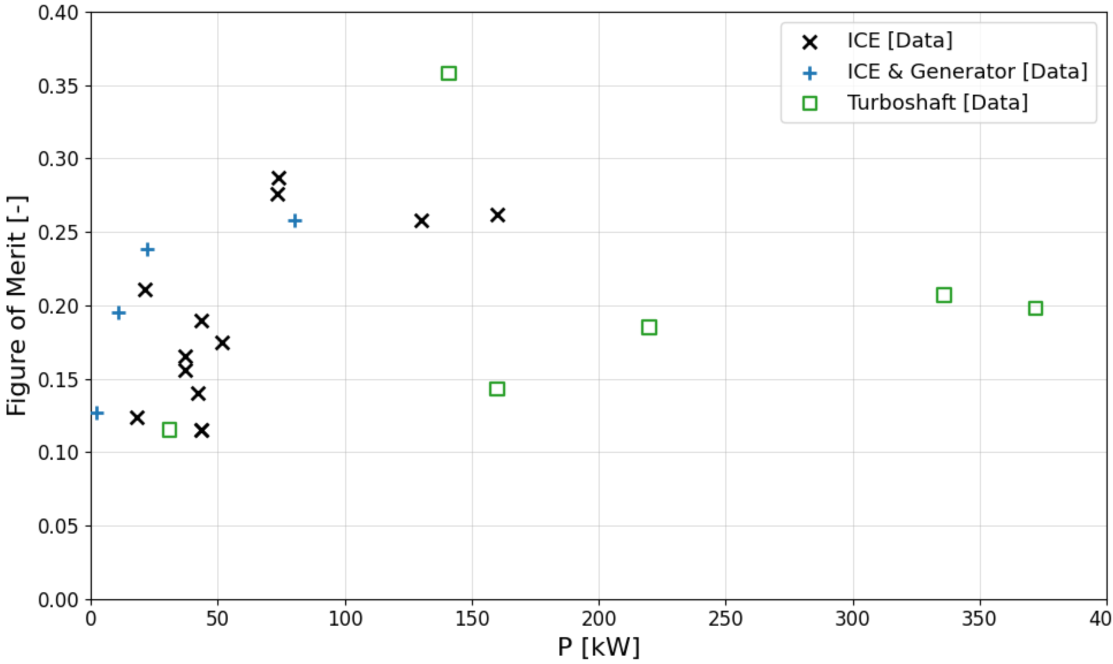

Figure 5.4: Combustion Engine Figures of Merit

Comparable values can be found in literature, as listed in Table 5.5.

Reference	**Efficiency** $[-]$	**Scope**
Gas Turbine (Bertram et al. [183])	0.5	
Internal Combustion Engine (Zong et al. [177])	min: 0.2 max: 0.4	
Ultralight Aircraft Engine (Gundlach [175])	min: 0.16 max: 0.21	$15\ kW/kg \leq P \leq 90\ kW/kg$
General Aviation Engine (Gundlach [175])	min: 0.21 max: 0.31	$67\ kW/kg \leq P \leq 224\ kW/kg$

Table 5.5: Combustion Engine Efficiency Figures and Ranges for UAV and hybrid-electric Powertrains

For this work, a FoM of 0.23 is chosen for the combustion engines of the design studies further discussed in Section 5.1.9. Together with the remaining efficiency values retained from Bertram et al. [183], this results in a powertrain efficiency of 0.2.

5.1.7 Influence of Wind Speed

Offshore drone operations are particularly sensitive to the prevailing environmental conditions at sea. The helicopter model previously developed for the DLR SoSID-Toolkit evaluates performance curves across the full flight-speed envelope of a helicopter [128]. This enables a comparatively simple consideration of wind effects as described in section 4.4.1, since the ground speed is held constant while the true airspeed is adjusted accordingly.

The same approach shall now be applied to the VTOL-UAVs. Although this method reflects operational reality only to a limited extent, it requires no fundamental modifications to the existing SoSID-Toolkit and is assumed to be sufficiently accurate for non-extreme weather conditions. At present, VTOL-AD provides performance points for each flight phase and several mass levels, but only for a single fixed airspeed. The cruise-flight power evaluation in VTOL-AD is based on the calculation of the total drag coefficient C_D as a sum of the parasite or zero-lift drag coefficient $C_{D,0}$ and the induced drag coefficient $C_{D,i}$ as shown in Equation (4.1.7.1) [130].

$$C_D = C_{D,0} + C_{D,i} \tag{4.1.7.1}$$

The cruise power P is then calcutaled with the following equation and the air density ρ, the flight speed v_{TAS} and the reference area S:

$$P = (C_{D,0} + C_{D,i}) \frac{\rho \cdot v_{TAS}^3 \cdot S}{2} \tag{4.1.7.2}$$

For climb and descent, VTOL-AD applies the following relation with the weight force W and the vertical speed v_c [130]:

$$P = W \cdot v_c + (C_{D,0} + C_{D,i}) \frac{\rho \cdot v_{TAS}^3 \cdot S}{2} \tag{4.1.7.3}$$

These relations are now evaluated for additional airspeeds and stored for each vehicle. Based on the resulting four power values per mass, the SoSID propulsion module constructs a third-order polynomial curve.

All vehicles use the same set of speed offsets: starting from the nominal cruise speed, the first point is evaluated at minus 10 m/s, the next at cruise speed plus 10 m/s, and the last additional point at plus 15 m/s. The resulting power curves for three selected mass levels, together with the discrete VTOL-AD data points, are shown in Figure 5.5 for one of the UAV concepts used in the simulations.

5.1.8 Validation

The validation of the VTOL-AD adaptations for UAVs was carried out using data from commercially available aircraft that are relevant for the use case, complemented by a suitable research configuration. It must be kept in mind that this represents only a small number of data points and that several parameters were not available as explicit numerical values but had to be inferred from published dimensions, images, and drawings. Furthermore, it

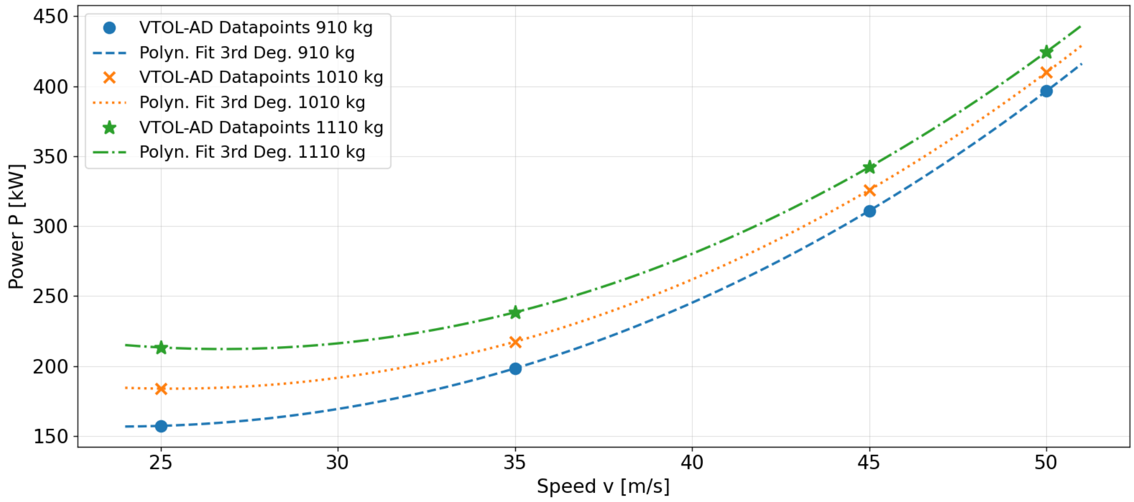

Figure 5.5: Power Curves for multiple Weights and VTOL-AD Datapoints

should be emphasised that, for example, the published range figures of the commercial aircraft do not include additional information on the flight profile, such as cruise altitude, environmental conditions, or reserve range. As a consequence, numerous quantities had to be estimated; these are marked accordingly in Table 5.6.

Manufacturer **Model** **Configuration**	**Dufour** **Aero**-200 Tiltwing	**Skyways** **V3 B2** Lift + Cruise	
MTOM	208	163.3	[kg]
Wing Span	6.12	7.92	[m]
Useful Load	38	45	[kg]
Cruise Speed	35	28	[m/s]
Fuselage Length	2.9*	3.5*	[m]
Fuselage Diameter	0.6*	0.9*	[m]
Wing Aspect Ratio	8*	22*	[-]
Horizontal Stab. Aspect Ratio	4.5*	8*	[-]
Vertical Stab. Aspect Ratio	2*	5*	[-]
Battery Mass	10*	10*	[kg]
Max. Disk Loading	500*	260*	[N/m^2]
Stall Speed	20	27	[m/s]
Powertrain Efficiency	0.1*	0.28*	[-]
$C_{L,\mathrm{max}}$	1.8*	1.7*	[-]

Table 5.6: Key parameters of the Dufour Aero-200 and Skyways V3 B2, entries marked with * are estimated from aircraft images and engineering judgement

With these values, a design process in VTOL-AD was carried out and the resulting designs were evaluated for the payload and fuel combinations specified by the manufacturers. It must be noted that the estimated values for the powertrain efficiency and the maximum lift coefficient were adjusted iteratively with the design results in order to obtain the best possible match. For the Dufour Aero-200, the resulting powertrain efficiency is comparatively low as a result of this aircraft beeing a tiltwing configuration with a serial hybrid powertrain. The more favourable value for the Skyways V3 B2 follows from its Lift+Cruise concept, where the combustion engine directly drives the cruise propeller and no additional generator, power electronics, cables or electric motors reduce the efficiency in cruise.

It is necessary to highlight a particular characteristic of VTOL-AD at this point. Due to the original tool requirements, which were tailored to battery-electric eVTOL aircraft, the performance calculation does not subtract the mass of the fuel consumed during the flight. As a consequence, the ranges of the aircraft computed with VTOL-AD are conservative and would increase if fuel burn were represented in a more realistic manner, as is typically done by the UAV manufacturers and as implemented in the SoSID-Toolkit. Since the fuel masses of the validated UAVs are comparatively small relative to the $MTOM$, this deviation is accepted. The powertrain efficiency of the commercial UAVs considered here can therefore be expected to be higher in reality than the value obtained in this analysis.

The values were therefore adjusted on the basis of the data discussed in Section 5.1.6 and design studies, assuming a cruise altitude of $200\ m$ at ISA sea-level conditions, a vertical climb and descent rate of 1 m/s up to an altitude of 25 m, and an additional climb segment with a vertical rate of 3.6 m/s until the cruise altitude is reached. This means as well that the resulting aircraft parameter values cannot be transferred unchanged to other contexts. The specified maximum lift coefficients are likewise intended for use only within the VTOL-AD tool.

For the Skyways V3 B2, a typical value for a wing without flaps was selected, which should be close to the actual value due to the Lift+Cruise configuration. This parameter is relevant for the required wing area, which depends on the coefficient and the minimum flight speed. In the case of the Skyways V3 B2, this minimum speed can be comparatively high, since in this configuration the transition phase can be supported by the thrust of the vertical propellers until the cruise speed is reached.

This is not strictly valid for tiltwing configurations such as the Dufour Aero-200. Here the minimum flight speed is much more critical, because the vertical thrust contribution decreases as the transition progresses. The Dufour Aero-200 is equipped with flaps, so its real maximum lift coefficient is very likely to be significantly higher than the value assumed here, and the wing areas directly blown by the rotors should further increase the effective lift. For this reason, the coefficient used here is only valid in the context of these VTOL-AD calculations and does not reflect the actual maximum lift coefficient of the Dufour Aero-200.

The results for the Dufour Aero-200 are listed in Table 5.7. The overall good agreement is reflected in the small deviations between the manufacturer data and the VTOL-AD result, with the range at the highest payload showing the largest relative deviation, while no proportional relationship between the deviation and the range or payload can be identified from the remaining data points.

	MTOM [kg]	Wing Span [m]	Range at 20 kg Payload [km]	Range at 15 kg Payload [km]	Range at 10 kg Payload [km]	Range at 5 kg Payload [km]
Manufacturer	208.0	6.12	200.0	300.0	400.00	500.0
VTOL-AD	218.8	6.27	225.7	297.5	416.96	497.7
Difference rel. to Man. data	5.20%	2.45%	12.86%	-0.83%	4.24%	-0.46%

Table 5.7: Comparison of manufacturer and VTOL-AD data for the Dufour Aero-200

The same conclusion can be drawn from the results for the Skyways V3 B3 UAV. Here as well, the deviations remain within an acceptable range, as indicated by the values in Table 5.8. For both UAVs, the MTOM was slightly overestimated by slightly over 5%. Since the results only reflect two design points, no correction factor was introduced. Because of the small deviations regarding the $MTOM$ and range, the changes to VTOL-AD are regarded as justified and valid, especially those regarding the propulsion system.

	MTOM [kg]	Wing Span [m]	Range at 34 kg Payload [km]	Range at 10 kg Payload [km]
Manufacturer	163.3	7.92	1852	555.6
VTOL-AD	172.33	6.84	1804	548.22
Difference rel. to Man. data	5.53%	-13.64%	-2.59%	-1.33

Table 5.8: Comparison of manufacturer and VTOL-AD data for the Skyways V3 B2

Since no detailed mass data are available for these aircraft with respect to individual components such as the propulsion system, wings, tail surfaces, or fuselage, the results can only be compared in terms of total mass, range, and wing dimensions. For this purpose, design data of a Lift+Cruise reference configuration were used, for which these quantities were determined both for a baseline and for three optimised variants obtained with different conceptual-design tools, and which lies in the relevant payload and range regime, although it is equipped with a purely battery-electric powertrain only [186]. Here as well, not all input data were directly available and had to be estimated either from drawings or from other published information; these values are marked accordingly in Table 5.9 that lists the aircraft parameters. For these aircraft, that is, for the three designs of the same vehicle, the mission profile is specified so that its parameters could be transferred to VTOL-AD. In this case, the cruise segment is defined to cover a distance of 96.6 km at an altitude of 300 m and a cruise speed of 49.2 m/s. Purely vertical climb and descent are to be flown up to an altitude of 12.2 m with a rate of 2.54 m/s, while the subsequent climb and descent phases use the same ROC with varying horizontal speeds. This variation, as well as the loiter segment, is neglected in the VTOL-AD calculation for simplicity, and the design target cruise range is instead set to 120 km. Furthermore, the battery mass is fixed to 313 kg based on the results for the baseline configuration, and the stated specific energy of 300 Wh/kg is used in order to keep variations caused by the solver strategy as small as possible. That also means that the range is fixed by this value together with the efficiency of the propulsion. The efficiency was not given for the baseline configuration but as a result of the three design tools and was therefore derived from those results and set to 0.82.

Because of the Lift+Cruise concept the propeller and motor mass estimations, which were developed for tiltrotor concepts, were modified so that an additional cruise propeller and motor was included. Based on preliminary results regarding the cruise power and speed and data from commercially available propellers, the cruise propeller weight was estimated to 5 kg [187]. The cruise motor mass was calculated with the same method and corresponding specific power as the vertical lift propellers, but for the cruise flight power.

The resulting VTOL-AD design yields a mission range of 129 km for the specified (sim-

	eVTOL UAV Baseline	
MTOM	1154	[kg]
Wing Span	10.97	[m]
Payload	181.1	[kg]
Specific Energy	300.0	[Wh/kg]
Battery Mass	313.0*	[kg]
Cruise Speed	49.2	[m/s]
Fuselage Length	4.3*	[m]
Fuselage Diameter	1.25*	[m]
Wing Aspect Ratio	12.5*	[-]
Horizontal Stab. Aspect Ratio	5*	[-]
Vertical Stab. Aspect Ratio	3*	[-]
Max. Disk Loading	810*	[N/m^2]
Stall Speed	30*	[m/s]
Powertrain Efficiency	0.82*	[-]
$C_{L,\text{max}}$	2.0*	[-]

Table 5.9: Key parameters of the reseach eVTOL UAV [186], entries marked with * are estimated from aircraft images and engineering judgement.

plified) mission profile. This deviation is considered acceptable and arises from the not exactly identical mission profile and indicates small discrepancies in the performance calculation. A component mass breakdown and the mass fractions resulting from the three design tools used by Vegh et al. [186] and VTOL-AD is given in Table 5.10 as well as the relative difference to the VTOL-AD averaged over the three results from Vegh et al. [186].

The largest deviation can be found at the “Other Systems“ mass component. In VTOL-AD, a fixed mass of 10 kg is assumed here and should reflect mainly the avionic systems and sensors onboard. Actuators, which could explain the large deviation, are considered to be included in the VTOL-AD wing mass method for UAVs. This could also explain, why the VTOL-AD estimation of the UAVs wing mass is significantly higher. In total numbers, the average difference between the VTOL-AD results and the results obtained by Vegh et al. [186] regarding the “Other Systems“ equals 113 kg. The wing mass from VTOL-AD is on average 140 kg heavier. It is not known, which components are exactly considered for the “Other Systems“ by Vegh et al. [186], however this seems like a probable cause for the deviations. The propeller masses also differ largely. VTOL-AD outputs a mass per propeller of 0.6 kg for the vertical lift propellers, while for the cruise propeller, an estimated mass of 5 kg was inserted in the calculations. For two bladed VTOL-UAV propellers, this estimation is realistic, as comparisons with commercially available propellers [188].

In general, the results for the mission range, the $MTOM$ and the empty mass fraction and the L/D ratio during cruise of the aircraft are congruent between all four methods. The methods presented used by Vegh et al. [186] also do offer some possible deviations from a real UAV. The mass estimation of the NDARC and HYDRA tools is based mainly on parametric methods including data from manned fixed-wing and rotary wing aircraft. The CREATION-tool however uses physics based approaches for the wing, fuselage and propeller mass and delivers a close match to the VTOL-AD results as the other two tools. Based on this and the good consistency of results regarding the flight performance and $MTOM$ of the research configuration as well as for the two investigated commercial cargo VTOL-UAVs, the adjusted VTOL-AD is regarded as validated enough to perform the con-

	Unit	NDARC	CREATION	HYDRA	VTOL-AD	Avg. Diff. rel. to VTOL-AD
Other Systems	[kg]	128.1	126.2	114.3	10	1128.7%
Landing Gear	[kg]	70.2	42.6	53.3	0	-
Propeller	[kg]	61	44.5	48.9	12.6	308.5%
Battery	[kg]	321.8	319.9	298.2	313	0.0%
Motor System	[kg]	160.6	174.7	148.6	120.8	33.5%
Fuselage	[kg]	89	91.4	89.8	79.0	13.2%
Wings + Booms + Empennage	[kg]	134.2	236.5	129.4	321.0	-48.1%
Payload	[kg]	181	181	181	181	0.0%
MTOM	[kg]	1145.9	1216.8	1063.5	1037.4	10.1%
Empty Mass Fraction	[-]	0.84	0.85	0.83	0.83	1.2%
Airframe Mass Fraction	[-]	0.26	0.3	0.26	0.39	-29.9%
Propulsion Mass Fraction	[-]	0.59	0.55	0.57	0.44	29.6%
L/D_{cruise}	[-]	6.32	6.64	6.09	6.53	-2.8%

Table 5.10: Mass breakdown and mass fractions for different conceptual design tools

ceptual design of cargo carrying VTOL UAVs with battery-electric and hybrid propulsion systems.

5.1.9 UAV Designs

To assess the applicability of UAVs for the offshore scenario, several UAV designs were generated with the adapted VTOL-AD tool. The validation in Section 5.1.8 showed that the adapted VTOL-AD is suitable for the conceptual design of tiltrotor, tiltwing, and Lift + Cruise UAVs. In line with the findings from Section 2.1.4 and due to the range requirements arising from the offshore use case, a hybrid drivetrain was selected. With regard to the configuration, a tiltrotor aircraft was chosen, and a serial hybrid drivetrain was defined accordingly. Within this frame, several distinct UAV models were derived.

These models differ primarily in three payloads, which directly determine the fuselage dimensions, and in three design ranges for each payload. The cruise speed was kept constant for all designs. To distinguish these designs from commercial UAVs and other research configurations, they are referred to in the following as “Arctic Tern”, abbreviated AT, and the fuselage sizes are categorised as small (S), medium (M), and large (L). The corresponding design range R and payload P are further specified with their respective values in kilograms and kilometres. Here, too, it must be taken into account that VTOL-AD does not model the reduction of fuel mass during flight, so the resulting values must be regarded as conservative estimates. An overview of these data is provided in Table 5.11.

Design Name	**Payload** $[kg]$	**Mission Range** $[km]$	**Fuselage Length** $[m]$	**Fuselage Diameter** $[m]$
AT S 20P/250R	20	250	3.05	0.65
AT S 20P/500R	20	500	3.05	0.65
AT S 20P/750R	20	750	3.05	0.65
AT M 100P/250R	100	250	4.90	1.30
AT M 100P/500R	100	500	4.90	1.30
AT M 100P/750R	100	750	4.90	1.30
AT L 200P/250R	200	250	6.10	1.30
AT L 200P/500R	200	500	6.10	1.30
AT L 200P/750R	200	750	6.10	1.30

Table 5.11: Arctic Tern VTOL-UAV Variants and Fuselage Dimensions

For the defined fuselage dimensions which are needed for the VTOL-AD inputs, each payload category is assigned a single fuselage size, since only one payload mass with a corresponding volume is assumed in each case. The S fuselage size and the 20 kg payload are based on current commercial UAVs and are intended to cover the delivery of tools, spare parts, and other equipment that are required spontaneously during maintenance in the OWF. The M and L fuselage sizes with 100 kg and 200 kg are intended to transport one or several equipment bags so that only personnel need to transfer from the CTV to the turbines and the time spent on moving equipment can be minimised.

To determine the fuselage sizes, assumptions were made regarding the required cargo volume, and it was checked whether a combustion engine in the relevant power class can be accommodated as well as the fuel tank.

For the AT S fuselage, a propulsion system with a maximum power of 50 kW was selected based on design studies, corresponding to the configuration with the largest range, and thus also the highest $MTOM$ and the highest power requirement. A Hirth 3503 two-stroke engine was chosen for this purpose [189]. In addition, it was verified that the required fuel volume for the selected configuration can be integrated. As shown in Figure 5.6, the components fit within the fuselage cross-section and sufficient space remains for additional systems and the primary structure.

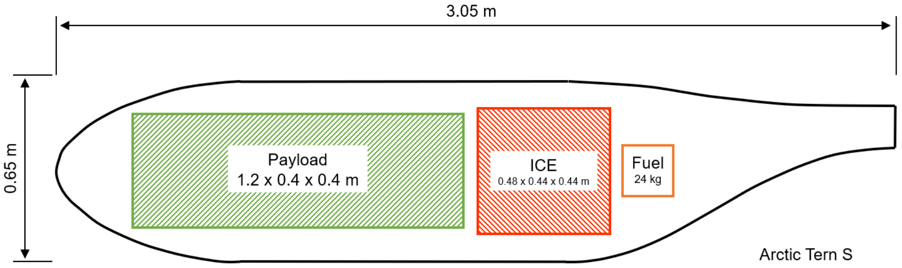

Figure 5.6: Drawing of the AT S Fuselage Cross Section

For the AT M fuselage, the same procedure was followed. Due to the higher power demand, a Rolls-Royce M250 C20 turboshaft engine was selected instead of an internal combustion engine [190]. In this case as well, the component dimensions are consistent, and it can be assumed that sufficient space is available for systems and structure.

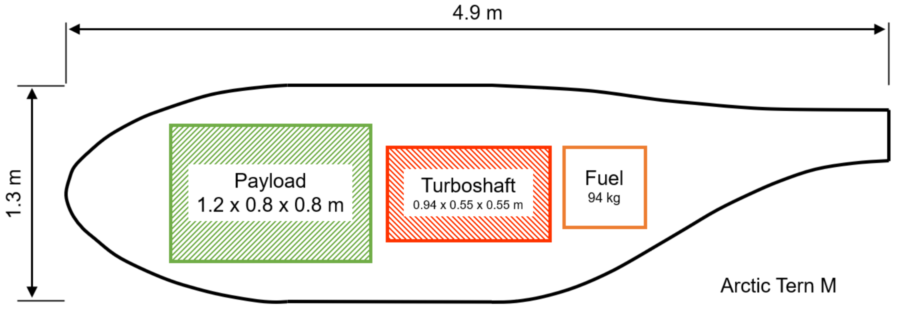

Figure 5.7: Drawing of the AT M Fuselage Cross Section

In contrast to the AT M fuselage, the payload section of the L version is twice as long. The fuselage was therefore extended accordingly, without changing its diameter. It is assumed that, for an economically and logistically efficient implementation of this use case, standardised containers are employed. The L configuration is therefore designed to carry two containers of identical weight and size, while the M configuration is intended to transport one such container. Here, a turboshaft engine is used as well, in this case a Rolls-Royce RR300 [191].

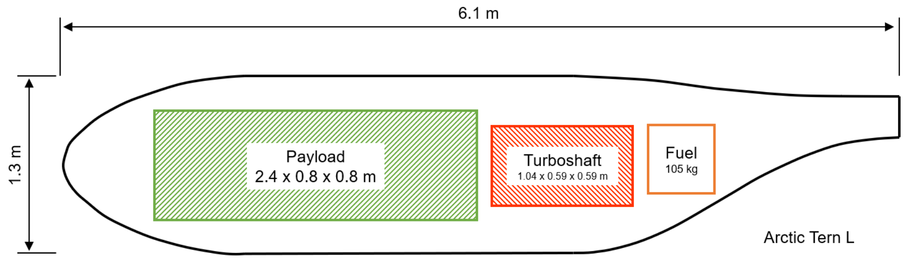

Figure 5.8: Drawing of the AT L Fuselage Cross Section

The design ranges represent a simple flight mission at a cruise altitude of 200 m, whose parameters are summarised in Table 5.12. An explicit modelling of an offshore mission with a hover flight phase above a turbine was omitted so that these settings remain as comparable as possible to the manufacturer data of other aircraft collected in Section 2.1.4. The ranges partly exceed the distances of the OWFs from the coast shown in Section 4.5.2 significantly, which is intended to allow several turbines to be served within a single flight for suitable payload capacities, while the hover segments are comparatively energy intensive.

In addition to the fuselage data, the mission definition, and the payload, further input parameters especially regarding the rotors are required. These are listed in Table 5.13.

With these inputs, the aircraft summarised in Table 5.14 were generated, including the corresponding aircraft input files for the DLR SoSID-Toolkit which can be found under Appendix C. Minor deviations can be observed by comparing the input design ranges to the ranges calcutaled by VTOL-AD for the corresponding aircraft, these deviations emerged during the VTOL-AD sizing process. The resulting glide ratios of the AT designs are well

Parameter	Value	Unit
Total Taxi/Start Time	60	[s]
Vertical Takeoff Speed	1	[m/s]
Vertical Landing Speed	1	[m/s]
Vertical Climb Altitude	15.3	[m]
Vertical Cruise Climb Speed	3.6	[m/s]
Vertical Cruise Descent Speed	3.6	[m/s]
Cruise Speed	35	[m/s]
Cruise Altitude	200	[m]

Table 5.12: Mission Profile Parameters

	eVTOL UAV Baseline	
Wing Aspect Ratio	21.0	[-]
Horizontal Stab. Aspect Ratio	8	[-]
Vertical Stab. Aspect Ratio	5	[-]
Stall Speed	33.0	[m/s]
$C_{L,\text{max}}$	2.0	[-]
N_{Ult}	5.7	[-]
Onboard Systems Mass	10.0	[kg]
n_{rotors}	8	[-]
$n_{rotorblades}$	2	[-]
Rotor Solidity	0.16	[-]
Rotor rel. Thickness	0.12	[-]
Rotor ind. Power Factor	1.7	[-]
Rotor Parasite Drag	0.01	[-]
Rotor max. Tip Mach No.	0.6	[-]
Rotor max. $C_{L,mean}$	0.7	[-]
Max. Disk Loading	500	[N/m^2]
Battery Specific Energy	250	[Wh/kg]
Powertrain Efficiency	0.2	[-]
Propeller Efficiency	0.87	[-]

Table 5.13: Design Input Parameters of the Arctic Tern VTOL UAV Configurations

comparable with the values computed for the research configurations by Vegh et al. [186] and the NASA UAM reference vehicles with comperable configurations [192]. While the AT designs range between $5.7 \leq L/D \leq 8.8$, the battery-electric cargo UAV research configurations resulted in $6.09 \leq L/D \leq 6.64$ depending on the design tool, and the NASA reference tiltwing and Lift+Cruise aircraft $7.9 \leq L/D \leq 8.6$.

Comparing the glide ratio and disk loading with the design space of eVTOL aircraft of different configurations according to McDonald and German [193] as in Figure 5.9 yields a plausible picture, although it is clear that this is not a battery-powered, crewed aircraft and the design space therefore not exactly identical.

The disk loading of all AT designs is an input sizing parameter and was kept constant as given in Table 5.13. Compared with the eVTOL design space and the research configurations from Vegh et al. [186] ranging between a disk loading of 55 to 85 kg/m^2, the AT

	Wing Span $[m]$	**MTOM** $[kg]$	**Empty Mass** $[kg]$	**Rotor Dia.** $[m]$	**Inst. Power** $[kW]$	L/D $[-]$	**Range** $[km]$
AT S 20P/250R	4.17	112.5	86.2	0.59	29.6	5.7	242
AT S 20P/500R	4.57	135.5	100.8	0.65	35.6	5.9	495
AT S 20P/750R	5.09	167.9	121.5	0.72	44.1	6.1	748
AT M 100P/250R	8.78	499.6	376.5	1.25	131.3	7.2	247
AT M 100P/500R	9.77	618.8	464.4	1.39	162.7	7.4	499
AT M 100P/750R	11.22	815.3	612.4	1.60	214.3	7.7	750
AT L 200P/250R	13.06	1105.5	859.1	1.86	290.6	8.0	248
AT L 200P/500R	15.08	1473.0	1157.2	2.14	387.3	8.3	499
AT L 200P/750R	19.28	2408.4	1955.7	2.74	633.2	8.8	748

Table 5.14: Arctic Tern UAV Results

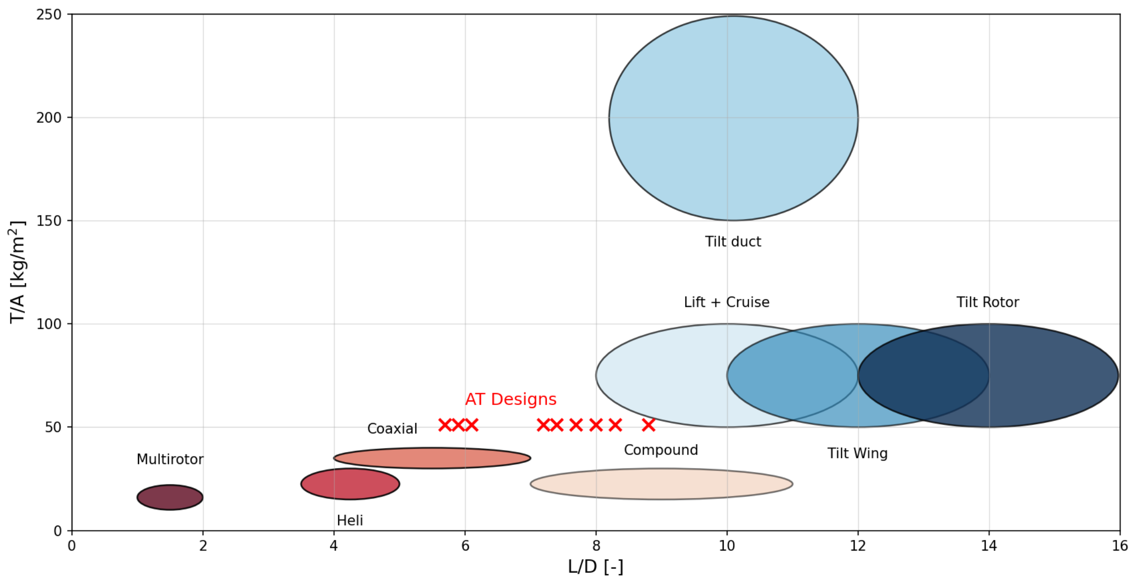

Figure 5.9: Location of the Arctic Tern Designs in the eVTOL Design Space based on McDonald and German [193]

design disk loading of 51 kg/m^2 is at the lower end of both spectrums.

The efficiency in hover can be expressed with the power loading T/P, which is a function of the disk loading [36]. Lower disk loadings lead to higher power loadings and therefore higher hover efficiencies. This relationship explains the suitability of helicopters for long hover flight times, since their rotor area is comparatively larger than for other VTOL configurations. For classic crewed VTOL aircraft, a diagram of the hover efficiency over the disk loading was established by Maisel, Giulianetti, and Dugan [194] with corresponding design spaces as displayed in Figure 5.10. All Arctic Tern designs have the same hover efficiency and the same disk loading, resulting in a single point in the diagram.

It can be observed, that the Arctic Tern designs fall within the overall band of possible aircraft designs, although with a slightly higher hover efficiency than the crewed tilt rotor aircraft. With regard to the deviations to the assumptions embedded in the diagram such

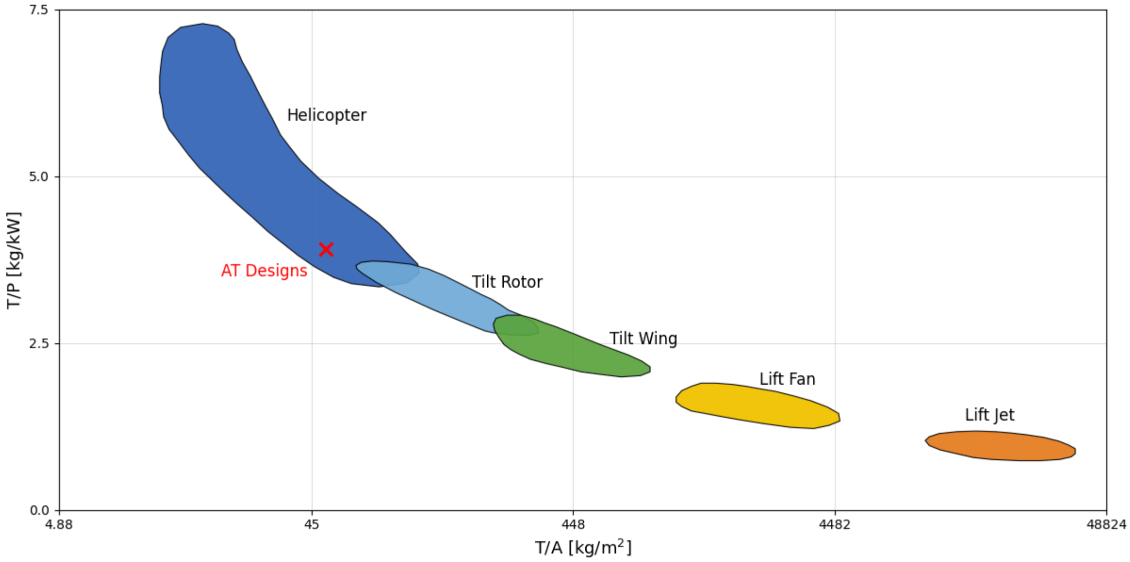

Figure 5.10: Comparison of the Hover Efficiency against Disk Loading for VTOL Configurations based on Maisel, Giulianetti, and Dugan [194] and the Arctic Tern Designs

as the crew onboard, this is seen as plausible.

Based on the resulting geometric parameters, the resulting aircraft configurations are illustrated in Figure 5.11. It must be noted, that the distance between the stabilisers and the wing was generally enlarged so that the empennage is placed outside the vertical propulsors downwash and at the end of the fuselage without changing the stabilisers parameters. With regard to this modification, the vertical and horizontal stabiliser area could be reduced.

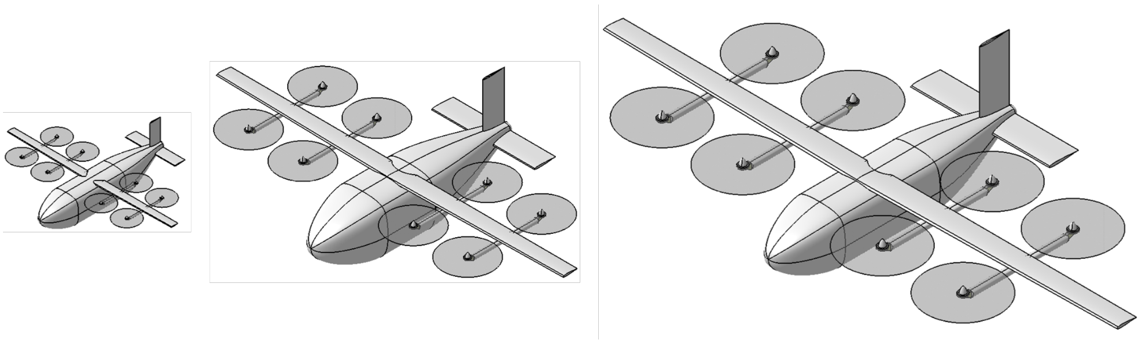

Figure 5.11: Three-dimensional Graphical Representation of the Arctic Tern S, M, and L Designs for 250 km Design Range

In the top view, the effects of the different range requirements for each fuselage and payload size become clearly visible, as shown in Figure 5.12.

Figure 5.13 shows the hover and cruise flight configurations for the AT S 20P/250R design. Due to the tiltrotor concept, only the propulsion angle changes.

The mass fractions within a given design and relative to the other Arctic Tern configurations can be compared in Figure 5.14. The increase between the AT L 200P/500R and AT L 200P/750R designs is significantly larger than the steps between the other size or range

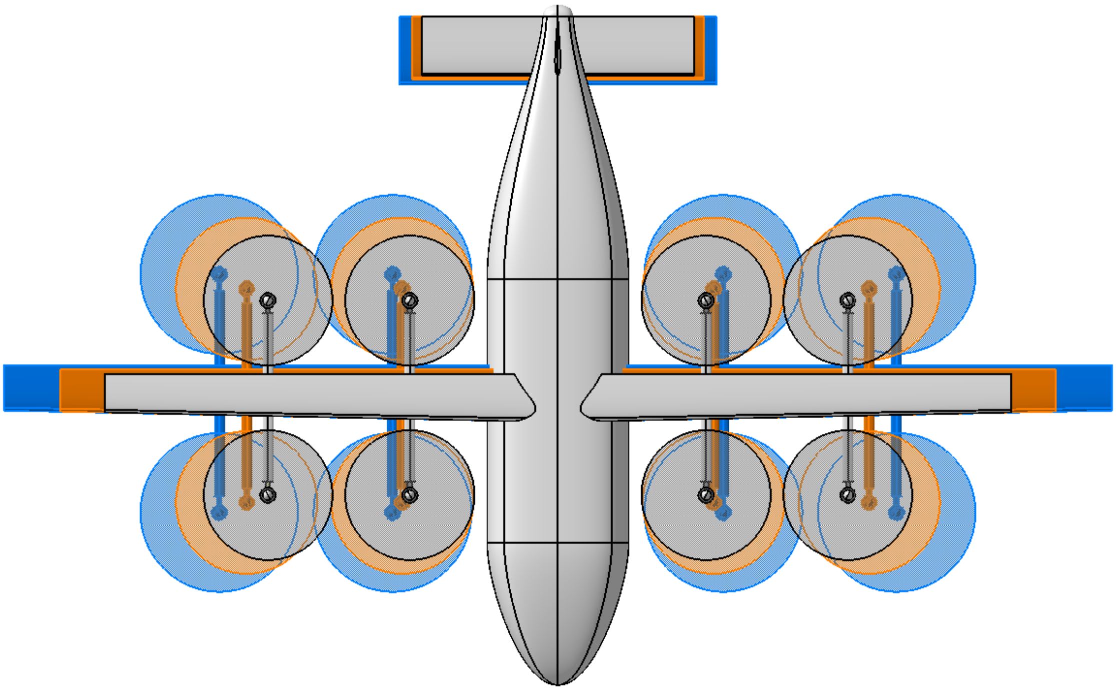

Figure 5.12: Comparison of the Top View of the Arctic Tern S UAV Designs for Design Ranges of 250 km (White), 500 km (Orange) and 750 km (Blue)

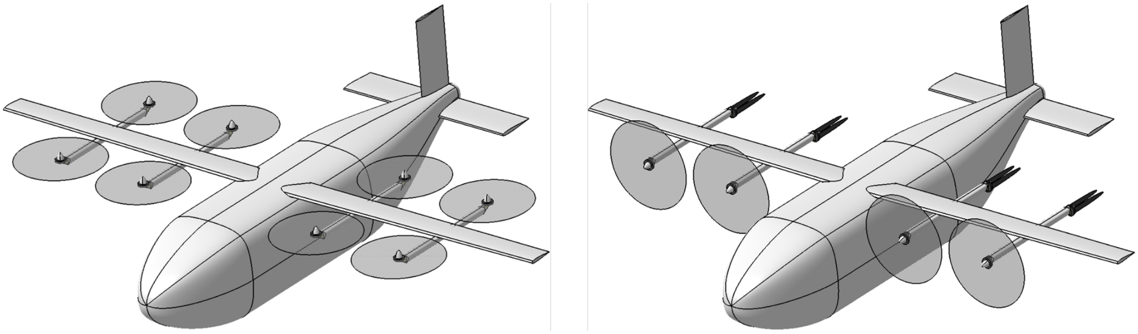

Figure 5.13: Arctic Tern S 20P/250R UAV in Hover and Cruise Configuration

increments and overall an exponential growth of the total mass can be assumed. In terms of total mass, the AT L 200P/750R design also lies outside the typical UAV range, so that a detailed investigation of the sizing relations specifically for uncrewed cargo aircraft with VTOL capabilities in this size region would be highly valuable and could lead to refined results when using the VTOL-AD tool. The comparatively small fuel-mass fraction relative to the total weight can likewise be observed, which means that the simplification in VTOL-AD to neglect fuel burn in the mass calculation during flight is considered acceptable within the scope of conceptual design.

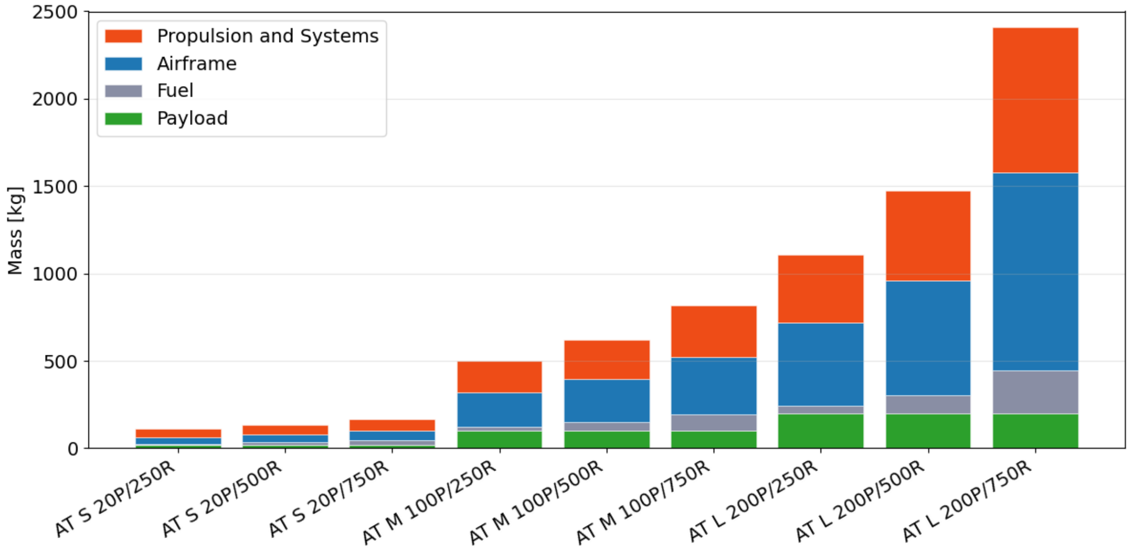

Figure 5.14: Breakdown of the Main Component Masses

Using the VTOL-AD results, payload-range diagrams were generated for the proposed aircraft configurations. Here, it must again be taken into account that VTOL-AD does not reduce fuel mass during flight, so the actual range would be higher in practice. In addition, the maximum payload is fixed to the value determined in the sizing process, and the tank volume is limited to the amount of fuel required for the design range. As a result, the diagram qualitatively resembles that of a battery-electric aircraft in terms of its overall shape.

On the one hand, the tank volume is constrained because the fuselage sizing was only carried out for the corresponding fuel quantity, so any increase in tank size could require a revised fuselage geometry. On the other hand, the payload is limited because, in the simulations conducted in this work, the carried payloads and the maximum payload of the UAVs are directly linked to the OWF distances and the UAV design ranges. Consequently, a UAV could not perform a mission with less than its design payload and additional fuel that it could not also complete with the available fuel volume.

A further constraint, which has not yet been treated in detail due to the conceptual nature of the study, also applies. For safely lowering heavier loads as well as retrieving equipment from a wind turbine, a hoist system is required, which itself is subject to operational limitations. In the context of this work, it is assumed that this hoist system can only handle the design payload.

The resulting payload-range diagram for all AT designs is given in Figure 5.15.

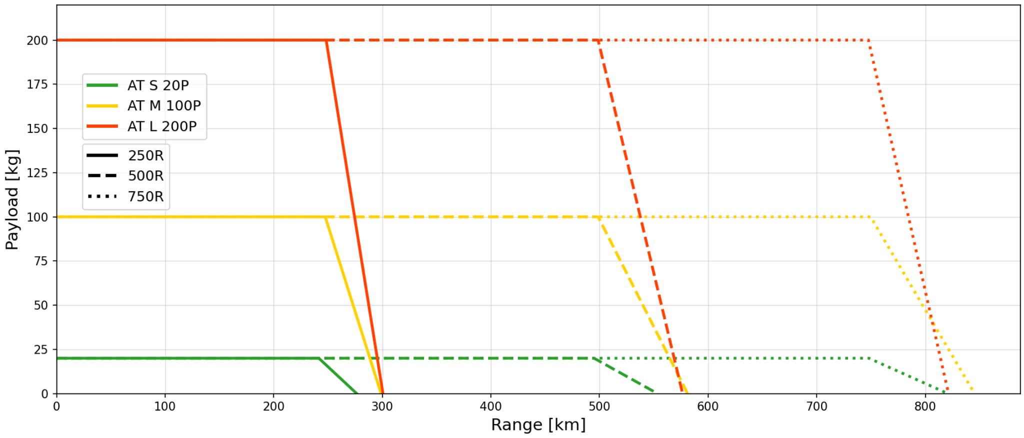

Figure 5.15: Payload Range Diagrams for all Arctic Tern Designs

In Figure 5.16, the payload-range diagram including the corresponding fuel mass is pictured exemplary for the AT M designs, all diagrams can be found in Appendix D.

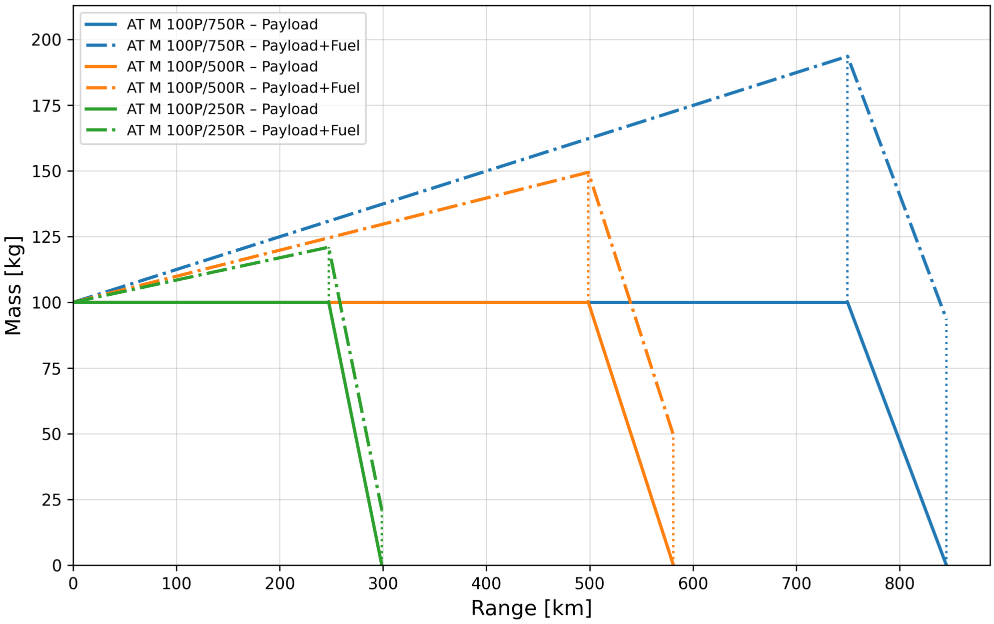

Figure 5.16: Payload Range Diagram with Fuel Mass for the Arctic Tern M Designs

When the diagrams are grouped according to the design ranges, the plots shown in Figure 5.17 and Figure 5.18 are obtained, the plot for 500 km design range is to be found in Appendix D as well. Small deviations in the maximum range without payload can be observed between the configurations of a given design range. Since the ferry range is not used as a target quantity in the VTOL-AD sizing process, these deviations are considered plausible and not problematic for the following simulations.

The diagrams also highlight the high fuel mass relative to payload weight for the configurations with a design range of 750 km. Because the VTOL-AD performance calculation does not account for the reduction in fuel mass over the mission, so the actually achievable range will be higher in this case. If this effect would be included, a reduction in the

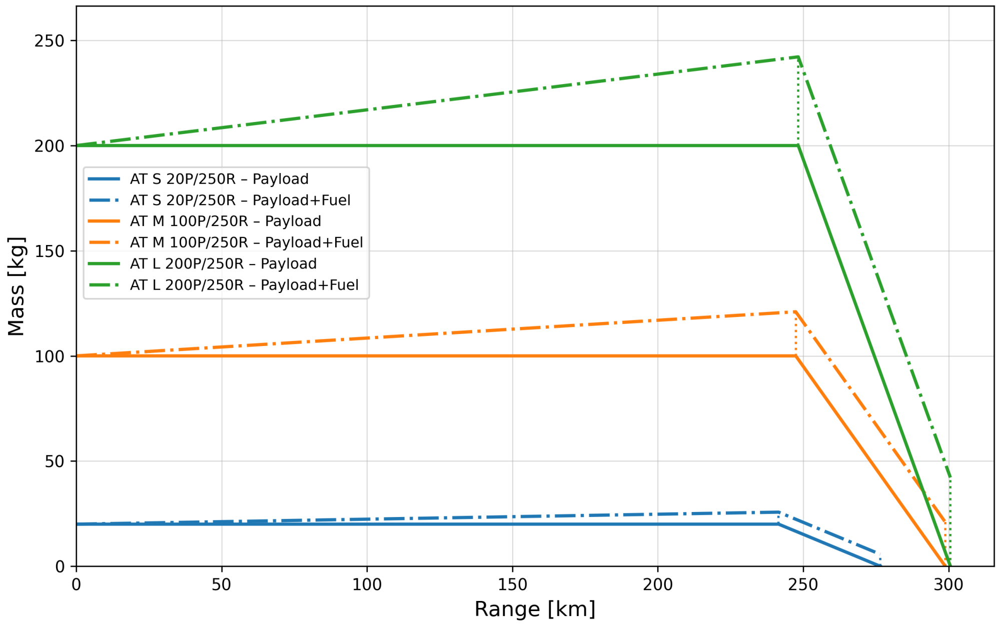

Figure 5.17: Payload Range Diagrams for the Arctic Tern Designs with 250 km Design Range

maximum fuel mass and in the empty weight can be expected.

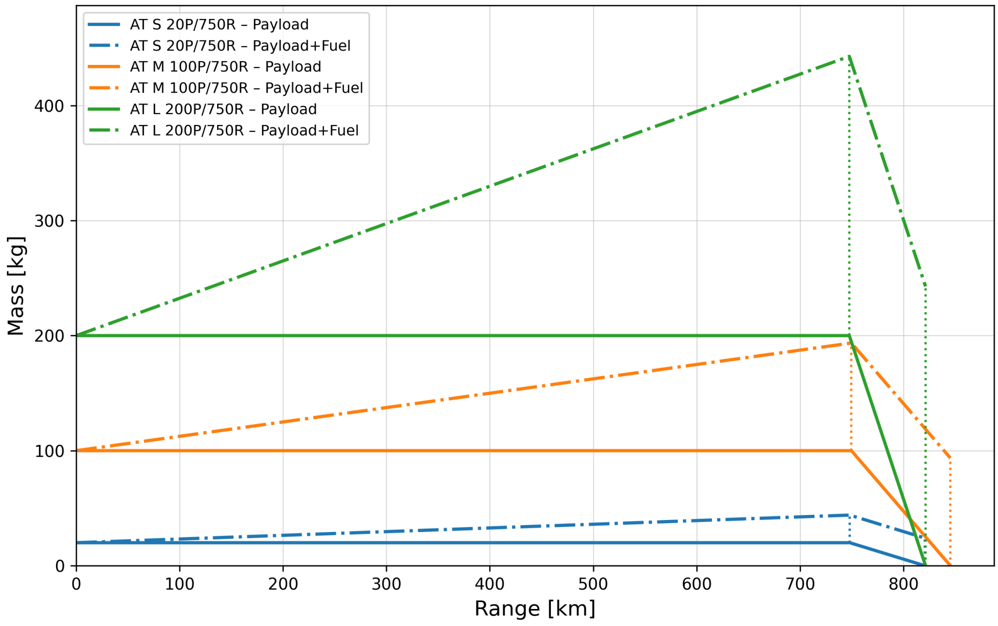

Figure 5.18: Payload Range Diagrams for the Arctic Tern Designs with 750 km Design Range

To situate the VTOL-AD Arctic Tern designs within the spectrum of commercial UAVs that were discussed in more detail in Section 2.1.4 and the research configurations by Vegh et al. [186] listed in Section 5.1.8, several plots were generated comparing $MTOM$, wingspan, payload, range and cruise speed.

Plotting the payload over design range for the AT-Designs and the corresponding datapoints from other UAVs in Figure 5.19 clearly highlights the pattern of the Arctic Tern design parameters. These configurations are located within the general region populated by numerous other aircraft of various types, while a few outliers can be identified that clearly prioritise either very high payload or very high range.

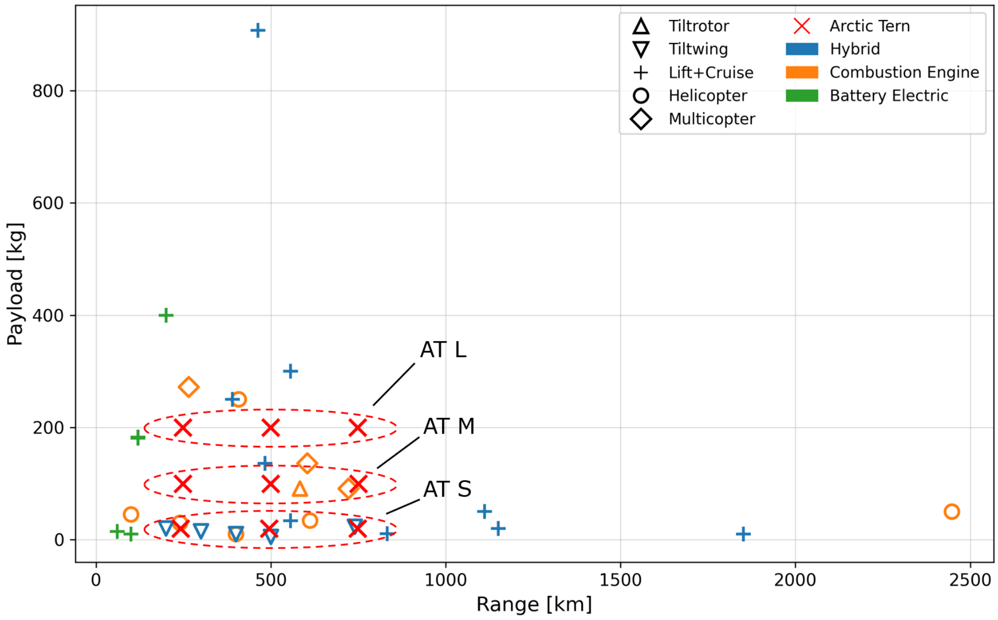

Figure 5.19: Overview of the Payload and Design Range Data

Figure 5.20 shows that the Arctic Tern designs in principle fall within the existing design space. It also becomes apparent that most data points lie in the region below 2000 kg $MTOM$ and a range of 1000 km, which is also the case for most Arctic Tern designs. The largest design, AT L 200P/750R, is located outside this region and slightly separated from the other Arctic Tern designs, but remains plausible when compared with the nearest Lift+Cruise aircraft such as the Beta ALIA MV250 or the Pipistrel Nuuva V300, especially since only one to at most three data points are available for these vehicles and the achievable range can be expected to increase for reduced payload.

The remaining AT L designs lie close to other Lift+Cruise configurations, where the powertrains are likewise implemented as hybrid systems for the larger ranges. Of particular interest is the proximity of the AT L 200P/250R design to the research configurations by Vegh et al. [186], which are very similar in terms of $MTOM$ and payload but use a battery-electric powertrain, which explains their lower range. The AT M designs are located in a region that is otherwise populated mainly by helicopter configurations or multirotor aircraft powered by combustion engines. The designs of the AT S series lie in a region that contains many other concepts with comparable configurations.

The comparison of the data in the plot with payload over $MTOM$ as in Figure 5.21 likewise reveals a similar overall trend. The designs of the AT S series are entirely located within the range of commercial concepts. The AT M series again falls into the region populated by helicopters and multirotor aircraft powered by combustion engines. The two AT L designs with ranges of 250 km and 500 km lie in the region of comparable hybrid-powered Lift+Cruise configurations, whereas AT L 200P/750R is positioned further away from this

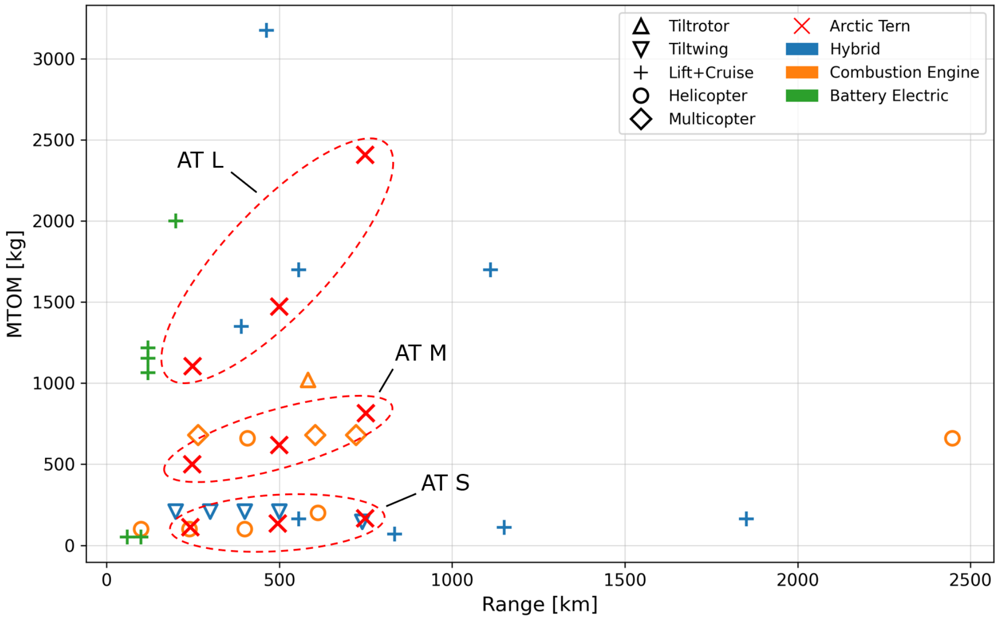

Figure 5.20: Overview of the MTOM and Range Data

cluster.

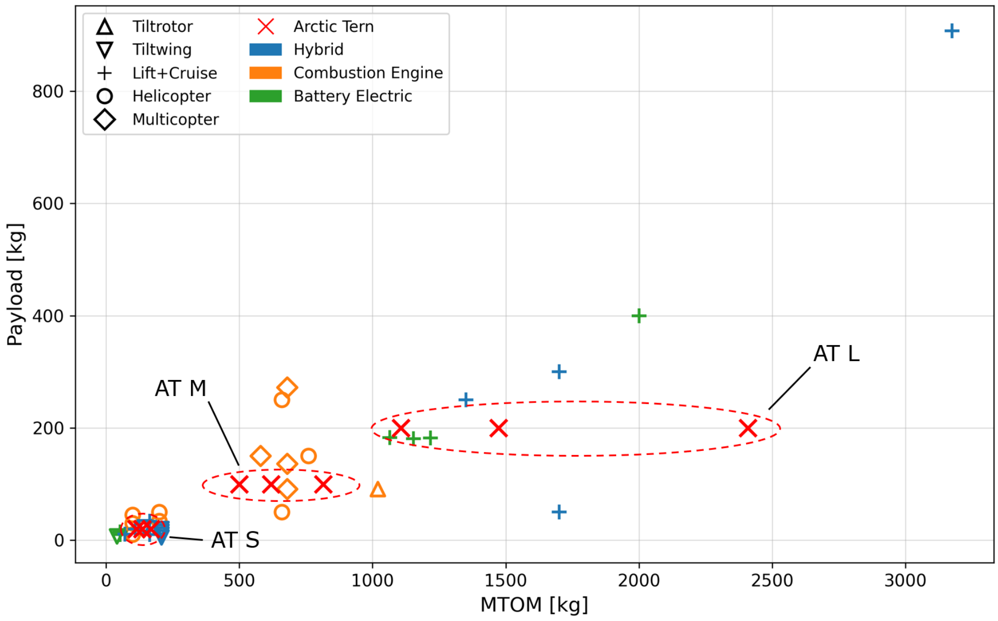

Figure 5.21: Overview of the Payload and MTOM Data

From the plot of wingspan over $MTOM$ it can be observed that the Arctic Tern designs generally follow the trend of commercial UAVs and research configurations, although the M and L series exhibit larger spans than comparable aircraft. This indicates that the chosen maximum aspect ratio of $AR = 21$ is comparatively high. As a consequence, especially for the M and L series, the wing mass fraction relative to the total $MTOM$ is comparatively high, as shown in the mass-breakdown overview in Figure 5.14. The UAV designs are nevertheless considered fundamentally plausible within the scope of conceptual design. However, in a detailed design process, the wing masses and the maximum achievable aspect ratio would need to be examined thoroughly from a structural and aeroelastic perspective.

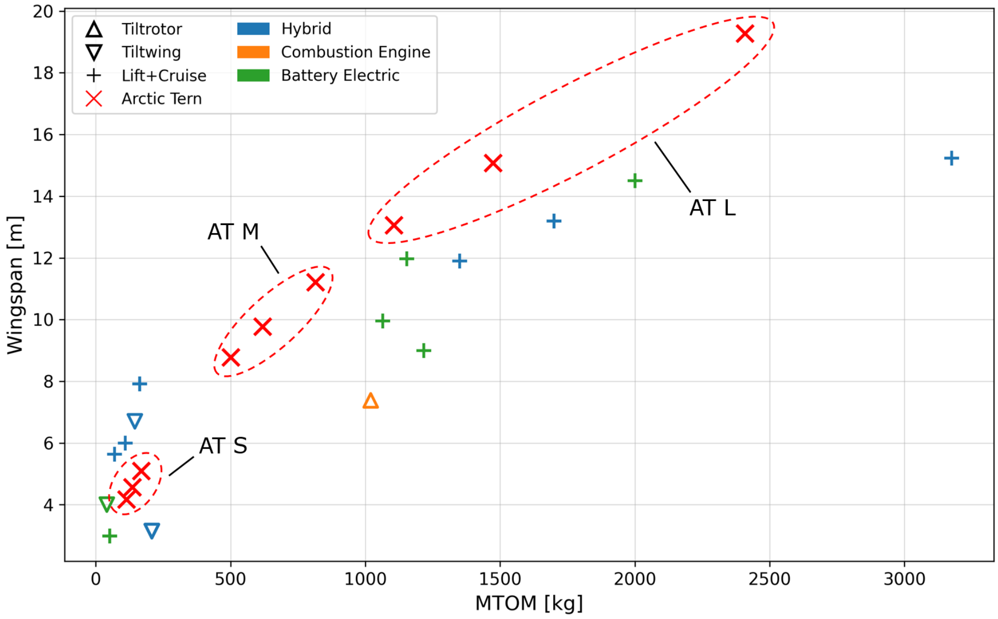

Figure 5.22: Overview of the Wingspan and MTOM Data

In Figure 5.23, the cruise flight speeds in relation to the $MTOM$ are shown. For this comparison, not the maximum cruise speeds were used but the cruise speed corresponding to the maximum range. For the Arctic Tern designs, the cruise speed in the mission definition was set to $35\ m/s$. The designs therefore cluster around this speed, with the smaller AT S configurations exhibiting a lower speed for maximum range that falls in the same region as comparable commercial designs. For the larger Arctic Tern configurations, the speed increases with $MTOM$, although the commercial UAVs and the research configurations by Vegh et al. [186] show higher cruise speeds.

Based on the comparison with the speeds of the larger commercial UAVs and research configurations, it can be assumed that a higher design mission cruise speed for the AT M and L designs could lead to more results closer to the field of existing UAVs. All reference configurations in this area employ a Lift+Cruise architecture, in which the minimum flight speed can be higher than for tilt-based configurations like the Arctic Tern designs, if the vertical propulsion units continue to contribute to lift during the transition until the cruise speed is reached. This allows for a smaller wing, which is consistent with the differences in wingspan observed in Figure 5.22 and would also reduce the wing weight.

Another driving point is that the aspect ratio was set to a comparatively high value, which leads to a lower best range cruise speed.

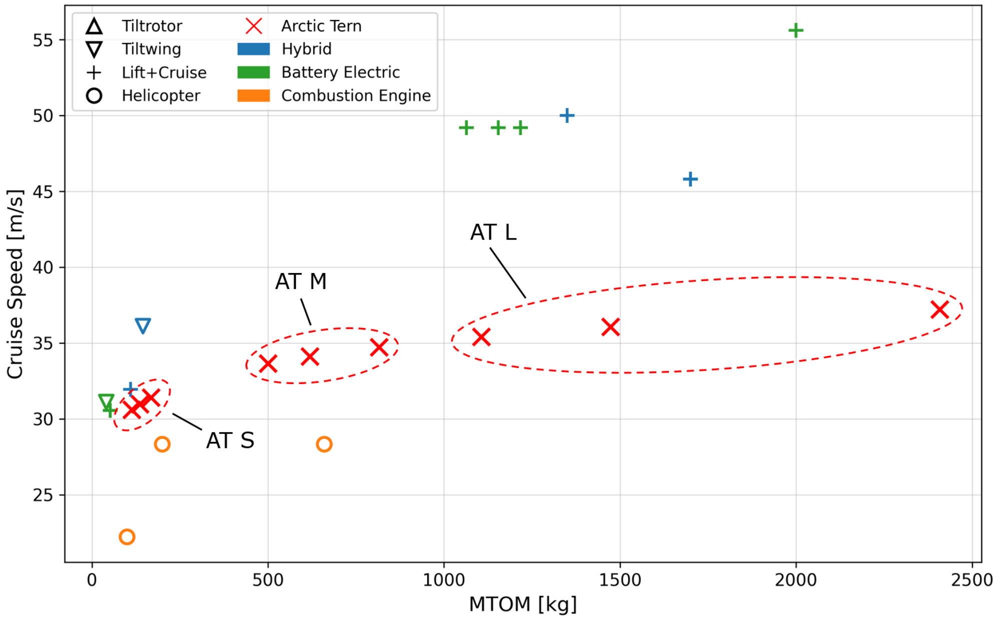

Figure 5.23: Overview of the Cruise Speed and MTOM Data

5.2 Systems of Systems Simulation

5.2.1 Design of Experiments

The UAVs designed in the previous chapter are now to be deployed within a systems-of-systems context. For this purpose, the same simulation parameters and boundary conditions as in Section 4.6 are applied. However, using the drone designs, the three logistics strategies involving UAV participation can now be simulated in combination with the conventional transport assets. This enables an evaluation of the resulting changes at the systems-of-systems level due to UAV deployment. Compared to Table 4.9, the modified simulation parameters listed in Table 5.15 were applied.

First, the supplementary use of drones for spontaneous material resupply to teams at the turbines is addressed. As mentioned in Section 2.2.2.2.3, this strategy has already been implemented in operational campaigns and is currently the closest to routine deployment, due to the availability of UAVs with suitable performance characteristics and an emerging landscape of service providers and supporting infrastructure. For a CTV-based strategy, this enables flexible resupply in the first place. Helicopters are relieved accordingly and do not need to cover long flight distances to deliver only a few kilograms of material. In

Parameter	Value	Unit
Strategies	CTV and UAV for spont. deliveries, CTV and UAV for all deliveries, Helicopter and UAV for spont. deliveries	[-]
CTV Fleetsize	1	[-]
Helicopter Fleetsize	1, 2, 3	[-]
UAV Fleetsize	1, 2, 4, 6, 8	[-]

Table 5.15: Changed Simulation Parameters for UAV supported Logistic Strategy Study

all simulations for this strategy, drones of the AT S series were used, AT S 20P/250R for distances of 80 km, AT S 20P/500R for 120 km and AT S 20P/500R for 160 km.

5.2.2 Assessment of Helicopters with UAVs for spontaneous Demands

Figure 5.24 illustrates the sequence of a UAV resupply operation with a CTV as the primary asset. In the left view of the SoSID toolkit GUI, the morning trip of the CTV to the wind farm can be seen, during which all teams and all preplanned equipment are transferred to the turbines. The UAV remains at the service hub. In the middle view, after completing the transfers, the CTV is located at the loiter position within the wind farm. A spontaneous demand has been triggered at one turbine, which is indicated by the orange coloring of the turbine icon. The UAV is en route to this turbine and, as indicated by its orange coloring, carries material but no personnel. In the right view, the drone returns to the mainland after completing the material transfer. As indicated by the supplied turbine now being shown in yellow rather than orange, the spontaneous demand has been resolved and the team can complete the maintenance task. The UAV icon is now colored red, indicating that it is flying without payload as intended. For helicopter operations supported by UAVs for spontaneous demands, a similar picture emerges, with the main difference being that helicopters do not remain in the OWF and that, even without UAV support, a capability for spontaneous material resupply already exists. If the helicopter-and-UAV strategy for spontaneous deliveries is selected, spontaneous demands are handled exclusively by UAVs, even if a helicopter might be available at that time.

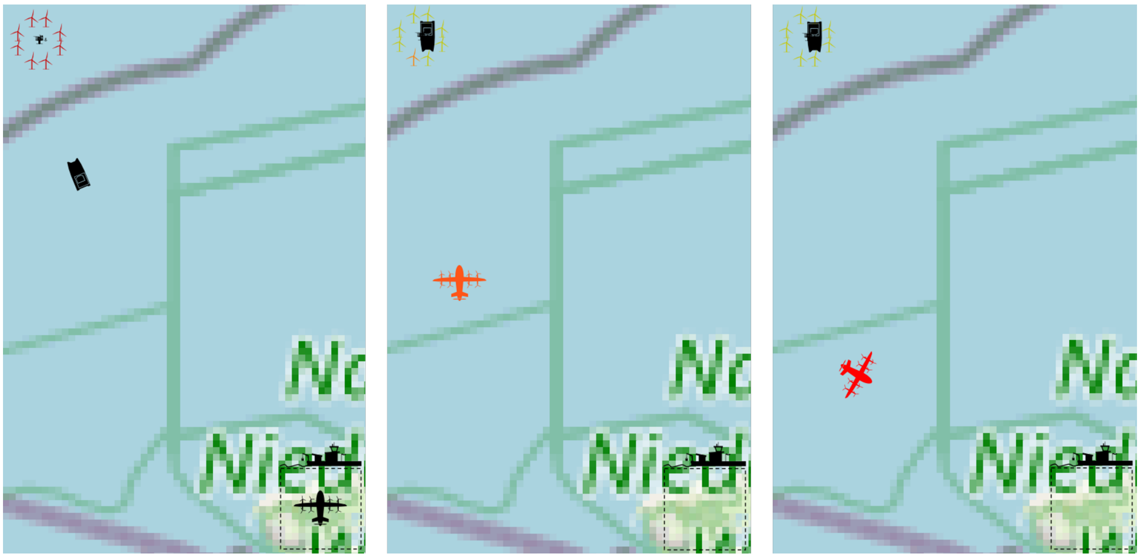

Figure 5.24: Initial Team and Equipment Delivery with CTV (left), Spontaneous Demand and UAV en route (middle), Returning flight of UAV after successful Delivery (right)

When analyzing the results, several effects become apparent, some of which were already discussed in Section 4.6. Accordingly, the impact of UAV deployment also depends on how the baseline assets of the selected logistics strategy perform. For shorter distances and shorter maintenance durations, for example in the following case with a maintenance duration of 3 h per turbine and a helicopter fleet size of two, a comparatively high number of maintenance hours was enabled and maintenance tasks were completed, as indicated by Figures 4.41 and 4.40.

Figure 5.25 presents the results for using drones for spontaneous deliveries compared to the purely helicopter-based strategy at a spontaneous demand probability of 0.6. Based on the developed ConOps, a reduction in helicopter flights is expected, since helicopters no longer need to perform the spontaneous resupply missions. Instead, the number of UAV flights increases with larger UAV fleet sizes, in parallel with a reduction in total fleet energy consumption, while the values stabilize for larger UAV fleets. Under the selected scenario, employing drones for spontaneous deliveries reduces total fleet energy consumption by approximately 20 Energy production initially increases significantly when more than one drone is used, but then stabilises at an increase of also approximately 20%. Maintenance is completed at all turbines within the simulation period. Compared to the baseline, the key benefit is that teams no longer need to wait for helicopter availability to receive replacement parts. Since simultaneous spontaneous demands occur comparatively rarely, a small number of drones is already sufficient to handle them in a satisfactory manner. At this point, the UAV cruise speed limits further acceleration of the maintenance process. Because all maintenance tasks were already completed even without UAV support, the relative improvement remains limited. Using only a single UAV results in a slightly worse outcome, which can be explained by simultaneously occurring demands and the lower speed compared to the helicopter.

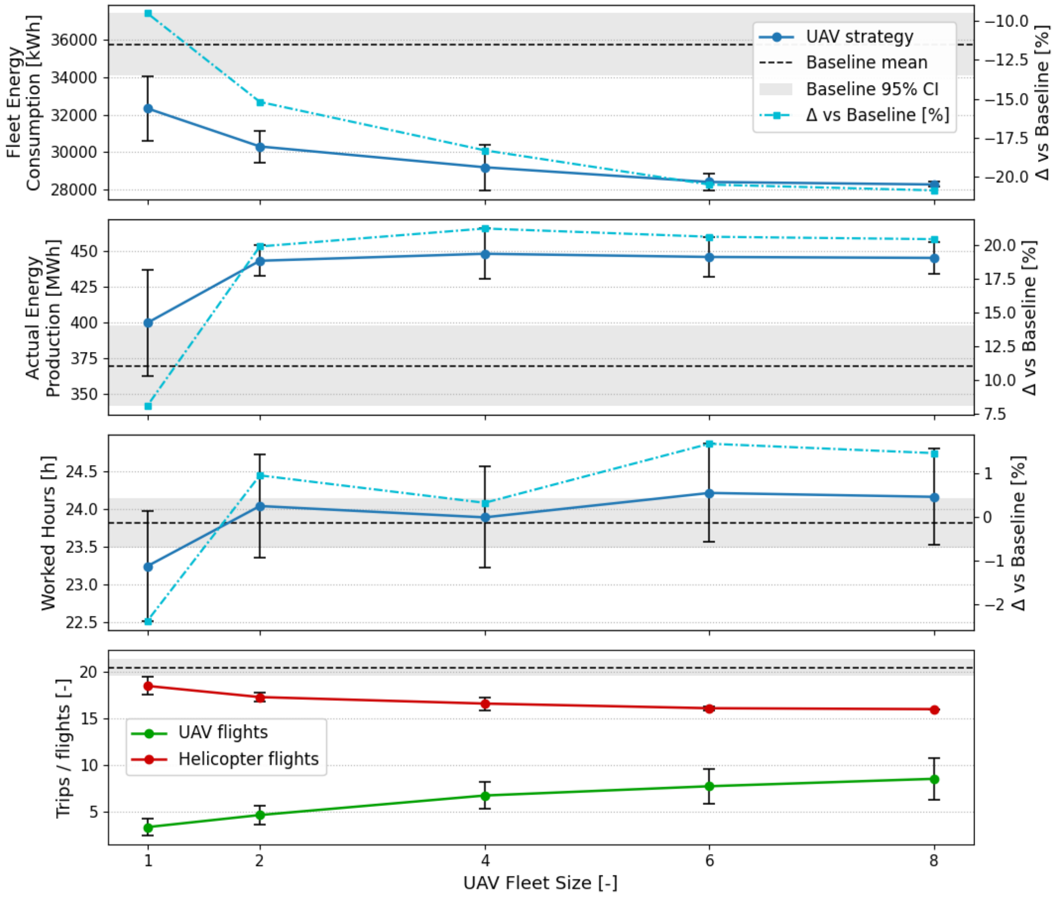

Figure 5.25: DOE Results for the Helicopter and AT S 20P/250R UAV for spont. Deliveries Strategy with 3 h Maintenance Time, 0.6 Probability of spont. Demands, 2 Helicopters and 80 km Distance

With increasing distance, shown in Figure 5.26 for a distance of 120 km between the OWF and the service hub, a qualitatively similar picture emerges. However, fleet energy consumption is reduced by only about 7%, which is attributable to the larger drone used in this case. At a distance of 160 km, the results shown in Figure 5.27 make it clear that the benefits of UAV support reach their limits. Due to the larger distance and longer transfer times, the available work window is already more constrained. This particularly affects the UAVs because of the daylight requirements. Owing to the large distances, the consequently required larger drone, and the fact that no helicopter flights can be avoided, the total energy consumption of the deployed aircraft increases. As already observed in the baseline evaluation, two helicopters at a distance of 160 km and a higher probability of spontaneous demands can no longer satisfy all spontaneous demands and therefore execute fewer flights than at shorter distances. Since the longer distances, combined with daylight constraints, lead to a smaller operational window for UAVs, and since the distances also delay the maintenance teams in starting their work, the number of UAV flights is also reduced compared to the shorter distances. The distance-dependent effects are clearly visible in Figure 5.28. The relationship between energy consumption and distance is of particular interest. The three-dimensional representation of these quantities in Figure 5.29 indicates a linear dependence of the relative difference in total energy consumption on the wind farm distance, while a logarithmic trend is apparent particularly at shorter distances. If the number of deployed helicopters is increased from two to three, the trends become more stable, since the execution of maintenance processes is again

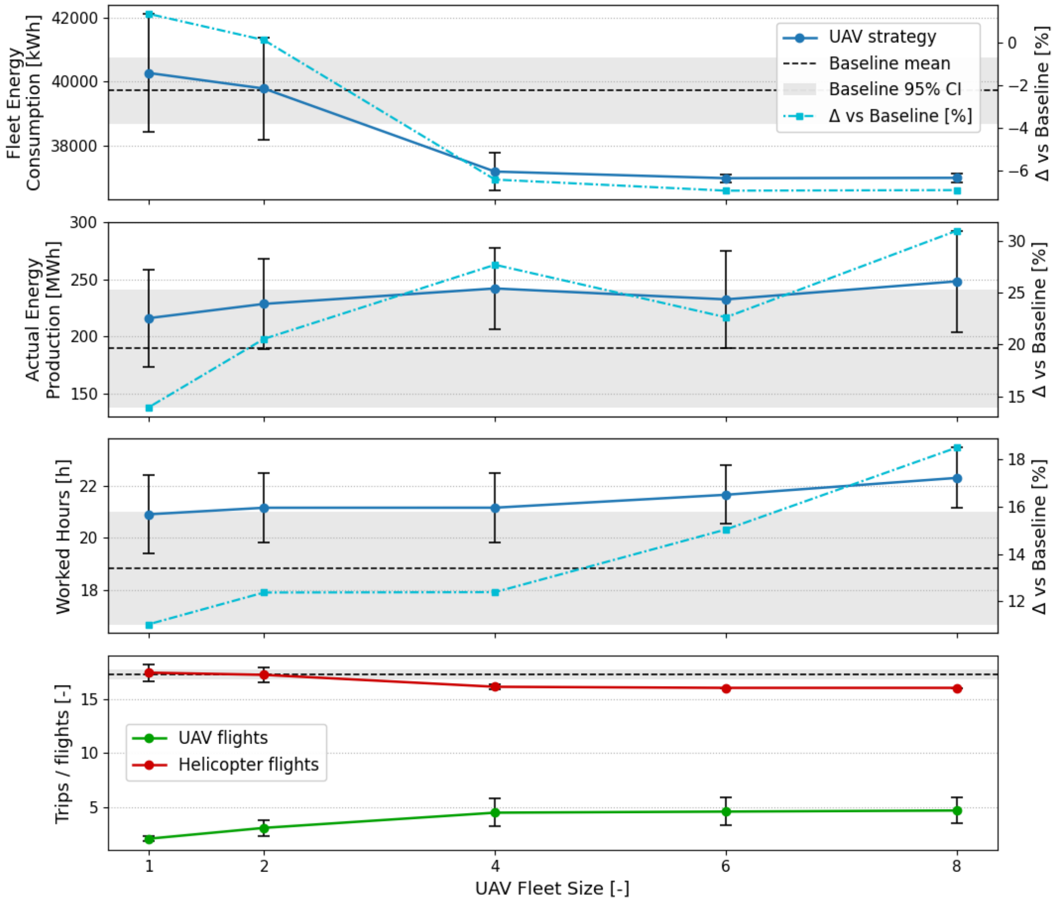

Figure 5.26: DOE Results for the Helicopter and AT S 20P/500R UAV for spont. Deliveries Strategy with 3 h Maintenance Time, 0.6 Probability of spont. Demands, 2 Helicopters and 120 km Distance

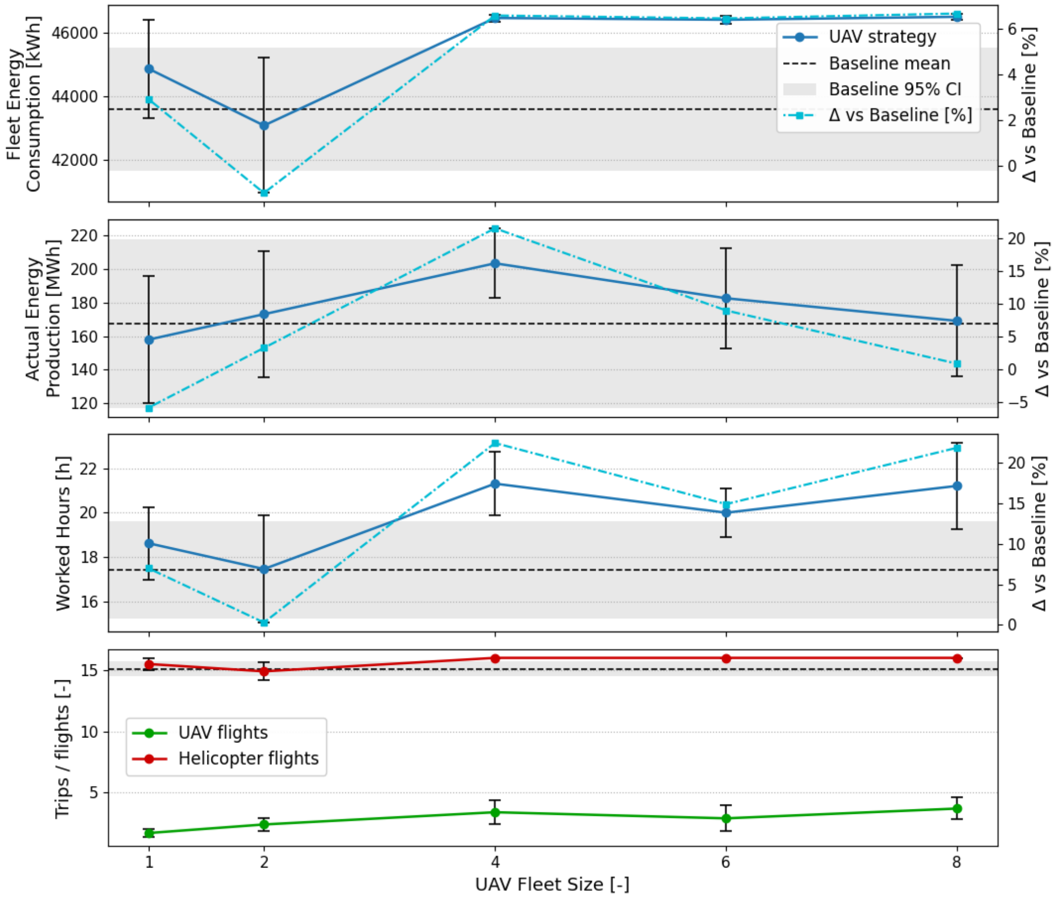

Figure 5.27: DOE Results for the Helicopter and AT S 20P/750R UAV for spont. Deliveries Strategy with 3 h Maintenance Time, 0.6 Probability of spont. Demands, 2 Helicopters and 160 km Distance

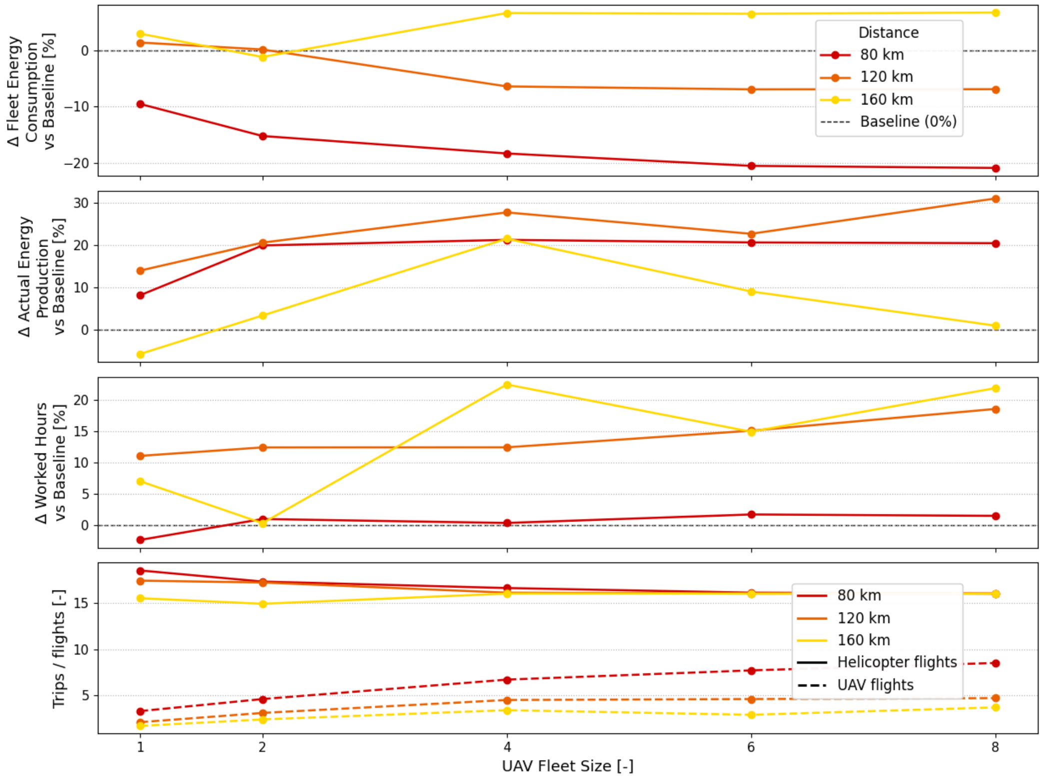

Figure 5.28: Relative Difference between the Helicopter Only Strategy and the Helicopter and UAV for spont. Deliveries Strategy with 3 h Maintenance Time, 0.6 Probability of spont. Demands and 2 Helicopters

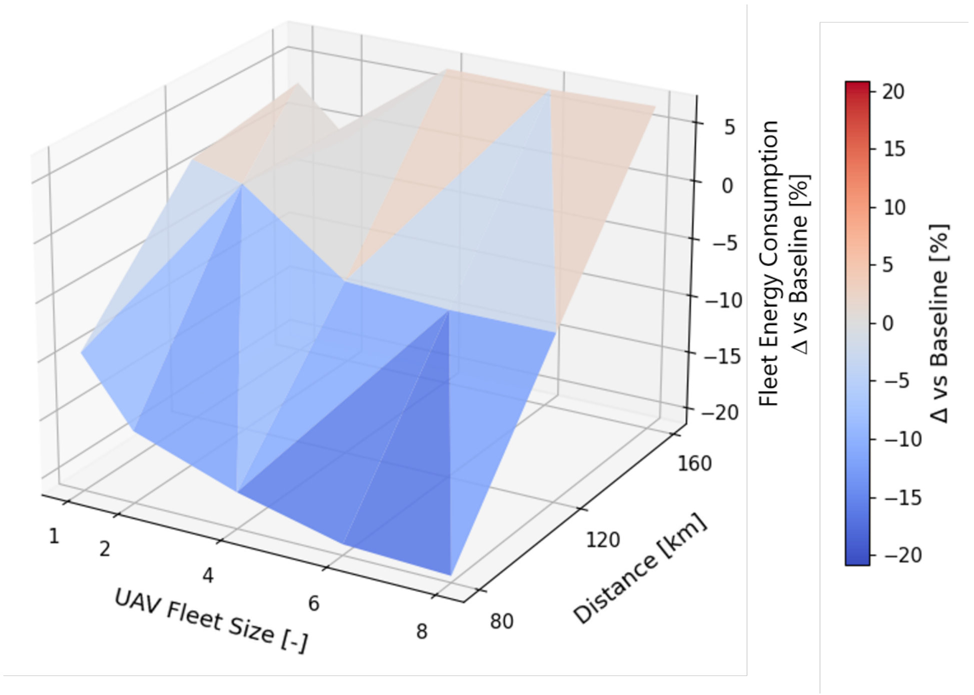

Figure 5.29: Relative Energy Consumption Difference between the Helicopter Only Strategy and the Helicopter and UAV for spont. Deliveries Strategy with 3 h Maintenance Time, 0.6 Probability of spont. Demands and 2 Helicopters

ensured even at a higher probability of interruptions and at larger distances. In this case, an increasing benefit with growing distance between the wind farm and the service hub becomes apparent with respect to enabled maintenance hours and enabled energy production. At the same time, the benefit in terms of reduced energy consumption decreases as distance increases. This indicates that, for UAV-based spontaneous deliveries to provide a meaningful advantage, the baseline assets of the logistics strategy must already be selected appropriately in terms of fleet size and vehicle type in order to achieve clear benefits.

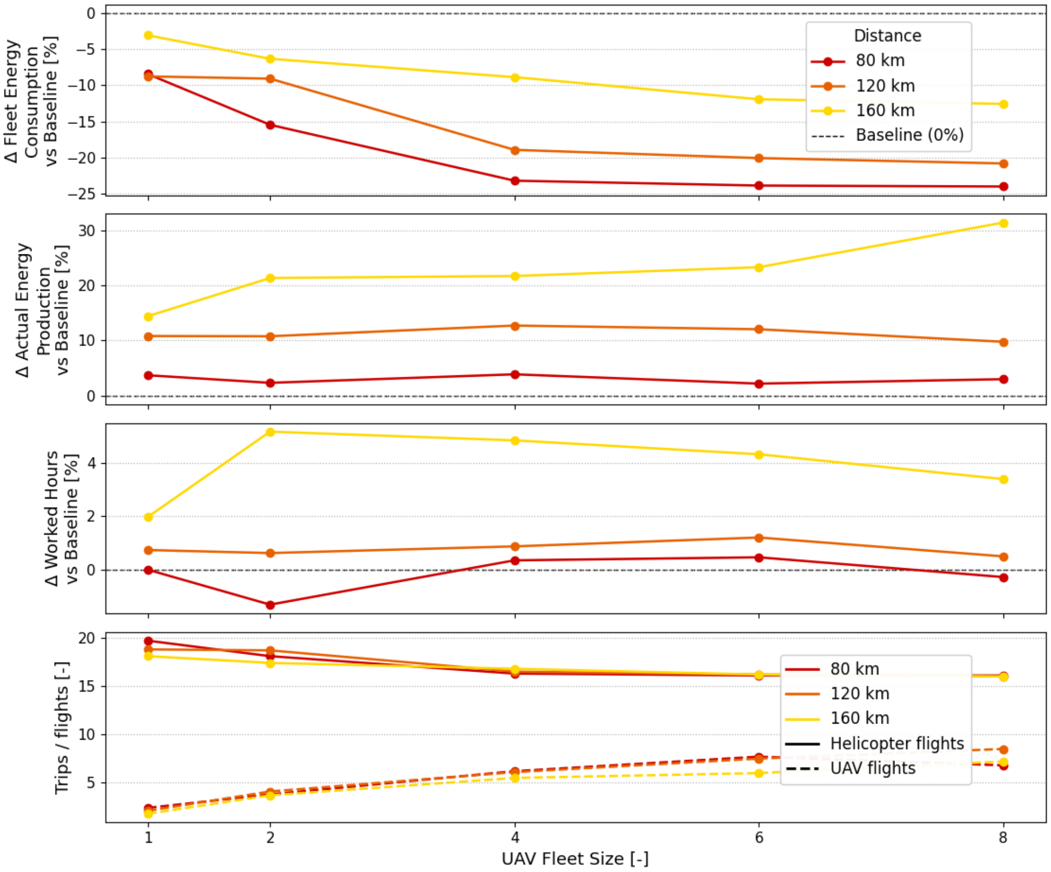

Figure 5.30: Relative Difference between the Helicopter Only Strategy and the Helicopter and UAV for spont. Deliveries Strategy with 3 h Maintenance Time, 0.6 Probability of spont. Demands and 3 Helicopters

5.2.3 Assessment of a CTV with UAVs for spontaneous Demands

For the use of UAVs in combination with CTVs, a clear advantage can be observed, independent of the wind farm distance, in terms of wind farm energy production and the number of enabled maintenance hours. It must be taken into account that, under the baseline strategy that relies solely on a CTV, maintenance work is aborted when spontaneous demands occur. While in the helicopter baselines spontaneous demands can generally be fulfilled under suitable boundary conditions, this represents a key difference for the CTV case, and it can already lead to an advantage even when only a single UAV is deployed.

Figure 5.31 shows the results for a distance of 80 km and an increased probability of spontaneous work interruptions of 0.6 during a maintenance process with a duration of 3 h. As indicated by the trends in energy production and maintenance hours as well as by the number of trips, a fleet of four UAVs is already sufficient to cover the occurring demands. Deploying additional UAVs does not lead to more flights and therefore does not further improve the maintenance process. For larger UAV fleets, a slightly increased total energy

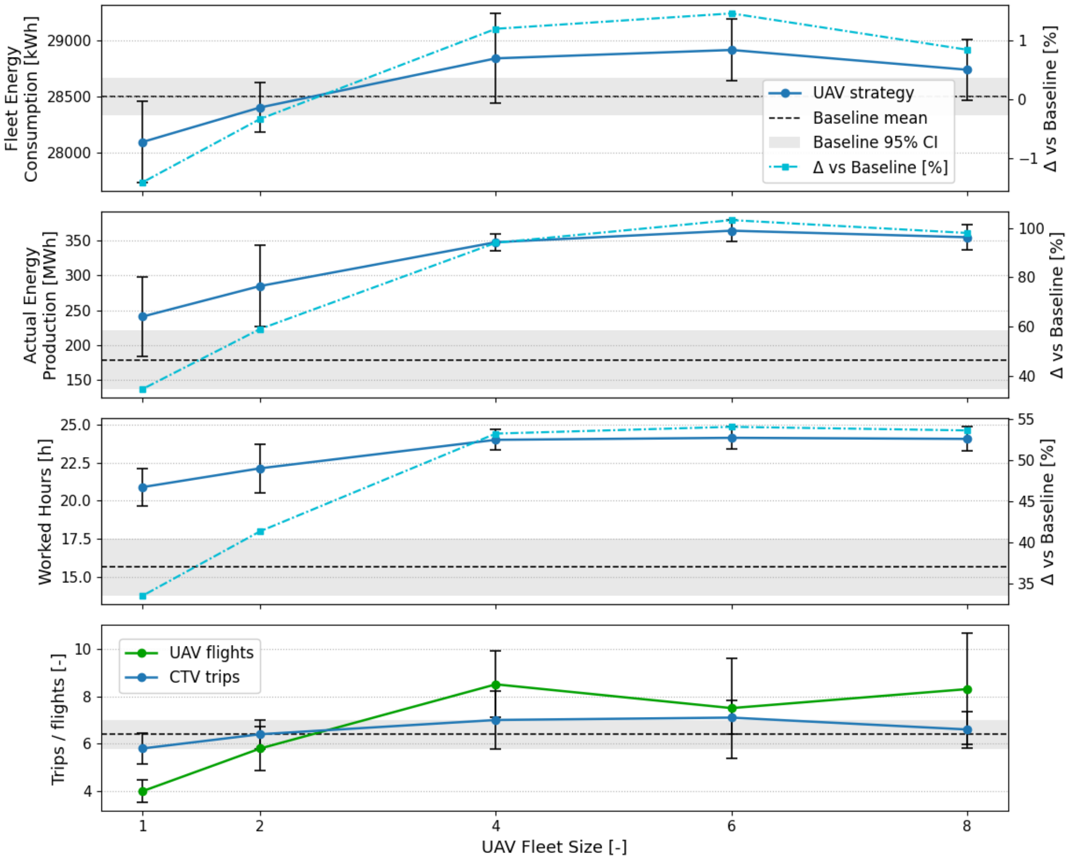

Figure 5.31: DOE Results for the CTV and AT S 20P/250R UAV for spont. Deliveries Strategy with 3 h Maintenance Time, 0.6 Probability of spont. Demands and 80 km Distance

consumption can be observed. Due to the comparatively small aircraft with low energy consumption, this remains a relative increase of only 1-2% compared to the baseline. For small UAV fleets, a slight reduction in energy consumption is even visible. The reason lies in the CTV ConOps. In the CTV-only strategy, when a spontaneous demand is detected, the CTV travels to the affected turbine, picks up the team, and returns to the loiter point. If maintenance tasks are completed at the end of the day together with other tasks because the spontaneous resupply was performed by a drone, a pickup mission with multiple stops at the relevant turbines can be planned, without returning to the loiter point after each stop. However, this effect is quantitatively very small and not of high relevance.

Since multiple maintenance tasks can now be completed at all compared to the baseline, the increase in wind farm energy production is very pronounced at approximately 100%. The worked hours also increase strongly by more than 50%, since maintenance is no longer aborted after a spontaneous demand. The slight deviations in the number of CTV trips compared to the baseline result from mission planning and from how the CTV processes demands and operational steps. A mission with a preplanned pickup of multiple teams results in only one trip, whereas individual pickups of teams that either completed their work or had to abort due to a spontaneous demand occur as separate missions. Depending on completion times and on the timing of spontaneous demands, trip counts therefore vary, which explains the comparatively wide confidence interval observed for this metric.

Increasing the distance between the wind farm and the service hub leads to the results shown in Figure 5.32. These are qualitatively and quantitatively very similar to the results discussed previously for 80 km. With a further increase in distance to 160 km, the results shown in Figure 5.33 indicate that the UAV fleet size required for convergence of the maintenance-hours and energy-production results increases. Instead of convergence being reached from four UAVs onward, it is now observed from six drones onward. Since the aircraft operate at a constant speed, the time spent in transit increases as well, which reduces availability for accepting subsequent tasks. When comparing the relative differences to the baseline for the three distances as overlaid in Figure 5.34, it becomes apparent that the effects of UAV deployment on the metrics are overall relatively close to each other and are not strongly dependent on distance. The number of flights, however, shows that more flights are conducted at shorter distances, and that flight counts decrease as distance increases. As for the helicopter-based strategy, this can be explained by the progressively reduced operational windows. With an increased maintenance duration of

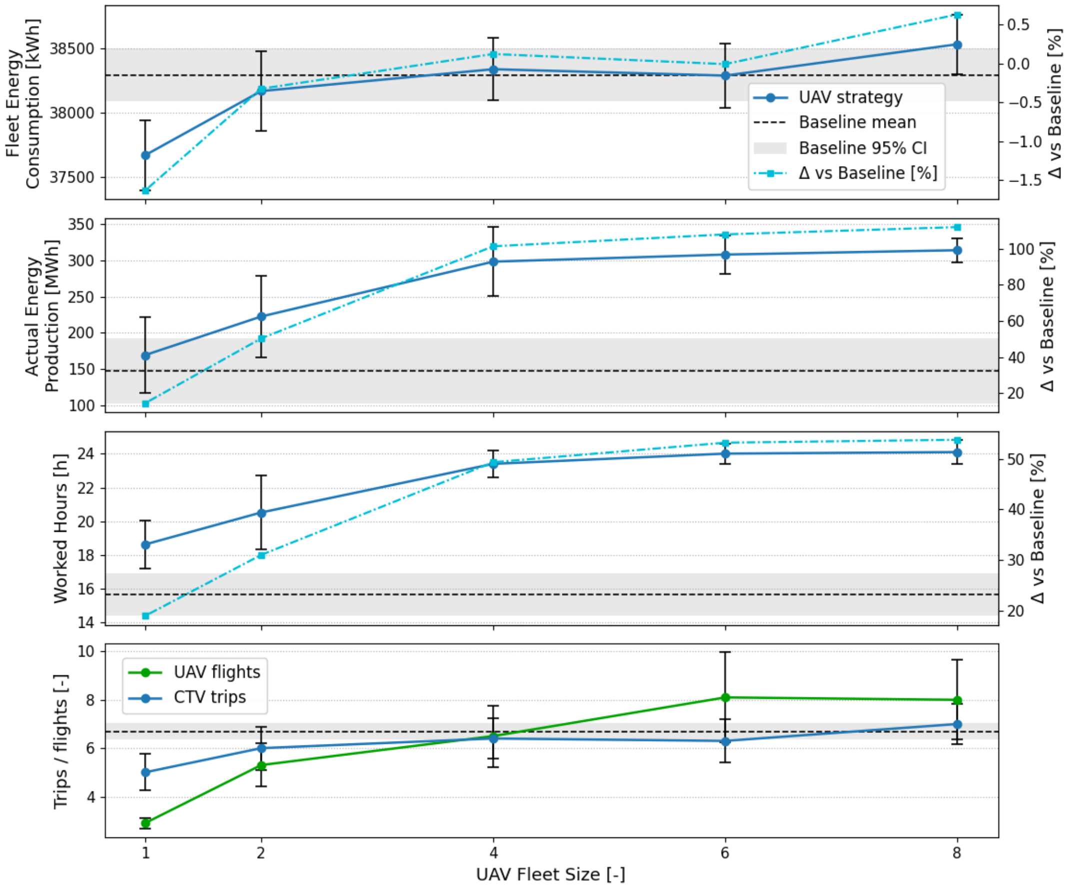

Figure 5.32: DOE Results for the CTV and AT S 20P/500R UAV for spont. Deliveries Strategy with 3 h Maintenance Time, 0.6 Probability of spont. Demands and 120 km Distance

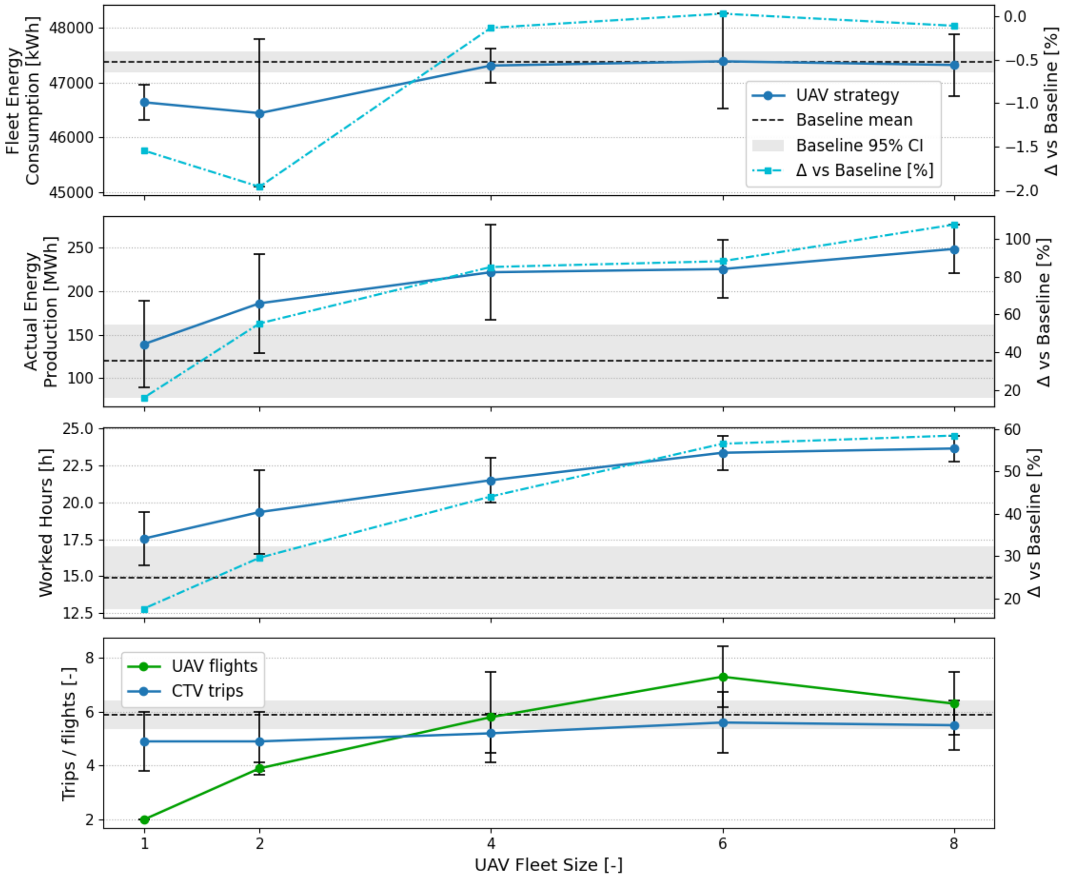

Figure 5.33: DOE Results for the CTV and AT S 20P/750R UAV for spont. Deliveries Strategy with 3 h Maintenance Time, 0.6 Probability of spont. Demands and 160 km Distance

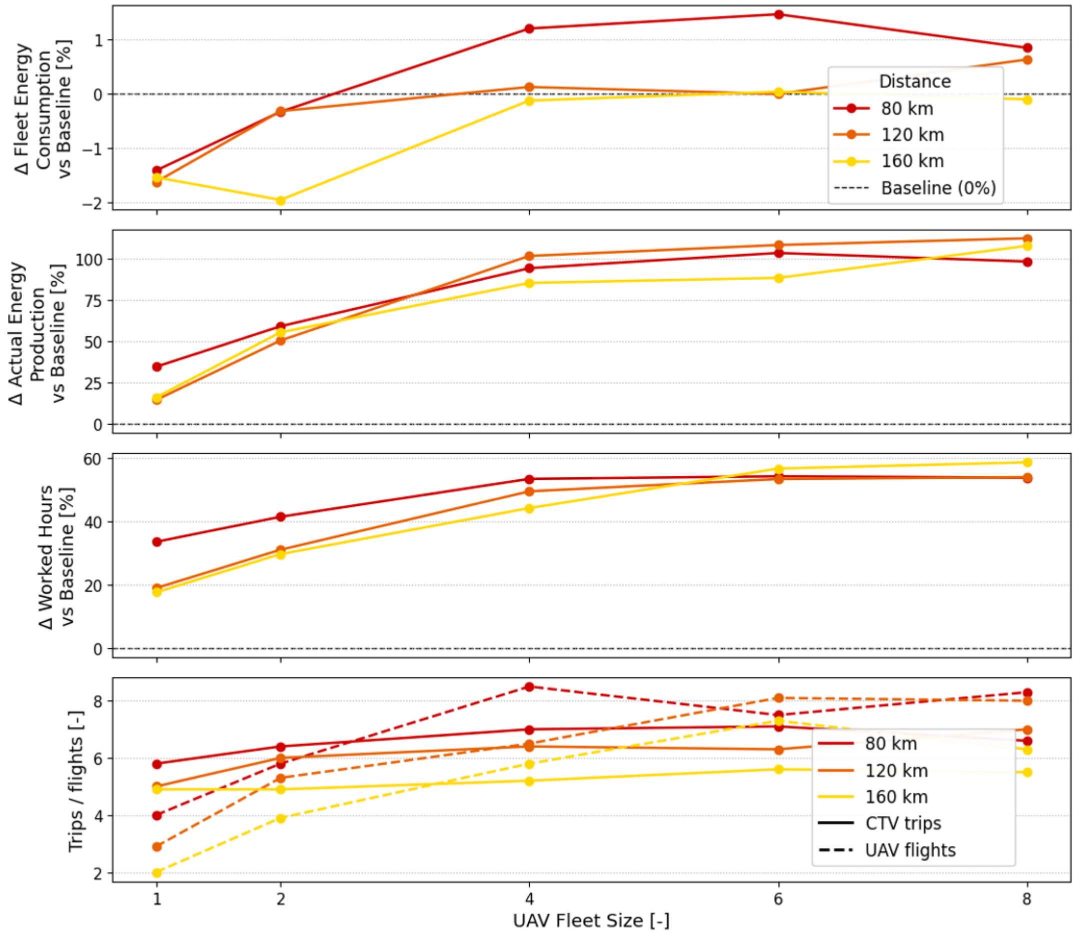

Figure 5.34: Relative Difference between the CTV Only and the CTV and UAV for spont. Deliveries Strategy with 3 h Maintenance Time and 0.6 Probability of spont. Demands

7 h, the effects that already became apparent in the baseline studies occur again, as illustrated in Figure 5.35. An improvement in enabled maintenance hours becomes visible and is now more strongly dependent on distance ranging from 40% for 80 km to 10% for 160 km.

However, this does not lead to increased energy production. The comparatively strong reduction can be explained by the fact that, already in the baseline scenario, as shown in Figures 4.37 and 4.40, hardly any maintenance tasks can be completed. In many cases, only a small number of turbines return to operational status at all, and only in a limited number of simulation runs.

With UAV-based deliveries, maintenance hours increase, but maintenance tasks still cannot be completed. Since teams are no longer picked up prematurely, the overall collection of teams also occurs earlier once the return trip to the service hub starts in the evening. If the simulation were to run over multiple days, a benefit of UAV deployment would nevertheless become apparent due to the increased maintenance hours.

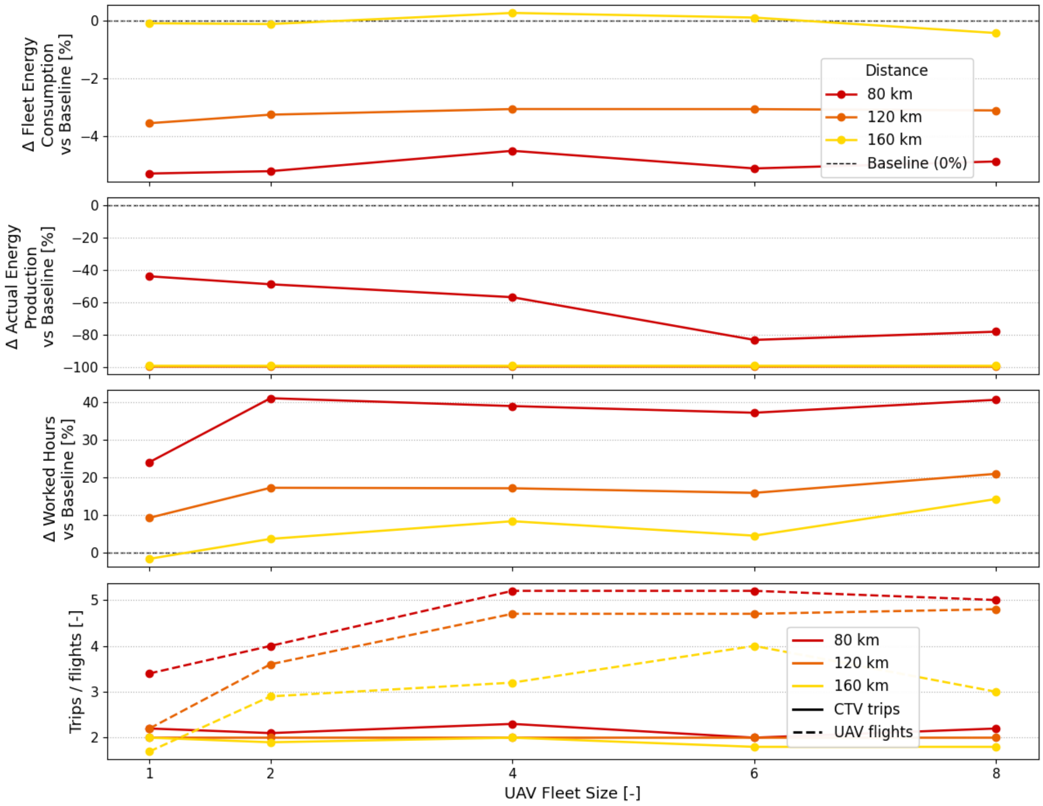

Figure 5.35: Relative Difference between the CTV Only and the CTV and UAV for spont. Deliveries Strategy with 7 h Maintenance Time and 0.6 Probability of spont. Demands

5.2.4 Assessment of UAVs for all Equipment Transports

With increasing technological progress in UAV technology, higher payloads and also the retrieval of loads become feasible, which leads to the CTV-for-teams and UAV-for-equipment strategy. Compared to the baseline logistics vehicle, the key advantage is flexible aerial transport with reduced transfer times to the turbines, such that only the CTV remains as the baseline asset. Due to the differing ConOps and operational limits of the deployed vehicles, this strategy exhibits behavior that is significantly different from the other strategies.

Figure 5.36 shows the initial transport of teams and equipment into the wind farm under this strategy. In the left view of the SoSID toolkit GUI, sunrise has not yet occurred. The CTV can already depart, and its arrival time was calculated such that the first transfer takes place in daylight. The four wind turbines shown are all colored red and therefore require maintenance. The UAVs have not yet departed, since they are subject to a general night-flight prohibition.

Shortly after sunrise, the situation shown in the middle view is obtained. The UAVs are now en route, while the CTV can transfer teams onto the wind turbines. Indicating that they are transporting cargo only, the UAV icons are colored orange. The UAVs used in this example are capable, in terms of payload and range, of carrying the equipment required for two wind turbines. Therefore, only two drones are flying to the wind farm, while the remaining aircraft stay at the service hub.

The right view shows the situation during the equipment transfer. At the observation time, the wind turbine in the upper left is being supplied simultaneously by the CTV with personnel and by the drone with equipment.

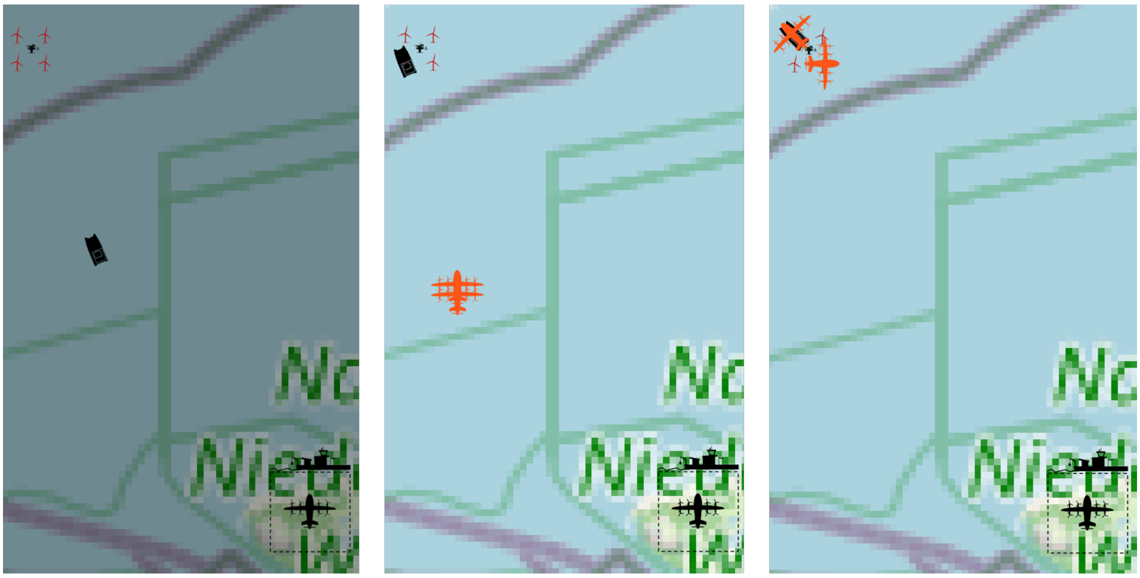

Figure 5.36: Initial CTV Trip to the OWF (left), CTV Flights with Equipment after Sunrise (center) and Transfer of Equipment by the UAVs (right)

Once the teams and the equipment have arrived at all turbines, including the associated process times until the start of maintenance, and all maintenance activities are in progress, the status shown in the left view of Figure 5.37 is obtained. The CTV is located at its loiter position within the OWF, and all drones are at the service hub.

If, as shown in the middle view, a spontaneous demand occurs, it is also satisfied by a UAV.

The right view shows a snapshot during the final phase of the maintenance activities. The two turbines on the left are still under maintenance, as indicated by the yellow color coding. The turbine in the lower right, in contrast, is shown in black and is back in operation, since the team there has already been picked up by the CTV and the equipment has been retrieved by a drone. This drone is shown on the return leg, close to the service hub, and is colored orange because it is now carrying the equipment. Shortly after completion of the work at the lower-right turbine and before the snapshot was taken, the team at the upper-right turbine also finished its maintenance task. The CTV is currently en route to this turbine, or already close to it. The red icon indicates that the transfer has not yet been completed. In addition, a drone is flying toward the wind farm. Since it is flying empty before the pickup, it is shown in red.

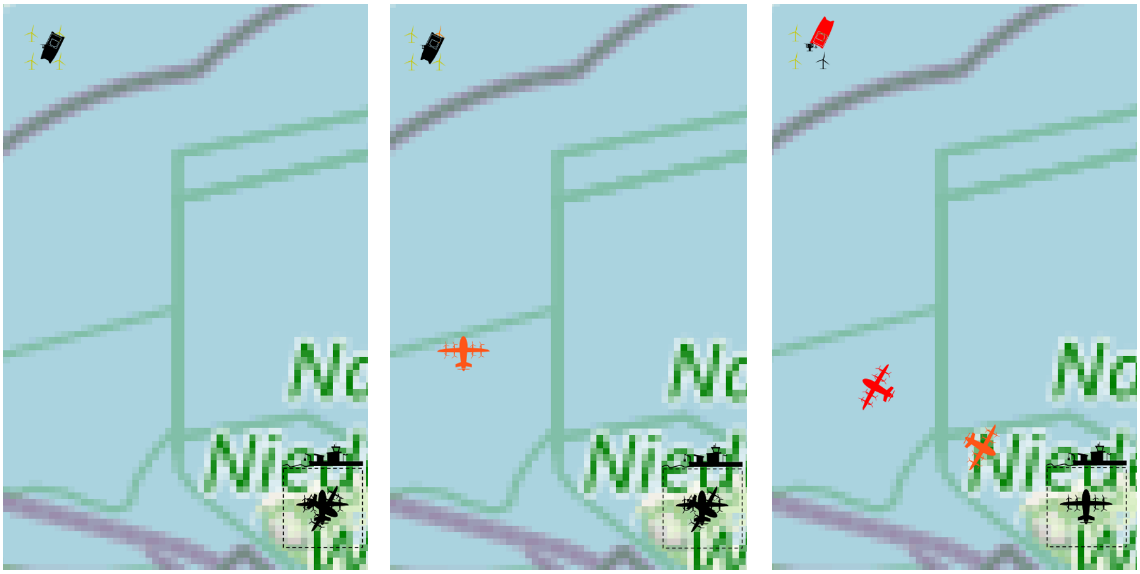

Figure 5.37: State after all Teams and Equipment were delivered (left), Spontaneous Delivery of Goods by UAV (center) and Pick Up Operations in Progress (right)

For a distance of 80 km, a maintenance duration of 3 h, and a probability of spontaneous material demands of 0.6, the previously introduced metrics are shown in Figure 5.38, where the AT M 100P/250R is deployed. Here, a converged behavior of energy production and enabled maintenance hours can again be observed from a UAV fleet size of four onward.

Total energy consumption increases noticeably with increasing UAV fleet size by up to 15%, since the UAVs are now significantly larger and more energy intensive than the smaller drones of the AT S series used for spontaneous equipment deliveries. In addition, no CTV travel can be reduced through UAV deployment. Energy production can be improved from four deployed UAVs onward. For smaller fleets, a reduction in energy production is observed, since with a limited number of aircraft it takes significantly longer until maintenance activities can start at all turbines. For the AT M series, payload is sized to supply exactly one wind turbine with all required equipment. Therefore, the maximum fleet size was aligned with the number of turbines in the wind farm. Notably, slightly smaller fleets already deliver comparable results in terms of energy production.

Quantitatively, the curve for enabled maintenance hours shows a similar behavior and indicates an increase in worked hours of more than 50% due to using UAVs for all equipment transport. As becomes clear from the trends in flight counts and energy consumption over UAV fleet size, the number of flights still increases even when eight UAVs are used. This matches the situation described previously for the initial material transport into the OWF. The impact of these additional flights at the SoS level is only slightly visible in the plot of actual energy production and is not significant at a distance of 80 km. This will change when considering results for longer distances between the OWF and the servicehub.

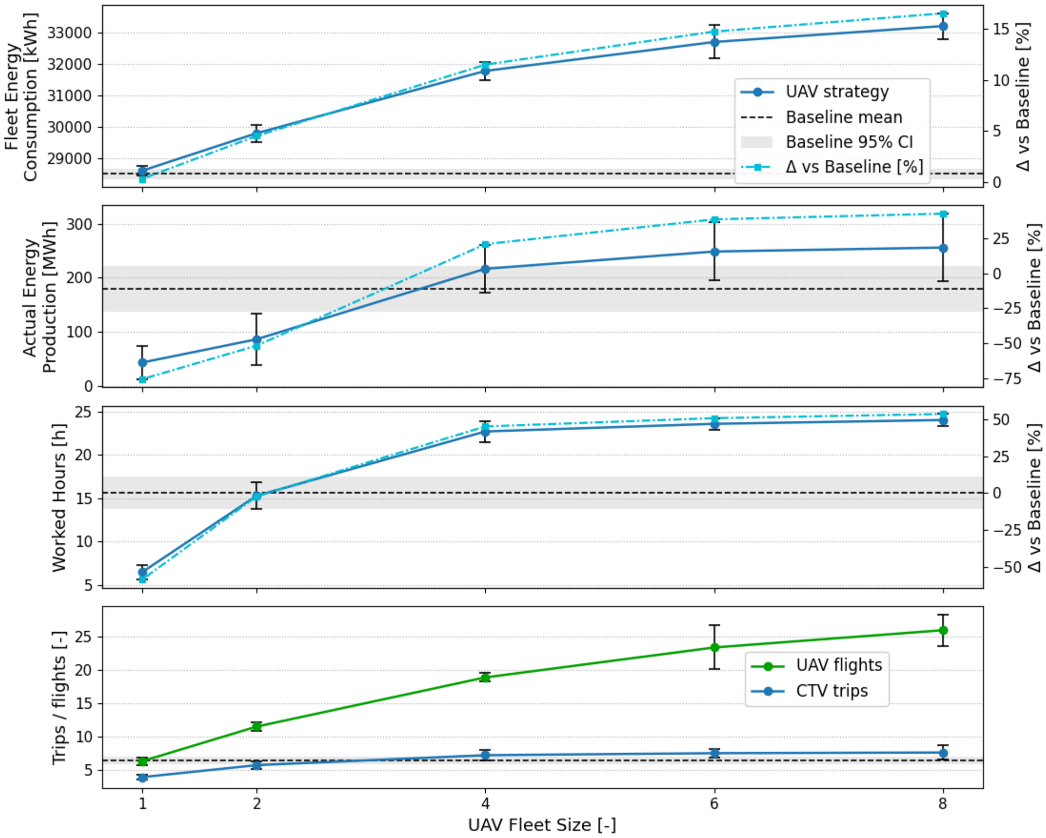

Figure 5.38: DOE Results for the CTV and AT M 100P/250R UAV for all Equipment Strategy with 3 h Maintenance Time, 0.6 Probability of spont. Demands and 80 km Distance

The results for an increased distance of 120 km are shown in Figure 5.39. While the overall curve shapes remain very similar, the advantage of a fleet of eight UAVs becomes more pronounced due to the longer flight distances. The visible step between six and eight aircraft is largely driven by the initial delivery situation. With four and six aircraft, two delivery waves of flights to the wind farm are required before all maintenance activities can start. With eight aircraft, this can be achieved in a single wave, which allows the work to be completed earlier in the day and therefore enables the wind turbines to produce energy for a longer period.

With a further increase in distance to 160 km, no qualitatively or quantitatively significant differences can be identified in the results shown in Figure 5.40.

The comparison of the relative differences to the respective baseline in Figure 5.41 shows that the improvement in maintenance hours within the wind farm is hardly dependent on distance. However, the two longer distances exhibit an increased energy demand compared to the 80 km case. The improvement in energy production shows clear distance dependencies, and the previously discussed effect of using eight UAVs is clearly visible for the 120 km and 160 km distances. The number of executed UAV flights decreases noticeably at 160 km, reflecting the combined impact of long flight legs and the constrained operational flight window.

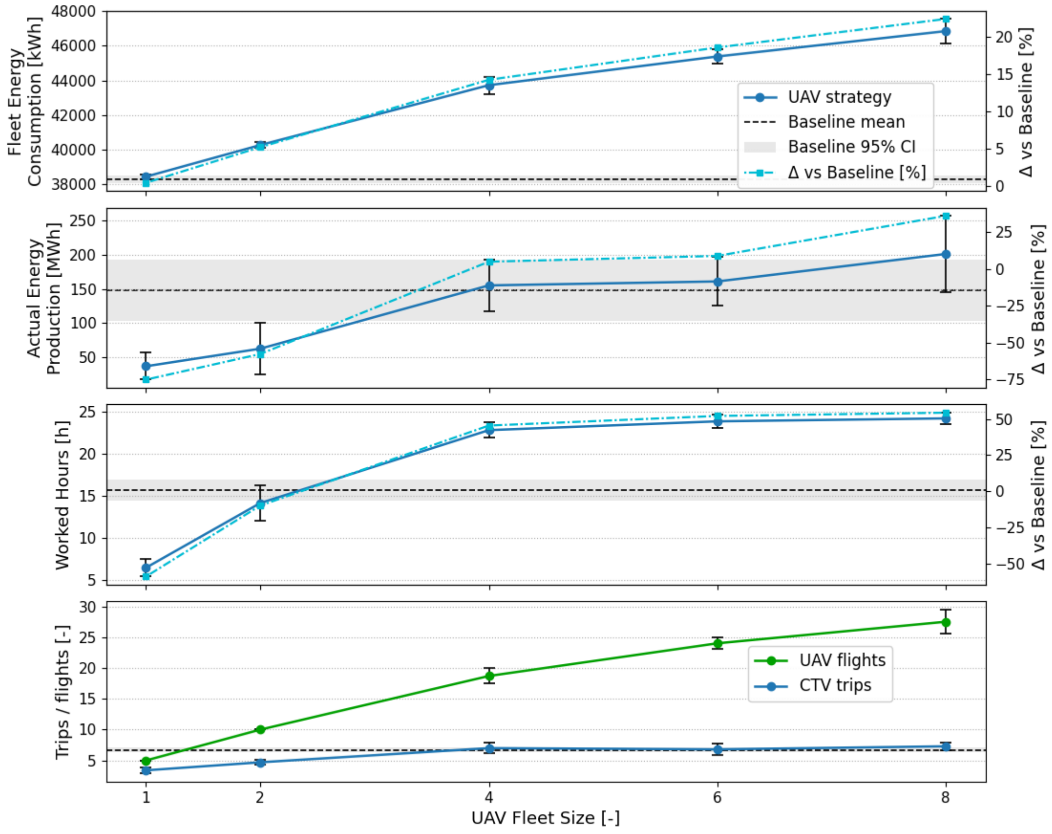

Figure 5.39: DOE Results for the CTV and AT M 100P/500R UAV for all Equipment Strategy with 3 h Maintenance Time, 0.6 Probability of spont. Demands and 120 km Distance

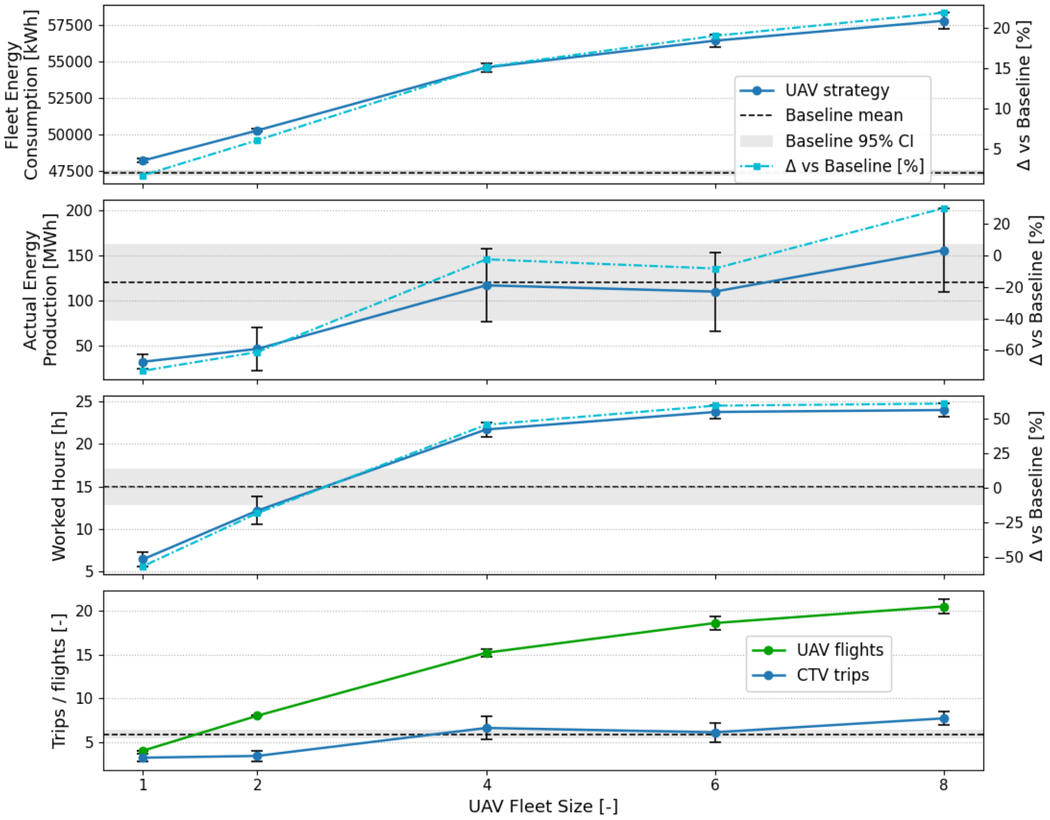

Figure 5.40: DOE Results for the CTV and AT M 100P/750R UAV for all Equipment Strategy with 3 h Maintenance Time, 0.6 Probability of spont. Demands and 160 km Distance

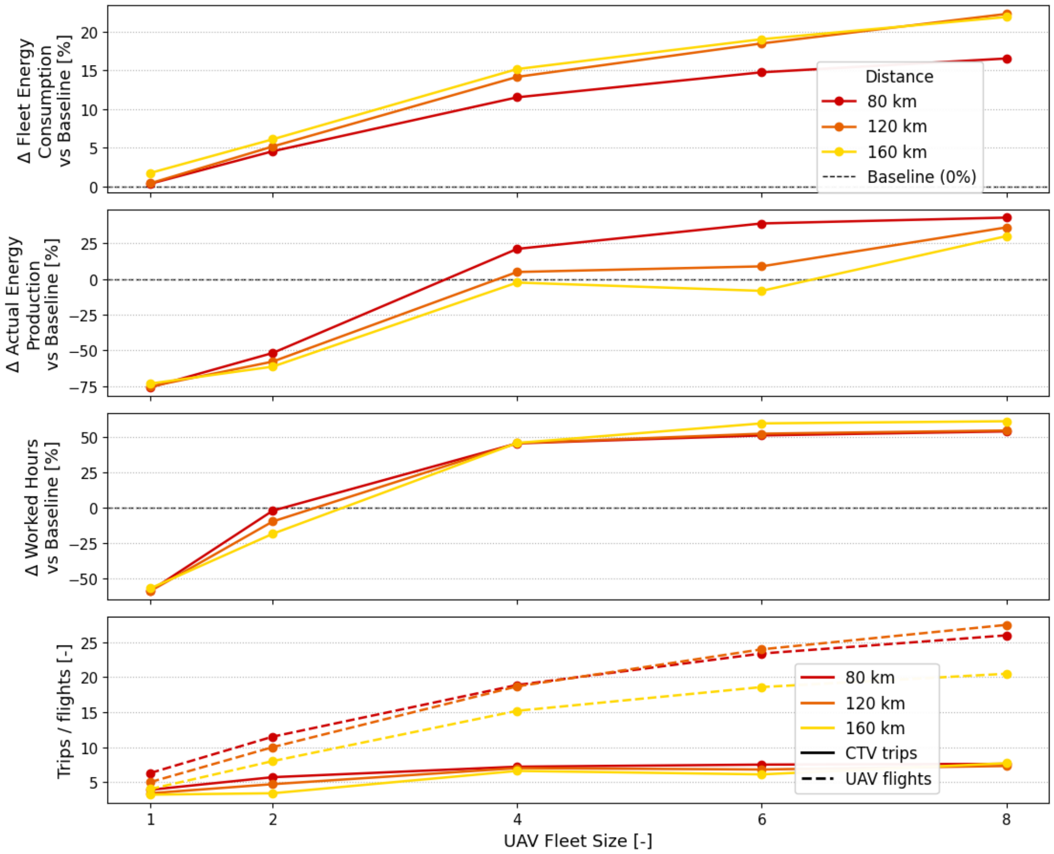

Figure 5.41: Relative Differences between the CTV Only and the CTV and AT M UAVs for all Equipment Strategy with 3 h Maintenance Time and 0.6 Probability of spont. Demands

With an increased maintenance duration, similar to the case where UAVs are used only for spontaneous deliveries, the results indicate that energy production cannot be improved and even deteriorates, although a clear improvement in enabled maintenance hours can be observed. However, this improvement decreases with increasing distance, from almost 50% at an 80 km distance to approximately 12% at 160 km. For the 80 km case, the kink in energy production and maintenance hours when using eight UAVs is still visible, whereas it is no longer apparent at larger distances. As already discussed for spontaneous deliveries by drone, the baseline vehicle is less well suited in this case, and UAV deployment cannot fully compensate for the larger distances or longer maintenance durations. Nevertheless, over a longer simulation horizon, a positive effect on energy production would also emerge.

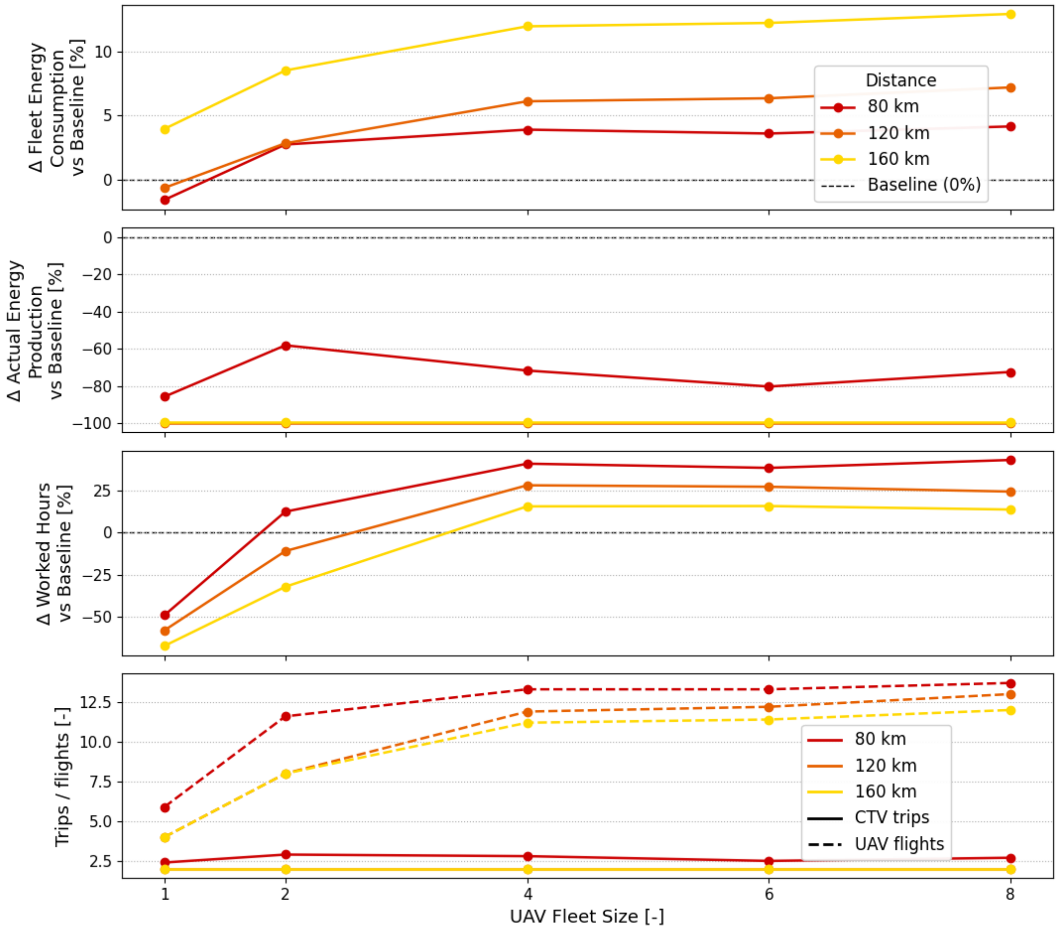

Figure 5.42: Relative Differences between the CTV Only and the CTV and AT M UAVs for all Equipment Strategy with 7 h Maintenance Time and 0.6 Probability of spont. Demands

When visualizing the maintenance time differences in three dimensions over UAV fleet size and distance, as shown in Figure 5.43, a linear relationship between the time advantage and distance becomes apparent, while an approximately logarithmic behavior can be observed with respect to UAV fleet size. The linear distance dependence occurs only for the increased maintenance hours, as becomes clear when comparing these results with those shown in Figure 5.41.

Using the complete dataset from the DOE simulations, all strategies can be compared across variations in fleet sizes, distances, and maintenance-related variables. In the fol-

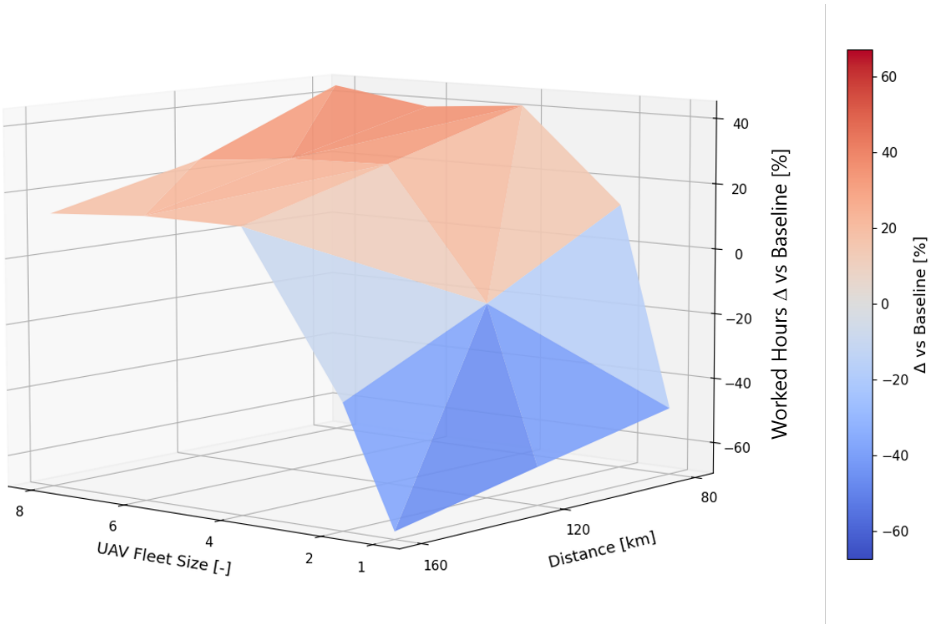

Figure 5.43: Relative Differences of Working Hours between the CTV Only and the CTV and AT M UAVs for all Equipment Strategy with 7 h Maintenance Time and 0.6 Probability of spont. Demands

lowing, the CTV-only strategy is used as the baseline, such that it represents the zero line in the percentage-difference plots. The strategy in which the CTV serves as the base asset for personnel transport and all equipment transport is performed by drones is shown as a solid red line. Strategies that use UAVs for spontaneous equipment resupply are shown as dashed lines, with an orange line for cases with a CTV as the base vehicle and blue tones for helicopter-based cases depending on helicopter fleet size. The results for the helicopter-only strategy are shown as dotted lines in green tones. A denser dot or dash pattern indicates a larger number of deployed helicopters.

Figure 5.44 presents the differences relative to the baseline for a distance of 80 km between the wind farm and the service hub, with a spontaneous demand probability of 0.3 and a maintenance duration of 3 h. As already known from the baseline study in Section 4.6, a single helicopter consumes less energy but also results in a clearly reduced number of maintenance hours and, consequently, a lower OWF energy output. Using drones for spontaneous deliveries in combination with only one helicopter does not lead to improvements. For two deployed helicopters, an improvement in energy production and a reduction in fleet energy consumption can be observed. With three deployed helicopters, UAV support also reduces fleet energy consumption, but energy production is no longer increased. No other strategy reaches the energy production level achieved in this case.

For enabled maintenance hours, the helicopter-based strategies with more than two helicopters converge with the strategy using UAVs for spontaneous deliveries toward the result achieved by the strategy that uses the CTV for personnel and UAVs for equipment, starting from a UAV fleet size of four drones. With this strategy, energy production can be improved by up to 40%, although it does not reach the results of the larger helicopter fleets. A significantly better performance, but still below the helicopter strategies, is achieved by the strategy with a CTV as the base vehicle and UAVs for spontaneous deliveries, across

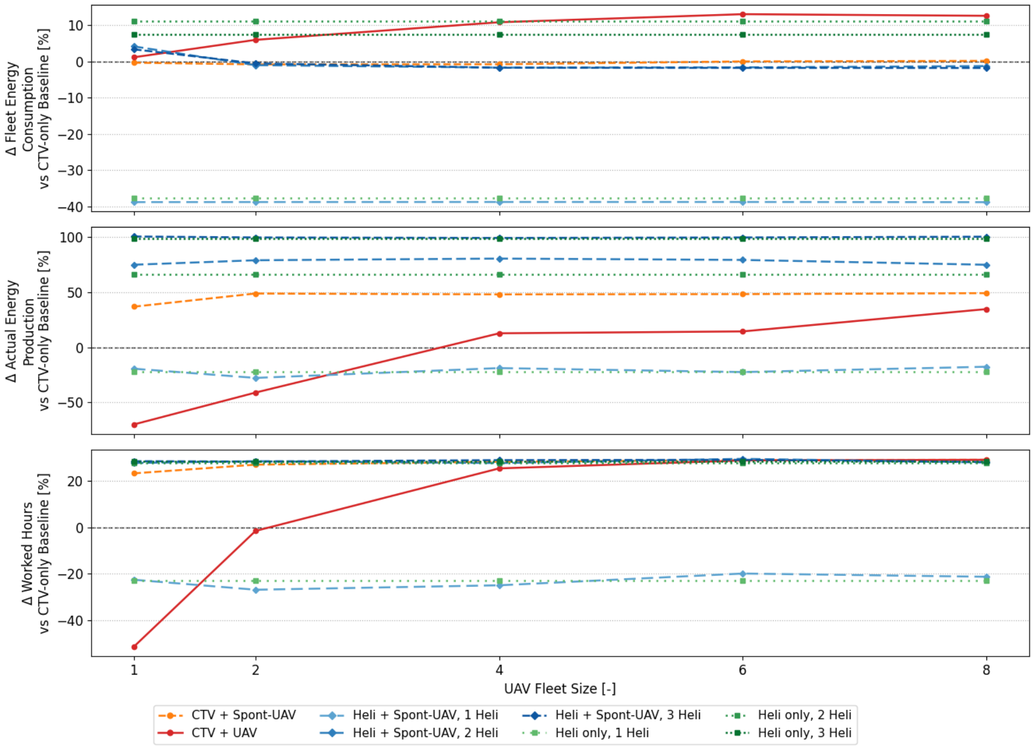

Figure 5.44: Relative Differences between all Strategies at 80 km Distance, 3 h Maintenance Time and 0.3 Probability of spont. Demands

all UAV fleet sizes. Here, an increase in energy output of 50% can be observed. Notably, using UAVs for all cargo deliveries from a fleet size of four drones onward reaches the same level, and even slightly exceeds, the helicopter-based strategies.

This trend becomes significantly more pronounced with increasing distance, as can be observed for a distance of 120 km in Figure 5.45. With a fleet size of eight UAVs, corresponding to the number of turbines requiring maintenance, the CTV-and-UAV strategy now also exceeds the energy production that can be achieved with two helicopters, even when UAV support is included. For maintenance hours, this applies only in comparison to the purely helicopter-based strategies with up to two helicopters. In general, it should be noted that using UAVs for spontaneous deliveries improves the two-helicopter cases even at smaller UAV fleet sizes and reduces total energy consumption. If the distance is increased again to 160 km, the situation shown in Figure 5.46 is obtained. Here, it can be seen that even when three helicopters are deployed, supplementary drone operations not only reduce the consumed energy, but also result in increased energy production. The CTV strategies with drone support achieve, from a fleet size of four onward, approximately the same maintenance hours for the technician teams as would otherwise only be possible by deploying three helicopters. If the probability of spontaneous demands is increased to 0.6, as shown in Figure 5.47 for a distance of 160 km, a fundamentally significantly higher enabled energy production is observed across all strategies in comparison. In addition, the energy demand increases noticeably, particularly for the case of three helicopters without additional UAV support. At the same time, the combined use of UAVs, especially in the case of three deployed helicopters, results in a clear reduction in energy demand. This strategy also yields the highest values for enabled energy production. The strategy that uses UAVs for all equipment transports slightly exceeds, at maximum fleet size,

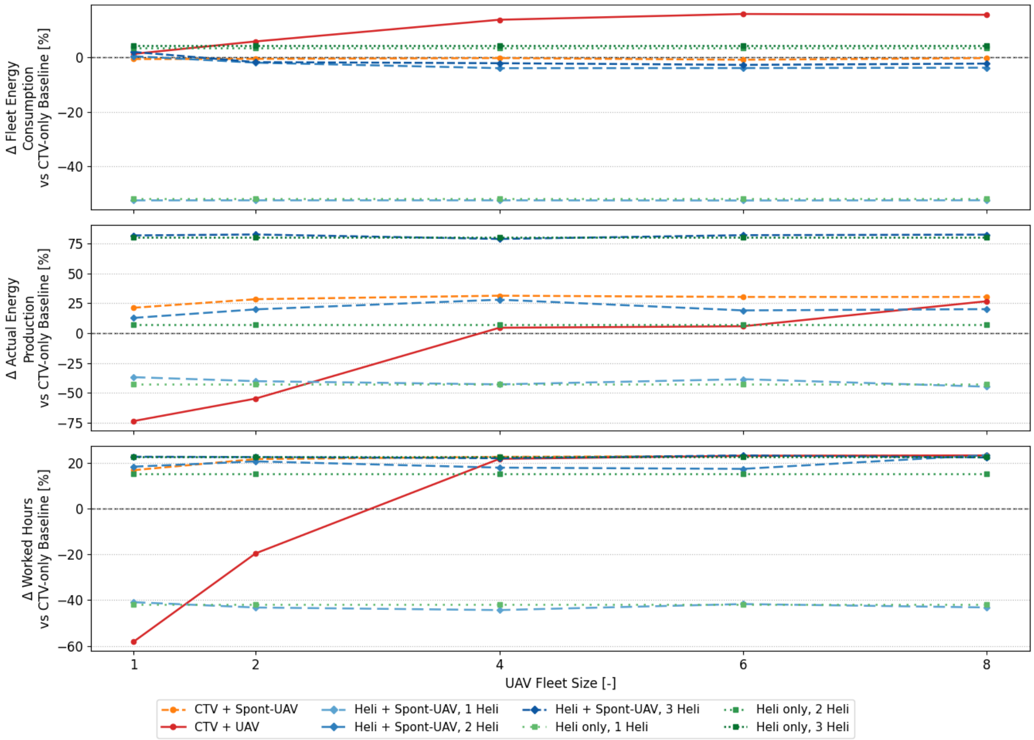

Figure 5.45: Relative Differences between all Strategies at 120 km Distance, 3 h Maintenance Time and 0.3 Probability of spont. Demands

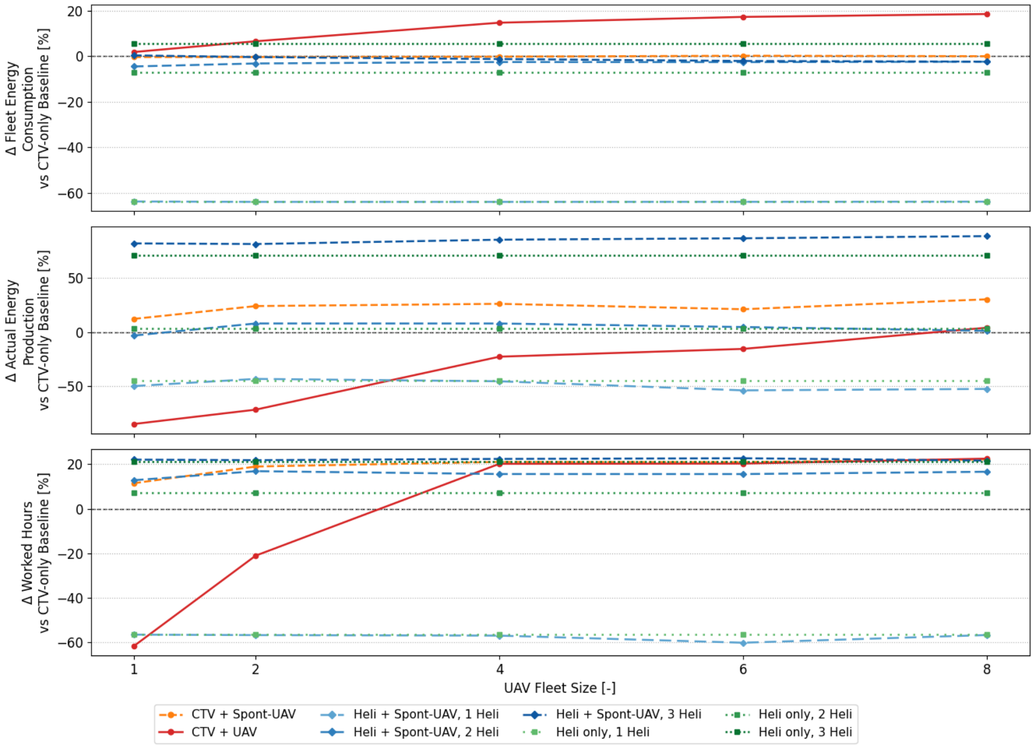

Figure 5.46: Relative Differences between all Strategies at 160 km Distance, 3 h Maintenance Time and 0.3 Probability of spont. Demands

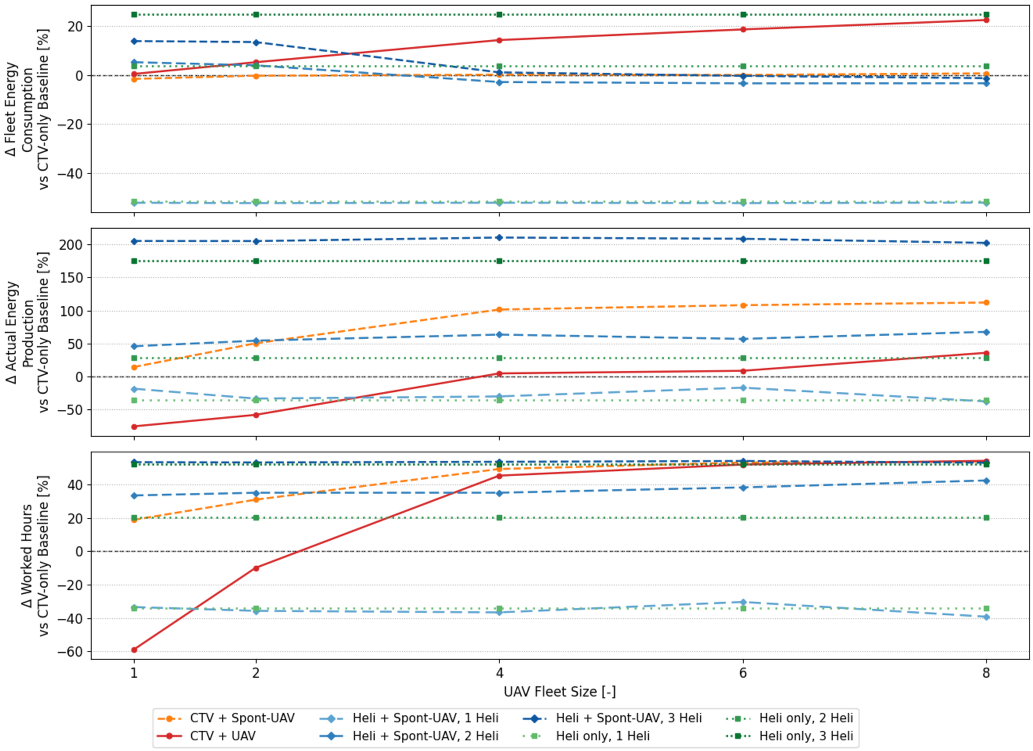

Figure 5.47: Relative Differences between all Strategies at 120 km Distance, 3 h Maintenance Time and 0.6 Probability of spont. Demands

the energy production values achieved with only two helicopters and therefore provides an improvement of approximately 35% relative to the baseline. In contrast, the strategy with a CTV as the personnel transport vehicle and UAVs only for spontaneous deliveries achieves an improvement of more than 100% and thus also exceeds the case of two helicopters with supplementary drone operations. For both probability cases, and increasingly for higher interruption probabilities, UAV deployment therefore provides improvements on the selected metrics, with both helicopter-based and vessel-based strategies benefiting significantly.

If the required maintenance duration per wind turbine is increased to 7 h, the curves shown in Figure 5.48 are obtained. It must again be noted that, under the baseline and also for small helicopter fleets, the longer maintenance duration leads to numerous maintenance processes not being completed. This means that several turbines do not return to energy-producing operation within the simulation period. The relative values for energy production are therefore not meaningful to interpret in this case. Consequently, the evaluation of enabled maintenance hours becomes more relevant, since in a multi-day simulation process this would also translate into increased wind farm energy output. In this case, no clear advantage of UAVs in combined use with helicopters is observed beyond a reduction in total energy consumption. In contrast, using UAVs for spontaneous deliveries as a supplement to the CTV, already from two drones onward, and the strategy in which all equipment transport is performed by drones, from four deployed aircraft onward, show comparatively good results that lie between the outcomes achieved with two and three deployed helicopters.

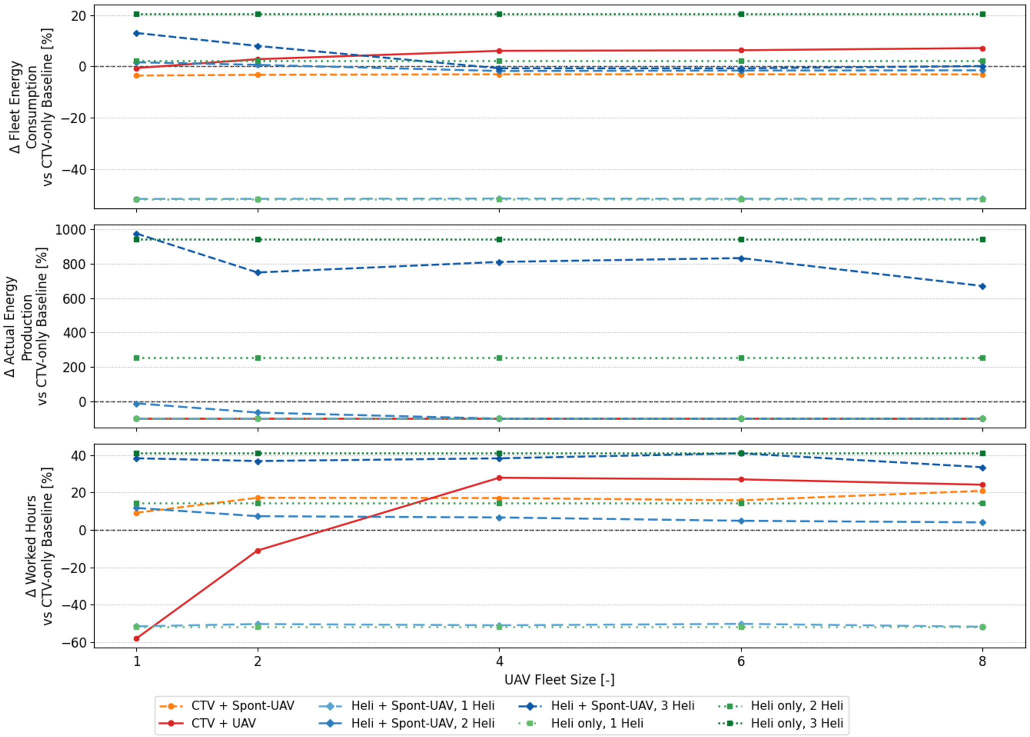

Figure 5.48: Relative Differences between all Strategies at 120 km Distance, 7 h Maintenance Time and 0.6 Probability of spont. Demands

5.2.5 Assessment of larger UAVs

The previously discussed results for the strategy using a CTV for personnel and UAVs for all equipment transport were fully simulated using the AT M designs. Due to the limited payload, these aircraft were able to supply only one wind turbine with maintenance equipment per flight. If spontaneous deliveries occurred within the simulation, these items cannot be retrieved together with the remaining equipment during pickup, and an additional flight is required. The AT L designs, with twice the payload, can supply two turbines. In general, it must be considered that range must also cover the additional hover phase. To investigate how a larger UAV design behaves at the SoS level, the same simulation runs were therefore also performed with the AT L variants, with the design range again adjusted to the wind farm distance.

Figure 5.49 reports the percentage differences relative to the AT M simulation runs for the shorter maintenance duration of 3 h and a probability of spontaneous material demands of 0.3. As expected, the energy demand of the larger UAVs increases noticeably and shows a strong dependence on wind farm distance. During the initial material delivery, two demands are addressed by one UAV rather than two. However, for subsequent demands, the queuing process is no longer simultaneous. Since the available UAVs do not wait for additional potential demands, the larger UAVs in this case perform the same flights with the same payload as the smaller drones. This is also reflected by the comparatively small reduction in flight counts. With increasing fleet size, the probability that a UAV is available at the time a demand occurs becomes higher. In that case, the demand can be accepted immediately, which explains the increase, particularly at larger distances. When considering enabled wind farm energy production, it is also evident that for small fleet sizes there is in fact an advantage of the larger drones. For larger fleets, however,

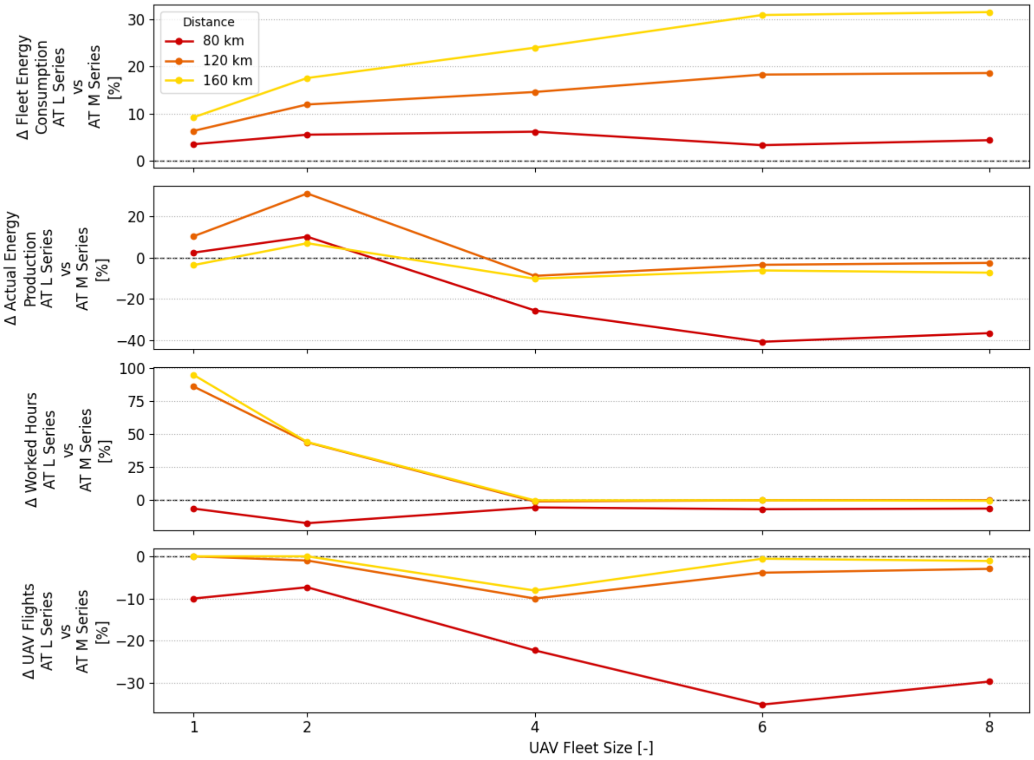

Figure 5.49: Relative Differences between the AT M and AT L Series of UAVs at 3 h Maintenance Time and 0.3 Probability of spont. Demands

a disadvantage emerges, most clearly for the shortest distance of 80 km. Since cruise speed is the same for all drones, the hover time at the first stop becomes relevant. In contrast, the smaller drones always perform a direct flight to the respective turbine. With larger fleet sizes, a drone is almost always available, such that direct deliveries without multiple stops can be executed faster. At the shortest distance, this effect is particularly pronounced due to the comparatively short flight time.

This behavior is also reflected in the performed maintenance hours. Here, for the two larger distances, the larger drones show clear advantages and can achieve substantial increases in enabled maintenance hours of more than 80% with fewer aircraft. However, with increasing fleet size the effect clearly decreases and converges from a fleet size of four aircraft onward to the respective result obtained with smaller drones. The negative effect for short distances due to the additional time required to deliver to the second asset also becomes very pronounced. These results suggest a dependence on the hover time above the wind turbines, which is assumed constant for all simulations, and on cruise speed. Further investigations and parameter studies would therefore be well motivated.

An increase in the probability of spontaneous material resupply during maintenance activities, as shown in Figure 5.50, does not yield any qualitatively or quantitatively significant changes. When increasing the maintenance duration, with the results for 7 h shown in Figure 5.51, it must be considered, as discussed previously, that maintenance tasks are typically not completed and therefore no, or only very limited, energy production can occur. However, the trend of improvements in enabled maintenance hours follows the same qualitative and quantitative behavior as for the shorter maintenance duration. It can therefore be stated that the differences between the aircraft designs are not strongly dependent on

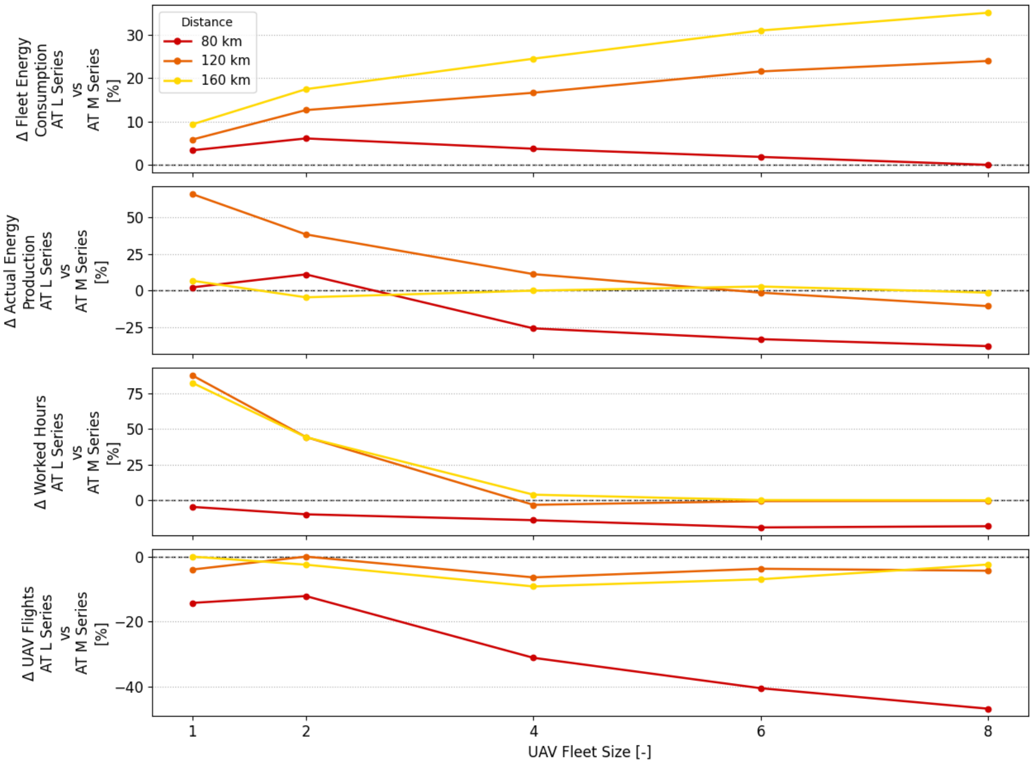

Figure 5.50: Relative Differences between the AT M and AT L Series of UAVs at 3 h Maintenance Time and 0.6 Probability of spont. Demands

maintenance duration or on the probability of spontaneous demands. At low fleet sizes, improvements in enabled maintenance hours and energy production can nevertheless be achieved, provided that an increased energy consumption of up to 20% is accepted.

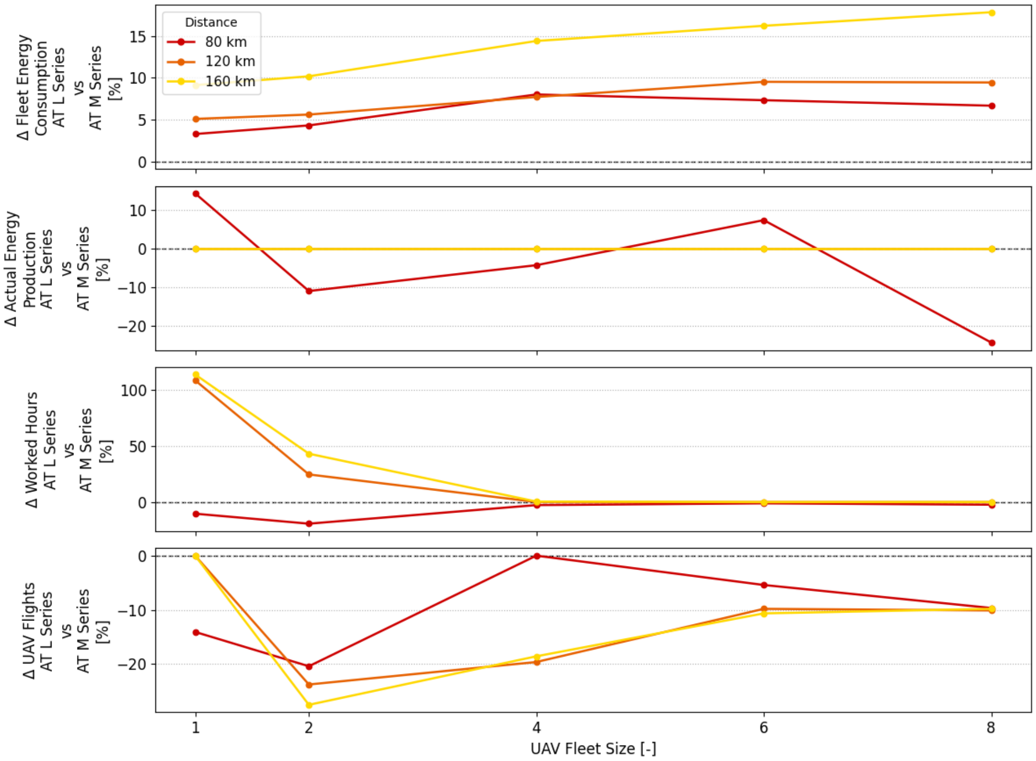

Figure 5.51: Relative Differences between the AT M and AT L Series of UAVs at 7 h Maintenance Time and 0.3 Probability of spont. Demands

Chapter 6

Conclusion and Future Work

The thesis sought to examine how UAVs and logistics strategies based on them at a SoS level influence offshore wind energy generation, with particular emphasis on the influence of the payload and range of the aircraft and the distance of a wind farm from the coast. To answer this question, the DLR SoSID toolkit was extended, suitable vehicle agents were developed, and ConOps were derived and integrated into the simulation environment.

The simulation results have shown that the ConOps, vehicle characteristics, environmental conditions, and simulation parameters introduce various non-linear effects at the SoS level. This confirms the suitability of agent-based modeling for simulating offshore logistics with UAV integration, as well as the appropriateness of treating the problem as a system of systems. Based on the results obtained, the effects of different drones and deployment strategies on energy production and maintenance processes could be quantified for the assumptions and scenarios considered, thereby answering the research question posed:

Positive effects from deploying drones in combination with vessels and helicopters were demonstrated through reductions in fleet energy consumption and increased wind turbine availability. At the same time, it became clear that the baseline assets on which drone-supported strategies build must already be selected appropriately in terms of vehicle type and fleet size for the given maintenance scenario. The use of drones for spontaneous deliveries of spare parts and tools required during maintenance, which has already been demonstrated in real-world operations, proved to be highly effective. This supports further expansion and development of this approach within the wind energy industry toward an economically viable and routine component of OWF O&M operations.

Using drones for all equipment transport also yielded favorable results with respect to enabled energy production and maintenance hours at the turbines within a single simulation day, but it also resulted in high energy consumption. The use of larger drones could improve energy production at smaller fleet sizes, but it led to even higher energy consumption. Due to the less mature technology, the need for more detailed studies and cost models becomes apparent in this context.

With the framework developed in this thesis, numerous further investigations and parameter variations are possible. As an immediate next step, multiple variations of equipment masses and the number of packages can be simulated and their effects can be evaluated, as well as the impact of increased or reduced cruise speeds of the UAVs. The effects of adverse weather conditions that exceed the operational limits of the vehicles and would therefore disrupt maintenance operations can also be investigated. Another relevant aspect would be an evaluation of the influence of larger wind turbines. The aircraft variations performed in this work were intentionally focused on the UAVs, while the CTV and helicopter models were not varied. However, other existing helicopter types or new concepts such as compound helicopter or tiltrotor configurations could be simulated in the same manner and may enable more efficient and more flexible operations [195]. The required data can be derived from design tools or from published studies and integrated directly into the simulation using the implemented helicopter modeling approach [196, 128].

Due to the high complexity of the modeled system of systems, a number of simplifications had to be applied. These can be addressed in the future by dedicated modules or corresponding extensions of the implemented code to represent the processes at higher resolution. With regard to the selection of vehicles and strategies, OSV vessels could be included as additional assets. In terms of vehicle allocation, an auction-based system that assigns available vehicles to tasks more flexibly could be implemented. This approach has already been implemented for other scenarios within the SoSID toolkit and can be adapted for the offshore industry and the specific use case by applying appropriate parameter values [132]. More flexible reactions to demands that arise during an ongoing flight, as well as combining deliveries and pickups within a single mission, would also constitute valuable extensions.

In addition, further aspects of the offshore environment could be investigated with respect to their influence on maintenance operations using different transport modes. Visibility conditions are a primary factor in this context. Icing conditions and collision risks with other airspace users, such as civil and military aviation and bird flocks, as well as with maritime traffic on the water, are also conceivable. Regarding operational procedures within the wind farm, a model for team transfers onto wind turbines could be implemented. Based on environmental data such as wave height and including a stochastic component, such a model could determine the duration and the overall success of a transfer.

A particularly relevant extension that could form the next development step would be the development and integration of a cost model that accounts for generated energy, maintenance costs, personnel costs, and vehicle costs. Approaches that could serve as a basis already exist [103, 197].

In summary, this thesis enabled extensive simulations with promising results for the benefitial use of UAVs for offshore wind energy logistics, but the framework can be expanded and optimized far beyond the scope of the performed investigations and coupled with experimental results obtained from test campaigns.

Bibliography

[1] John von Neumann. “The Mathematician”. In: *The Works of the Mind*. University of Chicago Press, 1947, pp. 180–196.

[2] Kaspar Knorr et al. *Energiewirtschaftliche Bedeutung der Offshore-Windenergie für die Energiewende*. Tech. rep. Fraunhofer IWES, 2017.

[3] Christopher Jung and Dirk Schindler. “The properties of the global offshore wind turbine fleet”. In: *Renewable and Sustainable Energy Reviews* 186 (2023). ISSN: 1364-0321. DOI: `https://doi.org/10.1016/j.rser.2023.113667`. URL: `https://www.sciencedirect.com/science/article/pii/S1364032123005245`.

[4] Alexandra Ionelia Diaconita, Gabriel Andrei, and Liliana Rusu. “An overview of the offshore wind energy potential for twelve significant geographical locations across the globe”. In: *Energy Reports* 8 (2022). Selected papers from 2022 7th International Conference on Advances on Clean Energy Research, pp. 194–201. ISSN: 2352-4847. DOI: `https://doi.org/10.1016/j.egyr.2022.10.193`. URL: `https://www.sciencedirect.com/science/article/pii/S2352484722021291`.

[5] *Windenergie-auf-See-Gesetz (WindSeeG)*. Bundesgesetzblatt I. § 1 Abs. 2. 2017. URL: `https://www.gesetze-im-internet.de/windseeg/`.

[6] Giuseppe Costanzo, Guy Brindley, and Pierre Tardieu. *Wind Energy in Europe: 2024 Statistics and the Outlook for 2025–2030*. Additional contributors: Alexandre Frémaux, Francesco Meloni, Lizet Ramirez. Editor: Rory O’Sullivan. Brussels: WindEurope, 2025. URL: `https://windeurope.org/data/products/wind-energy-in-europe-2024-statistics-and-the-outlook-for-2025-2030/`.

[7] European Commission. *An EU Strategy to harness the potential of offshore renewable energy for a climate neutral future*. Communication COM/2020/741 final, ELI-Number 52020DC0741. Brussels, 2020. URL: `https://eur-lex.europa.eu/legal-content/EN/TXT/?uri=CELEX:52020DC0741`.

[8] Frauke Reinig. *Mehr Windkraft, mehr Energiesicherheit*. NDR. Jan. 26, 2026. URL: `https://www.tagesschau.de/inland/nordseegipfel-energieversorgung-fazit-100.html` (visited on 01/27/2026).

[9] Matthias Ibeler. *Offshore-Windpark EnBW Baltic 1*. Accessed on 2025-02-12. EnBW. 2015. URL: `https://www.enbw.com/media/presse/images/mediathek/ausschnitt-enbw-windpark-baltic-1.jpg`.

[10] 50Hertz Transmission GmbH. *Baltic 1*. Accessed on 07 December 2025. 2025. URL: `https://www.50hertz.com/de/Netz/Netzausbau/RealisierteProjekteseit2012/Baltic1` (visited on 02/12/2025).

[11] *EnBW-Windpark He Dreiht*. 2025. URL: `https://www.enbw.com/unternehmen/themen/windkraft/offshore-windpark-he-dreiht/` (visited on 07/07/2025).

[12] C. Guedes Soares and H. Díaz. “Review of the current status, technology and future trends of offshore wind farms”. In: *Ocean Engineering* 209 (2020). ISSN: 0029-8018. DOI: `10.1016/j.oceaneng.2020.107381`.

[13] *NHV secures contract with Vestas for offshore wind operations in North Sea with super medium aircraft*. en. 2023. URL: `https://verticalmag.com/press-releases/nhv-secures-contract-with-vestas-for-offshore-wind-operations-in-north-sea-with-super-medium-aircraft/` (visited on 01/03/2026).

[14] Stefan Thimm. *Kein Offshore-Ausbau ohne Rettung*. 2023. URL: `%7Bhttps://background.tagesspiegel.de/energie-und-klima/briefing/kein-offshore-ausbau-ohne-rettung%7D` (visited on 07/07/2025).

[15] Iver Bakken Sperstad et al. "Testing the Robustness of Optimal Access Vessel Fleet Selection for Operation and Maintenance of Offshore Wind Farms". In: *Ocean Engineering* 145 (2017), pp. 334–343. DOI: `10.1016/j.oceaneng.2017.09.009`. URL: `https://www.sciencedirect.com/science/article/pii/S0029801817305280`.

[16] A. Allal et al. "Multi-agent based simulation-optimization of maintenance routing in offshore wind farms". In: *Computers & Industrial Engineering* 157 (2021), p. 107342. ISSN: 0360-8352. DOI: `10.1016/j.cie.2021.107342`.

[17] Marcel Wiggert et al. *Offshore TIMES: Offshore Transport, Inspection and Maintenance Software: Abschlussbericht*. Tech. rep. Bremerhaven: Fraunhofer-Institut für Windenergiesysteme (IWES), 2018. DOI: `10.2314/GBV:1032624132`. URL: `https://www.tib.eu/de/suchen/id/TIBKAT%3A1032624132`.

[18] Alexander Donkels et al. "Advances on the integration of transport drones into offshore wind farms". In: *CEAS Aeronautical Journal* (2025). DOI: `10.1007/s13272-025-00857-8`.

[19] RWE Offshore Wind GmbH. *RWE leistet Pionierarbeit mit dem Einsatz von Transportdrohnen in Offshore-Windparks*. Press release. Essen, Germany, 2025. URL: `https://www.rwe.com/-/media/RWE/documents/07-presse/rwe-offshore-wind-gmbh/2025/2025-10-15-rwe-leistet-pionierarbeit-mit-dem-einsatz-von-transportdrohnen-in-offshore-windparks.pdf`.

[20] RWE. *RWE successfully pioneers cargo drone operations at offshore wind farms*. Accessed on 07 December 2025. 2025. URL: `https://www.rwe.com/-/media/RWE/images/07-presse/rwe-offshore-wind-gmbh/open-graph/2025/OG-2025-10-15-rwe-successfully-pioneers-cargo-drone-operations-at-offshore-wind-farms.jpg`.

[21] Chao-Hung Chiang. "Assessing Regional Suitability for UAV Cargo Operations: Case of Taiwan". In: *Journal of Aeronautics, Astronautics and Aviation* 57.5 (2025), pp. 1289–1298. DOI: `10.6125/JoAAA.202505_57(5).10`.

[22] Judy E. Scott and Carlton H. Scott. "Drone Delivery Models for Healthcare". In: *Hawaii International Conference on System Sciences*. 2017. URL: `https://api.semanticscholar.org/CorpusID:27433971`.

[23] Taha Benarbia and Kyandoghere Kyamakya. "A Literature Review of Drone-Based Package Delivery Logistics Systems and Their Implementation Feasibility". In: *Sustainability* 14.1 (2022). ISSN: 2071-1050. DOI: `10.3390/su14010360`. URL: `https://www.mdpi.com/2071-1050/14/1/360`.

[24] Timothy Papandreou. *Beyond Hype: Drone Delivery Takes Flight In 2024*. Forbes. Mar. 2024. URL: `https://www.forbes.com/sites/timothypapandreou/2024/03/13/beyond-hype-drone-delivery-takes-flight-in-2024/`.

[25] Christian Seelos et al. *Making Health Innovations Thrive in Africa*. Oct. 2024. URL: `https://ssir.org/articles/entry/zipline-health-innovations-africa`.

[26] Johann C. Dauer, ed. *Automated Low-Altitude Air Delivery: Towards Autonomous Cargo Transportation with Drones*. Research Topics in Aerospace. Cham, Switzer-

land: Springer, 2022. ISBN: 978-3-030-83143-1. DOI: 10.1007/978-3-030-83144-8. URL: https://doi.org/10.1007/978-3-030-83144-8.

[27] Equinor ASA. *Equinor completes world's first logistics operation with a drone to an offshore installation*. Aug. 2020. URL: https://www.equinor.com/news/archive/20200828-drone-transport-troll.

[28] Kylie Ball and Guillermo Juarez. *Analysis of Traditional Aerial Systems and Fuel-Efficient Unmanned Aerial Vehicles (UAV) in Support of Spare Parts Delivery of Ships at Sea*. NPS-CE-25-460. Monterey, CA: Naval Postgraduate School, 2025.

[29] Federal Aviation Administration. *Aeronautical Information Manual (AIM): Chapter 11, Section 6. Advanced Air Mobility*. Version Change 1. United States Department of Transportation, Federal Aviation Administration. URL: https://www.faa.gov/air_traffic/publications/atpubs/aim_html/chap11_section_6.html (visited on 01/20/2026).

[30] BDLI (German Aerospace Industries Association). *Advanced Air Mobility. Mobility in the third dimension*. en. BDLI. URL: https://www.bdli.de/en/key-sectors/advanced-air-mobility (visited on 01/20/2026).

[31] BAE Systems. *What is Advanced Air Mobility*. en. BAE Systems. URL: https://www.baesystems.com/en-us/definition/what-is-advanced-air-mobility (visited on 01/20/2026).

[32] PwC Drone Powered Solutions. *Advanced Air Mobility: From Concept to Commercial Reality*. en. PwC, 2025. URL: https://cee.pwc.com/pdf-nf/PwC_DPS_Global_AAM_Report.pdf (visited on 01/20/2026).

[33] Federal Ministry for Digital and Transport (BMDV). *Advanced Air Mobility: Strategy for the Federal Ministry for Digital and Transport*. en. Strategy paper. Version 1.01. Bonn, Germany: Federal Ministry for Digital and Transport (BMDV), Feb. 2025. URL: https://www.bmv.de/SharedDocs/EN/Documents/K/advanced-air-mobility-strategy.pdf?__blob=publicationFile (visited on 01/20/2026).

[34] Alexander Donkels et al. "An Approach for Integration of Transport Drones Into Offshore Wind Farms". In: *DLRK*. Stuttgart: DGLR, 2023.

[35] Osita Ugwueze et al. "An Efficient and Robust Sizing Method for eVTOL Aircraft Configurations in Conceptual Design". In: *Aerospace* 10.3 (2023). ISSN: 2226-4310. DOI: 10.3390/aerospace10030311. URL: https://www.mdpi.com/2226-4310/10/3/311.

[36] Patrick Ratei. "Conceptual Aircraft Design and Comparison of Different eVTOL Aircraft for Urban Air Mobility". Project Thesis. DLR e.V., May 2021. URL: https://elib.dlr.de/148037/.

[37] Yaoming Zhou, Haoran Zhao, and Yaolong Liu. "An evaluative review of the VTOL technologies for unmanned and manned aerial vehicles". In: *Computer Communications* 149 (2020), pp. 356–369. ISSN: 0140-3664. DOI: https://doi.org/10.1016/j.comcom.2019.10.016. URL: https://www.sciencedirect.com/science/article/pii/S014036641930996X.

[38] Schiebel. *Camcopter S-100 system*. URL: https://schiebel.net/products/camcopter-s-100-system-2/.

[39] DJI. *Flycart 30 Technische Daten*. URL: https://www.dji.com/de/flycart-30/specs.

[40] Skyways. *Skyways cargo UAV portfolio*. URL: https://www.skyways.com/.

[41] Dufour Aerospace. *Aero-200 product page*. URL: https://www.dufour.aero/aero-200.

[42] Bell. *Eagle Eye Tiltrotor UAV*. URL: https://www.naval-technology.com/projects/belleagleeyeuav/.

[43] Thorben Hammer and Stefanie de Graaf. “EVALUATION OF HYBRID ELECTRIC POWERTRAIN TOPOLOGIES AND THEIR INTEGRATION IN FUTURE AIRCRAFT CONCEPTS FOR GENERAL AVIATION”. In: *Aerospace Europe Conference 2023 – 10*TH *EUCASS – 9*TH *CEAS*. 2023. DOI: `10.13009/EUCASS2023-908`. URL: `https://elib.dlr.de/200234/`.

[44] Werner Pluta. *DHL-Paketkopter: Post testet fliegende Arzneimittel-Lieferung nach Juist*. de. Golem.de. Sept. 24, 2014. URL: `https://www.golem.de/news/dhl-paketkopter-post-testet-fliegende-arzneimittel-lieferung-nach-juist-1409-109440.html` (visited on 01/21/2026).

[45] Imperial War Museums. *A Brief History of Drones*. en. Imperial War Museums. URL: `https://www.iwm.org.uk/history/a-brief-history-of-drones` (visited on 01/21/2026).

[46] Gyrodyne Helicopter Historical Foundation. *The Model QH-50C DASH*. en. Gyrodyne Helicopter Historical Foundation. 2013. URL: `https://www.gyrodynehelicopters.com/qh-50c1.htm` (visited on 01/21/2026).

[47] Clinton Purtell, Seock-Jin Hong, and Brian Hiatt. “Bibliometric analysis on advanced air mobility and drones”. In: *Journal of Air Transport Management* 116 (2024), p. 102569. ISSN: 0969-6997. DOI: `https://doi.org/10.1016/j.jairtraman.2024.102569`. URL: `https://www.sciencedirect.com/science/article/pii/S0969699724000346`.

[48] Francesco Betti Sorbelli. “UAV-Based Delivery Systems: A Systematic Review, Current Trends, and Research Challenges”. In: *ACM J. Auton. Transport. Syst.* 1.3 (May 2024). DOI: `10.1145/3649224`. URL: `https://doi.org/10.1145/3649224`.

[49] Simon Zieher et al. “Drones for automated parcel delivery: Use case identification and derivation of technical requirements”. In: *Transportation Research Interdisciplinary Perspectives* 28 (2024), p. 101253. ISSN: 2590-1982. DOI: `https://doi.org/10.1016/j.trip.2024.101253`. URL: `https://www.sciencedirect.com/science/article/pii/S2590198224002392`.

[50] BBC News. *Amazon makes first drone delivery*. en. BBC. Dec. 14, 2016. URL: `https://www.bbc.com/news/technology-38320067` (visited on 01/21/2026).

[51] Katherine Tangalakis-Lippert. *Burrito per Drohne: Wo die Liefer-Revolution vor dem Wendepunkt steht*. de. Business Insider Deutschland. Oct. 6, 2025. URL: `https://www.businessinsider.de/wirtschaft/burrito-per-drohne-wo-die-liefer-revolution-vor-dem-wendepunkt-steht/` (visited on 01/21/2026).

[52] Annie Palmer. *Amazon resumes drone deliveries after two-month pause*. en. CNBC. Mar. 31, 2025. URL: `https://www.cnbc.com/2025/03/31/amazon-resumes-drone-deliveries-after-two-month-pause.html` (visited on 01/21/2026).

[53] pat. *DHL gibt Drohnenpläne auf - kein »fliegender Postbote«*. de. DER SPIEGEL. Aug. 8, 2021. URL: `https://www.spiegel.de/wirtschaft/ausgeflogen-dhl-gibt-drohnenplaene-auf-a-aeb5a25d-3c3e-4f8a-8825-15ba53d12826` (visited on 01/21/2026).

[54] Wingcopter. *Einkäufe aus der Luft: Wingcopter-Drohnen liefern erstmalig in Deutschland Güter des täglichen Bedarfs*. de. Wingcopter GmbH. Oct. 5, 2023. URL: `https://wingcopter.com/odenwald_liefermichel2` (visited on 01/21/2026).

[55] Therese Meitinger. *Lieferdrohnen: Erster Linienflugbetrieb in Deutschland startet*. de. LOGISTIK HEUTE. Feb. 21, 2024. URL: `https://logistik-heute.de/news/lieferdrohnen-erster-linienflugbetrieb-deutschland-startet-87802.html` (visited on 01/21/2026).

[56] Asklepios Kliniken. *Deutschlandpremiere: Asklepios startet ersten Drohnen- Linienflugbetrieb für Laborproben*. de. Asklepios Kliniken GmbH & Co. KGaA. Mar. 24,

2025. URL: https://www.asklepios.com/konzern/unternehmen/aktuelles/meldungen/meldung/20250324-deutschlandpremiere-erster-linienflugbetrieb-laborproben (visited on 01/21/2026).

[57] Medifly Hamburg. *Projektbeschreibung*. de. Medifly Hamburg. URL: https://medifly.hamburg/projektbeschreibung/ (visited on 01/21/2026).

[58] Thomas Newdick. *Kaman's Kargo Logistics Drone For The Marines Now In Flight Test*. en. The War Zone (TWZ). Apr. 30, 2024. URL: https://www.twz.com/air/kamans-kargo-logistics-drone-for-the-marines-now-in-flight-test (visited on 01/22/2026).

[59] Mark Phelps. *Successful Remote-Piloted Flight For Cessna Caravan*. en. AVweb. Dec. 6, 2023. URL: https://avweb.com/aviation-news/successful-remote-piloted-flight-for-cessna-caravan/ (visited on 01/22/2026).

[60] Airbus U.S. Space & Defense, Inc. *MQ-72C Lakota Connector*. en. Airbus U.S. Space & Defense, Inc. URL: https://airbusus.com/mq-72c-lakota-connector/ (visited on 01/22/2026).

[61] Joseph Trevithick. *UH-60 Black Hawk Cargo Drone With Clamshell Nose Breaks Cover (Updated)*. en. The War Zone (TWZ). Oct. 13, 2025. URL: https://www.twz.com/air/uh-60-black-hawk-cargo-drone-with-clamshell-nose-breaks-cover (visited on 01/22/2026).

[62] Gareth Jennings. *France orders VSR700 unmanned helicopters*. en. Janes. Jan. 16, 2026. URL: https://www.janes.com/osint-insights/defence-news/air/france-orders-vsr700-unmanned-helicopters (visited on 01/22/2026).

[63] BETA Technologies. *ALIA MV250 Defense*. URL: https://beta.team/defense.

[64] Joby Aviation, Inc. *Joby Collaborates with L3Harris to Pursue Defense Applications for Autonomous Hybrid VTOL Aircraft*. en. Joby Aviation, Inc. Aug. 1, 2025. URL: https://www.jobyaviation.com/news/joby-lhx-collaboration/ (visited on 01/22/2026).

[65] Schiebel. *Camcopter S-300 UAS selected for European defence project*. URL: https://www.navalnews.com/naval-news/2025/01/schiebel-camcopter-s-300-uas-selected-for-major-european-defence-project/.

[66] Zhengru Ren et al. "Offshore wind turbine operations and maintenance: A state-of-the-art review". In: *Renewable and Sustainable Energy Reviews* 144 (2021), p. 110886. ISSN: 1364-0321. DOI: https://doi.org/10.1016/j.rser.2021.110886. URL: https://www.sciencedirect.com/science/article/pii/S1364032121001805.

[67] Chenyu Zhao et al. "Strategic Deployment of Service Vessels for Improved Offshore Wind Farm Maintenance and Availability". English. In: *Marine Energy Research* 1.1 (Sept. 2024). ISSN: 3008-0932. DOI: 10.70322/mer.2024.10003.

[68] Bundesamt für Seeschifffahrt und Hydrographie (BSH). *Standard Konstruktion - Mindestanforderungen an die konstruktive Ausführung von Offshore-Bauwerken in der ausschließlichen Wirtschaftszone (AWZ)*. Accessed: 2026-01-03. June 2021. URL: https://www.bsh.de/DE/PUBLIKATIONEN/_Anlagen/Downloads/Offshore/Standards/Standard-Konstruktive-Ausfuehrung-von-Offshore-Windenergieanlagen-Aktualisierung-01-06-21.pdf.

[69] Siemens Gamesa. *SG 14-236 DD Offshore Wind Turbine*. Siemens Gamesa. 2025. URL: https://www.siemensgamesa.com/global/en/home/products-and-services/offshore/wind-turbine-sg-14-236-dd.html (visited on 01/03/2026).

[70] B. Hu, P. Stumpf, and W. van der Deijl. *Offshore Wind Access 2019*. TNO report TNO 2019 R10633. Third edition. Petten, The Netherlands: TNO, May 12, 2019.

[71] European Union Aviation Safety Agency (EASA). *EASA Airworthiness Directive No. 2014-0188R2: Emergency Flotation System - Rotorcraft Flight Manual (Supplement)*. Tech. rep. AD 2014-0188R2. Airworthiness Directive issued under Regulation (EC) No 216/2008 and EU 748/2012, effective 25 March 2015. European Union Aviation Safety Agency, Mar. 25, 2015. URL: `https://ad.easa.europa.eu/blob/EASA_AD_2014_0188_R2.pdf`.

[72] *KN Helicpters - North Sea Windfarms*. 2024. URL: `https://www.youtube.com/watch?v=y_MikAQuUrM` (visited on 01/03/2026).

[73] *Helidecks*. 2025. URL: `https://www.helidecks.de/helideck-karten.html` (visited on 01/03/2026).

[74] *Good Practice Guidelines: G+ Offshore Wind Farm Transfer*. 2nd ed. London: Energy Institute, Oct. 2024. ISBN: 978-1-78725-443-5.

[75] Tobias Warnecke and Rüdiger Franz. “”Offshorerettung” - Funktionsweise der Rettungskette”. In: *Notfall Rettungsmed* 26 (2023), pp. 183–186. DOI: `10.1007/s10049-022-01110-z`.

[76] *Civil Range*. en. 2019. URL: `https://mediaassets.airbus.com/pm_38_379_379543-7neugrgrhp.pdf` (visited on 01/03/2026).

[77] Mike Chase. *Airbus H145 vs Sikorsky S-76D vs Leonardo AW169*. en. 2021. URL: `https://www.avbuyer.com/articles/helicopter-comparisons/airbus-h145-vs-sikorsky-s-76d-vs-leonardo-aw169-113044` (visited on 01/03/2026).

[78] *AW139*. en. 2023. URL: `https://www.leonardodrs.com/wp-content/uploads/2023/08/body_aw139_7ton_2_data_sheet.pdf` (visited on 01/03/2026).

[79] M. Stuhr et al. “Notfallmedizinische Versorgung in Offshore-Windparks”. In: *DAnaesthesist* 65 (2016), pp. 369–379. DOI: `10.1007/s00101-016-0154-7`.

[80] *Erfolgreiche Validierung des Rettungskonzepts im Offshore-Windpark Global Tech I*. 2021. URL: `https://globaltechone.de/erfolgreiche-validierung-des-rettungskonzepts-im-offshore-windpark-global-tech-i-offshore-wind/` (visited on 01/03/2026).

[81] Ute Pröttel. *Die Drohne, die Windräder vollautomatisch überwacht*. Süddeutsche Zeitung. July 7, 2019. URL: `https://www.sueddeutsche.de/muenchen/starnberg/berg-windraeder-drohne-wartung-1.4514186` (visited on 01/03/2026).

[82] SkySpecs. *Inspections*. URL: `https://skyspecs.com/product/inspections/` (visited on 01/03/2026).

[83] DRONIQ GmbH. *Windkraftbefliegung per Drohne*. 2025. URL: `https://droniq.de/windkraftbefliegung/` (visited on 01/03/2026).

[84] Giovanni Rinaldi, Philipp R. Thies, and Lars Johanning. “Current Status and Future Trends in the Operation and Maintenance of Offshore Wind Turbines: A Review”. In: *Energies* 14.9 (2021). ISSN: 1996-1073. DOI: `10.3390/en14092484`. URL: `https://www.mdpi.com/1996-1073/14/9/2484`.

[85] *Anwendungsempfehlung: Drohnen in Windkraftprojekten und Windenergieanlagen*. German. Bundesverband WindEnergie e.V. (BWE), Sachverständigenbeirat. Mar. 12, 2025. URL: `https://www.wind-energie.de/fileadmin/redaktion/dokumente/verband/Fachgremien/Beiraete/Sachverstaendigenbeirat/20250312_Anwendungsempfehlung_Drohnen_wkp_wea.pdf` (visited on 01/03/2026).

[86] Seong-Jun Heo and Wongi S. Na. “Review of Drone-Based Technologies for Wind Turbine Blade Inspection”. In: *Electronics* 14.2 (2025). ISSN: 2079-9292. DOI: `10.3390/electronics14020227`. URL: `https://www.mdpi.com/2079-9292/14/2/227`.

[87] Christian Schläger, Torge Lorenz, and David Baumgärtner. “Impact of Innovative Maintenance Technologies on Offshore Wind Farm Performance”. In: *Journal of Physics: Conference Series*. Vol. 3025. 1. IOP Publishing. 2025, p. 012019.

[88] AAU Energy. *Wind turbine inspection drone (image), Drone and Robotics Laboratory*. Overview page: https://www.energy.aau.dk/laboratories/drone-and-robotics-laboratory. Aalborg University. URL: `https://www.aaudxp-cms.aau.dk/media/x51g4z5w/011.jpg?width=960&format=webp` (visited on 01/03/2026).

[89] Khristopher Kabbabe Poleo, William J. Crowther, and Mike Barnes. "Estimating the impact of drone-based inspection on the Levelised Cost of electricity for offshore wind farms". In: *Results in Engineering* 9 (2021), p. 100201. ISSN: 2590-1230. DOI: `https://doi.org/10.1016/j.rineng.2021.100201`. URL: `https://www.sciencedirect.com/science/article/pii/S2590123021000025`.

[90] Gabriel Fontenla-Carrera et al. "Efficient offshore wind farm inspections using a support vessel and UAVs". In: *Ocean Engineering* 332 (2025), p. 121416. ISSN: 0029-8018. DOI: `https://doi.org/10.1016/j.oceaneng.2025.121416`. URL: `https://www.sciencedirect.com/science/article/pii/S0029801825011291`.

[91] Xianfei Huang et al. "Study on a Boat-Assisted Drone Inspection Scheme for the Modern Large-Scale Offshore Wind Farm". In: *IEEE Systems Journal* 17.3 (2023), pp. 4509–4520. DOI: `10.1109/JSYST.2023.3272948`.

[92] *Drone-based full-circuit tests of lightning protection systems to maximize efficiency*. Voliro. 2024. URL: `https://voliro.com/industry/drone-based-full-circuit-tests-of-lighting-protection-systems-to-maximize-efficiency/` (visited on 01/03/2026).

[93] Flylogix Ltd. *Wind Turbine Inspection Services*. 2025. URL: `https://www.flylogix.com/wind/` (visited on 01/03/2026).

[94] Vattenfall AB. *Intelligent drones increase offshore wind efficiency*. 2025. URL: `https://group.vattenfall.com/press-and-media/newsroom/2025/intelligent-drones-increase-offshore-wind-efficiency` (visited on 01/03/2026).

[95] Ørsted. *Ørsted launches worlds first heavy-lift cargo drone for offshore logistics*. 2024. URL: `https://orsted.com/en/media/news/2024/08/orsted-launches-worlds-first-heavy-lift-cargo-dron-13977050` (visited on 01/04/2026).

[96] FlyingBasket. *SkyLift and FlyingBasket Deliver UK's First Large-Scale Offshore Drone Delivery Programme*. 2025. URL: `https://flyingbasket.com/blog/news-1/skylift-and-flyingbasket-deliver-uks-first-large-scale-offshore-drone-delivery-programme-29` (visited on 01/03/2026).

[97] *FOD4Wind Final report*. Tech. rep. Final report of the FOD4wind project, funded by the EUDP programme. Available at `https://www.offshoreenergy.dk/2025/03/06/fod4wind-slutrapport-eudp/`. EUDP (Energiteknologisk Udviklings- og Demonstrationsprogram), Mar. 2025. URL: `https://www.offshoreenergy.dk/2025/03/06/fod4wind-slutrapport-eudp/`.

[98] RWE Offshore Wind GmbH. *RWE leistet Pionierarbeit mit dem Einsatz von Transportdrohnen in Offshore-Windparks*. Pressemitteilung, Essen. Oct. 15, 2025. URL: `https://www.rwe.com/presse/rwe-offshore-wind-gmbh/2025-10-15-rwe-leistet-pionierarbeit-mit-dem-einsatz-von-transportdrohnen-in-offshore-windparks/` (visited on 01/03/2026).

[99] DSV. *DSV and Ørsted to test cargo drones at Anholt Offshore Wind Farm*. Press release. June 29, 2022. URL: `https://www.dsv.com/en/about-dsv/press/news/com/2022/06/dsv-and-oersted-to-test-cargo-drones` (visited on 01/03/2026).

[100] RigiTech. *Precision payload dropping prototype by RigiTech transforms operations at Ørsted Anholt Offshore Wind Farm in Denmark*. URL: `https://rigi.tech/precision-payload-dropping-prototype-by-rigitech-transforms-operations-at-orsted-anholt-offshore-wind-farm-in-denmark/` (visited on 01/03/2026).

[101] EnBW Energie Baden-Württemberg AG. *Offshore Logistics Drones. Ein gemeinsames Forschungsprojekt von EnBW und DLR*. de. URL: https://www.enbw.com/unternehmen/themen/windkraft/offshore-logistics-drones/ (visited on 01/03/2026).

[102] Simon Schopferer et al. “Offshore Wind Farm Delivery with Autonomous Drones: A Holistic View of System Architecture and Onboard Capabilities”. In: *Drones* 9.295 (4 2025). DOI: 10.3390/drones9040295.

[103] Jan Pertz, Klaus Lütjens, and Stefan Haag. “Unveiling Economic Opportunities fir Air Transport Logistic Services in Offshore Windfarms”. In: *ATRS 2024*. 2024.

[104] Skyports Drone Services. *Oil Major Equinor Trials Drones for On-Demand Critical Cargo Deliveries*. URL: https://skyportsdroneservices.com/equinor/ (visited on 01/03/2026).

[105] ARES Shipyard. *ARES 27 CTV Image*. Online image. Image of the ARES 27 CTV. URL: https://www.ares.global/public/images/vessels/03-utility-support-craft/03-crew-boats-support-vessels/03-ares-27-ctv/10-ares-27-ctv.jpg.

[106] Strategic Marine. *Introducing Stratcat 27 CTV*. YouTube video. Accessed on 2025-02-12. Sept. 2020. URL: https://www.youtube.com/watch?v=rMYZJfNXCv4.

[107] Damen Shipyards Group. *Fast Crew Supplier 2710 Purus Tigers*. Image of the fast crew supplier vessel *Purus Tigers* (FCS 2710). URL: https://medialibrary.damen.com/transform/52e77fb6-5254-46dc-93df-2899eb2e4cda/FAST-CREW-SUPPLIER-2710-532919-PURUS-TIGERS-1839-DAMEN?io=transform:fill,width:750,height:579&quality=75 (visited on 02/13/2025).

[108] Orla Donnelly and James Carroll. “Daylight Considerations for Offshore Wind Operations and Maintenance”. In: *Journal of Physics: Conference Series* 2875.1 (Nov. 2024), p. 012018. DOI: 10.1088/1742-6596/2875/1/012018. URL: https://doi.org/10.1088/1742-6596/2875/1/012018.

[109] LD Armateurs. *Crew Transfer Vessel (CTV) support vessel image*. Image from the Renewable Marine Energy section on the LD Armateurs website; support vessel for offshore wind energy. LD Armateurs. 2025. URL: https://www.lda.fr/wp-content/uploads/2023/10/navire-support-eolien-CTV-768x511.jpg (visited on 12/30/2025).

[110] Damen Shipyards. *Picture of SOV-9020 Bibby WaveMaster 1*. Accessed: 2026-01-03. Image available at: https://medialibrary.damen.com/transform/61f72d31-ca18-4c46-942a-51d6f0b3afc6/sov-9020-bibby-wavemaster-1-04?io=transform:fill,width:1080,height:774&quality=75. n.d. URL: https://www.damen.com/vessels/offshore/sov-9020-bibby-wavemaster-1.

[111] Yalcin Dalgic et al. “Advanced Logistics Planning for Offshore Wind Farm Operation and Maintenance Activities”. In: *Ocean Engineering* 101 (2015), pp. 211–226. DOI: 10.1016/j.oceaneng.2015.04.040. URL: https://www.sciencedirect.com/science/article/pii/S0029801815001213.

[112] Russell L. Ackoff. “Towards a System of Systems Concepts”. In: *Management Science* 17.11 (1971), pp. 661–671. ISSN: 00251909, 15265501. URL: http://www.jstor.org/stable/2629308 (visited on 01/09/2026).

[113] “ISO/IEC/IEEE International Standard – Systems and software engineering – System of systems (SoS) considerations in life cycle stages of a system”. In: *ISO/IEC/IEEE 21839:2019(E)* (2019), pp. 1–40. DOI: 10.1109/IEEESTD.2019.8767116.

[114] Vadim Kotov. “Systems of systems as communicating structures”. In: *Object-Oriented Technology and Computing Systems Re-Engineering*. USA: Horwood Publishing, Ltd., 1999, pp. 141–154. ISBN: 189856356X.

[115] Karlsruher Institut für Technologie (KIT) and IPEK-Institut für Produktentwicklung. *System of Systems*. Glossar der KaSPro (IPEK). Letzte Änderung: 02.05.2024. May 2, 2024. URL: https://www.ipek.kit.edu/11604.php (visited on 01/09/2026).

[116] Mark W. Maier. "Architecting principles for systems-of-systems". In: *Systems Engineering* 1.4 (1998), pp. 267–284. DOI: https://doi.org/10.1002/(SICI)1520-6858(1998)1:4<267::AID-SYS3>3.0.CO;2-D. URL: https://incose.onlinelibrary.wiley.com/doi/abs/10.1002/%28SICI%291520-6858%281998%291%3A4%3C267%3A%3AAID-SYS3%3E3.0.CO%3B2-D.

[117] Hadi Farhangi and Dincer Konur. "System of Systems Architecting Problems: Definitions, Formulations, and Analysis". In: *Procedia Computer Science* 140 (2018). Cyber Physical Systems and Deep Learning Chicago, Illinois November 5-7, 2018, pp. 29–36. ISSN: 1877-0509. DOI: https://doi.org/10.1016/j.procs.2018.10.289. URL: https://www.sciencedirect.com/science/article/pii/S1877050918319628.

[118] Daniel A. DeLaurentis, Kushal Moolchandani, and Cesare Guariniello. *System of Systems Modeling and Analysis*. Taylor & Francis Group, 2022.

[119] EnBW Energie Baden-Württemberg AG. *Comfortable access to the offshore wind farm: EnBW and Wallaby Boats christen a new kind of crew transfer vessel*. Press release. Apr. 22, 2024. URL: https://www.enbw.com/press/enbw-wallaby-boats-christen-a-new-kind-of-crew-transfer-vessel.html (visited on 01/09/2026).

[120] Ondřej Vaněk et al. "Agent-based model of maritime traffic in piracy-affected waters". In: *Transportation Research Part C: Emerging Technologies* 36 (2013), pp. 157–176. ISSN: 0968-090X. DOI: 10.1016/j.trc.2013.08.009.

[121] Peisen Xiong et al. "A Time Domain-Based Iterative Method for Helicopter Maritime Search Area Planning and Construction of the Simulation Environment". In: *IEEE Access* 8 (2020), pp. 191460–191471. DOI: 10.1109/ACCESS.2020.3032583.

[122] Behrooz Ashrafi et al. "An agent-based modelling framework for performance assessment of search and rescue operations in the Barents Sea". In: *Safety in Extreme Environments* 6 (2024), pp. 183–200. DOI: 10.1007/s42797-024-00101-2.

[123] Sofia Schön. "Model Fidelity in Mission Scenario Simulations for Systems of Systems: A Case Study of Maritime Search and Rescue". Licentiate thesis. Linköping University, 2023. ISBN: 978-91-8075-393-4. DOI: 10.3384/9789180753944. URL: https://doi.org/10.3384/9789180753944.

[124] Per Engelseth and T. M. Pettersen. "Agent-based modelling of offshore upstream petroleum logistics". In: *International Journal of Design & Nature and Ecodynamics* 11.4 (2016), pp. 635–643. DOI: 10.2495/DNE-V11-N4-635-643. URL: https://doi.org/10.2495/DNE-V11-N4-635-643.

[125] E. Mast, Gijs Kuik, and Gerard van Bussel. "Agent-based modelling for scenario development of offshore wind energy". In: (Jan. 2007).

[126] Arto Niemi et al. "Modeling Offshore Wind Farm Disturbances and Maintenance Service Responses within the Scope of Resilience". In: *Reliability Engineering & System Safety* 242 (2023). DOI: 10.1016/j.ress.2023.109719.

[127] M'hammed Sahnoun et al. "Modelling and simulation of operation and maintenance strategy for offshore wind farms based on multi-agent system". In: *Journal of Intelligent Manufacturing* 30.8 (Dec. 1, 2019), pp. 2981–2997. ISSN: 1572-8145. DOI: 10.1007/s10845-015-1171-0. URL: https://doi.org/10.1007/s10845-015-1171-0.

[128] Nils Raaf. “Development of a Helicopter Model for Agent-based Simulations in Maritime Scenarios”. Project Thesis. DLR e.V., Aug. 2025. URL: `https://elib.dlr.de/217726/`.

[129] Patrick Ratei, Nabih Naeem, and Prajwal Shiva Prakasha. “Development of an urban air mobility vehicle family concept by system of systems aircraft design and assessment”. In: *Journal of Physics: Conference Series* 2526.1 (2023), p. 012043. DOI: `10.1088/1742-6596/2526/1/012043`.

[130] Patrick Ratei. *Development of a Vertical Take-Off and Landing Aircraft Design Tool for the Application in a System of Systems Simulation Framework*. Tech. rep. Supervisor: Prajwal Shiva Prakasha (DLR). Hamburg University of Applied Sciences (HAW Hamburg), June 2022. URL: `https://elib.dlr.de/186947/`.

[131] Prajwal Shiva Prakasha et al. “Aircraft architecture and fleet assessment framework for urban air mobility using a system of systems approach”. In: *Aerospace Science and Technology* 125 (2022), p. 107072. ISSN: 1270-9638. DOI: `https://doi.org/10.1016/j.ast.2021.107072`.

[132] Menno Berger. *A Door-to-Door Multimodal Simulation-Based Framework for the Integration of Advanced Air Mobility Design and Operations*. Tech. rep. Delft University of Technology, 2023.

[133] Nikolaos Kalliatakis et al. “IMPROVING AERIAL WILDFIRE FIGHTING EFFECTIVENESS USING FUTURE CLIMATE SENSITIVITIES AND NOVEL AIRCRAFT CONCEPTS”. In: *READ 2024*. 2024.

[134] Nikolaos Kalliatakis et al. “A system of systems framework for strategic cargo airlift using agent-based modelling”. In: *13th EASN International Conference on Innovation in Aviation and Space for Opening New Horizons*. Vol. 2716. Journal of Physics: Conference Series 012048. IOP Science, Sept. 2023. DOI: `10.1088/1742-6596/2716/1/012048`. URL: `https://elib.dlr.de/203259/`.

[135] Yalcin Dalgic et al. “Advanced logistics planning for offshore wind farm operation and maintenance activities”. In: *Ocean Engineering* 101 (2015), pp. 211–226. ISSN: 0029-8018. DOI: `10.1016/j.oceaneng.2015.04.040`.

[136] E. Cheynet et al. “Tall wind profile validation of ERA5, NORA3, and NEWA datasets using lidar observations”. In: *Wind Energy Science* 10.4 (2025), pp. 733–754. DOI: `10.5194/wes-10-733-2025`. URL: `https://wes.copernicus.org/articles/10/733/2025/`.

[137] Konstantinos Christakos et al. *Metocean Engine: Developing Open-Access Tools for In-Depth Metocean Analysis*. Poster. EERA DeepWind 2024. Norwegian Meteorological Institute and Bergen Offshore Wind Centre, 2024. URL: `https://www.sintef.no/globalassets/project/eera-deepwind-2024/posters/metocean_clio_michel_poster_79_metoceanenginedevelopingopenaccesstoolsforindepthmetoceananalysis_michel.pdf`.

[138] I. M. Solbrekke, A. Sorteberg, and H. Haakenstad. “The 3 km Norwegian reanalysis (NORA3) – a validation of offshore wind resources in the North Sea and the Norwegian Sea”. In: *Wind Energy Science* 6.6 (2021), pp. 1501–1519. DOI: `10.5194/wes-6-1501-2021`. URL: `https://wes.copernicus.org/articles/6/1501/2021/`.

[139] Ida Marie Solbrekke and Asgeir Sorteberg. “NORA3-WP: A high-resolution offshore wind power dataset for the Baltic, North, Norwegian, and Barents Seas”. In: *Scientific Data* 9.1 (2022), p. 362. ISSN: 2052-4463. DOI: `10.1038/s41597-022-01451-x`. URL: `https://doi.org/10.1038/s41597-022-01451-x`.

[140] Metocean API Community. *Metocean API: Documentation*. Accessed: 2025-12-26. 2023. URL: `https://metocean-api.readthedocs.io/en/stable/`.

[141] Spektrum der Wissen- schaft. *Logarithmisches Windgesetz*. Spektrum der Wissenschaft Verlagsgesellschaft. URL: `https://www.spektrum.de/lexikon/geographie/logarithmisches-windgesetz/4787` (visited on 01/03/2026).

[142] R. I. Harris and D. M. Deaves. “The structure of strong winds”. In: *Proc. of the CIRIA Conference “Wind Engineering in the Eighties”*. Paper 4. London, 1980.

[143] E. Cheynet. *Gridded NORA3 data: automated and remote data extraction*. `https://github.com/ECheynet/NORA3/releases/tag/v1.6`. Version 1.6, accessed 23 December 2025. 2025.

[144] Klaus Gersten Hermann Schlichting. *Boundary-Layer Theory*. 9th ed. Springer-Verlag Berlin Heidelberg, 2017. ISBN: 978-3-662-52919-5. DOI: `10.1007/978-3-662-52919-5`. URL: `https://doi.org/10.1007/978-3-662-52919-5`.

[145] B. Lange and J. Højstrup. “The influence of waves on the offshore wind resource”. English. In: *Offshore wind energy in Mediterranean and other European seas: Technology and potential applications. Proceedings*. European Seminar Offshore Wind Energy in Mediterranean and Other European Seas, OWEMES 2000 ; Conference date: 13-04-2000 Through 15-04-2000. ENEA, 2000, pp. 491–503.

[146] Øyvind Breivik et al. “The Impact of a Reduced High-Wind Charnock Parameter on Wave Growth With Application to the North Sea, the Norwegian Sea, and the Arctic Ocean”. In: *Journal of Geophysical Research: Oceans* 127.3 (2022). DOI: `https://doi.org/10.1029/2021JC018196`. eprint: `https://agupubs.onlinelibrary.wiley.com/doi/pdf/10.1029/2021JC018196`. URL: `https://agupubs.onlinelibrary.wiley.com/doi/abs/10.1029/2021JC018196`.

[147] Tobias Lampe et al. “Case Study based Investigation on Impact of Added Wave Resistance Models on Vessel Power Consumption and Routing”. In: *ASME 2025 44th International Conference on Ocean, Offshore and Arctic Engineering, OMAE 2025*. Aug. 2025. URL: `https://elib.dlr.de/216113/`.

[148] Global Climate Observing System (GCOS) / World Meteorological Organization. *Sea State — Essential Climate Variable (ECV)*. Global Climate Observing System (GCOS). 2025. URL: `https://gcos.wmo.int/site/global-climate-observing-system-gcos/essential-climate-variables/sea-state` (visited on 12/26/2025).

[149] Deutscher Wetterdienst. *Signifikante Wellenhöhe*. Deutscher Wetterdienst. URL: `https://www.dwd.de/DE/service/lexikon/begriffe/S/Signifikante_Wellenhoehe.html` (visited on 12/26/2025).

[150] Paul Crossland et al. “Motion-Induced Interruptions Aboard Ship: Model Development and Application to Ship Design”. In: *Occupational Ergonomics* 7 (Jan. 2007), pp. 183–199. DOI: `10.3233/OER-2007-7304`.

[151] Inger M. Solbrekke and Asgeir Sorteberg. “NORA3-WP: A high-resolution offshore wind power dataset for the Baltic, North, Norwegian, and Barents Seas”. In: *Scientific Data* 9 (2022), p. 362. DOI: `10.1038/s41597-022-01451-x`. URL: `https://doi.org/10.1038/s41597-022-01451-x`.

[152] Yiannis Katsigiannis and George Stavrakakis. “Estimation of wind energy production in various sites in Australia for different wind turbine classes: a comparative technical and economic”. In: *Renew Energy* 67 (Jan. 2013), pp. 1–7.

[153] Alexandra Diaconita, Gabriel Andrei, and Liliana Rusu. “An overview of the offshore wind energy potential for twelve significant geographical locations across the globe”. In: *Energy Reports* 8 (Dec. 2022), pp. 194–201. DOI: `10.1016/j.egyr.2022.10.193`.

[154] Luca Lanzilao and Johan Meyers. “A new wake-merging method for wind-farm power prediction in the presence of heterogeneous background velocity fields”. In:

Wind Energy 25.2 (2022), pp. 237–259. DOI: 10.1002/we.2669. eprint: https://onlinelibrary.wiley.com/doi/pdf/10.1002/we.2669. URL: https://onlinelibrary.wiley.com/doi/10.1002/we.2669.

[155] Offshore WIND. *Siemens Presents 6 MW Direct Drive Wind Turbine at EWEA Offshore*. Accessed on 2025-12-13. Nov. 29, 2011. URL: https://www.offshorewind.biz/2011/11/29/the-netherlands-siemens-presents-6mw-direct-drive-wind-turbine-at-ewea-offshore/ (visited on 12/13/2025).

[156] The Wind Power. *Siemens SWT-6.0-154*. Manufacturers and turbines database. Sheet updated on 4 June 2018. 2018. URL: https://www.thewindpower.net/turbine_en_807_siemens_swt-6.0-154.php.

[157] Internationales Wirtschaftsforum Regenerative Energien (IWR). *Milliarden-Auftrag für Siemens: DONG bestellt 97 x 6 MW für Offshore-Windparks*. IWR. Nov. 18, 2013. URL: https://www.iwr.de/news/milliarden-auftrag-fuer-siemens-dong-bestellt-97-x-6-mw-fuer-offshore-windparks-news25028.

[158] Offshore WIND. *Veja Mate all done four months early*. Offshorewind.biz. May 31, 2017. URL: https://www.offshorewind.biz/2017/05/31/veja-mate-all-done-four-months-early/.

[159] Deutsche WindGuard GmbH. *Status des Offshore-Windenergieausbaus in Deutschland - Jahr 2024*. Im Auftrag von BWE, BWO, Stiftung OFFSHORE-WINDENERGIE, VDMA Power Systems, WAB e.V. und WindEnergy Network e.V. Varel: Deutsche WindGuard GmbH, Feb. 4, 2025. 12 pp. URL: https://www.wind-energie.de/fileadmin/redaktion/dokumente/publikationen-oeffentlich/themen/06-zahlen-und-fakten/20250204_Status_des_Offshore_Windenergieausbaus_Jahr_2024.pdf.

[160] Bundesamt für Seeschifffahrt und Hydrographie (BSH). *Erste Ergebnisse zum Projekt Auslegung von Offshore-Windparks und Netzanbindungssystemen*. Tech. rep. Bundesamt für Seeschifffahrt und Hydrographie, 2018. URL: https://www.bsh.de/DE/THEMEN/Offshore/Meeresfachplanung/_Anlagen/Downloads/Aktuelles_FEP_Erste_Ergebnisse_zum_Projekt_Auslegung_von_Offshore_Windparks_und_Netzanbindgssystemen.pdf?__blob=publicationFile&v=2 (visited on 12/14/2025).

[161] MingWei Ge et al. *Offshore Wind Turbine Technology*. 1st ed. Singapore: Springer Singapore, 2025. ISBN: 978-981-96-2175-0. DOI: 10.1007/978-981-96-2175-0. URL: https://link.springer.com/book/10.1007/978-981-96-2175-0 (visited on 01/07/2026).

[162] Iain Dinwoodie et al. “Reference Cases for Verification of Operation and Maintenance Simulation Models for Offshore Wind Farms”. In: *Wind Engineering* 39.1 (2015), pp. 1–14. DOI: 10.1260/0309-524X.39.1.1. eprint: https://doi.org/10.1260/0309-524X.39.1.1. URL: https://doi.org/10.1260/0309-524X.39.1.1.

[163] Ned Dawson. *KN Helicopters windfarm and green energy support operation*. Photo in: Green and Growing KN Helicopters’ windfarm and green energy support operation, HeliOps Magazine. 2025. URL: https://www.heliopsmag.com/media/website_pages/heliops/articles/green-and-growing-kn-helicopters-windfarm-and-green-energy-support-operation/KN-21336.webp (visited on 12/13/2025).

[164] Berend G. van der Wall and Paul H. Lehmann. “About the impact of wind turbine blade tip vortices on helicopter rotor trim and rotor blade motion”. In: *CEAS Aeronautical Journal* 9.1 (2018), pp. 67–84. ISSN: 1869-5590. DOI: 10.1007/s13272-017-0276-x. URL: https://doi.org/10.1007/s13272-017-0276-x.

[165] Damen Shipyards Group. *Fast Crew Supplier 2710*. Product sheet. Revision 2021-06-10. 2021.

[166] ARES Shipyard. *ARES 27 CTV Crew Transfer Vessel*. Product sheet. Antalya Free Zone, Antalya, Turkey: ARES Shipyard. URL: `https://www.ares.global/public/images/uploads/d/ships/pdf/27-ctv_1687353595.pdf`.

[167] Strategic Marine Group. *StratCat 27 Hybrid CTV: Crew Transfer Vessel*. Product sheet. Singapore: Strategic Marine (S) Pte Ltd.

[168] Iraklis Lazakis and Shahroz Khan. "An optimization framework for daily route planning and scheduling of maintenance vessel activities in offshore wind farms". In: *Ocean Engineering* 225 (2021), p. 108752. ISSN: 0029-8018. DOI: `10.1016/j.oceaneng.2021.108752`.

[169] M. Almat. "Concept Design of a Crew Transfer Vessel". Master thesis, Delft University of Technology. MA thesis. Delft University of Technology, 2015. URL: `https://resolver.tudelft.nl/uuid:321b9564-f03c-4468-9de9-ce312ac398eb`.

[170] Young-Rong Kim, Ehsan Esmailian, and Sverre Steen. "A meta-model for added resistance in waves". In: *Ocean Engineering* 266 (2022), p. 112749. ISSN: 0029-8018. DOI: `https://doi.org/10.1016/j.oceaneng.2022.112749`. URL: `https://www.sciencedirect.com/science/article/pii/S0029801822020327`.

[171] Anthony F. Molland, Stephen R. Turnock, and Dominic A. Hudson. *Ship Resistance and Propulsion: Practical Estimation of Propulsive Power*. Cambridge University Press, 2011.

[172] NOAA Global Monitoring Division. *General Solar Position Calculations*. `https://gml.noaa.gov/grad/solcalc/solareqns.PDF`. (Visited on 12/21/2025).

[173] Jannik Heinze, Simon Schopferer, and Maarten Uijt de Haag. "Trajectory Planning for Offshore Wind Farm Logistics with Unmanned Helicopters". In: *43rd AIAA DATC/IEEE Digital Avionics Systems Conference, DASC 2024*. Oct. 2024. URL: `https://elib.dlr.de/206320/`.

[174] BSH, GSM Risk, and Maritime Research GmbH. *Untersuchung von Schifffahrtsrouten in der deutschen Ausschließlichen Wirtschaftszone der Nordsee im Rahmen des Flächenentwicklungsplans 2025*. Gutachten. Online verfügbar, abgerufen am 02. Januar 2026. Bundesamt für Seeschifffahrt und Hydrographie (BSH), Sept. 2023. URL: `https://www.bsh.de/DE/THEMEN/Offshore/Meeresfachplanung/Flaechenentwicklungsplan_2025/Anlagen/Downloads_FEP2025/Gutachten_Schifffahrtsrouten_Nordsee.html`.

[175] Jay Gundlach. *Designing Unmanned Aircraft Systems: A Comprehensive Approach*. AIAA Education Series. Reston, Virginia: American Institute of Aeronautics and Astronautics, 2012. ISBN: 978-1-60086-843-5.

[176] Felix Götten et al. "Full Configuration Drag Estimation of Short-to-Medium Range Fixed-Wing UAVs and Its Impact on Initial Sizing Optimization". In: *CEAS Aeronautical Journal* 12 (2021), pp. 589–603. DOI: `10.1007/s13272-021-00522-w`. URL: `https://doi.org/10.1007/s13272-021-00522-w`.

[177] Jianan Zong et al. "Evaluation and Comparison of Hybrid Wing VTOL UAV with Four Different Electric Propulsion Systems". In: *Aerospace* 8.9 (2021), p. 256. DOI: `10.3390/aerospace8090256`. URL: `https://www.mdpi.com/2226-4310/8/9/256`.

[178] Laura Babetto and Eike Stumpf. "Recent Development of a Conceptual Design Methodology for Unmanned Aerial Vehicles". In: *AIAA Aviation 2021 Forum*. 2021. DOI: `10.2514/6.2021-3219`. URL: `https://arc.aiaa.org/doi/abs/10.2514/6.2021-3219`.

[179] Ivo Poelma. *Development of a Toolchain for the Conceptual Design of Fixed-Wing VTOL UAVs*. Tech. rep. Inholland University of Applied Sciences, 2024. URL: `https://elib.dlr.de/206234/`.

[180] Akshay R. Kadhiresan and Michael J. Duffy. “Conceptual Design and Mission Analysis for eVTOL Urban Air Mobility Flight Vehicle Configurations”. In: *AIAA Aviation 2019 Forum*. 2019. DOI: `10.2514/6.2019-2873`. URL: `https://arc.aiaa.org/doi/abs/10.2514/6.2019-2873`.

[181] Jan Roskam. *Airplane Design Part V: Component Weight Estimation*. Lawrence, Kansas: DARcorporation, 1999.

[182] W. H. Gerard. “Prediction of Sailplane Wing Weight for Preliminary Design”. In: *Weight Engineering* (1998).

[183] Oliver Bertram et al. “UAM Vehicle Design with Emphasis on Electric Powertrain Architectures”. In: *AIAA SciTech 2022 Forum*. 2022. URL: `https://elib.dlr.de/146611/`.

[184] D. F. Finger. “Comparative Performance and Benefit Assessment of VTOL and CTOL UAVs”. In: *DLRK*. Braunschweig: DGLR, 2016.

[185] Ufuk Cakin et al. “Initial Sizing of Hybrid Electric VTOL Aircraft for Intercity Urban Air Mobility”. In: *AIAA Aviation 2020 Forum*. American Institute of Aeronautics and Astronautics. 2020. DOI: `10.2514/6.2020-3173`. URL: `https://arc.aiaa.org/doi/10.2514/6.2020-3173`.

[186] J. Michael Vegh et al. “A comparison of three conceptual design approaches applied to an electric distributed lift aircraft”. In: *CEAS Aeronautical Journal* 16.4 (2025), pp. 1227–1241. ISSN: 1869-5590. DOI: `10.1007/s13272-024-00766-2`. URL: `https://doi.org/10.1007/s13272-024-00766-2`.

[187] Sensenich Propeller Manufacturing Company. *Specification Sheets: Aircraft Composite Propellers*. product brochure. 2018. URL: `https://www.sensenich.com/wp-content/uploads/2018/01/Specification_Sheets_Aircraft_Composite_Brochure__1267393035.pdf`.

[188] T-MOTOR. *U15XXL Combo Pack Manned Aircraft Type UAV Motor 29KV Thunder 300A 24S*. `https://store.tmotor.com/de/product/u15xxl-manned-aircraft-combo.html`. Accessed: 2025-02-17. 2025.

[189] Hirth. *Hirth 3503*. URL: `https://hirthengines.com/de/3503-liquid-cooled-70hp-two-stroke-engine/` (visited on 01/03/2026).

[190] Rolls-Royce. *M250/RR300 FIRST Network Directory (2024)*. URL: `https://www.rolls-royce.com/~/media/Files/R/Rolls-Royce/documents/civil-aerospace-downloads/helicopters/2024-m250-rr300-first-network-directory.pdf` (visited on 01/03/2026).

[191] Rolls-Royce. *RR300 Helicopters*. URL: `https://www.rolls-royce.com/products-and-services/civil-aerospace/helicopters/rr300.aspx#section-overview` (visited on 01/03/2026).

[192] W. Johnson and C. Silva. “NASA concept vehicles and the engineering of advanced air mobility aircraft”. In: *The Aeronautical Journal* 126.1295 (2022), pp. 59–91. DOI: `10.1017/aer.2021.92`.

[193] R. McDonald and B. German. “eVTOL Stored Energy Overview”. In: *Uber Elevate Summit* (2017), pp. 14–20.

[194] Martin Maisel, Demo Giulianetti, and Daniel Dugan. “The History of the XV-15 Tilt Rotor Research Aircraft from Concept to Flight”. In: (Feb. 2000).

[195] *Helicopter Hoisting For Offshore Wind: Deutsche Bucht Repair Project*. NHV Group. Jan. 28, 2026. URL: `https://nhv.be/about/news/helicopter-hoisting`

-for-offshore-wind-deutsche-bucht-blade-repair-project (visited on 02/02/2026).
[196] Tom Berger. *Handling Qualities Requirements and Control Design for High-Speed Rotorcraft*. Tech. rep. SR-FCDD-AMV-20-01. DTIC Report AD1091413. Redstone Arsenal, AL: U.S. Army Combat Capabilities Development Command Aviation & Missile Center, Technology Development Directorate, Feb. 2020, p. 360. URL: https://apps.dtic.mil/sti/pdfs/AD1091413.pdf.
[197] Robert Scott and Julius M. Vegh. “Progress Toward a New Conceptual Assessment Tool for Aircraft Cost”. In: *Proceedings of the Vertical Flight Society 76th Annual Forum* (2020). URL: https://api.semanticscholar.org/CorpusID:259661263.
[198] FlyingBasket. *FB3 Heavy cargo UAV*. URL: https://flyingbasket.com/fb3-order.
[199] Malloy Aeronautics. *T-150 Heavy lift UAS*. URL: https://www.malloyaeronautics.com/heavy-lift-uas/t150.
[200] Malloy Aeronautics. *T-400 Heavy lift UAS*. URL: https://www.malloyaeronautics.com/heavy-lift-uas/t400.
[201] Griff Aviation. *Griff 30 product page*. URL: https://www.griffaviation.com/products/griff-30.
[202] Griff Aviation. *Griff 60 product page*. URL: https://www.griffaviation.com/products/griff-60.
[203] Flowcopter. *Products FC100*. URL: https://www.flowcopter.com/products.
[204] Pterodynamics. *Transwing VTOL UAV aircraft*. URL: https://pterodynamics.com/.
[205] Phoenix-Wings. *PW.Orca heavy-duty drone*. URL: https://phoenixwings.com/pworca/.
[206] AutoFlight. *CarryAll C2000CG cargo eVTOL*. URL: https://www.aerospacetestinginternational.com/news/autoflight-delivers-first-certified-one-ton-evtol-aircraft.html.
[207] MADDOS. *VTOL 600h long-range UAV*. URL: https://maddos.com/uav/.
[208] LODD Autonomous. *Hili middle-mile cargo UAV*. URL: https://lodd.com/middle-mile/.
[209] Pipistrel. *Air Cargo Nuuva V300*. URL: https://www.pipistrel-aircraft.com/air-cargo/#1680717339675-b6d1143d-a61a168081189914316808844191571681230128279.
[210] Elroy Air. *Chaparral aircraft*. URL: https://elroyair.com/chaparral/aircraft/.
[211] Rotron Aerospace. *Talon DT-300X military UAV*. URL: https://rotronaero.com/talon-dt300x-military/.
[212] Airbus. *VSR700 technical information*. URL: https://www.airbus.com/en/products-services/defence/uas/vsr700/vsr700-technical-information.
[213] LAFLAMME Aero. *LX300 product page*. URL: https://laflamme.aero/en/lx300/.
[214] Leonardo. *AWHERO remotely piloted helicopter*. URL: https://aeronautics.leonardo.com/en/products/awhero.
[215] Leonardo. *Proteus RWUAS concept*. URL: https://uk.leonardo.com/en/innovation/capability-areas/future-aviation/proteus.
[216] Avilus. *Wespe*. Accessed 21 Dec 2025. URL: https://www.avilus.com/solution/wespe (visited on 12/21/2025).
[217] Hirth. *Hirth 3507*. URL: https://hirthengines.com/de/3507-water-cooled-engine-with-heavy-fuel-capability/ (visited on 01/03/2026).

[218] Hirth. *Hirth 2301*. URL: `https://hirthengines.com/de/2301-air-cooled-two-stroke-boxer-engine-for-light-aviation-devices/` (visited on 01/03/2026).

[219] Hirth. *Hirth 2302*. URL: `https://hirthengines.com/de/2302-air-cooled-two-stroke-engine-for-ultralight-aviation/` (visited on 01/03/2026).

[220] Currawong Engineering. *Cortex Hybrid 50cc Engine (Cortex Series)*. URL: `https://www.currawongeng.com/cortex-series/` (visited on 01/03/2026).

[221] TEI. *TEI-PG50 2-Stroke Gasoline Aviation Engine*. URL: `https://www.tei.com.tr/en/products/tei-pg50-2-stroke-gasoline-aviation-engine` (visited on 01/03/2026).

[222] TEI. *TEI-TP38 Turboprop Engine*. URL: `https://www.tei.com.tr/en/products/tei-tp38-turboprop-engine` (visited on 01/03/2026).

[223] UAVHE. *GT1-124*. URL: `https://uavhe.eu/products/gt1-124-2/` (visited on 01/03/2026).

[224] UAVHE. *PT1-124*. URL: `https://uavhe.eu/products/pt1-124/` (visited on 01/03/2026).

[225] UAVHE. *RW1-79APU*. URL: `https://uavhe.eu/products/rw1-79/` (visited on 01/03/2026).

[226] UAVHE. *RW1-500APU*. URL: `https://uavhe.eu/products/rw1-500apu/` (visited on 01/03/2026).

[227] Limbach Flugmotoren. *Aircraft engines from 15 kW to 40 kW. Small and efficient*. URL: `https://limflug.de/en/products/engines-15kw-40kw.php` (visited on 01/03/2026).

[228] Limbach Flugmotoren. *Aircraft engines from 41 kW to 55 kW. Economical and highly efficient*. URL: `https://limflug.de/en/products/engines-41kw-55kw.php` (visited on 01/03/2026).

[229] Limbach Flugmotoren. *Aircraft engines from 56 kW to 75 kW. Fuel-efficient powerhouses*. URL: `https://limflug.de/en/products/engines-56kw-75kw.php` (visited on 01/03/2026).

[230] BRP-Rotax. *Rotax 912 S/ULS*. URL: `https://www.rotax.com/powertrains/detail/rotax-912-s-uls` (visited on 01/03/2026).

[231] BRP-Rotax. *Rotax 912 A/F/UL*. URL: `https://www.rotax.com/powertrains/detail/rotax-912-a-f-ul` (visited on 01/03/2026).

[232] BRP-Rotax. *Rotax 914 F/UL*. URL: `https://www.rotax.com/powertrains/detail/rotax-914-f-ul` (visited on 01/03/2026).

[233] BRP-Rotax. *Rotax 915 iS A/iS C A*. URL: `https://www.rotax.com/powertrains/detail/rotax-915-is-isc-a` (visited on 01/03/2026).

[234] BRP-Rotax. *ROTAX 916 IS A/ISC A/IS C24/ISC C24*. URL: `https://www.rotax.com/powertrains/detail/rotax-916-is-a-isc-a-is-c24-isc-c24` (visited on 01/03/2026).

[235] Wankel SuperTec. *KKM 503d - Wankel SuperTec*. URL: `https://www.wankelsupertec.de/service/kkm-503d/` (visited on 01/03/2026).

[236] Wankel SuperTec. *KKM 504d - Wankel SuperTec*. URL: `https://www.wankelsupertec.de/service/kkm-504d/` (visited on 01/03/2026).

[237] Turbotech. *URBOTECH Solutions*. URL: `https://www.turbotech-aero.com/solutions/` (visited on 01/03/2026).

[238] PBS Aerospace. *PBS TS100 Turboshaft Engine*. URL: `https://www.pbsaerospace.com/aerospace-products/engines/turboshaft-engines/ts-100-turboshaft-engine-1` (visited on 01/03/2026).

Appendix A

UAV Data

Manufacturer	Model	MTOM $[kg]$	Wingspan/ Rotor Dia. $[m]$	Payload $[kg]$	Cruise Speed $[m/s]$	Range $[km]$	Prop.	Config.	Ref.
DJI	Flycart 30	95		40			BE	MC	[39]
FlyingBasket	FB3	170		100		28	BE	MC	[198]
Malloy Aeronautics	T-150			68		25	BE	MC	[199]
Malloy Aeronautics	T-400			165		37.5	BE	MC	[200]
Griff Aviation	GRIFF 30			30		60	BE	MC	[201]
Griff Aviation	GRIFF 60			60			BE	MC	[202]
Flowcopter	FC100	580		150			CE	MC	[203]
Bell	Eagle Eye	1020	7.38	91		583	CE	TR	[42]
Pterodynamics	P4 Transwing	41	4	6.8	31.1		BE	TW	[204]
Pterodynamics	P5 Transwing	145	6.7	23	36.1	740	H	TW	[204]
Dufour Aerospace	Aero-200	208	3.14	20		200	H	TW	[41]
				15		300			[41]
				10		400			[41]
				5		500	H		[41]
Phoenix-Wings	PW.Orca	52	2.98	15	30.6	60	BE	L+C	[205]
				10		100			[205]
Autoflight	CarryAll C2000CG	2000	14.5	400	55.6	200	BE	L+C	[206]
Skyways	V2	70.3	5.64	11		833	H	L+C	[40]
Skyways	V3 B2	163.3	7.92	10		1851	H	L+C	[40]
				34		556			[40]
MADDOS	VTOL 600h	110	6	20	32	1150	H	L+C	[207]
LODD Autonomous	Hili	1350	11.9	250	50	390	H	L+C	[208]
Pipistrel	Nuuva V300	1700	13.2	300	45.8	556	H	L+C	[209]
				50		1111			[209]
Beta	ALIA MV250	3175	15.24	907		463	H	L+C	[63]
Elroy Air	Chaparral		8	136	63.9	483	H	L+C	[210]
Schiebel	Camcopter S-100	200	3.4	34	28.3	612	CE	H	[38]
				50					[38]
Schiebel	Camcopter S-300	660	5.3	250	28.3	408	CE	H	[65]

continued on next page

Manufacturer	Model	MTOM $[kg]$	Wingspan/ Rotor Dia. $[m]$	Payload $[kg]$	Cruise Speed $[m/s]$	Range $[km]$	Prop.	Config.	Ref.
				50		2448			[65]
Rotron Aerospace	TALON DT-300X HYBRID	100	3.5	10	22.2	400	CE	H	[211]
				30		240			[211]
				45		100			[211]
Airbus	VSR 700	760	7.2	150			CE	H	[212]
LAFLAMME	LX300	595	4	180			CE	H	[213]
Leonardo	AWHERO	200		40			CE	H	[214]
Leonardo	Proteus	3000		1500			CE	H	[215]
Avilus	Wespe Piston	650	6.5	200	33.3	300	CE	H	[216]
Avilus	Wespe Turbine	900	6.5	350	33.3	300	CE	H	[216]
Kaman	Kargo	690		272		265	CE	MC	[58]
				136		604			
				91		722			

Appendix B

Engine Data

Manu-facturer	**Product**	**Type**	**Power** [kW]	**Weight** [kg]	**SFC** [g/kWh]	**FoM** [-]	**Ref**
Hirth	3503	ICE	51.67	36	436	0.175	[189]
Hirth	3507	ICE	42.28	36	545	0.14	[217]
Hirth	2301	ICE	43.52	34	660	0.115	[218]
Hirth	2302	ICE	43.52	34	660	0.115	[219]
Currawong	Cortex-50	ICE & Generator	2.1	4.7	600	0.127	[220]
TEI	TEI-PG50	ICE	43.52	20	400	0.19	[221]
TEI	TEI-TP38	Turboshaft	31	11.5	660	0.115	[222]
UAVHE	GT1-124	ICE & Generator	22	13.3	320	0.238	[223]
UAVHE	PT1-124	ICE	21.3	13.9	360	0.211	[224]
UAVHE	RW1-79APU	ICE & Generator	11	9	390	0.195	[225]
UAVHE	RW1-500APU	ICE & Generator	80	36	295	0.258	[226]
LIMBACH	L275EF	ICE	18	15	611.55	0.124	[227]
LIMBACH	L550EF	ICE	37	15	489.24	0.156	[227]
LIMBACH	L550E	ICE	37	16	462.06	0.165	[227]
LIMBACH	L 1700 EA	ICE	41	69			[228]
LIMBACH	L 2000 EA	ICE	51	73			[229]
LIMBACH	L 2000 EB	ICE	51	76.5			[229]
LIMBACH	L 2400 EB	ICE	62	82			[229]
LIMBACH	L 2400 DF/EF	ICE	74	76	265	0.287	[229]
ROTAX	912 S/ULS	ICE	73.5	56.6	275.51	0.276	[230]
ROTAX	912 A/F/UL	ICE	59.6	55.4			[231]
ROTAX	914 F/UL	ICE	84.8	64			[232]
ROTAX	915 iS A /iSCA	ICE	104	82.2			[233]
ROTAX	916 IS A	ICE	117	85.8			[234]
Wankel Supertec	KKM 503d	ICE	130	82	295	0.258	[235]

continued on next page

Manufacturer	**Product**	**Type**	**Power** [kW]	**Weight** [kg]	**SFC** [g/kWh]	**FoM** [-]	**Ref**
Wankel Supertec	KKM 504d	ICE	160	82	290	0.262	[236]
Turbotech	TP-R90	Turboshaft	141	85	212.77	0.358	[237]
Turbotech	TG-R90	Turbogenerator	85	64			[237]
PBS Aerospace	PBS TS100	Turboshaft	160	62	532.22	0.143	[238]
Rolls-Royce	RR300	Turboshaft	220	91	410.6	0.185	[191] [190]
Rolls-Royce	M250 Series III C28B	Turboshaft	336	78	367.44	0.207	[190]
Rolls-Royce	M250 Series II C20R	Turboshaft	372	107	383.87	0.198	[190]

Appendix C

Vehicle Input Files

Listing C.1: AT S 20P/250R JSON Input File

```
{
    "icon": "CARGO_UAV.svg",
    "takeoff_landing_type": "vertipad",
    "mtom": 112,
    "empty_mass": 86,
    "payload": 20.0,
    "persons_on_board": 0,
    "battery_mass_fraction": 0.005,
    "actual_charger_power": 150.014,
    "propulsion_input": {
        "architecture": "serialhybrid",
        "total_propellant": 242919.131,
        "fuel_propellant": 242508.09674167365,
        "electric_propellant": 513.7928480351035,
        "electric_reserve_propellant": 513.7928480351035,
        "propellant_unit": "kJ",
        "efficiency_electric": 0.903168,
        "efficiency_combustion": 0.2,
        "refueling_rate": 486043.2,
        "battery_swap_enabled": true,
        "battery_swap_time": 600,
        "charging_power": 135.012,
        "taxi_out_power": {
            "92": 0.0,
            "97": 0.0,
            "102": 0.0,
            "107": 0.0,
            "112": 0.0},
        "taxi_in_power": {
            "92": 0.0,
            "97": 0.0,
            "102": 0.0,
            "107": 0.0,
            "112": 0.0},
        "transition_power": {
            "92": 67.38,
            "97": 71.869,
            "102": 76.486,
            "107": 81.228,
            "112": 86.091},
        "retransition_power": {
            "92": 67.38,
            "97": 71.869,
            "102": 76.486,
            "107": 81.228,
            "112": 86.091},
        "takeoff_power": {
            "92": 112.911,
            "97": 121.322,
```

```
            "102": 129.947,
            "107": 138.781,
            "112": 147.818},
        "cruise_climb_power": {
            "92": 48.336,
            "97": 50.247,
            "102": 52.206,
            "107": 54.213,
            "112": 56.267},
        "cruise_climb_power_p10": {
            "92": 70.853,
            "97": 72.562,
            "102": 74.308,
            "107": 76.092,
            "112": 77.912},
        "cruise_climb_power_p15": {
            "92": 87.302,
            "97": 88.94,
            "102": 90.612,
            "107": 92.317,
            "112": 94.056},
        "cruise_climb_power_m10": {
            "92": 37.865,
            "97": 40.14,
            "102": 42.481,
            "107": 44.89,
            "112": 47.365},
        "cruise_power": {
            "92": 29.51,
            "97": 30.438,
            "102": 31.416,
            "107": 32.443,
            "112": 33.519},
        "cruise_power_p10": {
            "92": 51.45,
            "97": 52.172,
            "102": 52.933,
            "107": 53.731,
            "112": 54.568},
        "cruise_power_p15": {
            "92": 67.508,
            "97": 68.158,
            "102": 68.842,
            "107": 69.561,
            "112": 70.314},
        "cruise_power_m10": {
            "92": 19.414,
            "97": 20.714,
            "102": 22.083,
            "107": 23.521,
            "112": 25.026},
        "cruise_descent_power": {
            "92": 11.276,
            "97": 11.183,
            "102": 11.137,
            "107": 11.14,
            "112": 11.19},
        "cruise_descent_power_p10": {
            "92": 33.793,
            "97": 33.498,
            "102": 33.24,
            "107": 33.019,
            "112": 32.835},
        "cruise_descent_power_p15": {
            "92": 50.241,
            "97": 49.876,
            "102": 49.543,
            "107": 49.244,
            "112": 48.979},
        "cruise_descent_power_m10": {
            "92": 0.805,
            "97": 1.075,
```

```
            "102": 1.412,
            "107": 1.817,
            "112": 2.288},
        "landing_power": {
            "92": 112.911,
            "97": 121.322,
            "102": 129.947,
            "107": 138.781,
            "112": 147.818},
        "hover_power": {
            "92": 108.57,
            "97": 116.777,
            "102": 125.196,
            "107": 133.824,
            "112": 142.655},
        "loiter_power": {
            "92": 30.103,
            "97": 30.991,
            "102": 31.927,
            "107": 32.909,
            "112": 33.938
        }
    },
    "profile_parameters": {
        "taxi_out_duration": 60.0,
        "taxi_in_duration": 60.0,
        "transition_duration": 17.845,
        "retransition_duration": 17.845,
        "takeoff_altitude": 15.24,
        "takeoff_climb_rate": 1.016,
        "takeoff_ground_speed": 0.0,
        "cruise_climb_rate": 3.556,
        "cruise_climb_ground_speed": 35.0,
        "cruise_altitude": 200.0,
        "cruise_speed": 35.0,
        "cruise_descent_rate": 3.556,
        "cruise_descent_ground_speed": 35.0,
        "landing_altitude": 15.24,
        "landing_descent_rate": 1.016,
        "landing_ground_speed": 0.0,
        "loiter_speed": 22.973
    },
    "pwl_map": {
        "taxi_out": 12.54,
        "taxi_in": 12.54,
        "transition": 76.611,
        "retransition": 76.611,
        "takeoff": 130.156,
        "cruise_climb": 52.254,
        "cruise": 31.465,
        "cruise_descent": 11.185,
        "landing": 130.156,
        "hover": 125.405,
        "loiter": 31.974
    }
}
```

Listing C.2: AT S 20P/500R JSON Input File

```
{
    "icon": "CARGO_UAV.svg",
    "takeoff_landing_type": "vertipad",
    "mtom": 135,
    "empty_mass": 101,
    "payload": 20.0,
    "persons_on_board": 0,
    "battery_mass_fraction": 0.01,
    "actual_charger_power": 350.952,
    "propulsion_input": {
        "architecture": "serialhybrid",
        "total_propellant": 568302.531,
```

```
        "fuel_propellant": 567340.9280951374,
        "electric_propellant": 1063.918,
        "electric_reserve_propellant": 1063.918,
        "propellant_unit": "kJ",
        "efficiency_electric": 0.903168,
        "efficiency_combustion": 0.2,
        "refueling_rate": 1137085.2000000002,
        "battery_swap_enabled": true,
        "battery_swap_time": 600,
        "charging_power": 315.857,
        "taxi_out_power": {
            "115": 0.0,
            "120": 0.0,
            "125": 0.0,
            "130": 0.0,
            "135": 0.0},
        "taxi_in_power": {
            "115": 0.0,
            "120": 0.0,
            "125": 0.0,
            "130": 0.0,
            "135": 0.0},
        "transition_power": {
            "115": 84.306,
            "120": 88.872,
            "125": 93.542,
            "130": 98.314,
            "135": 103.188},
        "retransition_power": {
            "115": 84.306,
            "120": 88.872,
            "125": 93.542,
            "130": 98.314,
            "135": 103.188},
        "takeoff_power": {
            "115": 142.904,
            "120": 151.443,
            "125": 160.158,
            "130": 169.044,
            "135": 178.098},
        "cruise_climb_power": {
            "115": 58.586,
            "120": 60.526,
            "125": 62.505,
            "130": 64.524,
            "135": 66.582},
        "cruise_climb_power_p10": {
            "115": 84.189,
            "120": 85.92,
            "125": 87.682,
            "130": 89.475,
            "135": 91.299},
        "cruise_climb_power_p15": {
            "115": 102.993,
            "120": 104.651,
            "125": 106.337,
            "130": 108.051,
            "135": 109.793},
        "cruise_climb_power_m10": {
            "115": 47.035,
            "120": 49.35,
            "125": 51.72,
            "130": 54.145,
            "135": 56.626},
        "cruise_power": {
            "115": 35.125,
            "120": 36.083,
            "125": 37.082,
            "130": 38.121,
            "135": 39.2},
        "cruise_power_p10": {
            "115": 60.059,
```

```
            "120": 60.804,
            "125": 61.581,
            "130": 62.389,
            "135": 63.229},
        "cruise_power_p15": {
            "115": 78.412,
            "120": 79.083,
            "125": 79.782,
            "130": 80.509,
            "135": 81.265},
        "cruise_power_m10": {
            "115": 24.016,
            "120": 25.357,
            "125": 26.755,
            "130": 28.21,
            "135": 29.721},
        "cruise_descent_power": {
            "115": 12.292,
            "120": 12.227,
            "125": 12.202,
            "130": 12.217,
            "135": 12.271},
        "cruise_descent_power_p10": {
            "115": 37.895,
            "120": 37.622,
            "125": 37.38,
            "130": 37.168,
            "135": 36.988},
        "cruise_descent_power_p15": {
            "115": 56.699,
            "120": 56.353,
            "125": 56.035,
            "130": 55.744,
            "135": 55.482},
        "cruise_descent_power_m10": {
            "115": 0.741,
            "120": 1.051,
            "125": 1.417,
            "130": 1.838,
            "135": 2.315},
        "landing_power": {
            "115": 142.904,
            "120": 151.443,
            "125": 160.158,
            "130": 169.044,
            "135": 178.098},
        "hover_power": {
            "115": 137.506,
            "120": 145.84,
            "125": 154.349,
            "130": 163.029,
            "135": 171.878},
        "loiter_power": {
            "115": 35.753,
            "120": 36.67,
            "125": 37.626,
            "130": 38.62,
            "135": 39.653
        }
    },
    "profile_parameters": {
        "taxi_out_duration": 60.0,
        "taxi_in_duration": 60.0,
        "transition_duration": 17.845,
        "retransition_duration": 17.845,
        "takeoff_altitude": 15.24,
        "takeoff_climb_rate": 1.016,
        "takeoff_ground_speed": 0.0,
        "cruise_climb_rate": 3.556,
        "cruise_climb_ground_speed": 35.0,
        "cruise_altitude": 200.0,
        "cruise_speed": 35.0,
```

```
        "cruise_descent_rate": 3.556,
        "cruise_descent_ground_speed": 35.0,
        "landing_altitude": 15.24,
        "landing_descent_rate": 1.016,
        "landing_ground_speed": 0.0,
        "loiter_speed": 23.248
    },
    "pwl_map": {
        "taxi_out": 15.452,
        "taxi_in": 15.452,
        "transition": 93.644,
        "retransition": 93.644,
        "takeoff": 160.329,
        "cruise_climb": 62.545,
        "cruise": 37.122,
        "cruise_descent": 12.242,
        "landing": 160.329,
        "hover": 154.52,
        "loiter": 37.664
    }
}
```

Listing C.3: AT S 20P/750R JSON Input File

```
{
    "icon": "CARGO_UAV.svg",
    "takeoff_landing_type": "vertipad",
    "mtom": 168,
    "empty_mass": 122,
    "payload": 20.0,
    "persons_on_board": 0,
    "battery_mass_fraction": 0.014,
    "actual_charger_power": 630.569,
    "propulsion_input": {
        "architecture": "serialhybrid",
        "total_propellant": 1021089.417,
        "fuel_propellant": 1019361.6759597309,
        "electric_propellant": 1300.464,
        "electric_reserve_propellant": 1300.464,
        "propellant_unit": "kJ",
        "efficiency_electric": 0.903168,
        "efficiency_combustion": 0.2,
        "refueling_rate": 2043043.1999999997,
        "battery_swap_enabled": true,
        "battery_swap_time": 600,
        "charging_power": 567.512,
        "taxi_out_power": {
            "148": 0.0,
            "153": 0.0,
            "158": 0.0,
            "163": 0.0,
            "168": 0.0},
        "taxi_in_power": {
            "148": 0.0,
            "153": 0.0,
            "158": 0.0,
            "163": 0.0,
            "168": 0.0},
        "transition_power": {
            "148": 108.098,
            "153": 112.734,
            "158": 117.454,
            "163": 122.256,
            "168": 127.139},
        "retransition_power": {
            "148": 108.098,
            "153": 112.734,
            "158": 117.454,
            "163": 122.256,
            "168": 127.139},
        "takeoff_power": {
```

```
            "148": 185.235,
            "153": 193.893,
            "158": 202.691,
            "163": 211.626,
            "168": 220.697},
        "cruise_climb_power": {
            "148": 72.81,
            "153": 74.776,
            "158": 76.774,
            "163": 78.805,
            "168": 80.867},
        "cruise_climb_power_p10": {
            "148": 102.492,
            "153": 104.244,
            "158": 106.021,
            "163": 107.822,
            "168": 109.649},
        "cruise_climb_power_p15": {
            "148": 124.428,
            "153": 126.105,
            "158": 127.804,
            "163": 129.526,
            "168": 131.27},
        "cruise_climb_power_m10": {
            "148": 59.896,
            "153": 62.248,
            "158": 64.644,
            "163": 67.086,
            "168": 69.573},
        "cruise_power": {
            "148": 42.834,
            "153": 43.819,
            "158": 44.838,
            "163": 45.889,
            "168": 46.972},
        "cruise_power_p10": {
            "148": 71.724,
            "153": 72.49,
            "158": 73.282,
            "163": 74.1,
            "168": 74.942},
        "cruise_power_p15": {
            "148": 93.128,
            "153": 93.818,
            "158": 94.53,
            "163": 95.266,
            "168": 96.025},
        "cruise_power_m10": {
            "148": 30.452,
            "153": 31.832,
            "158": 33.257,
            "163": 34.728,
            "168": 36.246},
        "cruise_descent_power": {
            "148": 13.525,
            "153": 13.487,
            "158": 13.481,
            "163": 13.508,
            "168": 13.566},
        "cruise_descent_power_p10": {
            "148": 43.207,
            "153": 42.955,
            "158": 42.728,
            "163": 42.525,
            "168": 42.348},
        "cruise_descent_power_p15": {
            "148": 65.143,
            "153": 64.816,
            "158": 64.511,
            "163": 64.229,
            "168": 63.969},
        "cruise_descent_power_m10": {
```

```
            "148": 0.611,
            "153": 0.959,
            "158": 1.351,
            "163": 1.789,
            "168": 2.271},
        "landing_power": {
            "148": 185.235,
            "153": 193.893,
            "158": 202.691,
            "163": 211.626,
            "168": 220.697},
        "hover_power": {
            "148": 178.35,
            "153": 186.803,
            "158": 195.395,
            "163": 204.124,
            "168": 212.988},
        "loiter_power": {
            "148": 43.501,
            "153": 44.444,
            "158": 45.418,
            "163": 46.424,
            "168": 47.461
        }
    },
    "profile_parameters": {
        "taxi_out_duration": 60.0,
        "taxi_in_duration": 60.0,
        "transition_duration": 17.845,
        "retransition_duration": 17.845,
        "takeoff_altitude": 15.24,
        "takeoff_climb_rate": 1.016,
        "takeoff_ground_speed": 0.0,
        "cruise_climb_rate": 3.556,
        "cruise_climb_ground_speed": 35.0,
        "cruise_altitude": 200.0,
        "cruise_speed": 35.0,
        "cruise_descent_rate": 3.556,
        "cruise_descent_ground_speed": 35.0,
        "landing_altitude": 15.24,
        "landing_descent_rate": 1.016,
        "landing_ground_speed": 0.0,
        "loiter_speed": 23.568
    },
    "pwl_map": {
        "taxi_out": 19.553,
        "taxi_in": 19.553,
        "transition": 117.536,
        "retransition": 117.536,
        "takeoff": 202.828,
        "cruise_climb": 76.806,
        "cruise": 44.87,
        "cruise_descent": 13.513,
        "landing": 202.828,
        "hover": 195.532,
        "loiter": 45.449
    }
}
```

Listing C.4: AT M 100P/250R JSON Input File

```
{
    "icon": "CARGO_UAV.svg",
    "takeoff_landing_type": "vertipad",
    "mtom": 500,
    "empty_mass": 377,
    "payload": 100.0,
    "persons_on_board": 0,
    "battery_mass_fraction": 0.004,
    "actual_charger_power": 551.045,
    "propulsion_input": {
```

```
        "architecture": "serialhybrid",
        "total_propellant": 892316.174,
        "fuel_propellant": 890806.336313649,
        "electric_propellant": 1887.2976648769263,
        "electric_reserve_propellant": 1887.2976648769263,
        "propellant_unit": "kJ",
        "efficiency_electric": 0.903168,
        "efficiency_combustion": 0.2,
        "refueling_rate": 1785387.5999999999,
        "battery_swap_enabled": true,
        "battery_swap_time": 600,
        "charging_power": 495.941,
        "taxi_out_power": {
            "400": 0.0,
            "425": 0.0,
            "450": 0.0,
            "475": 0.0,
            "500": 0.0},
        "taxi_in_power": {
            "400": 0.0,
            "425": 0.0,
            "450": 0.0,
            "475": 0.0,
            "500": 0.0},
        "transition_power": {
            "400": 276.007,
            "425": 298.173,
            "450": 321.06,
            "475": 344.65,
            "500": 368.928},
        "retransition_power": {
            "400": 276.007,
            "425": 298.173,
            "450": 321.06,
            "475": 344.65,
            "500": 368.928},
        "takeoff_power": {
            "400": 483.21,
            "425": 524.786,
            "450": 567.578,
            "475": 611.552,
            "500": 656.675},
        "cruise_climb_power": {
            "400": 180.126,
            "425": 189.575,
            "450": 199.294,
            "475": 209.282,
            "500": 219.54},
        "cruise_climb_power_p10": {
            "400": 246.352,
            "425": 254.815,
            "450": 263.487,
            "475": 272.369,
            "500": 281.46},
        "cruise_climb_power_p15": {
            "400": 295.538,
            "425": 303.656,
            "450": 311.962,
            "475": 320.457,
            "500": 329.14},
        "cruise_climb_power_m10": {
            "400": 152.167,
            "425": 163.392,
            "450": 174.994,
            "475": 186.973,
            "500": 199.329},
        "cruise_power": {
            "400": 99.352,
            "425": 103.889,
            "450": 108.702,
            "475": 113.789,
            "500": 119.152},
```

```
        "cruise_power_p10": {
            "400": 163.78,
            "425": 167.309,
            "450": 171.052,
            "475": 175.009,
            "500": 179.18},
        "cruise_power_p15": {
            "400": 211.764,
            "425": 214.94,
            "450": 218.308,
            "475": 221.87,
            "500": 225.624},
        "cruise_power_m10": {
            "400": 72.617,
            "425": 78.969,
            "450": 85.706,
            "475": 92.828,
            "500": 100.336},
        "cruise_descent_power": {
            "400": 19.957,
            "425": 19.386,
            "450": 19.084,
            "475": 19.051,
            "500": 19.288},
        "cruise_descent_power_p10": {
            "400": 86.183,
            "425": 84.625,
            "450": 83.277,
            "475": 82.138,
            "500": 81.208},
        "cruise_descent_power_p15": {
            "400": 135.369,
            "425": 133.466,
            "450": 131.752,
            "475": 130.226,
            "500": 128.888},
        "cruise_descent_power_m10": {
            "400": 0.0,
            "425": 0.0,
            "450": 0.0,
            "475": 0.0,
            "500": 0.0},
        "landing_power": {
            "400": 483.21,
            "425": 524.786,
            "450": 567.578,
            "475": 611.552,
            "500": 656.675},
        "hover_power": {
            "400": 464.378,
            "425": 504.934,
            "450": 546.701,
            "475": 589.646,
            "500": 633.738},
        "loiter_power": {
            "400": 100.73,
            "425": 105.072,
            "450": 109.676,
            "475": 114.544,
            "500": 119.675
        }
    },
    "profile_parameters": {
        "taxi_out_duration": 60.0,
        "taxi_in_duration": 60.0,
        "transition_duration": 17.845,
        "retransition_duration": 17.845,
        "takeoff_altitude": 15.24,
        "takeoff_climb_rate": 1.016,
        "takeoff_ground_speed": 0.0,
        "cruise_climb_rate": 3.556,
        "cruise_climb_ground_speed": 35.0,
```

```
        "cruise_altitude": 200.0,
        "cruise_speed": 35.0,
        "cruise_descent_rate": 3.556,
        "cruise_descent_ground_speed": 35.0,
        "landing_altitude": 15.24,
        "landing_descent_rate": 1.016,
        "landing_ground_speed": 0.0,
        "loiter_speed": 25.268
    },
    "pwl_map": {
        "taxi_out": 54.788,
        "taxi_in": 54.788,
        "transition": 321.763,
        "retransition": 321.763,
        "takeoff": 568.76,
        "cruise_climb": 199.564,
        "cruise": 108.977,
        "cruise_descent": 19.353,
        "landing": 568.76,
        "hover": 547.88,
        "loiter": 109.94
    }
}
```

Listing C.5: AT M 100P/500R JSON Input File

```
{
    "icon": "CARGO_UAV.svg",
    "takeoff_landing_type": "vertipad",
    "mtom": 619,
    "empty_mass": 464,
    "payload": 100.0,
    "persons_on_board": 0,
    "battery_mass_fraction": 0.008,
    "actual_charger_power": 1299.576,
    "propulsion_input": {
        "architecture": "serialhybrid",
        "total_propellant": 2104422.585,
        "fuel_propellant": 2100861.807216464,
        "electric_propellant": 4409.601,
        "electric_reserve_propellant": 4409.601,
        "propellant_unit": "kJ",
        "efficiency_electric": 0.903168,
        "efficiency_combustion": 0.2,
        "refueling_rate": 4210624.8,
        "battery_swap_enabled": true,
        "battery_swap_time": 600,
        "charging_power": 1169.618,
        "taxi_out_power": {
            "519": 0.0,
            "544": 0.0,
            "569": 0.0,
            "594": 0.0,
            "619": 0.0},
        "taxi_in_power": {
            "519": 0.0,
            "544": 0.0,
            "569": 0.0,
            "594": 0.0,
            "619": 0.0},
        "transition_power": {
            "519": 360.995,
            "544": 383.649,
            "569": 406.876,
            "594": 430.667,
            "619": 455.011},
        "retransition_power": {
            "519": 360.995,
            "544": 383.649,
            "569": 406.876,
            "594": 430.667,
```

```
            "619": 455.011},
        "takeoff_power": {
            "519": 638.011,
            "544": 680.411,
            "569": 723.777,
            "594": 768.086,
            "619": 813.318},
        "cruise_climb_power": {
            "519": 227.758,
            "544": 237.389,
            "569": 247.237,
            "594": 257.303,
            "619": 267.587},
        "cruise_climb_power_p10": {
            "519": 303.982,
            "544": 312.586,
            "569": 321.359,
            "594": 330.302,
            "619": 339.413},
        "cruise_climb_power_p15": {
            "519": 361.159,
            "544": 369.404,
            "569": 377.801,
            "594": 386.35,
            "619": 395.052},
        "cruise_climb_power_m10": {
            "519": 197.559,
            "544": 209.038,
            "569": 220.822,
            "594": 232.91,
            "619": 245.302},
        "cruise_power": {
            "519": 123.124,
            "544": 127.846,
            "569": 132.791,
            "594": 137.958,
            "619": 143.347},
        "cruise_power_p10": {
            "519": 197.208,
            "544": 200.881,
            "569": 204.727,
            "594": 208.746,
            "619": 212.937},
        "cruise_power_p15": {
            "519": 252.964,
            "544": 256.269,
            "569": 259.731,
            "594": 263.348,
            "619": 267.12},
        "cruise_power_m10": {
            "519": 94.417,
            "544": 101.028,
            "569": 107.951,
            "594": 115.185,
            "619": 122.73},
        "cruise_descent_power": {
            "519": 19.82,
            "544": 19.431,
            "569": 19.258,
            "594": 19.303,
            "619": 19.566},
        "cruise_descent_power_p10": {
            "519": 96.045,
            "544": 94.628,
            "569": 93.381,
            "594": 92.302,
            "619": 91.393},
        "cruise_descent_power_p15": {
            "519": 153.222,
            "544": 151.446,
            "569": 149.822,
            "594": 148.351,
```

```
            "619": 147.031},
        "cruise_descent_power_m10": {
            "519": 0.0,
            "544": 0.0,
            "569": 0.0,
            "594": 0.0,
            "619": 0.0},
        "landing_power": {
            "519": 638.011,
            "544": 680.411,
            "569": 723.777,
            "594": 768.086,
            "619": 813.318},
        "hover_power": {
            "519": 613.714,
            "544": 655.09,
            "569": 697.43,
            "594": 740.71,
            "619": 784.911},
        "loiter_power": {
            "519": 124.454,
            "544": 128.973,
            "569": 133.704,
            "594": 138.648,
            "619": 143.805
        }
    },
    "profile_parameters": {
        "taxi_out_duration": 60.0,
        "taxi_in_duration": 60.0,
        "transition_duration": 17.845,
        "retransition_duration": 17.845,
        "takeoff_altitude": 15.24,
        "takeoff_climb_rate": 1.016,
        "takeoff_ground_speed": 0.0,
        "cruise_climb_rate": 3.556,
        "cruise_climb_ground_speed": 35.0,
        "cruise_altitude": 200.0,
        "cruise_speed": 35.0,
        "cruise_descent_rate": 3.556,
        "cruise_descent_ground_speed": 35.0,
        "landing_altitude": 15.24,
        "landing_descent_rate": 1.016,
        "landing_ground_speed": 0.0,
        "loiter_speed": 25.615
    },
    "pwl_map": {
        "taxi_out": 69.837,
        "taxi_in": 69.837,
        "transition": 407.439,
        "retransition": 407.439,
        "takeoff": 724.721,
        "cruise_climb": 247.455,
        "cruise": 133.013,
        "cruise_descent": 19.476,
        "landing": 724.721,
        "hover": 698.371,
        "loiter": 133.917
    }
}
```

Listing C.6: AT M 100P/750R JSON Input File

```
{
    "icon": "CARGO_UAV.svg",
    "takeoff_landing_type": "vertipad",
    "mtom": 815,
    "empty_mass": 612,
    "payload": 100.0,
    "persons_on_board": 0,
    "battery_mass_fraction": 0.011,
```

```
    "actual_charger_power": 2458.97,
    "propulsion_input": {
        "architecture": "serialhybrid",
        "total_propellant": 3981846.425,
        "fuel_propellant": 3975108.959037778,
        "electric_propellant": 5708.743,
        "electric_reserve_propellant": 5708.743,
        "propellant_unit": "kJ",
        "efficiency_electric": 0.903168,
        "efficiency_combustion": 0.2,
        "refueling_rate": 7967062.8,
        "battery_swap_enabled": true,
        "battery_swap_time": 600,
        "charging_power": 2213.073,
        "taxi_out_power": {
            "715": 0.0,
            "740": 0.0,
            "765": 0.0,
            "790": 0.0,
            "815": 0.0},
        "taxi_in_power": {
            "715": 0.0,
            "740": 0.0,
            "765": 0.0,
            "790": 0.0,
            "815": 0.0},
        "transition_power": {
            "715": 501.353,
            "740": 524.492,
            "765": 548.061,
            "790": 572.053,
            "815": 596.463},
        "retransition_power": {
            "715": 501.353,
            "740": 524.492,
            "765": 548.061,
            "790": 572.053,
            "815": 596.463},
        "takeoff_power": {
            "715": 894.5,
            "740": 937.716,
            "765": 981.653,
            "790": 1026.299,
            "815": 1071.642},
        "cruise_climb_power": {
            "715": 305.43,
            "740": 315.244,
            "765": 325.224,
            "790": 335.368,
            "815": 345.678},
        "cruise_climb_power_p10": {
            "715": 396.797,
            "740": 405.544,
            "765": 414.419,
            "790": 423.423,
            "815": 432.555},
        "cruise_climb_power_p15": {
            "715": 466.229,
            "740": 474.602,
            "765": 483.091,
            "790": 491.695,
            "815": 500.415},
        "cruise_climb_power_m10": {
            "715": 272.37,
            "740": 284.106,
            "765": 296.073,
            "790": 308.271,
            "815": 320.7},
        "cruise_power": {
            "715": 161.478,
            "740": 166.388,
            "765": 171.467,
```

```
            "790": 176.715,
            "815": 182.131},
        "cruise_power_p10": {
            "715": 250.169,
            "740": 253.987,
            "765": 257.938,
            "790": 262.019,
            "815": 266.231},
        "cruise_power_p15": {
            "715": 317.837,
            "740": 321.274,
            "765": 324.829,
            "790": 328.502,
            "815": 332.293},
        "cruise_power_m10": {
            "715": 130.339,
            "740": 137.213,
            "765": 144.324,
            "790": 151.67,
            "815": 159.252},
        "cruise_descent_power": {
            "715": 18.717,
            "740": 18.511,
            "765": 18.469,
            "790": 18.593,
            "815": 18.882},
        "cruise_descent_power_p10": {
            "715": 110.085,
            "740": 108.811,
            "765": 107.665,
            "790": 106.648,
            "815": 105.759},
        "cruise_descent_power_p15": {
            "715": 179.516,
            "740": 177.868,
            "765": 176.336,
            "790": 174.92,
            "815": 173.619},
        "cruise_descent_power_m10": {
            "715": 0.0,
            "740": 0.0,
            "765": 0.0,
            "790": 0.0,
            "815": 0.0},
        "landing_power": {
            "715": 894.5,
            "740": 937.716,
            "765": 981.653,
            "790": 1026.299,
            "815": 1071.642},
        "hover_power": {
            "715": 861.185,
            "740": 903.376,
            "765": 946.285,
            "790": 989.9,
            "815": 1034.212},
        "loiter_power": {
            "715": 162.669,
            "740": 167.367,
            "765": 172.226,
            "790": 177.247,
            "815": 182.429
        }
    },
    "profile_parameters": {
        "taxi_out_duration": 60.0,
        "taxi_in_duration": 60.0,
        "transition_duration": 17.845,
        "retransition_duration": 17.845,
        "takeoff_altitude": 15.24,
        "takeoff_climb_rate": 1.016,
        "takeoff_ground_speed": 0.0,
```

```
        "cruise_climb_rate": 3.556,
        "cruise_climb_ground_speed": 35.0,
        "cruise_altitude": 200.0,
        "cruise_speed": 35.0,
        "cruise_descent_rate": 3.556,
        "cruise_descent_ground_speed": 35.0,
        "landing_altitude": 15.24,
        "landing_descent_rate": 1.016,
        "landing_ground_speed": 0.0,
        "loiter_speed": 26.07
    },
    "pwl_map": {
        "taxi_out": 94.699,
        "taxi_in": 94.699,
        "transition": 548.484,
        "retransition": 548.484,
        "takeoff": 982.362,
        "cruise_climb": 325.389,
        "cruise": 171.636,
        "cruise_descent": 18.634,
        "landing": 982.362,
        "hover": 946.991,
        "loiter": 172.388
    }
}
```

Listing C.7: AT L 200P/250R JSON Input File

```
{
    "icon": "CARGO_UAV.svg",
    "takeoff_landing_type": "vertipad",
    "mtom": 815,
    "empty_mass": 612,
    "payload": 100.0,
    "persons_on_board": 0,
    "battery_mass_fraction": 0.011,
    "actual_charger_power": 2458.97,
    "propulsion_input": {
        "architecture": "serialhybrid",
        "total_propellant": 3981846.425,
        "fuel_propellant": 3975108.959037778,
        "electric_propellant": 5708.743,
        "electric_reserve_propellant": 5708.743,
        "propellant_unit": "kJ",
        "efficiency_electric": 0.903168,
        "efficiency_combustion": 0.2,
        "refueling_rate": 7967062.8,
        "battery_swap_enabled": true,
        "battery_swap_time": 600,
        "charging_power": 2213.073,
        "taxi_out_power": {
            "715": 0.0,
            "740": 0.0,
            "765": 0.0,
            "790": 0.0,
            "815": 0.0},
        "taxi_in_power": {
            "715": 0.0,
            "740": 0.0,
            "765": 0.0,
            "790": 0.0,
            "815": 0.0},
        "transition_power": {
            "715": 501.353,
            "740": 524.492,
            "765": 548.061,
            "790": 572.053,
            "815": 596.463},
        "retransition_power": {
            "715": 501.353,
            "740": 524.492,
```

```
            "765": 548.061,
            "790": 572.053,
            "815": 596.463},
        "takeoff_power": {
            "715": 894.5,
            "740": 937.716,
            "765": 981.653,
            "790": 1026.299,
            "815": 1071.642},
        "cruise_climb_power": {
            "715": 305.43,
            "740": 315.244,
            "765": 325.224,
            "790": 335.368,
            "815": 345.678},
        "cruise_climb_power_p10": {
            "715": 396.797,
            "740": 405.544,
            "765": 414.419,
            "790": 423.423,
            "815": 432.555},
        "cruise_climb_power_p15": {
            "715": 466.229,
            "740": 474.602,
            "765": 483.091,
            "790": 491.695,
            "815": 500.415},
        "cruise_climb_power_m10": {
            "715": 272.37,
            "740": 284.106,
            "765": 296.073,
            "790": 308.271,
            "815": 320.7},
        "cruise_power": {
            "715": 161.478,
            "740": 166.388,
            "765": 171.467,
            "790": 176.715,
            "815": 182.131},
        "cruise_power_p10": {
            "715": 250.169,
            "740": 253.987,
            "765": 257.938,
            "790": 262.019,
            "815": 266.231},
        "cruise_power_p15": {
            "715": 317.837,
            "740": 321.274,
            "765": 324.829,
            "790": 328.502,
            "815": 332.293},
        "cruise_power_m10": {
            "715": 130.339,
            "740": 137.213,
            "765": 144.324,
            "790": 151.67,
            "815": 159.252},
        "cruise_descent_power": {
            "715": 18.717,
            "740": 18.511,
            "765": 18.469,
            "790": 18.593,
            "815": 18.882},
        "cruise_descent_power_p10": {
            "715": 110.085,
            "740": 108.811,
            "765": 107.665,
            "790": 106.648,
            "815": 105.759},
        "cruise_descent_power_p15": {
            "715": 179.516,
            "740": 177.868,
```

```
            "765": 176.336,
            "790": 174.92,
            "815": 173.619},
        "cruise_descent_power_m10": {
            "715": 0.0,
            "740": 0.0,
            "765": 0.0,
            "790": 0.0,
            "815": 0.0},
        "landing_power": {
            "715": 894.5,
            "740": 937.716,
            "765": 981.653,
            "790": 1026.299,
            "815": 1071.642},
        "hover_power": {
            "715": 861.185,
            "740": 903.376,
            "765": 946.285,
            "790": 989.9,
            "815": 1034.212},
        "loiter_power": {
            "715": 162.669,
            "740": 167.367,
            "765": 172.226,
            "790": 177.247,
            "815": 182.429
        }
    },
    "profile_parameters": {
        "taxi_out_duration": 60.0,
        "taxi_in_duration": 60.0,
        "transition_duration": 17.845,
        "retransition_duration": 17.845,
        "takeoff_altitude": 15.24,
        "takeoff_climb_rate": 1.016,
        "takeoff_ground_speed": 0.0,
        "cruise_climb_rate": 3.556,
        "cruise_climb_ground_speed": 35.0,
        "cruise_altitude": 200.0,
        "cruise_speed": 35.0,
        "cruise_descent_rate": 3.556,
        "cruise_descent_ground_speed": 35.0,
        "landing_altitude": 15.24,
        "landing_descent_rate": 1.016,
        "landing_ground_speed": 0.0,
        "loiter_speed": 26.07
    },
    "pwl_map": {
        "taxi_out": 94.699,
        "taxi_in": 94.699,
        "transition": 548.484,
        "retransition": 548.484,
        "takeoff": 982.362,
        "cruise_climb": 325.389,
        "cruise": 171.636,
        "cruise_descent": 18.634,
        "landing": 982.362,
        "hover": 946.991,
        "loiter": 172.388
    }
}
```

Listing C.8: AT L 200P/500R JSON Input File

```
{
    "icon": "CARGO_UAV.svg",
    "takeoff_landing_type": "vertipad",
    "mtom": 1473,
    "empty_mass": 1157,
    "payload": 200.0,
```

```
    "persons_on_board": 0,
    "battery_mass_fraction": 0.007,
    "actual_charger_power": 2778.753,
    "propulsion_input": {
        "architecture": "serialhybrid",
        "total_propellant": 4499780.13,
        "fuel_propellant": 4492580.130094093,
        "electric_propellant": 9000.0,
        "electric_reserve_propellant": 9000.0,
        "propellant_unit": "kJ",
        "efficiency_electric": 0.903168,
        "efficiency_combustion": 0.2,
        "refueling_rate": 9003160.8,
        "battery_swap_enabled": true,
        "battery_swap_time": 600,
        "charging_power": 2500.878,
        "taxi_out_power": {
            "1273": 0.0,
            "1323": 0.0,
            "1373": 0.0,
            "1423": 0.0,
            "1473": 0.0},
        "taxi_in_power": {
            "1273": 0.0,
            "1323": 0.0,
            "1373": 0.0,
            "1423": 0.0,
            "1473": 0.0},
        "transition_power": {
            "1273": 877.491,
            "1323": 923.444,
            "1373": 970.352,
            "1423": 1018.2,
            "1473": 1066.976},
        "retransition_power": {
            "1273": 877.491,
            "1323": 923.444,
            "1373": 970.352,
            "1423": 1018.2,
            "1473": 1066.976},
        "takeoff_power": {
            "1273": 1583.066,
            "1323": 1668.953,
            "1373": 1756.444,
            "1423": 1845.509,
            "1473": 1936.12},
        "cruise_climb_power": {
            "1273": 520.375,
            "1323": 539.88,
            "1373": 559.751,
            "1423": 579.987,
            "1473": 600.588},
        "cruise_climb_power_p10": {
            "1273": 659.308,
            "1323": 676.705,
            "1373": 694.387,
            "1423": 712.353,
            "1473": 730.603},
        "cruise_climb_power_p15": {
            "1273": 766.113,
            "1323": 782.773,
            "1373": 799.688,
            "1423": 816.86,
            "1473": 834.287},
        "cruise_climb_power_m10": {
            "1273": 474.414,
            "1323": 497.713,
            "1373": 521.523,
            "1423": 545.846,
            "1473": 570.679},
        "cruise_power": {
            "1273": 264.622,
```

```
            "1323": 274.316,
            "1373": 284.383,
            "1423": 294.824,
            "1473": 305.638},
        "cruise_power_p10": {
            "1273": 399.33,
            "1323": 406.869,
            "1373": 414.7,
            "1423": 422.82,
            "1473": 431.231},
        "cruise_power_p15": {
            "1273": 503.373,
            "1323": 510.159,
            "1373": 517.206,
            "1423": 524.514,
            "1473": 532.084},
        "cruise_power_m10": {
            "1273": 221.764,
            "1323": 235.335,
            "1373": 249.429,
            "1423": 264.046,
            "1473": 279.186},
        "cruise_descent_power": {
            "1273": 10.123,
            "1323": 9.587,
            "1373": 9.416,
            "1423": 9.611,
            "1473": 10.171},
        "cruise_descent_power_p10": {
            "1273": 149.056,
            "1323": 146.412,
            "1373": 144.052,
            "1423": 141.977,
            "1473": 140.185},
        "cruise_descent_power_p15": {
            "1273": 255.861,
            "1323": 252.48,
            "1373": 249.354,
            "1423": 246.484,
            "1473": 243.869},
        "cruise_descent_power_m10": {
            "1273": 0.0,
            "1323": 0.0,
            "1373": 0.0,
            "1423": 0.0,
            "1473": 0.0},
        "landing_power": {
            "1273": 1583.066,
            "1323": 1668.953,
            "1373": 1756.444,
            "1423": 1845.509,
            "1473": 1936.12},
        "hover_power": {
            "1273": 1523.669,
            "1323": 1607.505,
            "1373": 1692.941,
            "1423": 1779.947,
            "1473": 1868.496},
        "loiter_power": {
            "1273": 265.876,
            "1323": 275.151,
            "1373": 284.784,
            "1423": 294.774,
            "1473": 305.121
        }
    },
    "profile_parameters": {
        "taxi_out_duration": 60.0,
        "taxi_in_duration": 60.0,
        "transition_duration": 17.845,
        "retransition_duration": 17.845,
        "takeoff_altitude": 15.24,
```

```
        "takeoff_climb_rate": 1.016,
        "takeoff_ground_speed": 0.0,
        "cruise_climb_rate": 3.556,
        "cruise_climb_ground_speed": 35.0,
        "cruise_altitude": 200.0,
        "cruise_speed": 35.0,
        "cruise_descent_rate": 3.556,
        "cruise_descent_ground_speed": 35.0,
        "landing_altitude": 15.24,
        "landing_descent_rate": 1.016,
        "landing_ground_speed": 0.0,
        "loiter_speed": 27.073
    },
    "pwl_map": {
        "taxi_out": 169.451,
        "taxi_in": 169.451,
        "transition": 971.292,
        "retransition": 971.292,
        "takeoff": 1758.018,
        "cruise_climb": 560.116,
        "cruise": 284.756,
        "cruise_descent": 9.782,
        "landing": 1758.018,
        "hover": 1694.512,
        "loiter": 285.141
    }
}
```

Listing C.9: AT L 200P/750R JSON Input File

```
{
    "icon": "CARGO_UAV.svg",
    "takeoff_landing_type": "vertipad",
    "mtom": 2408,
    "empty_mass": 1956,
    "payload": 200.0,
    "persons_on_board": 0,
    "battery_mass_fraction": 0.004,
    "actual_charger_power": 6370.474,
    "propulsion_input": {
        "architecture": "serialhybrid",
        "total_propellant": 10318368.292,
        "fuel_propellant": 10309368.29,
        "electric_propellant": 9000.0,
        "electric_reserve_propellant": 9000.0,
        "propellant_unit": "kJ",
        "efficiency_electric": 0.903168,
        "efficiency_combustion": 0.2,
        "refueling_rate": 20640337.2,
        "battery_swap_enabled": true,
        "battery_swap_time": 600,
        "charging_power": 5733.427,
        "taxi_out_power": {
            "2208": 0.0,
            "2258": 0.0,
            "2308": 0.0,
            "2358": 0.0,
            "2408": 0.0},
        "taxi_in_power": {
            "2208": 0.0,
            "2258": 0.0,
            "2308": 0.0,
            "2358": 0.0,
            "2408": 0.0},
        "transition_power": {
            "2208": 1539.56,
            "2258": 1586.808,
            "2308": 1634.63,
            "2358": 1683.02,
            "2408": 1731.974},
        "retransition_power": {
```

```
            "2208": 1539.56,
            "2258": 1586.808,
            "2308": 1634.63,
            "2358": 1683.02,
            "2408": 1731.974},
        "takeoff_power": {
            "2208": 2807.714,
            "2258": 2895.775,
            "2308": 2984.795,
            "2358": 3074.765,
            "2408": 3165.674},
        "cruise_climb_power": {
            "2208": 872.319,
            "2258": 892.321,
            "2308": 912.547,
            "2358": 932.996,
            "2408": 953.668},
        "cruise_climb_power_p10": {
            "2208": 1062.19,
            "2258": 1079.974,
            "2308": 1097.931,
            "2358": 1116.063,
            "2408": 1134.368},
        "cruise_climb_power_p15": {
            "2208": 1212.545,
            "2258": 1229.553,
            "2308": 1246.717,
            "2358": 1264.037,
            "2408": 1281.514},
        "cruise_climb_power_m10": {
            "2208": 824.916,
            "2258": 848.91,
            "2308": 873.218,
            "2358": 897.838,
            "2408": 922.771},
        "cruise_power": {
            "2208": 429.855,
            "2258": 440.056,
            "2308": 450.486,
            "2358": 461.144,
            "2408": 472.03},
        "cruise_power_p10": {
            "2208": 613.401,
            "2258": 621.335,
            "2308": 629.447,
            "2358": 637.737,
            "2408": 646.204},
        "cruise_power_p15": {
            "2208": 759.692,
            "2258": 766.833,
            "2308": 774.134,
            "2358": 781.595,
            "2408": 789.215},
        "cruise_power_m10": {
            "2208": 387.342,
            "2258": 401.624,
            "2308": 416.226,
            "2358": 431.147,
            "2408": 446.389},
        "cruise_descent_power": {
            "2208": 0.0,
            "2258": 0.0,
            "2308": 0.0,
            "2358": 0.0,
            "2408": 0.0},
        "cruise_descent_power_p10": {
            "2208": 176.987,
            "2258": 174.729,
            "2308": 172.645,
            "2358": 170.735,
            "2408": 168.999},
        "cruise_descent_power_p15": {
```

```
            "2208": 327.342,
            "2258": 324.309,
            "2308": 321.431,
            "2358": 318.71,
            "2408": 316.145},
        "cruise_descent_power_m10": {
            "2208": 0.0,
            "2258": 0.0,
            "2308": 0.0,
            "2358": 0.0,
            "2408": 0.0},
        "landing_power": {
            "2208": 2807.714,
            "2258": 2895.775,
            "2308": 2984.795,
            "2358": 3074.765,
            "2408": 3165.674},
        "hover_power": {
            "2208": 2705.384,
            "2258": 2791.388,
            "2308": 2878.35,
            "2358": 2966.258,
            "2408": 3055.104},
        "loiter_power": {
            "2208": 429.581,
            "2258": 439.342,
            "2308": 449.322,
            "2358": 459.52,
            "2408": 469.937
        }
    },
    "profile_parameters": {
        "taxi_out_duration": 60.0,
        "taxi_in_duration": 60.0,
        "transition_duration": 17.845,
        "retransition_duration": 17.845,
        "takeoff_altitude": 15.24,
        "takeoff_climb_rate": 1.016,
        "takeoff_ground_speed": 0.0,
        "cruise_climb_rate": 3.556,
        "cruise_climb_ground_speed": 35.0,
        "cruise_altitude": 200.0,
        "cruise_speed": 35.0,
        "cruise_descent_rate": 3.556,
        "cruise_descent_ground_speed": 35.0,
        "landing_altitude": 15.24,
        "landing_descent_rate": 1.016,
        "landing_ground_speed": 0.0,
        "loiter_speed": 27.937
    },
    "pwl_map": {
        "taxi_out": 287.93,
        "taxi_in": 287.93,
        "transition": 1635.198,
        "retransition": 1635.198,
        "takeoff": 2985.745,
        "cruise_climb": 912.77,
        "cruise": 450.714,
        "cruise_descent": -12.516,
        "landing": 2985.745,
        "hover": 2879.297,
        "loiter": 449.54
    }
}
```

Listing C.10: H135 JSON Input File

```
{
   "icon": "H135Icon.svg",
    "takeoff_landing_type": "vertipad",
    "empty_mass": 1990,
```

```
    "mtom": 2980,
    "payload": 540,
    "persons_on_board": 6,
    "propulsion_input": {
       "architecture": "helicopter",
       "total_propellant": 560,
       "reserve_propellant": 50,
       "propellant_unit": "kg",
       "sfc_poly_coeffs": [
          532.66518173, -2589.85468861, 5338.41555707, -6078.19168608,
          4176.45726924,-1778.71282843, 464.93422304,  -71.27892378,
          6.5662843
       ],
       "SFC0": 0.32,
       "BHP0": 457,
       "power_polynomials": {
          "1817": [-1.70139e-11, 1.54244e-08, -5.35482e-06, 8.94890e-04, -6.20226e-02,
              1.78634e-01, 2.68573e+02],
          "2090": [-1.70559e-11, 1.58953e-08, -5.68648e-06, 9.80937e-04, -7.10189e-02,
              2.76586e-01, 3.14851e+02],
          "2364": [-1.83099e-11, 1.72933e-08, -6.29050e-06, 1.10564e-03, -8.26437e-02,
              4.20050e-01, 3.66786e+02],
          "2637": [-1.88378e-11, 1.80412e-08, -6.67766e-06, 1.19843e-03, -9.24377e-02,
              5.47019e-01, 4.21353e+02],
          "2910": [-1.96307e-11, 1.90160e-08, -7.13373e-06, 1.30093e-03, -1.03001e-01,
              7.08749e-01, 4.79176e+02]
       },
       "refueling_rate": 2,
       "system_loss_factor": 1.015,
       "onboard_system_power": 10,
       "attachment_data": {
                        "Hoist":      {"weight": 80, "diameter": 0.25, "Cd": 0.2},
            "Floats":      {"weight": 76, "diameter": 0.25, "Cd":  0.2}
                }
    },
    "profile_parameters": {
       "taxi_out_duration": 1.0,
       "taxi_in_duration": 1.0,
       "transition_duration": 0.0,
       "retransition_duration": 0.0,
       "takeoff_altitude": 20.0,
       "takeoff_climb_rate": 5.0,
       "takeoff_ground_speed": 0.0,
       "cruise_altitude": 500.0,
       "cruise_speed": 64.0,
       "cruise_climb_rate": 8.0,
       "cruise_climb_ground_speed": 33.3,
       "cruise_descent_rate": 5,
       "cruise_descent_ground_speed": 43.6,
       "landing_altitude": 20.0,
       "landing_descent_rate": 2.5,
       "landing_ground_speed": 0.0,
       "loiter_speed": 30.0
    }
}
```

Listing C.11: CTV JSON Input File

```
{
{
  "icon": "CTV_Icon.svg",
  "takeoff_landing_type": "water",
  "empty_mass": 28000,
  "mtom": 130000,
  "payload": 4400,
  "persons_on_board": 24,
  "propulsion_input": {
    "architecture": "ship",
    "installed_power": 2162,
    "total_propellant": 28400,
    "reserve_propellant": 1000,
```

```
    "propellant_unit": "kg",
    "refueling_rate": 0.1,
    "cruise_sfc": 0.23,
    "loiter_sfc": 0.23,
    "v_design": 13.4,
    "zeta_design_max": 3.0
  },
  "profile_parameters": {
    "taxi_out_duration": 5.0,
    "taxi_in_duration": 5.0,
    "transition_duration": 0.0,
    "retransition_duration": 0.0,
    "takeoff_altitude": 0.0,
    "landing_altitude": 0.0,
    "cruise_altitude": 0.0,
    "cruise_speed": 12.3,
    "loiter_speed": 3.0,
    "takeoff_climb_rate": 0.01,
    "takeoff_ground_speed": 0.0,
    "cruise_climb_rate": 0.01,
    "cruise_climb_ground_speed": 12,
    "cruise_descent_rate": 0.01,
    "cruise_descent_ground_speed": 12,
    "landing_descent_rate": 0.01,
    "landing_ground_speed": 0.0
  },
  "wave_limit": 1.5,
  "wind_speed_limit": 25
}
}
```

Appendix D

Payload Range Diagrams

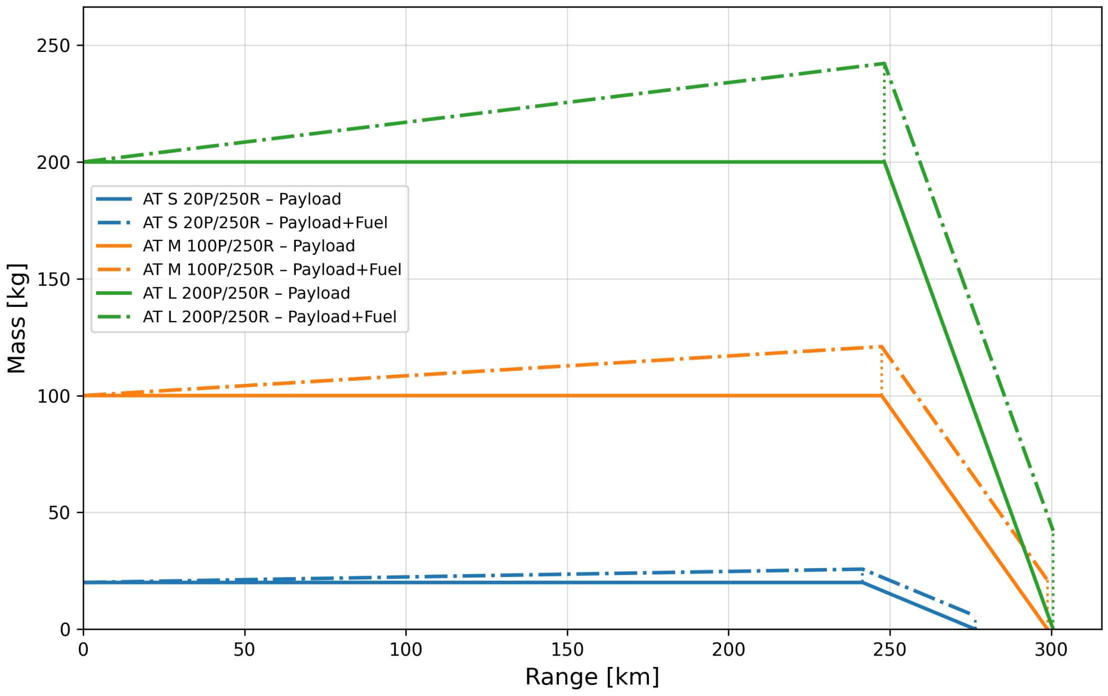

Figure D.1: Payload Range Diagrams for the Arctic Tern Designs with 250 km Design Range

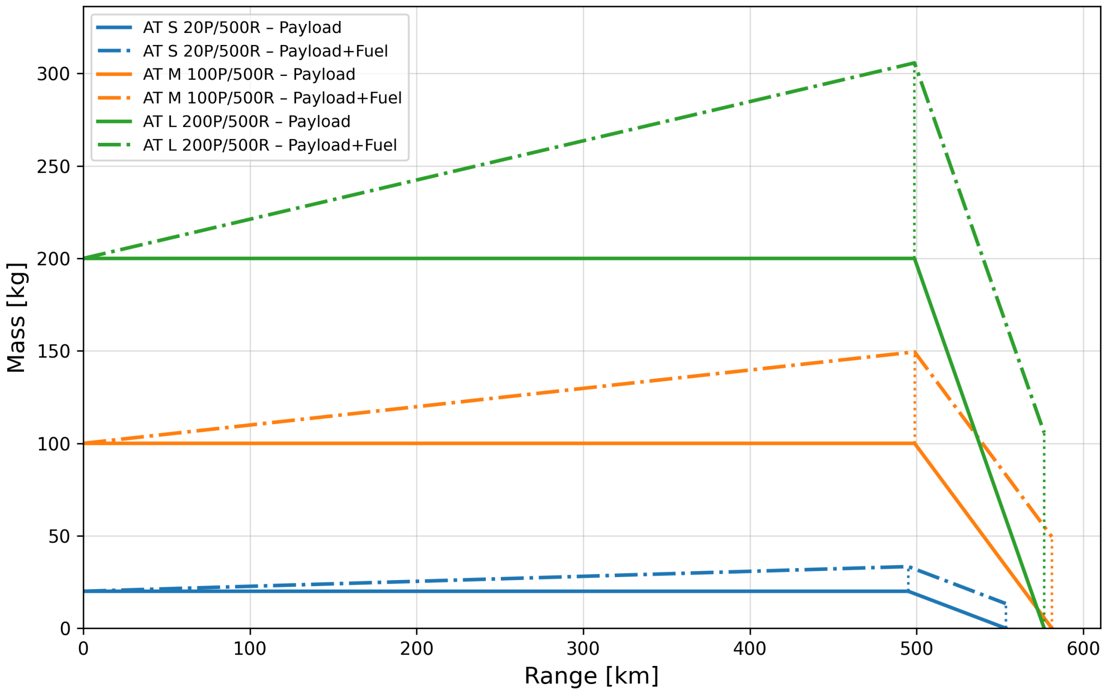

Figure D.2: Payload Range Diagrams for the Arctic Tern Designs with 500 km Design Range

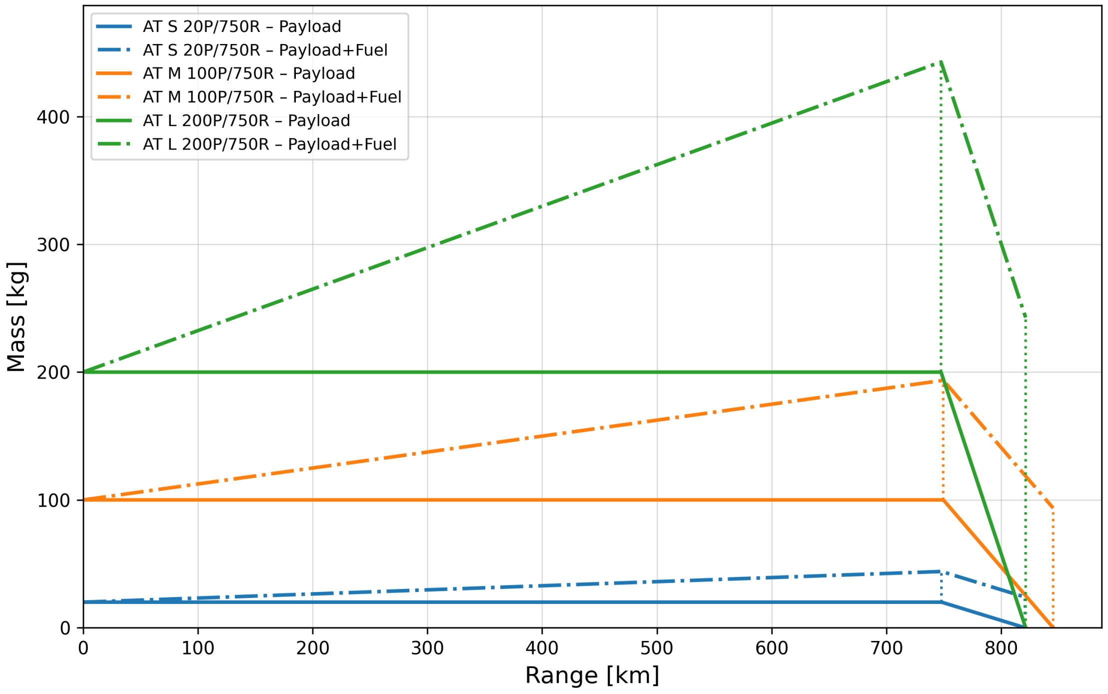

Figure D.3: Payload Range Diagrams for the Arctic Tern Designs with 750 km Design Range

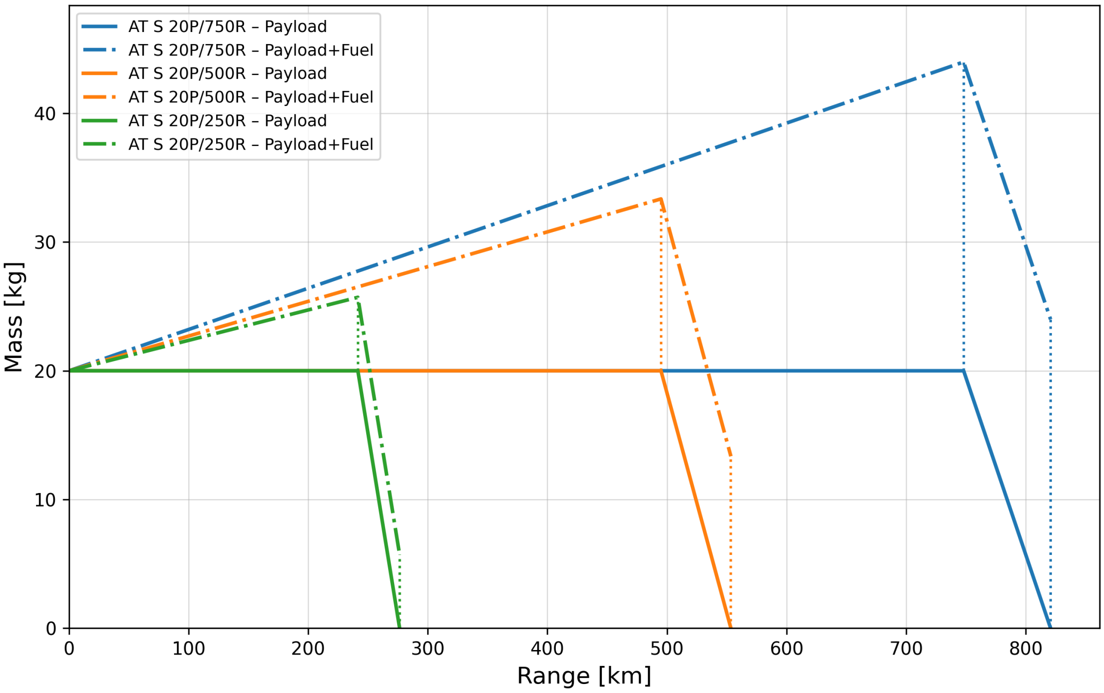

Figure D.4: Payload Range Diagrams for the Arctic Tern S Designs

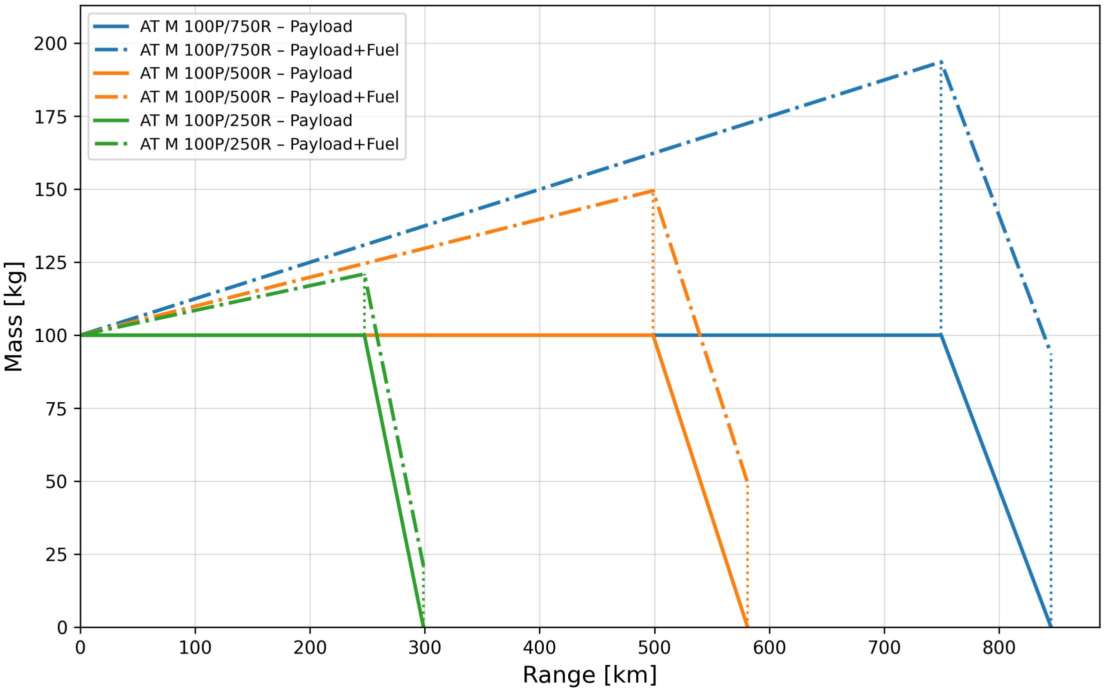

Figure D.5: Payload Range Diagrams for the Arctic Tern M Designs

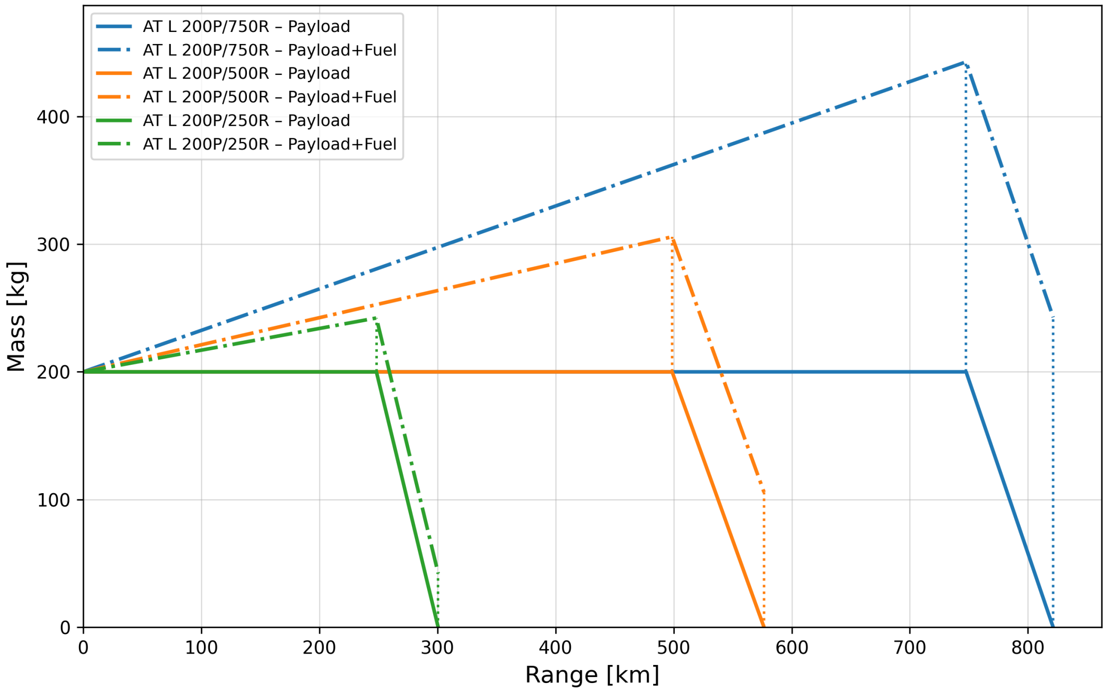

Figure D.6: Payload Range Diagrams for the Arctic Tern L Designs